Phase-Change Meta-Devices for Tuneable Bandpass Filtering in the Infrared

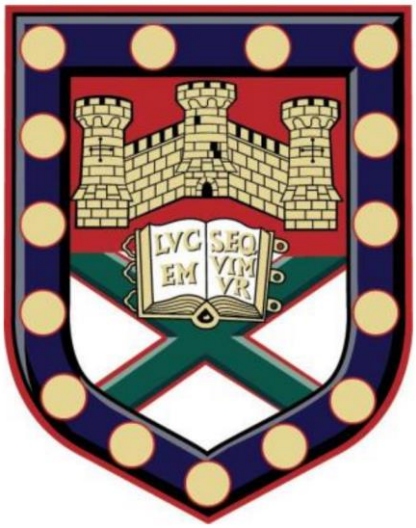

Liam Gareth Trimby

College of Engineering, Mathematics and Physical Sciences

University of Exeter

A thesis submitted for the degree of Doctor of Philosophy in Engineering

September 2019

Phase-Change Meta-Devices for Tuneable Bandpass Filtering in the infrared

Submitted by Liam Gareth Trimby to the University of Exeter as a thesis for the degree of Doctor of Philosophy in Engineering [CDT], September 2019.

Supervisors

C. David Wright[1]

Anna Baldycheva[1] Dan Hewak[2]

[1]Department of Engineering, Harrison Building, North Park Road, University of Exeter, EX4 4QF, UK
[2]Optoelectronics Research Centre, University of Southampton, SO17 1BJ, UK

I certify that all material in this thesis which is not my own work has been identified and that no material has previously been submitted and approved for the award of a degree by this or any other University.

Signature: ……..

Liam Gareth Trimby

September 2019

ABSTRACT

Tuneable light filters, especially those which are compact and fast to tune, are essential in a wide range of technologies, especially for multispectral imaging applications. However, state-of-the-art approaches to create such filters all possess drawbacks, with many wavelength regions poorly served. This thesis attempts to address this problem by combining metasurfaces which support extraordinary optical transmission (ultra-thin band-pass filters) with chalcogenide phase-change materials (adding dynamic tuneability).

The optical properties of phase-change materials are very different in their amorphous and crystalline states and switching between such states can be rapidly controlled via thermal excitations. In this work nine different phase-change materials, including alloys of GeTe, GeSbTe, GeSbSeTe and GaLaS, were optically and elementally characterised and assessed for their application-specific suitability. The resulting materials data was used to computationally design and evaluate a range of tuneable infrared filter device designs both optically and thermally. These filters exhibit high transmission (≈80% at best) with large spectral tuning ranges of approximately +50% relative to their shortest wavelength; this range is sufficient to cover entire atmospheric transmission windows. This is the first such combination of phase-change materials and extraordinary optical transmission for application from the visible through to long-wave infrared (14 μm) regions of the spectrum. A rigorous computational study was conducted to produce comprehensive design guidelines for such filters, and confirm the viability of in-situ electrical switching. Several filter devices were experimentally fabricated, and the viability for a number of applications, including tuneable filtering, chemical sensing and infrared displays, was investigated and confirmed computationally.

ACKNOWLEDGMENTS

First and foremost I would like to thank my supervisors at Exeter. David, for supporting my work, offering advice, and being very understanding about the numerous technical setbacks this project faced. I would like to thank my second supervisor Anna for offering genuinely positive feedback during the closing weeks of this thesis's creation. I'm very grateful for my collaborators in Southampton, Dan Hewak and Chris Craig, who provided significant support in terms of resources, and provided virtually all of my initial training despite me being from another institution. And Farah and Tanya at Cambridge who helped develop the chemical sensors in this thesis.

I would like to thank my friends from within the CDT who always provided a pleasant atmosphere in the lab if present; and especially to Angus and Joaquin for sympathising with my endless complaints about equipment shortages and breakdowns. I would also like to thank Arseny who taught me how to use several pieces of equipment when the usual channels were unavailable, and Yat-Yin, who helped significantly with the micro-heater switching studies in this thesis. My friends outside of the CDT were also hugely supportive, especially Bede, Aled, Kathryn, and Tybalt the cat, (who proved to be an excellent co-author of this thesis).

I'm extremely appreciative of the EPSRC and various companies/organisations which provided the financial and administrative support for my project. These include the Centre for Doctoral Training in Metamaterials at Exeter, QinetiQ, the Office of Naval Research Global, and the Chalcogenide Advanced Manufacturing Partnership.

Contents

LIST OF PUBLICATIONS AND PRESENTATIONS

Publications

1. **Liam Trimby**, Anna Baldycheva, C. David Wright "Phase-Change Band-Pass Filters for Multispectral Imaging", *Proceedings of SPIE, Photon. Phonon. Prop. Eng. Nanostruct., VIII,* Article 105412B. (2018)

2. S. G. C. Carrillo, **L. Trimby**, Y. Y. Au, V. K. Nagareddy, G. Rodriguez-Hernandez, P. Hosseini, C. Ríos, H. Bhaskaran, and C. D. Wright, "A Nonvolatile Phase-Change Metamaterial Color Display" *Adv. Opt. Materials,* vol. 1801782. (2019)

3. Jaoquin Faneca, **Liam Trimby**, Ioannis Zeimpekis, Matthew Delaney, Daniel W. Hewak, Frederic Y. Gardes, C. David Wright, and Anna Baldycheva "On-chip sub-wavelength Bragg grating design based on novel low loss phase-change materials" Optics Express. (2020).

4. E. Gemo, S. Vajjalakesava, **L. Trimby**, C. Ruiz De Galarreta Fanjul, S. García-Cuevas Carrillo, T. Bachmann, M. Riede, A. Alexeev, and C. D. Wright "A simple technique for refractive index determination of phase-change materials using nanocavity reflectometry", *Optical Material Express*. (under review)

5. **Liam Trimby**, Ioannis Zeimpekis, Christ Craig, Dan W. Hewak, C. David Wright, "GaLaS Phase-Change Material Properties for Optical Devices", *Optical Materials Express*. (in preparation)

6. **Liam Trimby**, Anna Baldycheva, C. David Wright "Design of phase-change EOT filters and their applications" *Journal to be selected.* (in preparation)

7. Yat-Yin, **Liam Trimby**, C. David Wright "Thermal Switching and Optical Properties of phase-change materials" *Optical Materials Express.* (In preparation)

The below publications are not directly related to the work of this thesis, but were nevertheless prepared during the funding period of this project.

8. Kunyapat Thummavichai, **Liam Trimby**, Nannan Wang, C. David Wright, Yongde Xia, and Yanqiu Zhu, "Low Temperature Annealing Improves the Electrochromic and Degradation Behavior of Tungsten Oxide (WOx) Thin Films", *J. Phys. Chem. C,* vol. 121, p 20498−20506. (2017)

9. Pablo Martinez Pancorbo and **Liam Trimby**, **"**Cradle-to-gate life-cycle assessment of future materials for commercial lithium-ion batteries: Raw materials issues", *Environmental Science & Technology*. (in preparation)

Presentations

1. **Liam Trimby**, Anna Baldycheva, David Wright, "Chalcogenide Perfect Absorbers for the Detection and Modulation of Infra-Red Radiation" *Defence Materials Forum*, Exeter, United Kingdom, 17th April 2016.

2. **Liam Trimby**, David Wright, "Phase-Change Metadevices Incorporating GaLaS", *Knowledge Transfer Network - Indstrial Applications of Metamaterials*, London, United Kingdom 29th March 2017.

3. **Liam Trimby**, Anna Baldycheva, David Wright, "Multispectral Imaging using Phase-Change Meta-Filters", SPIE West, San Francisco, California, 27th January – 1st February 2018.

4. **Liam Trimby**, Anna Baldycheva, David Wright, "Multispectral Imaging using Phase-Change Meta-Filters", 2nd International Symposium on Doped Amorphous Chalcogenides and Devices, Lake District, United Kingdom.

5. **Liam Trimby**, John Lincolin, Anna Baldycheva, David Wright, "Tunable Band-Pass Filters using Phase-Change Materials" *4th Cranfield Defence and Security Symposia*, Swindon, United Kingdom, 13th – 14th November.

6. **Liam Trimby**, Anna Baldycheva, David Wright, "Tunable Band-Pass Filters using Phase-change Materials", *European Phase-Change and Ovonic Symposium*, Catania, Italy, 8th – 10th September, 2018.

7. **Liam Trimby**, Anna Baldycheva, David Wright, "Tunable Band-Pass Filters using Phase-Change Materials", *Smart NanoMaterials, Advances, and Applications*, Paris, France, 10th – 13th December 2018.

8. **Liam Trimby**, David Wright, "Tunable Band-Pass Filters using Phase-change Materials", *MRS Spring 2019*, Phoenix, Arizona, 22nd – 26th April 2019.

9. **Liam Trimby**, Yat-Yin Au, and C. David Wright, "Electrical switching behaviour of $Ge_2Sb_2Se_xTe_{5-x}$ thin films using in-suti micro-heaters", *EPCOS 2019*, Grenoble France, 8th – 10th September 2019.

LIST OF FIGURES

List of Tables

LIST OF ABBREVIATIONS

Notation	Definition
PCM	Phase-change material
GST225	$Ge_2Sb_2Te_5$
GST326	$Ge_2Sb_2Te_5$
GSST2214	$Ge_2Sb_2Se_1Te_4$
GSST2223	$Ge_2Sb_2Se_2Te_3$
GSST2232	$Ge_2Sb_2Se_3Te_2$
GSST2241	$Ge_2Sb_2Se_4Te_1$
AIST	$Ag_{5.5}In_{6.5}Sb_{59}Te_{29}$
GLS	$Ga_{26}La_{14}S_{60}$
EOT	Extraordinary optical transmission
SEOT	Surface extraordinary optical transmission
LEOT	Localised extraordinary optical transmission
AIT	Absorption induced transparency
QCW	Quasi cylindrical waves
SPP	Surface plasmon polariton
LSP	Localised surface plasmon
PVD	Physical vapour deposition
AFM	Atomic force microscopy
EDS	Electron dispersive spectroscopy
XRD	X-ray diffractometry
XRR	X-ray reflectometry
RTA	Rapid thermal annealer
FTIR	Fourier transform interferometer
SNR	Signal-to-noise ratio
ENZ	Epsilon-near-zero
AOTF	Acousto-optic tuneable filters
RGB	Red, green, and blue
CMY	Cyan, magenta, and yellow
CRI	Colour reproduction index
PML	Perfectly matched layer

1 INTRODUCTION

Over the past few centuries optical light filters have gone from a curiosity to a ubiquitous component found in a wide array of different technologies and industries. Early uses of transmissive filters included reducing reflections or enhancing contrast in black and white photos, allowing infrared heat to escape the backside of an incandescent lamp, (while visible light was reflected), or simply to produce coloured lights. Modern filters are now found in medical equipment used for biological imaging and fluorescence microscopy, in optical telecommunications systems, chemical sensors, multispectral imaging systems, light detection and ranging (LIDAR), laser systems, automated quality control, and much more [1–3].

The simplest form of filter is simply a piece of material that absorbs unwanted portions of a light spectrum due to its molecular composition. More complex filters use thin-film coatings, such dichroic thin-film interference filters, or Fabry Pérot filters [4]. However, all these filters share a drawback, in that once fabricated their response is fixed. Dynamically tuneable filters however, open up a number of applications, with displays and multispectral imaging being of most interest to this thesis. There are several existing approaches to creating tuneable filters, which are discussed in sub-section 2.4.1. Each filtering approach has its own strengths and weaknesses. Generally speaking these filters are either slow to tune, only function over a narrow spectral region, are bulky, or have mediocre filtering performance. Therefore there exists a great need for compact, high performance transmissive filter technology which can be applied to spectral regions poorly served by more mature filter technologies. The work of this thesis attempts to address this by combining a type of plasmonic metasurface (provides fixed filtering) with phase-change materials (provides tunability).

The metasurfaces introduced in this thesis are designed to support extraordinary optical transmission (EOT), in which a thin metallic film patterned with an array of apertures is effectively transparent for a narrow spectral band, while all other light is predominantly reflected. Once a phase-change material (PCM) is incorporated

into the EOT filter, the resonance wavelength is modified by the optical properties of the phase-change layer. These PCMs can stably exist in either amorphous or crystalline phases (or an intermediate mixture), and can rapidly and repeatably switch between these phases via thermal excitations. This switching is fast, non-volatile, and produces significant contrast in optical (and electrical) properties. Temperatures above a certain threshold induce crystallisation, and even greater temperatures above the melting point followed by rapid quenching will cause the PCM to return to an amorphous glassy phase. A number of phase-change alloys (some being particularly novel) are experimentally characterised in chapter 4.

The filters developed in this thesis thus combine strengths of both plasmonic EOT filters and phase-change materials to create an ultra-thin, non-volatile, rapidly tuneable, band-pass transmission filter, with designs applicable from the visible to the long-wave-infrared. These phase-change EOT filters are thoroughly studied computationally in chapter 5; the resulting design guidelines used in chapter 6 to explore the use of these filters in a variety of areas, with multispectral imaging, chemical sensing and IR displays found to be particularly well suited applications.

1.1 THESIS OUTLINE

Chapter 2 provides background information on metasurfaces and extraordinary optical transmission. It then details the properties and switching mechanism of phase-change materials. Finally, chapter 2 explores current filter technology and the typical applications to which they are applied.

Chapter 3 covers the experimental and computational methods employed throughout this work. These methods are broadly split into three sections. Firstly computational methods used to design and optimise tuneable filters are detailed. Secondly, materials characterisation methods, which covers materials processing techniques, the evaluation of optical properties, and ease of phase-switching for a variety of phase-change materials. And finally, the methods with which the filters were fabricated and their performance evaluated are described.

Chapter 4 concerns the materials characterisation work, in which nine phase-change alloys are studied. The PCMs studied in this work are: GeTe, two alloys of germanium, antimony and tellurium, ($Ge_2Sb_2Te_5$ and $Ge_3Sb_2Te_6$), four selenium doped variants of the previous alloy, in which tellurium is substituted for selenium, ($Ge_2Sb_2Se_1Te_4$, $Ge_2Sb_2Se_2Te_3$, $Ge_2Sb_2Se_3Te_2$, $Ge_2Sb_2Se_4Te_1$), and finally two alloys which were suspected to possess especially good phase switching qualities for tuneable filter applications, ($Ag_{5.5}In_{6.5}Se_{59}Te_2$ and $Ga_{13}La_7S_{30}$). This is the first work to report on the crystalline properties of the alloy made from gallium, lanthanum and sulphur (GLS).The primary (but far from only) method used to extract optical properties (i.e. the real and imaginary index of refraction) was ellipsometry. The ability of the various PCM alloys to switch between phases was studied using micro-heater devices fabricated using e-beam lithography.

Chapter 5 details an extensive modelling study which initially explores the general characteristics of EOT filters (without a PCM). Specifically the impacts of varying different geometrical parameters are presented, and the impacts of different material properties are investigated. The chapter then moves onto the inclusion of PCMs, initially determining the most suitable way to incorporate the PCM into the EOT structure. The ideal PCM properties and thicknesses (depending upon application and spectral region) are identified and discussed. Finally, the ability of a metallic EOT structure to act as a Joule heater for in-situ electrically driven PCM phase transitions is investigated, and confirmed for some material and structural combinations.

Chapter 6 initially details the fabrication and testing of phase-change EOT filters. The chapter then moves onto assessing the viability and performance for three applications to which these filters should be well suited. These applications are multispectral imaging, chemical sensing, and displays, both visible and IR. For all applications niche scenarios are identified in which using the filters designed in this work would be a sensible choice. Of note is the multispectral imaging, in which the filters designed here may be a particularly good candidate. The chapter concludes by introducing two other metasurfaces incorporating the PCM $Ga_{13}La_7S_{30}$ which could serve as visible displays.

1.2 THESIS OBJECTIVES

The primary goal of this work was to explore the addition of phase-change materials into metasurfaces which use the EOT effect to filter light. This objective is split between understanding and optimising the filter devices, and exploring novel phase-change alloys which may provide superior performance or enable alternative functionalities. Objectives and key questions can be summarised as follows:

- **Investigating novel phase-change alloys**
  - Study the elemental and structural composition of the PCMs.
  - Rigorously characterise the optical properties of the PCMs.
  - Quantitatively study the thermal switching properties of the PCMs, and identify which are most easily and fully switchable.
  - How do the properties of these alloys compare?
- **Design of phase-change EOT filter devices**
  - Understanding how filter geometry effects the performance, such that the desired performance can be easily chosen for new designs.
  - How to best incorporate phase-change materials to add dynamic tunability to EOT filters?
  - How do the material properties effect a fixed EOT filter?
  - How does the device geometry and material properties effect the filters ability to use electrical joule heating to switch the PCM?
  - How to best fabricate these filter devices? And do they perform as well as simulations suggest?
  - Explore a variety of potential applications which make good use of the particular qualities of these filters.

In terms of extending the state-of-the-art and original knowledge, this thesis makes a number of contributions. These include:

(i) Systematic design of phase-change based EOT filters, in particular for their use in multispectral imaging applications (reported in publications 1 and 6).

(ii) Evaluation of the suitability of 'alternative' phase-change materials (including GaLaS and GeSbSeTe alloys) for meta-device type applications in the infrared, including their relative ability to phase-change (to be reported in publication 7).

(iii) In addition a novel method for the extraction of refractive index (n and k) of thin films using a reflectrometry based approach has been developed with colleagues (to be reported in publication 4)

(iv) Characterisation of the fundamental material properties of GaLaS thin films (to be reported in publication 5)

(v) Exploration of a number of novel visible and infrared display concepts (reported in publication 2).

2 BACKGROUND AND THEORY

This chapter details the concepts and ideas used and expanded upon in this thesis. Specifically the topics of metasurfaces, light filtering, extraordinary optical transmission (EOT) and phase-change materials are covered.

First, metasurfaces are introduced, which are the broad category within which the devices in this work fall into. This then expands into extraordinary optical transmission and plasmonics, which are the effects exploited by the filter devices in this work. Phase-change materials (PCMs) are then introduced, starting with their history and development, then their switching mechanisms and properties are explored. The combination of metasurfaces / EOT filters with PCMs is then discussed. This is an area of significant technological interest, and various approaches to adding reconfigurability to metasurfaces are first reviewed before moving onto phase-change metasurfaces and the advancements in this area. Finally, three applications to which the devices designed in this work should be well suited are discussed, along with other state-of-the-art approaches.

2.1 METASURFACES AND EXTRAORDINARY OPTICAL TRANSMISSION

This section introduces the concept of metasurfaces, and briefly covers some of the more intriguing advancements within the field, such as electromagnetic cloaking, solid-state beam steering, and negative refractive index. Extraordinary optical transmission is then introduced, and research concerning this topic is reviewed.

2.1.1 Metasurfaces in General

Metasurfaces (the 2D version of metamaterials [5]) are artificial materials whose surfaces are periodically structured with sub-wavelength features (resonators) which can provide exotic material properties not typically found in nature; these include properties such as negative refractive index [6], perfect absorption [7], non-specular reflection [8], and much more as explored briefly later in this chapter [9]. Metasurfaces are a relatively young field of research, which began gaining traction at the turn of the millennium. Before the field of metamaterials was formalised there was already significant pioneering work into plasmonics [1-2], and frequency selective surfaces [11].

The field of metamaterials and metasurfaces provides a toolset in which ultimate control of light (polarisation, phase, and amplitude) is theoretically possible. This is achieved by careful selection of surface geometry (typically subwavelength resonators, called meta-atoms) and materials such that the incident wave induces the desired electric and magnetic dipole moments onto the surface. Early metasurfaces had resonator dimensions of the same order as the wavelength that the surface was designed to interact with; and these were used in a variety of devices such as Fresnel plates, chirped lenses, reflect-and-transmit arrays and frequency selective surfaces [12,13]. More recently, with advancements in nanoscale fabrication and 3D printing, it became apparent that superior control of electromagnetic waves is achievable via the use of smaller, sub-wavelength structures, which restrict the generation of unwanted diffraction orders. These

sub-wavelength structures generally possess both magnetic and electric polarisations and allow for (theoretically) full control over the distribution of electromagnetic waves and their transmission and reflection. Figure 2.1 below illustrates a portion of the great variety of metasurface functionalities [14].

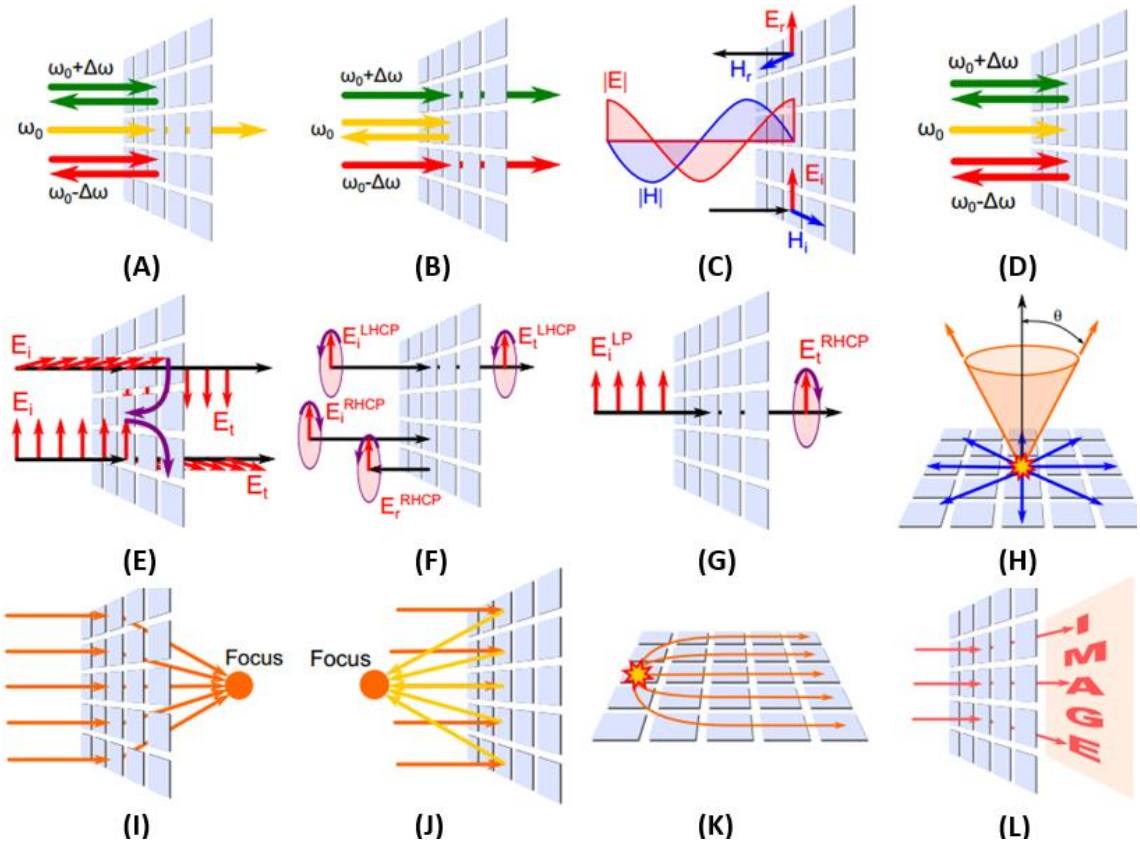

Figure 2.1. Example of some metasurface functionalities. **(A)** Band-pass frequency selective surface. **(B)** Band-stop frequency selective surface. **(C)** High impedance surface. **(D)** Narrow-band perfect absorber (MMPA). **(E)** Twist polariser. **(F)** Right-handed circular polarisation frequency selective surface. **(G)** Linear to circular polarisation converter. **(H)** Two-dimensional leaky wave antenna with conical beam pattern. **(I)** Focusing transmit array. **(J)** Focusing reflect array. **(K)** Flat luneburg lens. **(L)** Hologram projection. Reprinted from [14].

So far we have focused upon nano-scale electromagnetic metasurfaces; however, the field is very broad and also includes larger structures designed to interact with micro or radio waves. For example, Figure 2.2A shows a 3D printed radio frequency concave lens with a structural periodicity in the millimetre range. Unlike normal concave lenses which radiate waves out like spokes on a wheel, this lens focuses radio waves into a single point, demonstrating negative refractive index [15]. A number of mechanical structures can also be considered

metamaterials/metasurfaces; these materials are still built from smaller 'meta-atoms' but exhibit unusual mechanical responses (rather than electromagnetic) to mechanical stimuli due to their structure rather than molecular composition. Figure 2.2B shows the structure of one such mechanical metamaterial, in which stretching in one direction causes the material to expand perpendicularly, resulting in a negative poissons ratio (auxetic) [16]. There also exists a strong analogue between electromagnetic and acoustic waves, and many acoustic metamaterials/metasurfaces have been demonstrated, such as acoustic waveguides and lenses. Figure 2.2C shows an acoustic metamaterial lens made from cola cans capable of focusing beyond the diffraction limit of sound [17]. The remainder of this work will focus exclusively on devices which operate in the visible and infrared, such as the perfect absorber device structure shown in Figure 2.2D [18].

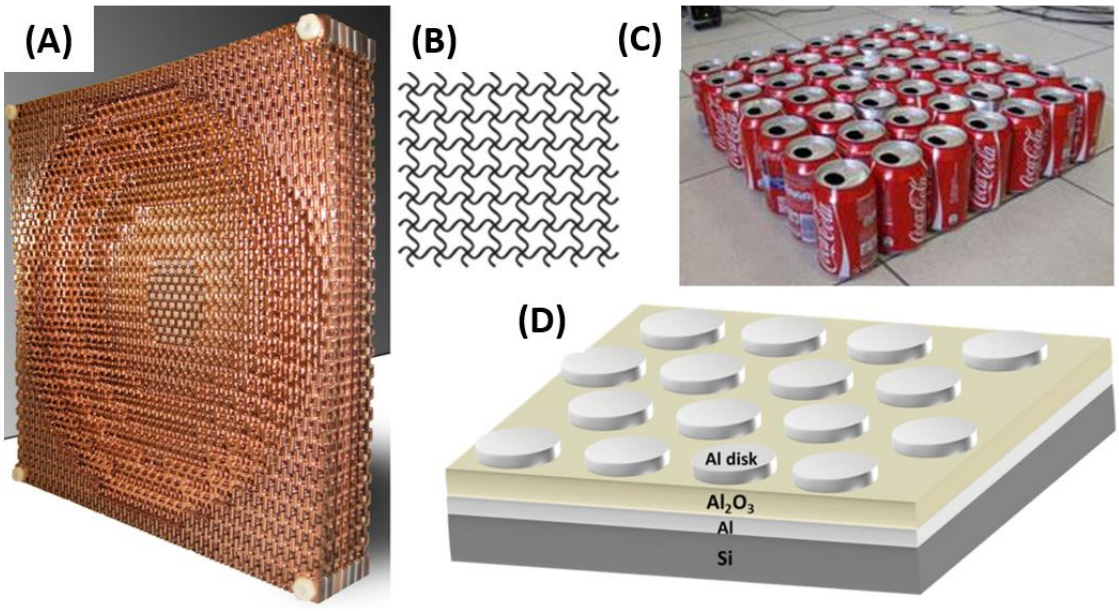

Figure 2.2. Examples of the variety of types of metamaterials/metasurfaces, highlighting the different scales and types of energy they can interact with. **(A)** Image of a 3D printed metamaterial radio frequency lens with negative refractive index. Reprinted from [15]. **(B)** Schematic structure of a mechanical metamaterial with negative Poissons ratio (auxetic). Reprinted from [16]. **(C)** Image of an acoustic metamaterial lens created using cola cans. Reprinted from [17] **(D)** CAD drawing of a metasurface perfect absorber. Reprinted from [18].

Initial research into metamaterials developed a number of analytical methods to aid in the understanding, design, and optimisation of these structures. The most notable of these analytical methods is transformation optics [19]. This involves transforming the coordinate system into one which distorts the path light would

take through it into whatever is desired, see Figure 2.3. This coordinate transformation implies a spatially non-uniform refractive index change, which can be extracted by re-writing Maxwell's equations in the new coordinate system and solving for the permittivity and permeability [20]. The required distribution of permittivity can then be achieved by distributing electromagnetic resonators, forming a metasurface/metamaterial.

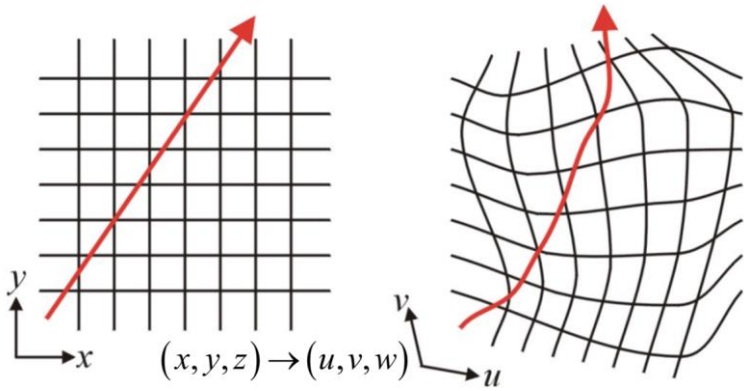

Figure 2.3. Example of light path being distorted due to a coordinate transform. Adapted from [21].

Nowadays sufficient computational power is readily available to accurately model, analyse, and optimise metasurface designs using finite element methods. In the past decade metasurfaces have seen a boom in research interest [22], with new structures and applications frequently being discovered and refined, thanks in part to the rapid and dramatic improvements in both computational power for design simulations. Improvements in nano-scale fabrication technology, driven by the semi-conductor industry, have also enabled the design of metamaterials and metasurfaces which interact with increasingly shorter wavelengths, now including visible light.

No introduction to metamaterials/metasurfaces would be complete without briefly discussing electromagnetic cloaking; a good example of a metamaterial made possible by developments in transformation optics [23]. These cloaks work (for a narrow wavelength band) by using a coordinate transformation to compress space from a volume (to be cloaked) into a shell surrounding that volume which incident waves are guided around, see Figure 2.4A. Because of the form-invariance of Maxwell's equations, only the components of the permittivity and

permeability are affected by the transformation [24], becoming spatially varying and anisotropic. Through careful design of these material properties the cloak plus the concealed volume appears to be free space when externally viewed. This was experimentally realised using split ring resonators, see Figure 2.4C.

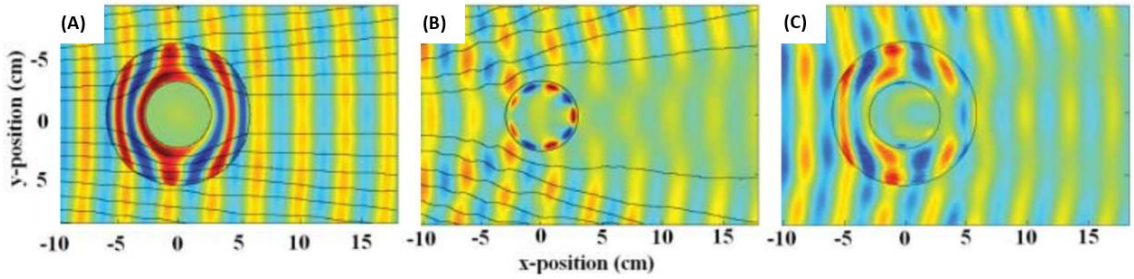

Figure 2.4. Snapshots of steady-state electric field intensity for an electromagnetic cloaking device. **(A)** Simulated performance of the cloak surrounding a copper cylinder. **(B)** Experimental measurement of bare copper cylinder. **(C)** Experimental measurement of copper cylinder concealed with the cloak. Adapted from [25].

2.1.2 Extraordinary Optical Transmission (EOT)

Light propagation through apertures has been thoroughly studied for centuries. While it was known that light transmits well through apertures much larger than its wavelength, this transmission rapidly (fourth power dependence) decreases as the aperture size approaches the wavelength, with sub-wavelength apertures yielding minimal far-field radiation [26].

This view remained accepted until 1998, when Ebessen et al. first introduced the concept of extraordinary optical transmission (EOT), and demonstrated that an array of appropriately spaced sub-wavelength apertures exhibits orders of magnitude greater transmission than that predicted by standard aperture theory [27]. A consequence of this enhancement is greater than unity transmission efficiency when normalised to the area of the apertures, due essentially to the high concentration of fields within the apertures. This phenomenon can be observed for a wide range of wavelengths, from visible to microwave, and is the primary resonance mechanism the devices in this thesis exploit.

It has taken many years to fully understand the EOT phenomenon due to the large number of effects which contribute towards the high transmission, with such

contributions depending on the wavelength regime. There are also many forms of EOT which depend on the distribution (isolated, random, periodic) and size of the apertures, and whether the metal layer is smooth or has been selectively corrugated, all of which are discussed later.

Initially it was believed that EOT could be fully explained by incident light exciting propagating surface plasmon polaritons (SPPs); these are collective oscillations of free electrons at a metal-dielectric interface [28,29]. These plasmons would encounter an aperture and propagate through it, re-radiating out and appearing like the original incident light. Subsequent research showed that plasmonics alone could not fully describe this phenomenon [30]. Coupling between evanescent waves and Quasi-cylindrical waves (QCW) were predicted to be the other contributing factors [31,32]. The relative contribution of QCW depends greatly upon the density of apertures, with the QCW only being significant for arrays with a periodicity similar to and shorter than the resonant wavelength [33]. This is the case for devices in this thesis, especially once the PCM layer has been deposited, which redshifts the resonant wavelength relative to a bare metal EOT structure.

The standard EOT case involves square arrays of sub-wavelength circular apertures with a periodic spacing $p_{m,n}$, in which m and n are integer values denoting the SP coupling order, i.e. whether the aperture spacing is to the nearest neighbour, next-nearest neighbour, etc, as shown in Figure 2.5. When referring to the period (p) more generally then the first order spacing is being discussed, with $p = p_{1,0} = p_{0,1}$. A simple way to conceptualise these EOT structures is as a diffraction grating in which light that diffracts sufficiently so as to make it in-plane with the EOT surface can then couple into the EOT structure. For normally incident light this diffraction angle θ is 90°, requiring that the spacing d between diffractive elements (EOT apertures) be equal to the desired resonance wavelength λ. This is described by equation $m \cdot \lambda = d \cdot sin\,(\theta)$ (1 below, in which m is the diffraction order, equal to 1 in this case.

$$m \cdot \lambda = d \cdot sin\,(\theta) \tag{1}$$

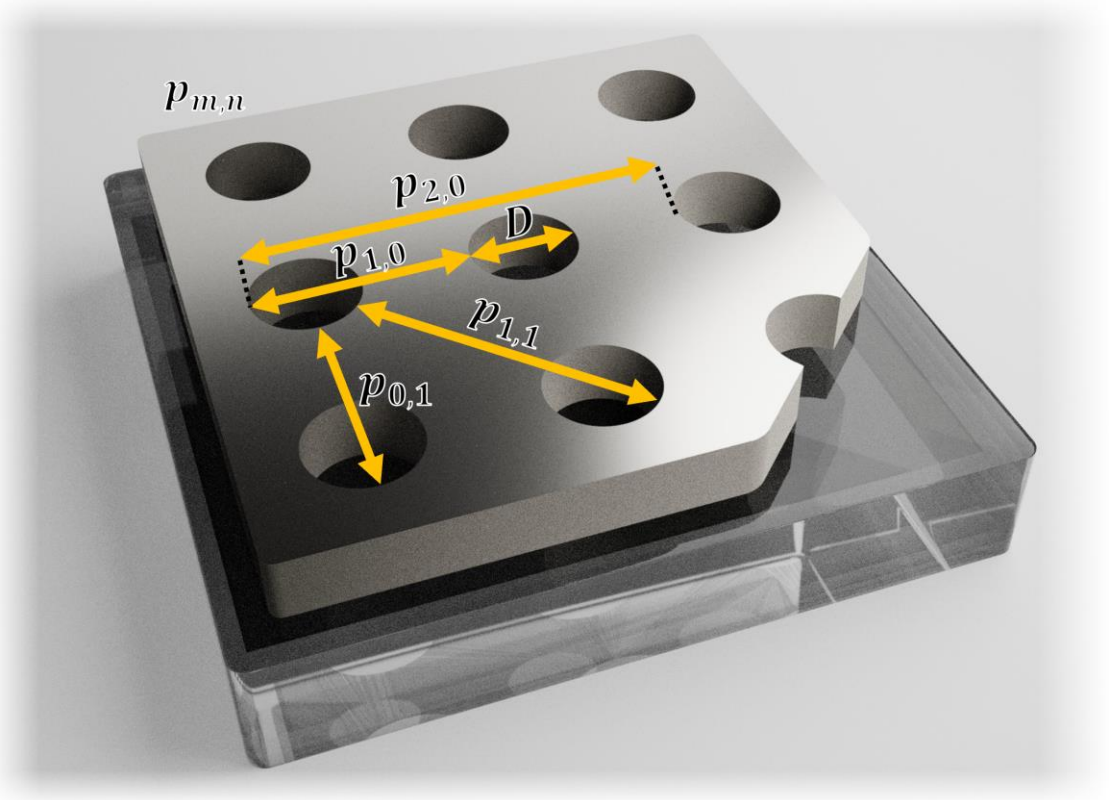

Figure 2.5. Diagram of typical EOT surface (Blender, cycles renderer). Circular apertures (in a metal, on a transparent substrate)) are arranged in a square array with a spacing to their nearest neighbours of p_{10}, and p_{11} to their next nearest. The aperture diameter D is $\frac{1}{2}p$ in this case.

2.1.2.1 Types of EOT

Extraordinary optical transmission has become an umbrella term referring to a number of resonant conditions which can occur in either isolated or arrayed apertures. These different EOT mechanisms can occur simultaneously, and their presence depends upon the shape, size, and distribution of the apertures, as well as the properties of surrounding materials. The ability of the metal to support plasmons in a given wavelength regime, and the thickness of this metal also plays an important role.

Surface enhanced EOT (SEOT) can be considered the conventional EOT mechanism, it was the first demonstrated [27], and is the primary EOT mechanism present in this thesis' devices. The primary mechanism for SEOT is the coupling of light into electromagnetic surface modes present at the dielectric-metal interfaces. A continuous metal film already possesses TM surface modes

(surface plasmon polaritons); however, these SPPs cannot normally be excited by incident radiation as both momentum and energy would not be conserved. The apertures modify the surface mode, relaxing the momentum conservation and allowing incident light to couple into the plasmons, meaning light that would have been reflected now remains at the dielectric-metal interface continually re-illuminating the hole with a chance of radiating out [34]. This coupling is very efficient thanks to the high density of local EM surface mode states. The transmission is greatest when the surface modes at both the substrate and superstrate interfaces occur for the same wavelength [35] (i.e. matched refractive indices either side of metal).

SEOT can be thought of as a Fano resonance as it occurs whenever two localised surface modes are able to weakly couple together through the aperture and into a radiating mode; this also contributes to the asymmetrical EOT resonance shape. This transmission mechanism is very general, and explains the existence of EOT even in regimes where plasmons cannot exist, such as the microwave. For these regimes in which metals act as perfect conductors, they are still able to support bound surface EM modes to support the enhanced transmission. This is because the metallic patterning causes the metal to exhibit an effective finite plasmon frequency. Ultimately the transmitted light is a combination of enhanced radiation from the surface plasmons and other contributions due to general diffraction.

Figure 2.6A shows an diagram illustrating EOT, in which the transmission wavelength λ_{res} occurs immediately after the first order $\lambda_{SP(1,0)}$ SP resonance. This is attributed to the coupling between nearest neighbour apertures. The second order SP resonance $\lambda_{SP,(1,1)}$ also corresponds to a transmission peak (of lower amplitude and shorter wavelength), and is due to coupling to the next nearest neighbouring aperture, see Figure 2.5B. The spectral location of the plasmonic resonances can be calculated using equations 2 and 3, in which m and n are integers representing the SP order, p is the periodic aperture spacing and ε_s and ε_m are the real parts of the relative permittivities of the substrate and

metal respectively [36]. These equations are only for the case where the superstrate is air, and have the following form.

$$\lambda_{SP,(m,n)} \approx \frac{\Delta_T}{\sqrt{m^2+n^2}} \tag{2}$$

$$\Delta_T = p \cdot \sqrt{\frac{\varepsilon_s \cdot \varepsilon_m}{\varepsilon_s + \varepsilon_m}} \tag{3}$$

The magnitude of the metal's real permittivity is substantially greater than that of the substrate (assuming a dielectric is used), resulting in $\Delta_T \approx p \cdot \sqrt{\varepsilon_s}$. For the first SP order ($m^2 + n^2 = 1$), equation 2 therefore closely resembles that of the Rayleigh wavelength, which in this case can be used to quickly estimate the primary SEOT resonance wavelength, see equation 4. This results in the wavelength of peak transparency (λ_{res}) occuring at a slightly longer wavelength than the Rayleigh wavelength, $\lambda_{res} > \lambda_R$.

$$\lambda_R = n_s \cdot p \tag{4}$$

λ_R denotes the minimum wavelength at which all incident light is transmitted as a single diffraction order, with all other diffraction being evanescent only. n_s is the substrate refractive index, and p is the periodicity (aperture spacing) of the array. Therefore the peak transmission wavelength is primarily determined by the properties of the surrounding dielectrics, and by the spacing between apertures. Aperture size, shape, and depth play a minimal role in resonant position, but do affect the shape of the resonance.

Unlike the other forms of EOT, in SEOT the cut-off wavelength λ_C is shorter than the Rayliegh wavelength, as shown in Figure 2.6B. This cut-off wavelength is determined by the aperture diameter (D), and is described by $\lambda_C = 2D$. If this wavelength becomes greater than the Rayleigh wavelength then the structure will not support SEOT.

By expressing the aperture diameter (D) as a proportion of their periodicity (p) yields $d = \frac{D}{p}$, the cut-off wavelength can then be described by $\lambda_C = 2d \cdot p$. Recalling that $\lambda_C < \lambda_R$ and re-arranging leads to equation 5. This places an upper limit upon the aperture size as a ratio of the aperture spacing (effectively a fill

factor); this limit is 50% for a metallic film surrounded by air, and larger for substrates with a refractive index greater than one (this is evident in Figure 5.9, in which the effects of aperture diameter are computationally studied).

$$d < \frac{1}{2} n_s \tag{5}$$

Localised EOT (LEOT) occurs in isolated apertures, and therefore the response is primarily determined by the aperture shape and size, rather than by their arrangement and spacing. The metal thickness and dielectric environment remain critical parameters [34].

This transmission has been attributed to localised surface plasmon modes at the edges of the apertures. These SPPs are present in the devices in this thesis, with the localised plasmons clearly present at the aperture edges in simulations (see section 5.1); however, it is a minimal contribution compared to SEOT.

Absorption-Induced Transparency (AIT) is a counter-intuitive effect in which the incorporation of an absorbing material within the apertures of an SEOT array may move the resonance wavelength near the region absorbed by the additional material. For example, the red absorbing dye added in Figure 2.6C increased transmission for red wavelengths [37]

This is because near a sharp absorption band (an electronic transition energy) of a material, the real part of the dielectric constant is high, and the imaginary part is relatively low [38]. This high refractive index path through the hole can act as a waveguide, working much like LEOT. If the absorbing material also coats the metallic surface, then it may also strengthen a weakly bound surface mode such that SEOT can also contribute towards the enhanced transmission.

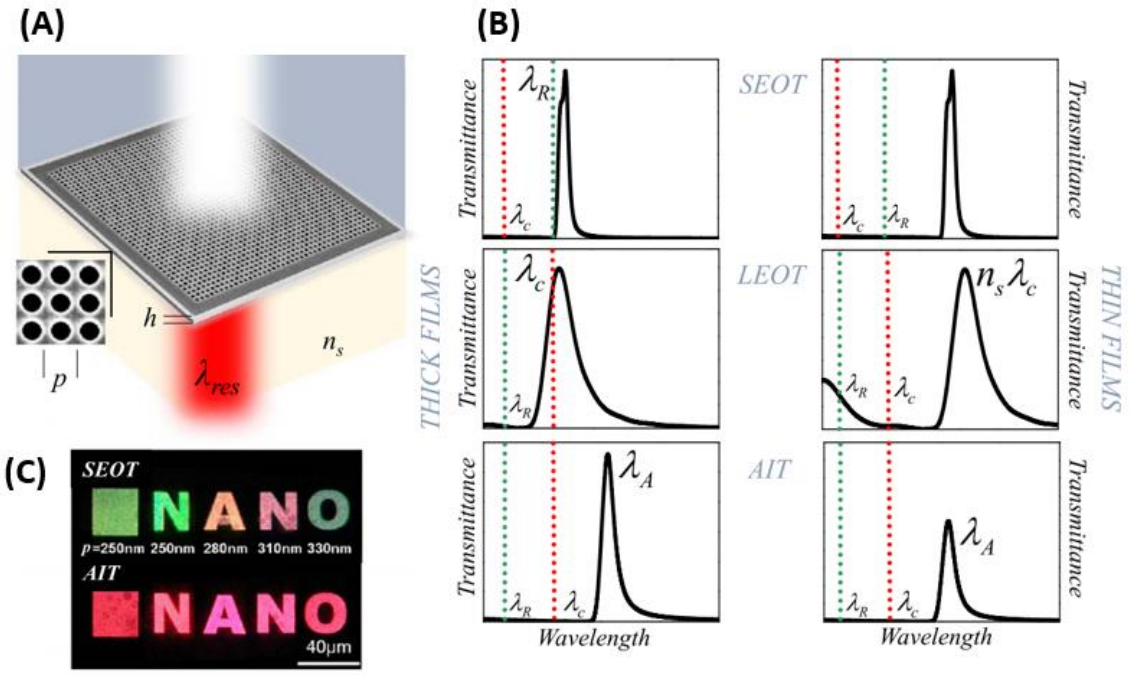

Figure 2.6. General overview of the types of EOT. **(A)** Typical setup for EOT in which a metallic array of thickness *h* sits upon a dielectric substrate of refractive index n_s patterned with circular apertures arranged in a square pattern with spacing p. In this case the filter is illuminated with white light, and transmits only red. **(B)** Example transmission of the different EOT mechanisms for both thick ($h < 2\lambda_{res}$) and thin films ($h \ll \lambda_{res}$). **(C)** Top is a micrograph image of SEOT filters of different periodicities to produce different colours. Bottom is after depositing a red dye to induce AIT which shifted all transmission towards the same red wavelength. Reprinted from [34].

The films in the work of this thesis can be considered metallically thin, and generate a hybrid of SEOT and LEOT modes. While the aperture spacing and material permittivity remain the primary parameters to control the resonance wavelength (like in SEOT), the shape of the resonances observed in this work's devices more closely resembles LEOT. There are plasmonic contributions from the metals, quasi-cylindrical wave contributions from the relatively high aperture density, and wave guiding contributions from the high dielectric constants exhibited by phase-change materials [39].

2.1.2.2 Alternatives to Circular Apertures

The standard aperture shapes used in EOT are circles; they are simple to model and fabricate, and are insensitive to polarisation. However, varying from this norm can greatly modify the behaviour of EOT filters; this includes the addition of new functionalities, such as polarisation selectivity.

High aspect ratio apertures (rectangular, annular, or triangular) can further enhance transmission by supporting additional localised EM modes [40,41]. However, this adds a degree of polarisation sensitivity.

Ellipse and slanted side walls on apertures effectively increase the surface area available to collect light when compared to straight walls. See Figure 2.7. This can further enhance transmission, and broadens the transparent region [42].

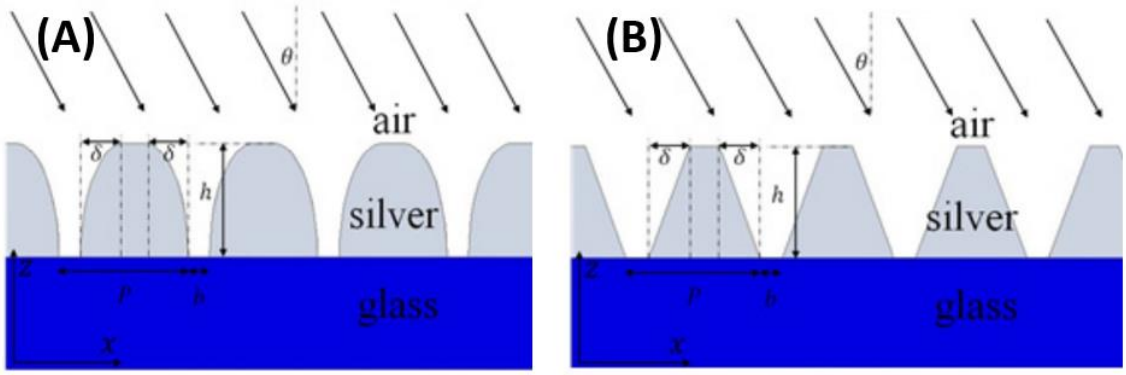

Figure 2.7. Schematic (side view) of tapered apertures. **(A)** Elliptically tapering **(B)** straight tapering. Reprinted from [42].

Bullseye rings or corrugation around a single hole drastically enhance transmission for LEOT, and marginally enhance SEOT [43,44]. This is because the rings help reflect and confine SPP propagation closely around the hole, thereby improving optical throughput. This large enhancement is present even for just three rings. The patterning on the radiating side of the structure results in strong angular confinement of transmitted light. These rings can be structured in a number of ways. Shown in Figure 2.8 is the case of sharp rings, as this appears to offer the greatest enhancement [43]. The rings can also be rounded, or cut into the metal surface rather than extruded out from it.

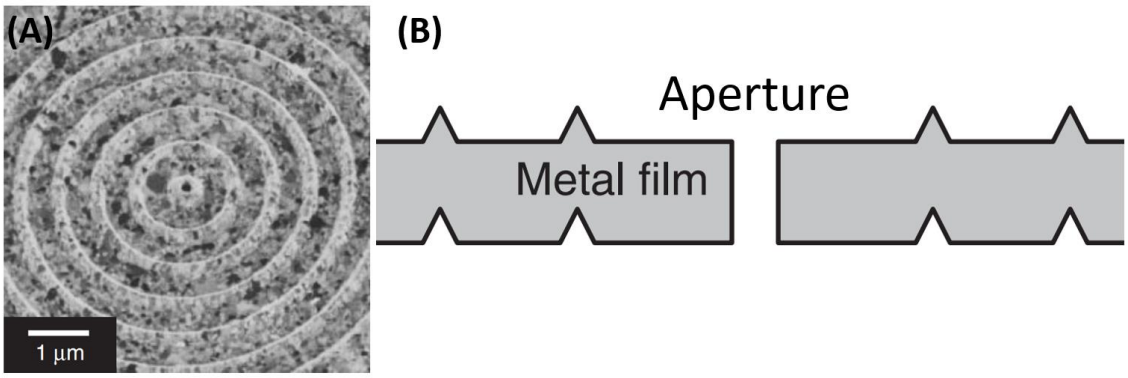

Figure 2.8. 'Bullseye' structure. **(A)** Scanning-ion microscope image of a fabricated device. **(B)** Schematic side view of bullseye rings. Adapted from [43].

Annular apertures (that is, those with a pillar of metal within them), appear to enhance transmission despite reducing the aperture area [45]. This is because they support additional guided modes through the structure, in a manner that is analogous to coaxial cables. This also results in a reduced sensitivity to angle of incidence, especially for the primary peak. See Figure 2.9.

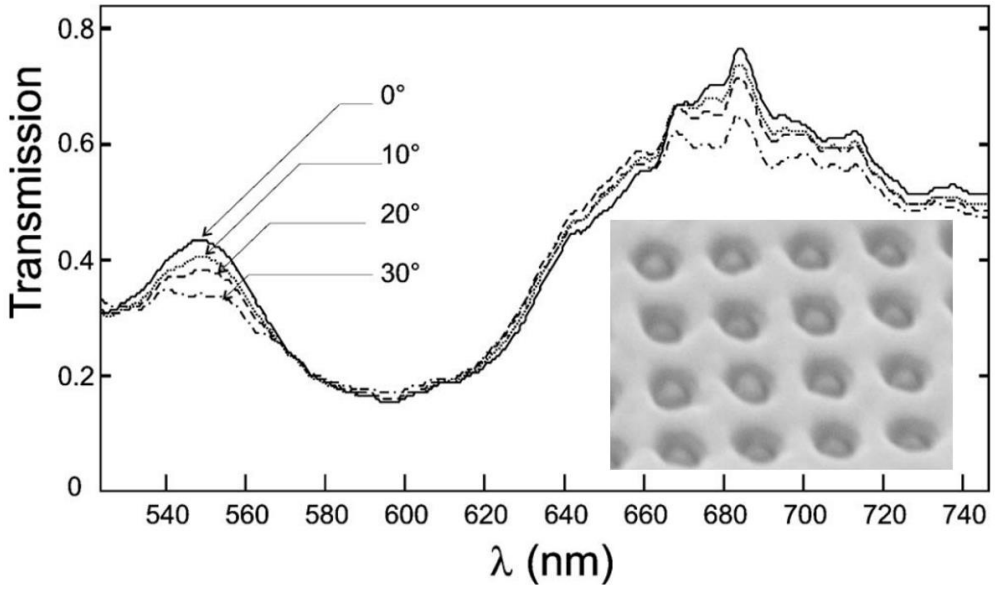

Figure 2.9. Transmission for different incident angles through an annular aperture array fabricated in 100 nm thick silver. **Inset:** SEM image of fabricated device. Adapted from [45].

An even greater level of angular insensitivity can be achieved with cross shaped apertures. See Figure 2.10. This approach not only has an advantage over annular apertures in terms of fabrication simplicity but allows good control over the characteristics of localised surface plasmons by modifying the arm length to width ratio. This means the localised surface plasmons (LSPs) and SPPs can be

well separated, so the SPPs don't significantly influence the LSPs at highly oblique angles and therefore maintain the shape and spectral location of the transmission. The polarisation sensitivity of this design can also be tailored by modifying the cross arms in only a single axis.

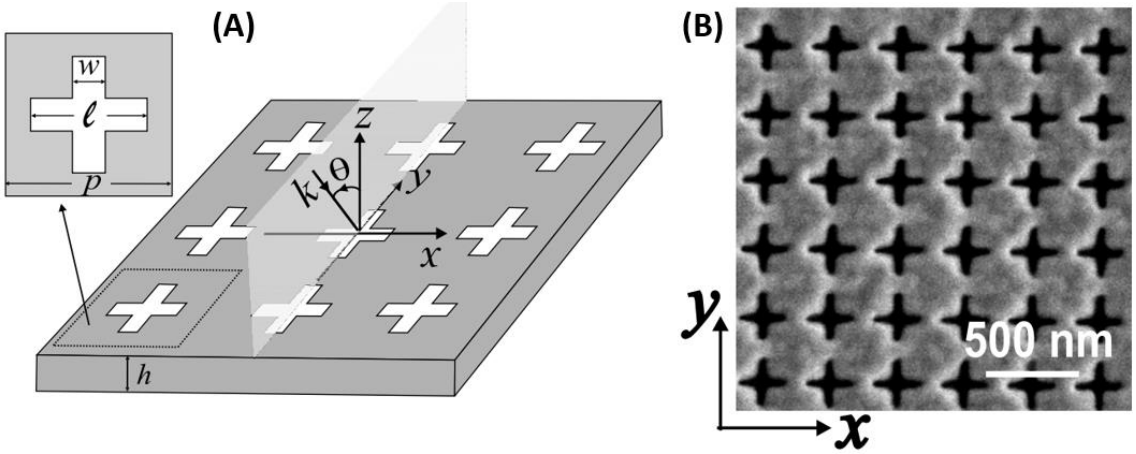

Figure 2.10. Schematic (top view) of cross shaped apertures. **(A)** Computer generated 3D image. **(B)** SEM image of fabricated device in silver for operation in the visible. Reprinted from [46].

EOT can manifest in continuous films that do not have apertures through the entire metallic layer, although the transmitted intensity is somewhat attenuated relative to the standard EOT configurations [47]. In this case a continuous metallic layer is shaped with depressions, in which the metal is very thin at the bottom, as shown in Figure 2.11. The variations in metallic thickness are what allow the formation of surface plasmons. The main advantage of this configuration is the ease of fabrication. A soft material such as polystyrene is easily spin coated (in solution) and then patterned using a stamp. A metal can then be sputtered at an angle and with rotation to produce a continuous film with varying thickness.

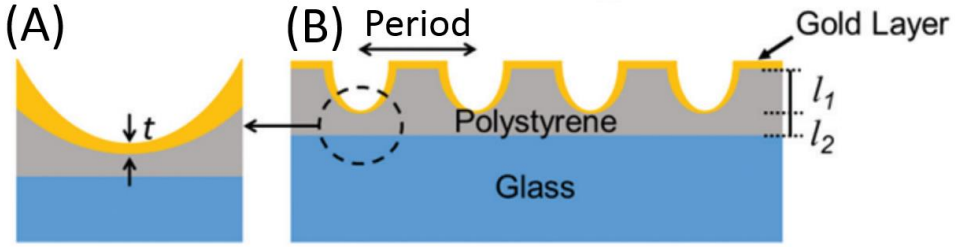

Figure 2.11. (A) Magnified view of the encircled region. **(B)** Cross sectional view of the gold-coated imprinted polystyrene surface with tapered depressions. Adapted from [47].

2.2 PHASE-CHANGE MATERIALS

2.2.1 Introduction and History

Phase change materials (PCM) are a class of alloys which can be structurally changed in a non-volatile manner via thermal excitation, see Figure 2.12. These structural changes produce significant changes in material properties. The discovery of phase-changing electrical properties dates back to pioneering work conducted by Alan Tower Waterman at Yale University in the early 1900s while studying thermionic emission of hot salts, and the PCM MoS_2 [48]. However, it wasn't until 1968 that Stanford R. Ovshinsky introduced the concept of electrically switchable PCMs, and proposed their use as memory [49]. The first commercial product exploiting phase-change materials was Panasonic's re-writable PD disc introduced in 1995, in which the reflectivity of the PCM was controlled and read using a laser. It was around this time that the material $Ge_2Sb_2Te_5$ (GST225) was developed and settled upon as a good balance between crystallisation speed, thermal stability, and reflectivity contrast [50]. This material has been extensively studied, and has become a material against which many other PCM alloys are benchmarked, and with which many devices are first prototyped. Currently research and development involving PCMs is broadly split between electrical memory devices, which are recently enjoying commercial adoption, and as an active component in nano-scale photonic devices, such as the metasurfaces in this work.

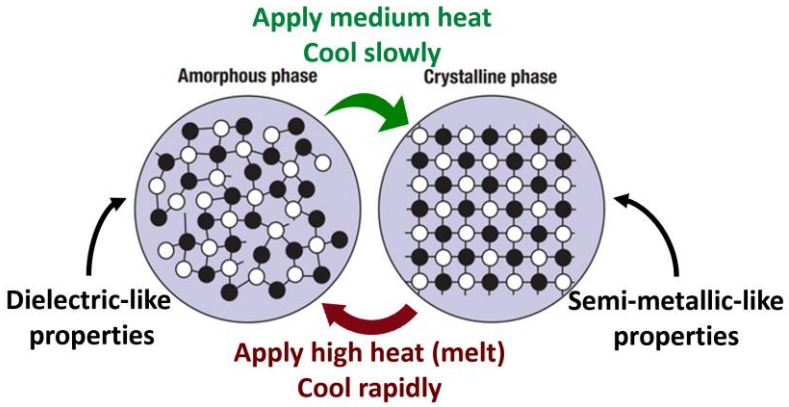

Figure 2.12. Illustrative diagram comparing atomic arrangement in amorphous and crystalline phases. Note that this is a generalisation, and specific properties, temperatures, and crystallisation rates vary substantially between PCM alloys. Adapted from [51].

Many materials have stable amorphous and crystalline phases, such as silicon. This property is also shared by PCMs, however a material must possess several additional properties to be considered a true PCM:

- Both phases stable (or metastable) at room temperature in the order of years or decades.
- Usefully large contrast in conductivity and permittivity.
- Can be cycled between phases many times. Up to 10^{15} reported [52]. (Though highly dependent upon specific device structure).
- Can transition between phases rapidly (sub-nanosecond has been demonstrated [53]).

Amorphous and crystalline are qualitative descriptions of how the atoms in a solid are arranged. In a crystalline solid the structure is ordered and a periodicity, or unit cell, can be assigned to the crystalline structure; perfectly crystalline solids therefore also possess translational symmetry for a long range order (>10 Å), meaning the relative position of atoms in the structure remains consistent for large distances within the material. Amorphous materials do not possess this long range order and do not display any translational symmetry in their atomic structure, though do show considerable short range order [54]. As illustrated in Figure 2.13, $Ge_2Sb_2Te_5$, and many other PCMs, possess several metastable crystalline phases, with each preferentially growing at different temperatures. It has been suggested that the cubic structure of many PCMs (when crystalline) is the primary contributor to their fast switching speeds and high cycle endurance [55].

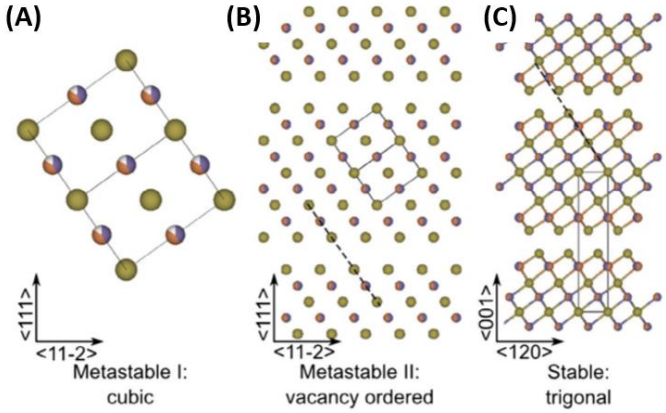

Figure 2.13. Schematics made using VESTA 3 of the stable and metastable crystalline phases of GST225. Blue lines represent a single unit cell. Dashed line across Te-v-Te planes are to aid identifying the cubic and rhombohedral stacking of the cubic and trigonal phase respectively. Reprinted from [56].

Depending upon the specific PCM alloy, the optical and electrical properties of the amorphous phase typically fall somewhere between a dielectric glass and a covalent semi-conductor. These exhibit relatively low optical losses and electrical conductivity. The crystalline phase is less analogous to other material classes, as recent work has shown it to potentially possess a unique bonding mechanism, named metavalent bonding [57]. This bonding is somewhere between metallic and covalent, and is thought to be responsible for the unusually large properties contrast between PCM phases.

Most technologically useful PCMs are binary, ternary or quaternary chalcogenide alloys. These are alloys containing at least one group VIA element (excluding oxygen), like tellurium, and at least one other electropositive element [58]. Unfortunately this also makes many PCMs susceptible to oxidation and diffusion into plasmonic metals [59]. Shown in Figure 2.14A is a section of the periodic table with the elements most commonly included in PCMs circled in red. Figure 2.14B is a ternary diagram showing a variety of PCM alloys; included is GST225, GST326, and AIST, which are all used in this thesis. Figure 2.14C briefly summarises the development of PCM memory from concept to commercialisation.

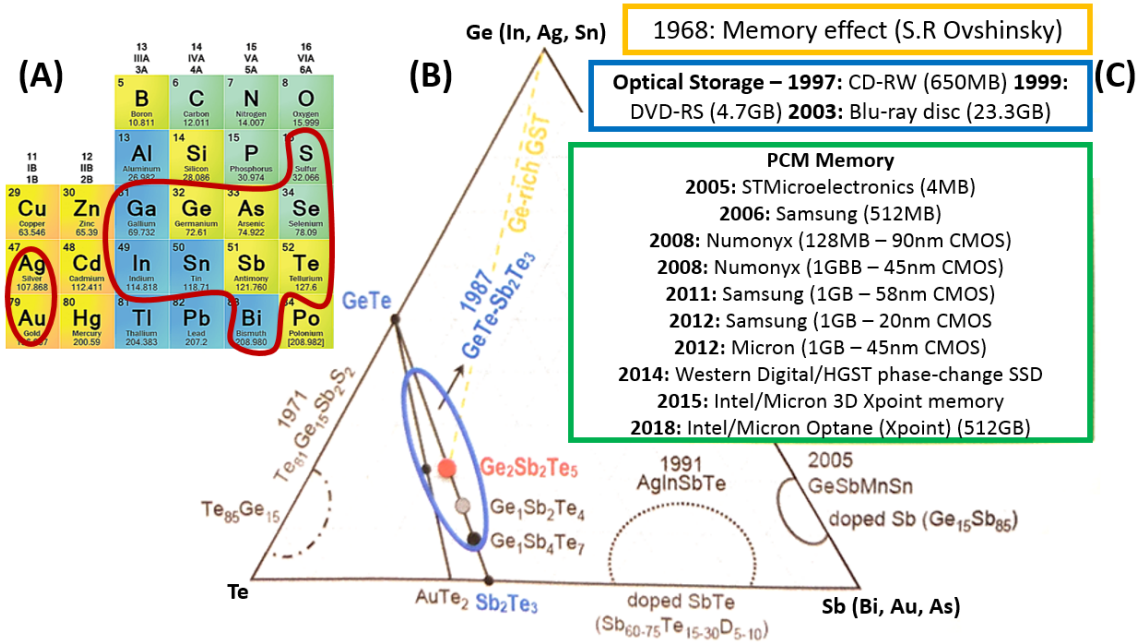

Figure 2.14. (A) Portion of periodic table with elements which are frequently used in PCM alloys ringed in red. **(B)** Ternary diagram showing several alloys developed for memory applications. **(C)** Brief list of achievements in commercial PCM memory research. Adapted from [60].

2.2.2 The Phase-Change Process

The phase-change process is thermally driven. When a portion of the amorphous material has enough free (thermal) energy it will re-arrange into an ordered crystalline state. This reordering predominantly does not break bonds, but instead changes bond angles and lengths; this causes the process to be relatively efficient and fast. The nucleation and growth model is widely used to describe this process, and breaks the crystallisation process into two mechanisms [61]. The first is that once some free (thermal) energy threshold has been reached, then a small cluster of material will re-organise itself into the crystalline phase; although without sufficient size it will be unstable. The second mechanism for crystallisation is that once a stable cluster has formed, it may then grow. This leads to the crystallisation process of different alloys being categorised as either nucleation or growth dominated; although the relative dominance of each mechanism is temperature dependant. The free thermal energy ($\Delta G_{cluster}$) required to produce a cluster of specific size is dependent upon the contribution from two material properties. The first is the Gibbs free energy difference between amorphous and crystalline phase per unit volume, which is a temperature

dependent material property ($G_{lc,V}$). The second contribution is from the interface energy between the amorphous and crystalline phases. This is always a positive term, meaning it increases the required energy and resists crystallisation. For larger crystal clusters, the volumetric contribution becomes dominant and the energy to crystallise becomes negative, denoting that the crystalline cluster is stable. This is described by equation 6 below, in which r is the crystalline cluster radius, and σ is the material's surface energy. Other notable models to describe the phase change process include the thermal-only model and field-induced crystallisation models [62,63].

$$\Delta G_{cluster}(r) = -\Delta G_{lc,V} \cdot \frac{4}{3}\pi r^3 + \sigma \cdot 4\pi r^2 \quad (6)$$

To crystallise the amorphous phase, the material must simply be held above its crystallisation temperature T_X, but below the melting temperature T_m; this is relatively trivial to achieve. The crystallisation rate is a temperature dependant property, with the peak rate temperature (T_p) usually being close to T_m. The exact crystallisation temperature and rate also appear to depend upon the rate at which the material is heated, and not just the temperature maintained during crystallisation.

To amorphise the crystalline phase, the material must be heated above its melt temperature such that the thermal energy breaks down the crystalline structure and the material becomes molten. The material must then be rapidly quenched through the crystallisation region and below T_X such that the material does not have enough time to crystallise, and is in effect frozen into the amorphous phase, see Figure 2.15. For GST225 used in optical this requires a cooling rate of approximately 10 K/ns [64].

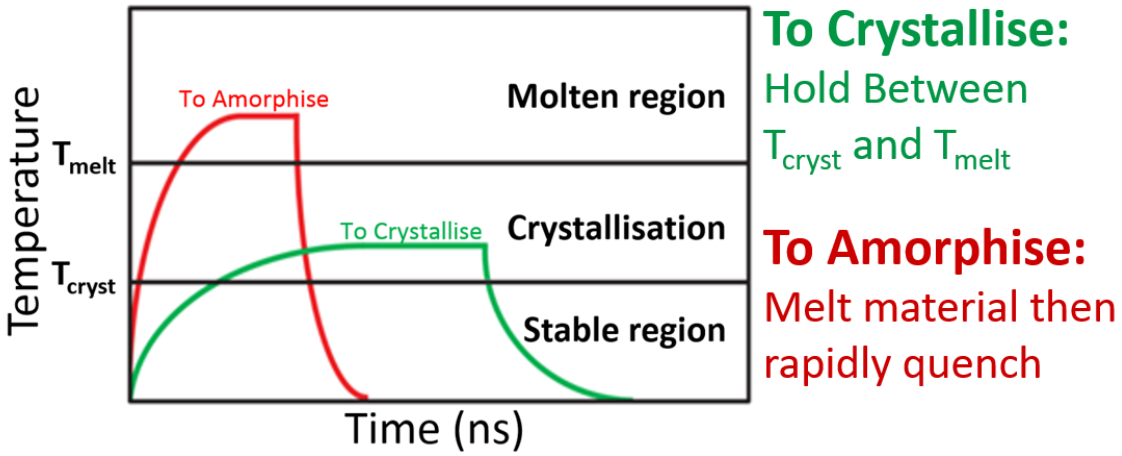

Figure 2.15. Qualitative plot to illustrate the temperature profiles needed to switch a PCM. Amorphisation requires the PCM to rapidly heated and molten (so as to minimise heat loss to the surroundings, which must remain cool to act as a heatsink), and then rapidly quenched so as to minimise time available for crystallisation. Crystallisation is trivial and just requires that the PCM be given enough thermal energy and time.

The crystalline phase is typically denser than the amorphous (approximately 8% for GST225), resulting in a volume reduction. This effect can be compounded by any voids or defects present in the as-deposited amorphous phase due to imperfect deposition, and can result in the PCM experiencing volume reductions of as much as a third after the first crystallisation. The volume reduction combined with imperfect re-amorphisation means that as-deposited amorphous properties are often quite different from that achievable via re-amorphisation in practicable devices; this can effectively reduce the optical and electrical contrast between phases.

Another characteristic to note about the crystallisation process is that incomplete or partially crystalline states are also (meta)stable, in which crystal clusters are dispersed in an amorphous matrix. These intermediate crystallisation states have corresponding intermediate properties somewhere between the fully crystalline and amorphous. This has been exploited for multi-level memory as discussed later, and for multispectral imaging as discussed in chapter 6 [65]. PCMs in which growth, not nucleation, are the primary crystallisation mechanism are less suitable for reliably accessing intermediate properties, due to the less homogenous nature of their crystallisation. For nucleation dominated PCMs a version of the effective medium formula can be used to estimate the properties for a given percentage of crystallisation [66]. This variant of the formula (equation

7) describes the permittivity of a mixed material in which crystalline spheres are suspended in an amorphous matrix.

$$\varepsilon(f, \varepsilon_a, \varepsilon_c) = \frac{1}{4}\left[2\varepsilon_p - \varepsilon_p^* + \sqrt{(2\varepsilon_p^{fc} - \varepsilon_p^{fa})^2 + 8\varepsilon_a\varepsilon_c}\right] \quad (7)$$

In which f is the fraction of crystallisation, ε_a and ε_c are the dielectric constants of the fully amorphous and crystalline phases respectively. ε_p^{fc} and ε_p^{fa} are the proportionally averaged material properties weighted by their respective volume fractions, described by: $\varepsilon_p^{fc} = (1-f)\varepsilon_a + f\varepsilon_c$ and $\varepsilon_p^{fa} = (1-f)\varepsilon_c + f\varepsilon_a$.

2.2.2.1 Switching Methods

There are numerous approaches for delivering the thermal energy needed to switch a PCM. Discussed below are the four broad categories of heating approaches

Thermal annealing usually involves the use of a hot plate, oven, or rapid thermal annealer (RTA) to heat the PCM and induce crystallisation. This approach works well on devices, blanket films, and even bulk samples. There is the further advantage that RTAs can control the atmosphere mix and pressure, somewhat mitigating the effects of oxidation for samples that for whatever reason could not be encapsulated. The temperature accuracy is also usually good, especially concerning RTAs. However, these heating methods cannot ramp temperatures up or down particularly quickly, making them unsuitable for achieving re-amorphisation. The majority of PCM switching in this thesis was done using a rapid thermal annealer or hot-plate.

Optical switching, as used in re-writable optical storage discs, exploits the high absorption of PCMs in the visible parts of the spectrum. A laser (typically 405 nm) is focused within the PCM layer, and the energy is absorbed as heat. This approach can deliver large amounts of energy concentrated in only the PCM film, resulting in very rapid heating. The concentrated and rapid heating also leaves the majority of the device/sample relatively cool, and able to act as a heatsink to facilitate the rapid quenching necessary for re-amorphisation.

Joule heater switching is particularly desirable as it allows for bit/pixel addressable in-situ switching, directly controllable with electrical signals. It involves the inclusion of micron-scale Joule heaters embedded within a device's structure next to the PCM layer. These heaters are usually made from metals, and ideally make use of metallic components already present within the device design. When optical transparency is required then heaters can be made from ITO or graphene [67]. Joule heating is the most applicable in-situ switching method for devices developed in this thesis, but it is energy inefficient, necessitates complex thermal design, and requires PCM alloys which are easier to amorphise.

Ovonic threshold switching is an uncommon property exhibited by many PCM alloys. Materials with this property experience a sudden (sub nano-second) and significant (approx. 4 orders of magnitude) drop in their electrical resistance when an electric field above a certain intensity (typically around 10^8 V/m) is applied across the material [68,69]. See Figure 2.16. Once switched in this manner the resistance is that of a conductor, with the effect being volatile. This kind of switching has excellent cycle endurance, with some PCM alloys having been experimentally switched billions of times [70]. In a PCM, this process results in the formation of conductive crystallised filaments, the radius of which depends on the current available for Joule heating, and the duration of excitation [71].

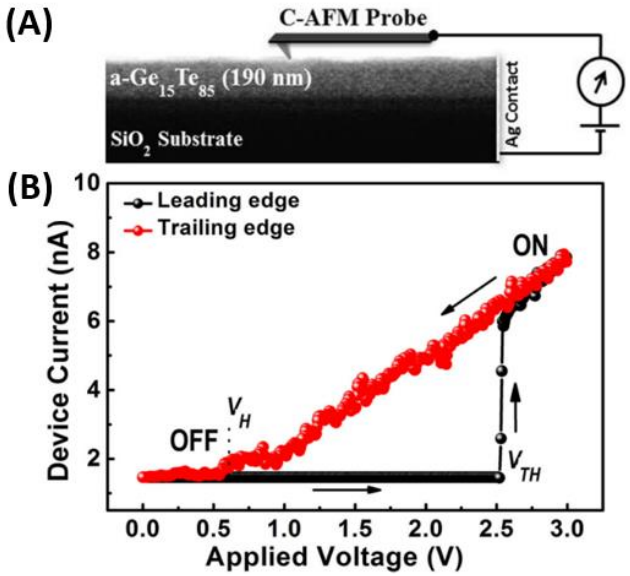

Figure 2.16. (A) Experimental setup for I-V curve measurement using contact atomic force microscopy. **(B)** Current / Voltage curve for GeTe6. At VTH the material resistance drops into an ON state, this persists until the voltage drops to VH. Reprinted from [71].

The precise mechanism that drives threshold switching is still disputed. Several non-linear transport mechanisms such as hopping conduction and field-induced delocalization of tail states have attempted to describe the switching; many of which were able to adequately describe the observed switching characteristics [72,73]. Switching speeds of these materials vary significantly, with compositions like $Te_{39}As_{36}Si_{17}Ge_7P_1$ displaying sub-nanosecond switching [68], whereas alloys not specifically formulated for threshold switching, such as GST225, switch in tens of nanoseconds. Switching speed is also highly dependent upon the applied electric field [74].

Threshold switching devices are of interest in selectors for memory cells. They are ideal candidates as they switch rapidly (fast read rates), with high cycle endurance. Furthermore, the ON/OFF resistance ratio allows for quick low power readings of the memory cells. Finally, the volatility is an advantage for selectors, as a second process is not required to stop accessing a particular memory cell. The threshold switching effect is also exploited in many devices incorporating phase-change materials [75]. In these cases the conductive filaments reduce the overall resistance of an otherwise amorphous and insulating volume. It is worth noting that it's impractical to fully crystallise large volumes using the conductive filaments as Joule heaters.

2.2.3 Phase-Change Materials Properties of Interest

There are many PCM alloys to choose from, and depending upon the application and switching method, different properties should be maximised or minimised when making this selection. Summarised in Table 1 are some of the critical material properties whose priorities will change depending on the application, switching method, and device scale. In general devices which employ a small PCM volume are easy to re-amorphise; and as such can prioritise performance enhancing properties, such as crystallisation speed, which otherwise can make re-amorphisation challenging.

Table 1. A non-comprehensive comparison of desirable material properties for a PCM depending upon its application, switching method, and device scale.

	Electrical PCM Memory (Smaller PCM volumes)	Electrical PCM Modulator (Smaller PCM volumes)	Optical Modulator (Larger PCM volumes)	Optical Modulator (Larger PCM volumes)	Optical PCM Memory (Larger PCM volumes)
Switching Method	Electrical threshold	Optical	Joule heater	Optical	Optical
Optical Contrast	N/A	N/A	HIGH	HIGH	HIGH
Electrical Contrast (ΔΩ)	HIGH	HIGH	N/A	N/A	N/A
Melting Temperature (°C)	MED	LOW – HIGH	HIGH	HIGH	LOW
Onset of crystallisation (°C)	LOW – MED	LOW – MED	HIGH	HIGH	HIGH
Crystallisation Speed	HIGH	MED – HIGH	LOW	MED – HIGH	LOW
Thermal conductivity	N/A	N/A	HIGH	HIGH	HIGH
Cyclability	HIGH	HIGH	LOW - HIGH	LOW – HIGH	LOW – HIGH
Stability	HIGH	N/A	N/A	N/A	HIGH

Contrast in permittivity and conductivity between phases is what makes a PCM useful; it's this contrast which make them a strong candidate for the active component in devices. A high contrast in refractive index, extinction coefficient (sometimes), and electrical resistance are desirable as it allows a smaller volume of PCM to be used. Smaller volumes are faster and more energy efficient to both cool and heat, enabling more complete switching of the PCM, while still inferring the usual benefits of scaling down, such as improved memory density or smaller device footprint. For example, when crystallised, GST225 becomes ≈4x more optically lossy, refractive index increases by ≈70%, and conductivity increases by ≈10^3 [76].

Switchability is an umbrella term used in this thesis which quantifies the extent to which a PCM can reliably be switched into the fully amorphous phase (fully crystalline is trivial). Switchability results from a combination of a PCM's thermal properties and crystallisation behaviour. A high thermal conductivity with a low heat capacity is always beneficial to this metric, as it enables fast, homogeneous heating and cooling. This is especially critical with larger volumes, in which the heat source / sink may be microns from the centre of the PCM volume.

The melting temperature, crystallisation speed, and range of temperatures which induce crystallisation combine to determine how swiftly the PCM volume must be cooled to minimise unwanted crystallisation. A high melting temperature is detrimental to power consumption, but will also amplify the heat-sinking effects of the surrounding materials to improve cooling rates. Melting temperature varies greatly, with some PCMs becoming molten at few hundred ^{o}C, with others stable over 800 ^{o}C. A narrow crystallisation region is also desirable, as this determines the range of temperatures the PCM volume must be rapidly cooled through when re-amorphising. This also determines the minimum temperature which will induce crystallisation, thereby determining thermal stability and maximum operating temperature. The ideal crystallisation speed is highly application specific; this property effectively determines how much optical/electrical contrast is lost per nanosecond during the re-amorphisation process. For the case of electrical memory, the tiny volumes mean re-amorphisation is easy, and therefore crystallisation speed should be maximised (often sub nanosecond). For optical devices volumes are relatively large, requiring a slow and narrow crystallisation band to make good use of the optical contrast.

Reactivity and diffusion are drawbacks which must be managed carefully. Most PCMs will readily react with both oxygen in the atmosphere, and a wide range of metals, especially at the temperatures required for switching [59]. This necessitates the use of protection and diffusion barriers within devices, increasing complexity and impairing performance. Not all PCMs are equally diffusive, with the high tellurium content in materials like GST225 causing it to mix especially well with many metals.

Stability can be broken into two types, long term stability (non-volatility) and cyclability; depending upon application, either, neither, or both may matter. Long-term instability manifests as a very gradual crystallisation. This is especially critical to manage for memory devices to avoid data loss. Long term stability is primarily improved by reductions in ease-of-crystallisation, and by increases to crystallisation and melt temperatures. The number of times a PCM volume can be cycled (often called endurance) is important for both memories and modulators. This is affected by the PCM volume size, device structure surrounding the PCM, and the specific alloy. Elemental segregation gradually occurs as a PCM is cycled, but is more pronounced in larger volumes. Structural degradation in devices can occur due to the approximately 8% reduction in volume when a PCM is crystalline versus amorphous. This necessitates full encapsulation of the PCM to be mitigated, in which the volume reduction instead manifests as internal stress.

2.2.4 Phase-Change Materials as Memory

It's important to discuss the memory applications of PCMs, as these have historically been the main driving force in PCM research. This sub-section briefly details the history of this R&D, and the breakthroughs which resulted in today's state-of-the-art PCM memory.

2.2.4.1 Optical Storage

Although phase-change materials had been studied for nearly a century [48], they did not enjoy mass commercial use until the advent of optically re-writable disks in 1995. These disks were coated in a layer of crystalline PCM which exhibited high reflectivity. Optical drives capable of writing to these disks had a relatively powerful laser which allowed them to melt and re-amorphise tiny dots of PCM. These amorphous dots have much lower reflectivity and are read as a logic HIGH. Huge economies of scale enabled rapid improvements in affordable high numerical aperture optics, blue laser diodes, and advanced coding schemes; these progressed CDs (650MB) to Blu-Ray (25GB per layer) in just nine years.

One recent area of PCM research has been into all-optical storage, in which a micron-scale phase-change layer is used to modulate the attenuation of an optical waveguide. Data is encoded by the PCM crystallinity, which modifies the waveguide transmission via absorption; data is then read using a low power optical pulse. Write/erase operations are carried out by relatively high power pulses (up to 15 mW), tens to hundreds of nanoseconds in length. The simplicity of this basic architecture allows for added complexity to magnify speed and energy efficiency, such as adding nano-ring resonators, 1D photonic-crystals, and plasmonic resonant structures [77,78]. No electrical signals need be involved whatsoever, although mixed-mode capability has recently been demonstrated [78]. A further advantage is that multilevel storage is possible, with up to 34-levels being experimentally achieved [79]. These kinds of memory devices can also perform basic computational tasks by exploiting the accumulation mechanism of crystallisation and signal correlation, with both logic gating and arithmetic calculation having been demonstrated [80,81].

Memory (like that described above) in which information storage and processing merge into the same biologically-inspired device is the critical component in overcoming the von-Neumann bottleneck. Integrated PCM all-optical memory has proven to be a promising candidate for this new class of component [82–85].

2.2.4.2 Electrical 'Storage' Class Memory

PCMs were originally developed and explored as an alternative to magnetic hard disk drives in the 1960s [86]. However, limitations in nano-fabrication meant that each memory cell was relatively large; this resulted in poor exploitation of the high scalability of PCMs. This necessitated high switching power, and the use of slow crystallising PCMs, which stalled research for decades. Interest in PCM memory was rekindled once the scalability of magnetic storage began reaching fundamental limits. In contrast, virtually every aspect of PCM performance is improved by reducing the volume of PCM, making it extremely scalable [87,88]

The basic PCM memory cell is a mushroom cell, see Figure 2.17A, in which a PCM volume is between a Joule heater, and a top electrode. Most of the PCM

volume is crystalline; only the portion of PCM directly covering the heater needs to amorphise to form a plug and block current flow. It's this change in resistance which distinguishes logical high and low.

Following Ovshinsky's work, the first 256 bit phase-change memory array was demonstrated in 1970 by R. G. Neale, D. L. Nelson and Gordon Moore [89]. Then in 1978, the first prototype of a 1024 bit PCM was demonstrated by Burroughs Corporation. However, until the development of fast crystallising PCMs in 1987, the energy needed to switch was uncompetitively high [90]. In recent years NAND flash technology has been facing scalability limitations, and phase-change memory has once again experienced a boom in research interest. It is now poised to begin replacing high-performance NAND flash, and this is an area of intensive research which continues to drive the majority of phase-change material research, such as the vertically stackable phase-change memory design shown in Figure 2.17B [78].

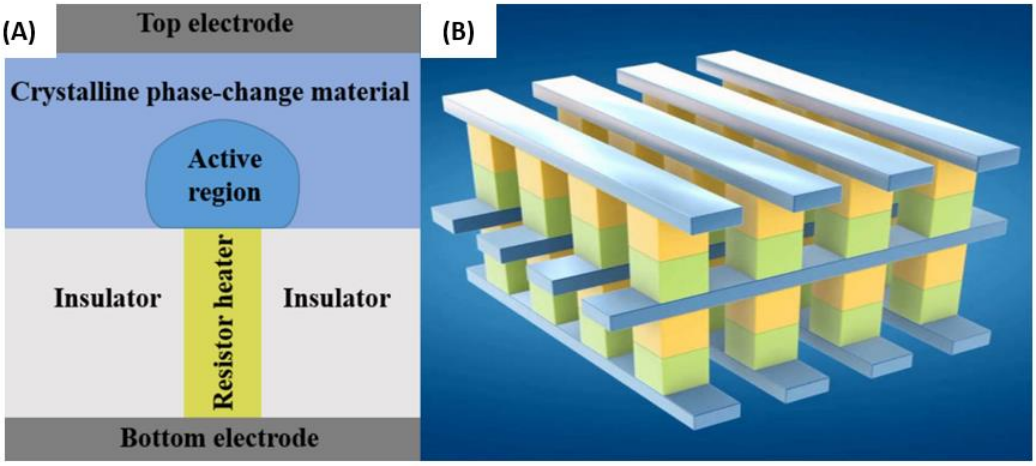

Figure 2.17. Diagrams of how phase-change memory devices are structured. **(A)** Illustrative diagram of phase-change memory mushroom cell, in which a portion of PCM (the active region) has been amorphised thereby increasing cell resistance. **(B)** Diagram of 3D stacked crossbar structure (2 layers) as found in Optane memory. Adapted from [91].

Recent advances in bit-selectors and lithography have enabled the creation of 3D stacked crossbar structures, which massively improve data density and enables further exploitation of PCMs inherent scalability. This has culminated in the development of Intel's Optane 'persistent memory', which is the fastest commercially available non-volatile memory, and can even replace or supplement a computer's RAM [92].

2.3 PHASE-CHANGE RECONFIGURABLE METASURFACES

Due to the resonating nature of metamaterials, they generally exhibit a high quality factor and interact with only a narrow wavelength band. Their properties and resonant wavelengths are determined by the geometry of their resonating elements, their constituent material properties, and the spatial distribution of these resonators. This means the properties of a metamaterial are usually fixed, but there are approaches to dynamically changing the geometry or material properties, as discussed here.

2.3.1 Approaches to Reconfigurability

Piezoelectric materials can act as tiny electrically controllable actuators, and can be used to stretch or compress layers within an optical device. This can be used to alter the spacing between resonators, or change the spacing between layers. For example the coupling (spacing) between a top layer of resonators and a metallic ground plane can be controlled [93].

Flexible substrates are another route for mechanically tuning metasurfaces, but are only practically applicable to devices whose response depends primarily upon the spacing between resonators. Stretching a substrate will further space resonators, and cause them to resonate at longer wavelengths [94,95].

High angular dependence is typically undesirable, however, this property exhibited by many metasurfaces can be exploited for tuning by simply rotating the surface in relation to the incident light. This approach to tunability keeps device complexity low, and can provide a large degree of tunability. However, it does require relatively large moving parts which place limits on tunability speed, compactness, and reliability.

The Kerr effect causes a change in refractive index when either an electric field (DC variant) is applied across a material, or when intense light is incident on the surface (AC variant) [96]. The magnitude of this effect depends upon a material's Kerr constant (K) (primarily determined by band gap energy), and the square of

the electric field (E) or light intensity, as described by equation 8. The DC variant is most applicable for adding on-demand tunability to metamaterials.

$$\Delta n = \lambda \mathrm{K} E^2 \tag{8}$$

The index change is typically negligible, but becomes significant for large electric field intensities, such as those producible across ultra-thin films like those found in many metasurfaces. Several metasurface type devices using the Kerr effect for tunability have been reported, such as an all-optical reflective switch [97].

The carrier density (and therefore optical properties) of some materials can be locally modified using a strong electric field. These materials usually have a near zero permittivity (also called ENZ). This switching is very fast and reliable, with a large contrast in properties. However, the modified volume is constrained to a surface layer, typically only a few nm thick. Despite this, there are now many examples of tuneable devices using this approach, with ITO being the leading candidate [98–102].

Liquid crystals can exist in several phases, and switched between them by applying electric fields. These phases manipulate the polarisation of light differently. While the wealth of research on liquid crystals, and their electrical control method is advantageous, they do have several notable drawbacks. The most significant drawback is their switching speed, which is just kHz at best. Liquid crystals are also highly absorbing in many technologically useful wavelength regimes. They also possess poor thermal stability, to the extent that they are the active sensing component in colour-changing thermometers. Despite the drawbacks, their unique switching properties have been explored in many nano-photonic devices [103].

Microfluidics involves the incorporation of micron-scale channels through a device in which fluids can flow. The scope of design choices this opens up is huge, with fluids used to modify the response of a device not only as a control mechanism, but also as a sensing mechanism. However, fabrication is especially challenging, as these devices need pumping systems, reservoirs, and are highly intolerant to defects [104].

2.3.2 Phase-change Metasurfaces

The properties of phase-change materials (as discussed in section 2.2) make them outstanding candidates for reconfigurable nano-photonic devices. The remaining challenges to fully overcome are engineering and process refinement oriented, and focus on improving switching reliability. PCMs can be thought of as a higher risk, higher reward route to reconfigurability, as the switching process is more complex, but with the potential of outperforming many other methods. Briefly discussed below are some of the recent achievements in phase-change metamaterials.

The typical approach for incorporating phase-change materials in metasurfaces is to use their refractive index to modify the surrounding properties of resonators, and therefore the wavelength which interacts with them. Good examples of this include beam-steerers and perfect absorbers [105,106].

Optical losses and PCM switching can both be improved by reducing the PCM volumes. This is best achieved by only placing a PCM in regions which experience high field concentrations. A good example of this is with all-dielectric metamaterials in which the fields are confined within dielectric resonators. Instead of building these resonators entirely from PCMs, the PCM is placed only in the most electromagnetically intense region , as demonstrated in [107].

Another interesting application for PCMs is in devices which are entirely made from PCMs, and are given structural properties by selectively crystallising or amorphising regions, usually via laser heating. These devices can be fabricated in just two steps, PCM deposition followed by laser writing. While they are not tuneable in the conventional sense, they can be reset and rewritten with relative ease. An alternative approach involves embedding micro-heaters into the structure so that it can be dynamically reconfigured, such as the lens in [108]. However, losses in the PCM are a barrier to achieving high performance with his approach.

2.4 TUNEABLE FILTERS AND THEIR APPLICATIONS

This section initially discusses the various technologies employed to provide tuneable filtering. Potential applications for the filter devices developed are then discussed. For each an emphasis is placed on how the advantages provided by the innate properties of PCMs and metasurfaces could enable devices with superior performance or form factor.

2.4.1 Reconfigurable Filters in General

Reconfigurable filters are found in a vast number of different technologies, and there are several approaches to create them. Covered briefly here are four types of electrically tuneable filters, each with their own strengths. It is against these filters against which those designed in this thesis are compared.

Monochromators are the most commonly used wavelength selection devices, and can operate in any wavelength range. There are several variants, with tuneable monochromators often using a single grating which is rotated using a stepper motor. The inertia that the motor must overcome greatly limits their tuning speed. However, monochromator spectral tuning range and resolution can be excellent depending on the chosen grating and focus length [109].

Microelectromechanical (MEMs) filters incorporate micron-scale moving parts. These structural changes can filter light in a variety of ways, such as controlling arrays of micro-mirrors [110], or by manipulating the topology of a surface which produces structural colour analogous to a reconfigurable butterfly wing [111]. This is typically achieved through the use of electrostatic forces.

Liquid Crystal filters, also known as Lyot-Ohman (a form of Birefringent filter), consist of a birefringent crystal and a liquid crystal waveplate sandwiched between a pair of parallel linear polarizers [112]. Polarised light passes into the birefringent crystals and splits into ordinary and extraordinary rays. This light then passes through the liquid crystal, which depending upon its applied voltage will produce constructive interference for particular wavelengths. This light then passes through the second polariser to finally select out a single wavelength

band. The electrical tuning speed is limited to milliseconds by the liquid crystals, and these filters are only available in the visible to NIR range due to liquid crystal absorption. Of particular note is the input aperture size, which does not affect filtering performance, and so can be large [113].

Acousto-optic tuneable filters (AOTFs) are solid state wavelength tuneable optical filters. AOTFs consist of a crystalline material attached to a piezoelectric transducer. By driving these transducers at the appropriate frequency, a series of perturbations traverse the material. Incident photons interact with these perturbations causing wavelength selective diffraction, resulting in a narrow band of wavelengths being refracted at a different angle, as shown in Figure 2.18. The selected wavelength may be varied by changing the applied frequency [114].

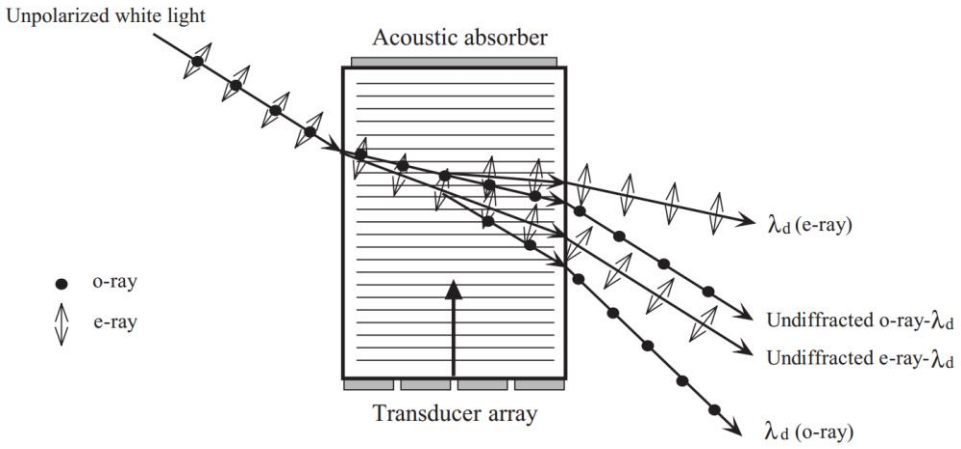

Figure 2.18. Diagram illustrating the operation of a noncollinear acousto-optic filter. In this case the unpolarised incident light is broken into ordinary and extraordinary polarisations.

AOTFs offer wide spectral tuning ranges, with suitable crystalline materials available from the UV to mid IR. These filters are extremely selective (narrow pass-band), for shorter wavelengths with the pass-bands increasing as a function of λ^2. Tuning speeds are fast (typically few μs), and are determined by how long it takes for the acoustic wave (of the new frequency) to entirely fill the crystal. Energy throughput is also impressive, with losses being as little as 10%. However, these devices tend to be relatively bulky, and the crystals expensive to produce.

2.4.2 Applications

Chapter 6 describes the implementation of the filters developed in this thesis for three applications, imaging, chemical sensing, and displays. Briefly discussed here are the current technologies used in these applications.

2.4.2.1 Multi/Hyperspectral Imaging

A typical colour image contains intensity values for three colour bands for every pixel. A multispectral image expands upon this, and contains intensity information for many of spectral bands. Multispectral images are typically represented as 3D data-cubes, in which the width and height are positions in the image, the depth is wavelength, and the colouring corresponds to the spectra, as shown in Figure 2.19. Given a spectral material database and appropriate computational processes, it is possible to estimate the material present at every pixel. This is hugely useful for a wide array of applications, from farming, recycling, space exploration, military surveillance, medical diagnostics, geographic surveying, and more [115].

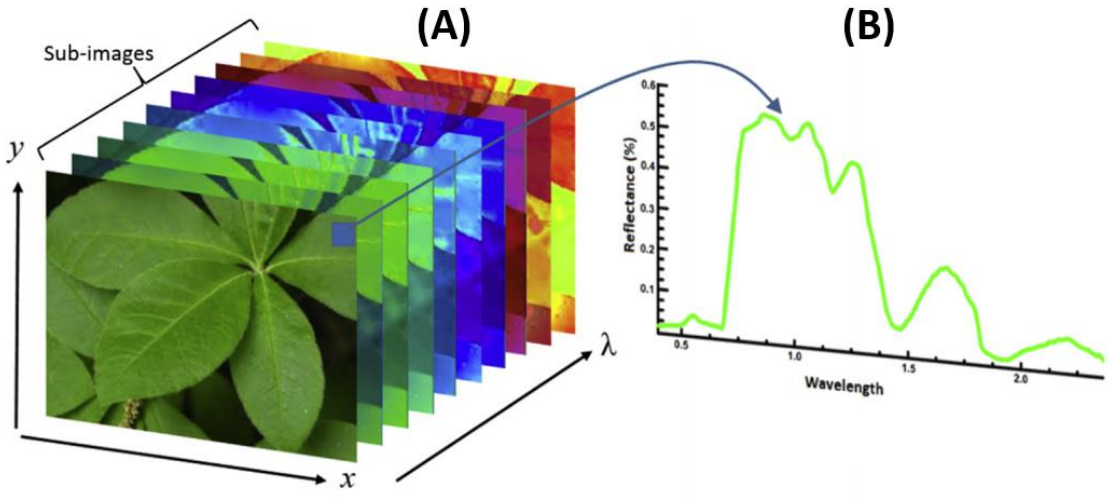

Figure 2.19. (A) Example of a hyperspectral image (hypercube) of a leaf. **(B)** Reflectance spectra of a single pixel from the hypercube, coloured to correspond to a human eyes perception. Reprinted from [116].

Basic Multi/hyperspectral imaging systems use a high-speed broadband monochrome camera placed behind a filter wheel which spins at a speed synched to the camera. Each complete image would require a full rotation of the filter wheel, and reduce the effective frames-per-second of the camera by the number

of filters in the wheel. These systems work well, but there are limits on the number of filters one can fit into a reasonably sized wheel, and how fast this wheel can be spun. More advanced methods of imaging make use of recent developments in tuneable filters like those discussed in 2.4.1.

The filters developed in this work would mimic the functionality of a filter wheel, while being substantially faster to tune spectrally, more energy efficient, solid state (reliable) and fabricable directly onto the objective lens of the camera, making it applicable to weight critical applications.

2.4.2.2 Chemical Sensing

Chemical detection is another highly ubiquitous application, which the filters developed here should be well suited. Sensors to determine the presence or composition of chemicals are found in virtually every building and vehicle. Such as carbon monoxide in homes, and fuel-air mixture monitors in combustion engines.

There are many optical approaches to chemical sensing which make use of metasurfaces [104]. In optics the main approaches involve detecting a change in refractive index (real and/or imaginary), or via Raman scattering. Here we focus exclusively on sensing via electromagnetic absorption caused by vibrational modes in an analytes molecular bonds; these are the fingerprints of its chemical composition.

Sensors which use changes in absorption as their detection methods can be relatively simple, and fundamentally just require a light source, a filter to focus upon a wavelength which is strongly absorbed by the analyte, and a detector. A recent example of such a sensor combines EOT and perfect absorption yielding an ultra-thin and sensitive sensing device; both EOT and perfect absorption are plasmonic effects which only activate in the wavelength of interest (improved selectivity), and greatly enhance electromagnetic fields (improved sensitivity) [117].

Sensitivity is enhanced by confining electromagnetic fields within the analyte. This is usually achieved by resonating structures designed to excite plasmons at

a frequency matched to the vibrational mode of an analyte, as demonstrated in [118]. This enhancement can improve sensitivity by several orders of magnitude, but the volume of analyte experiencing this enhancement is relatively tiny due to the infrared wavelength scales, and the rapidly decaying nature of plasmons. These small volumes and high sensitivity enhancements both necessitate and enable the use of microlitres of analyte, and therefore the use of microfluidics [118]. The combination of plasmonics and microfluidics is one the driving forces behind lab-on-chip systems, which look to revolutionise medical diagnoses and health monitoring.

Sensor tunability has a number of benefits. It can be used to greatly expand the variety of detectable compounds; or alternatively, sensors can be made self-referencing, so that the analyte of interest can be dissolved in a variety of solvents, or to compensate for other changes such as different light source intensities [119].

2.4.2.3 Visible and Infrared Displays

The vast majority of visible displays use liquid crystals as the mechanism to control light amplitude at each pixel. The displays consist of a backlight or reflective surface which transmits light through a polariser. This polarised light then passes through a layer of twisted nematic liquid crystals (with electrical control layers). Depending on the control signal the liquid crystal may rotate the light's polarisation such that it may pass through a second polariser at right angles to the first. This is amplitude tuning, with the actual colour produced by coloured glass, with each pixel being a combination of three pixels to make red, green and blue (RGB). This technology is now very mature, and resolution easily exceeds a human eyes ability to distinguish pixels at a reasonable viewing distance. However, the switching speed of liquid crystals is kHz at best, which is imperfect for reproducing fast motion. Another issue is that at best only 50% of the backlight is transmitted, making them inefficient. So called LED liquid crystal displays have an array of LEDs which provide some spatial control over backlight intensity. These LED arrays improves energy consumption and the contrast ratio, which otherwise suffers from the imperfect dark state.

Active Matrix Organic LEDs (AMOLEDs) are widely used in mobile electronics in which power consumption and image quality take precedence over per area cost. AMOLEDs are made from thin-films incorporating organic electroluminescent materials which can directly produce light. As with liquid crystals, this light then passes through coloured glass. The main advantage of AMOLEDs is that the dark state requires no energy and has extremely low leakage from neighbouring pixels, resulting in massive contrast ratios. In chapter 6 an alternative display technology using phase-change EOT filters is proposed. These filters are effectively coloured glass which can be electrically switched between a dark and coloured state, and have some unique characteristics.

Currently infrared displays are constructed from huge arrays of micro-resistors. Their purpose is to mimic the thermal profile of a scene, with each resistor being joule heated to the desired temperature. The uses of these displays are quite limited, and are primarily for training and testing control and vision systems. These micro-resistor displays have some major drawbacks. Their pixel size is large (several hundred micron), the emission profile from each pixel can only be of the form of black body radiation, and the displays have low refresh rates due to limitations in heating and cooling rates. Our proposed approach addresses all the limitations of these IR displays, and is discussed in sub-section 6.2.3.

3 METHODS

This chapter details both the computational and experimental techniques used to carry out the work described in subsequent chapters. This is broadly split into three branches; these are computational modelling, materials/device fabrication, and materials/device characterisation

This chapter provides an overview of all methods involved in the entire process, from materials characterisation, which feeds into device design, through fabrication, and finally device characterisation. In practise this was an iterative process, although primarily detailed here are the processes in their final form. Figure 3.1 provides an overview of the workflow of the work in this thesis.

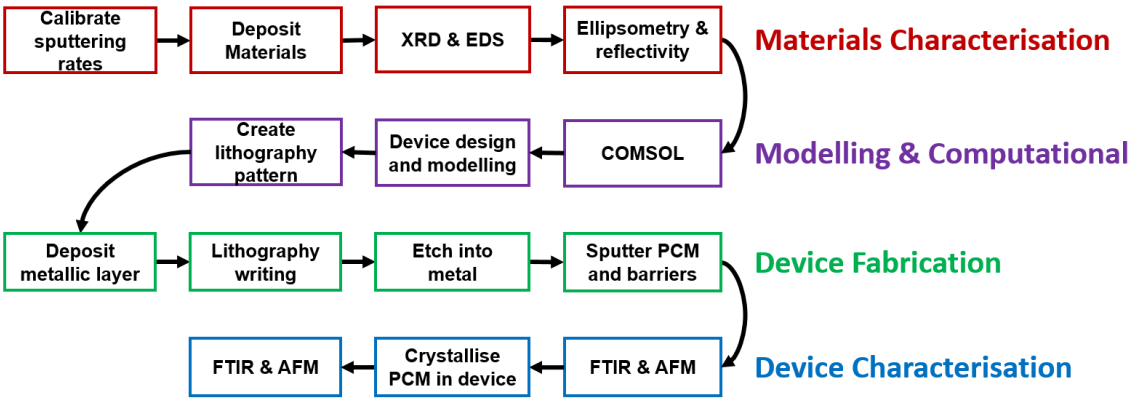

Figure 3.1. Overview of experimental process for production of devices.

3.1 COMPUTATIONAL SIMULATIONS

The majority of computational modelling work in this thesis was finite element, and performed using COMSOL Multiphysics. These finite element models were used in the electromagnetic design and optimisation of devices, and used experimentally gathered materials data (See chapter 4 for details on materials characterisation). The second use was to evaluate the thermal behaviour of various devices, and verify the potential for in-situ switching of PCMs. Other uses for modelling include verifying the impact of fabrication defects, simulating reflectance spectra to compare with experiments (both device and materials

characterisation), and to find the voltage-temperature relation of the heater devices used for the crystallisation study.

3.1.1 Electromagnetic Models

The primary purpose of the modelling work is to assist in the design of various optical devices, with the main focus being on EOT transmission filters. However, other devices explored include metal-insulator-metal perfect absorbers, and all-dielectric cylindrical resonators. For all of these devices the main quantity of interest is the transmission and/or reflectance as a function of wavelength. The distribution of electromagnetic fields is also of interest for determining the placement of the active phase-change layers; the E-field distribution is also of great importance for the sensing applications discussed in chapter 6.

For models including partially crystalline PCMs the effective media approximation was used to evaluate the properties of the PCM. This equation assumes spherical crystallites dispersed in an amorphous matrix, and is described in sub-section 2.2.2.1. Henceforth we will focus on the transmission filters, although the following is broadly applicable to all studied devices. For some simple cases analytic approximations exist to predict performance (see sub-section 2.1.2 for details). However, as the work of this thesis includes active (phase-change) layers and diffusion barriers, such analytical equations are only partly applicable. Instead, finite element modelling was used due to its versatility. The software package COMSOL was selected as it can simultaneously incorporate many physical aspects (electrical, thermal and electromagnetic) in a single model.

Models in COMSOL are constructed from domains, which are physical regions (2D or 3D) to which materials are assigned. It is to domains that all other properties (such as perfectly matched layers) are applied, and it is the interfaces between the domains to which boundary conditions are applied, see Figure 3.2A. COMSOL is finite element method, and therefore works by populating the structure with nodes, which break the model into regions, called the mesh, see Figure 3.2B. Each domain has a mesh applied to it; domains in which electric fields rapidly change (spatially) require a finer mesh. The finite element approach

requires significant computational resources, which scales in relation to the number of mesh nodes. The advantage of finite element modelling is that virtually any arbitrary structure can be evaluated without the need for analytical descriptions. In this work convergence studies were conducted to ensure accuracy of the resulting simulations. Devices were initially meshed very finely to guarantee convergence, and then the mesh density gradually reduced until results began to deviate. The coarsest mesh that still provided adequate convergence was then selected.

Fundamentally, COMSOL is evaluating Maxwell's equations (Equations 9 to 12) in each mesh element. These relate the electric charge density (ρ)**,** electric field, ($\mathbf{E}$) electric displacement field, (**D**) and current, (**J**) as well as the magnetic field intensity, (**H**) and the magnetic flux density, ($\mathbf{B}$).

$$\nabla \cdot \mathbf{D} = \rho \qquad (9)$$

$$\nabla \times \mathbf{E} = -\frac{\partial \boldsymbol{B}}{\partial t} \qquad (10)$$

$$\nabla \cdot \mathbf{B} = 0 \qquad (11)$$

$$\nabla \times \mathbf{H} = \mathbf{J} + \frac{\partial \boldsymbol{D}}{\partial t} \qquad (12)$$

COMSOL's frequency domain solver within the Radio Frequency module was used because the frequency of incident light within models is known, and both electric and magnetic fields are significant. With appropriate boundary conditions, and under certain assumptions (resultant fields will be 'wave-like', etc) used by this solver, COMSOL can then evaluate the Helmholtz wave equation in the below form (equation 13) to evaluate the electric and magnetic field distributions, producing results like those shown in Figure 3.2C.

$$\nabla \times \mu_r^{-1}(\nabla \times \mathbf{E}) - \omega^2 \epsilon_0 \mu_0 \left(\epsilon_r - \frac{j\sigma}{\omega \epsilon_0}\right) \mathbf{E} = 0 \qquad (13)$$

The 3D model shown in Figure 3.2 was constructed using three swept meshes joined together by two regions of free tetrahedral mesh. Swept meshes are computationally efficient and involve defining a 2D mesh that is then repeated in a third dimension. For the mesh that included the actual device, the mesh was defined by the number of nodes around the edge of the model (typically 8 per side), and by the number of nodes around the aperture circumference (typically 40). The two swept meshes which described the substrate and air were simply defined by a number of nodes on each edge of the model (also typically 8).

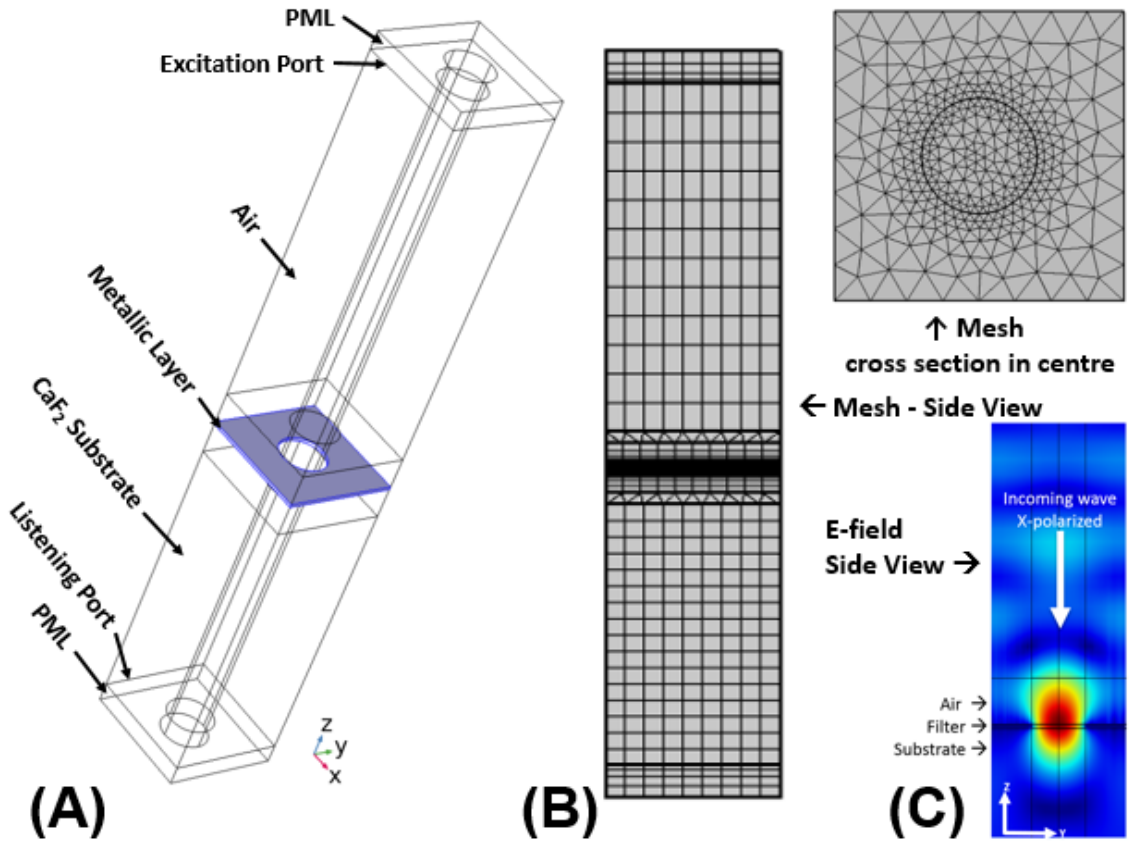

Figure 3.2. Overview of electromagnetic models used to simulate filter devices. A single repeatable (periodic) unit cell is shown. Device scales vary from a few hundred nm to several microns. **(A)** Wireframe diagram of electromagnetic model. Coloured in blue is the metallic layer. Labelled are the various materials and boundary conditions. **(B)** Side and top views of the models mesh. **(C)** Electric field distribution for a normally incident wave at resonant wavelength.

Described briefly below are the important boundary conditions used in the electromagnetic models described previously.

Floquet periodic boundary conditions cause the simulated structure to repeat infinitely (in a tessellated manner) along the axis normal to the boundary. This condition enables the modelling of infinite, periodic arrays, with only a single unit cell needing to be meshed. This condition is described by equation 14: in which $\mathbf{E}_{dst}$ is the electric field at the destination boundary, $\mathbf{E}_{src}$ is the electric field at the source boundary, $\mathbf{k}_F$ is the Floquet wave-vector and the term $\mathbf{r}_{dst}$-$\mathbf{r}_{src}$ denotes a spatial vector that starts at the source boundary and ends at the destination boundary. For the case of normal light incidence $\mathbf{k}_F$ equals zero.

$$\mathbf{E}_{\mathrm{dst}} = \mathbf{E}_{\mathrm{src}} e^{-i\mathbf{k}_F \cdot (\mathbf{r}_{\mathrm{dst}} - \mathbf{r}_{\mathrm{src}})} \tag{14}$$

Port boundary conditions allow one to specify the light source(s) and defines the scattering matrix. The scattering parameters contained in the scattering matrix make a correspondence between the amplitude and phase of the excitation that impinges upon the structure through the different ports and the phase and amplitude of the scattered waves after interacting with the device. In the specific case studied in this work, the models have two ports, one is an excitation port and another one is a listening port. The excitation port is placed on top of the model to emit electromagnetic radiation and the listening port is placed below the device. The reflected and transmitted energy can be calculated using the values of the fields at the port boundaries.

Perfect electric conductor domains, force the electric field to be perpendicular to the boundary, as described by equation 15 (where here $\mathbf{n}$ in the normal vector). This boundary condition can halve the computational domain of a model by exploiting a plane of symmetry within the solution of the fields.

$$\mathbf{n} \times \mathbf{E} = \mathbf{0} \tag{15}$$

Perfectly Matched Layers (PML) are a domain which mimics infinite free space. Any EM waves which enter a domain with this property are rapidly reduced to zero intensity without any reflection.

3.1.2 Electro-Thermal Models

The switching of phase-change materials in the devices in this thesis is thermally driven, with heat generated via electrical Joule heating, caused by passing a current through the metallic layer of devices. An electrothermal model was built to predict the temperature within the phase-change volume as a function of electrical pulse power and duration, see Figure 3.3. These models were essential in assessing and optimising the ability of a device to successfully crystallise and re-amorphise its PCM volume. These models also provided information on the electrical resistance and required switching power.

As with the electromagnetic models, only a single unit cell is considered for thermal modelling, from which characteristics of a large array can be extracted. The Electric Currents module in COMSOL was used to apply a voltage difference

between two ends of the unit cell, causing a current to flow, which in turn causes Joule heating. The Heat Transfer in Solids module is then used to predict the flow of heat into and out of the PCM layer during and after an electrical pulse. Only heat flow due to conduction is considered in this case, see equation 16.

$$Q = \rho C_p \frac{\partial T}{\partial t} - \nabla \cdot (k \nabla T) \tag{16}$$

Where C_p, ρ, and k are the material properties heat capacity, density, and thermal conductivity respectively. T is the temperature, and Q represents the volumetric heat source (due to Joule heating in this case).

The resistance of the unit cell (and by extension, the entire array) is easily extracted using Ohm's Law. This resistance can then be used to calculate the electrical properties for an arbitrarily sized array.

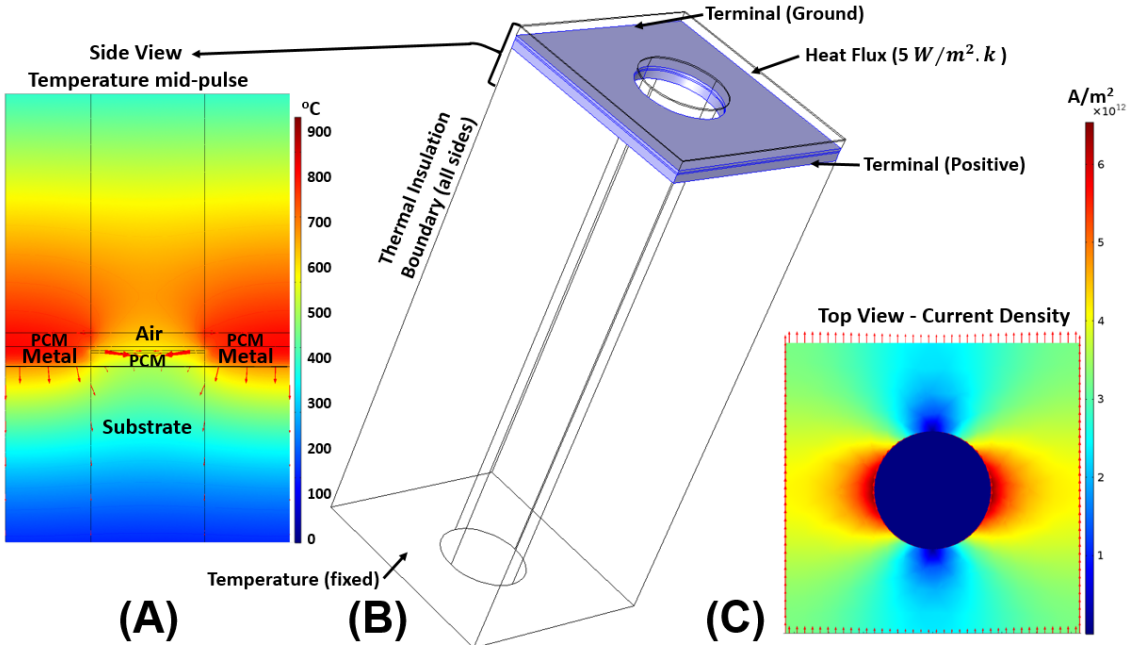

Figure 3.3. Overview of thermal models used to simulate PCM switching within filter devices. A single repeatable (periodic) unit cell is shown. Device scales vary from a few hundred nm to several microns. **(A)** Side view snapshot (coloured by temperature) as a filter device starts to heat due to current flowing through the metal layer **(B)** Wireframe diagram of thermal model. Coloured in blue is the metallic layer. Labelled are the boundary conditions. **(C)** Top view of device showing the non-uniform current density distribution.

Described briefly below are the important boundary and domain conditions used in the electrothermal models in this thesis.

Thermal insulation boundary reduces all heat flux through it to zero. It is used on all four sides of the model, as each unit cell will follow an identical temperature profile, there will be no heat flux between them.

Heat flux boundary conditions provide a fixed heat transfer between two domains. In this model the top boundary has a fixed heat flux to represent heat loss to the air directly above the model so as to avoid meshing a large air domain.

Temperature boundary conditions are used to set the parts of the model which are far from the heater to room temperature. This is placed at the bottom of the substrate, which acts as a heatsink

Terminal & Ground Boundary are placed on opposing sides of the metallic layer, and provide electrical power. Power, current or voltage can then be specified.

3.1.3 Design and Optimisation Approaches

When approaching a fresh design task, it was often possible to use analytical expressions from literature to estimate a sensible starting point. However, this starting point would still be sub-optimal, as the devices in this work are relatively novel, (especially the inclusion of phase-change materials and accompanying barrier layers). Once a starting point was found, parametric sweeps would be conducted to better understand how the device's response depended upon each geometric parameter. Once a number of sweeps were completed for a device in a particular spectral range, the device geometry could be roughly selected to produce the desired resonant response. The final optimisation step would sometimes involve applying a direct search algorithm; this step was not required for all devices, but proved especially useful for the metal-insulator-metal perfect absorbers. The direct search algorithm can suffer from finding local rather than global solutions, and as such is best used as the final stage of optimisation. It is part of the MATLAB Global Optimisation toolbox and involves saving the COMSOL model as a MATLAB script. Within the script the expression to minimise is defined. MATLAB will then run COMSOL (via Livelink for MATLAB) to iteratively solve the model, varying specified parameters until an optimal solution is found.

3.1.4 Calculating Colour

The ability of the studied devices in this project to produce colour was investigated mathematically. To do this, reflection or transmission spectra would be converted into the CIE colour space. CIE stands for Commission internationale de l'éclairage, and the CIE colour maps are standard methods for representing colour on a 2D plane [120] This allows the gamut of a device to be mapped out (see Figure 3.4), and for easy conversion into RGB.

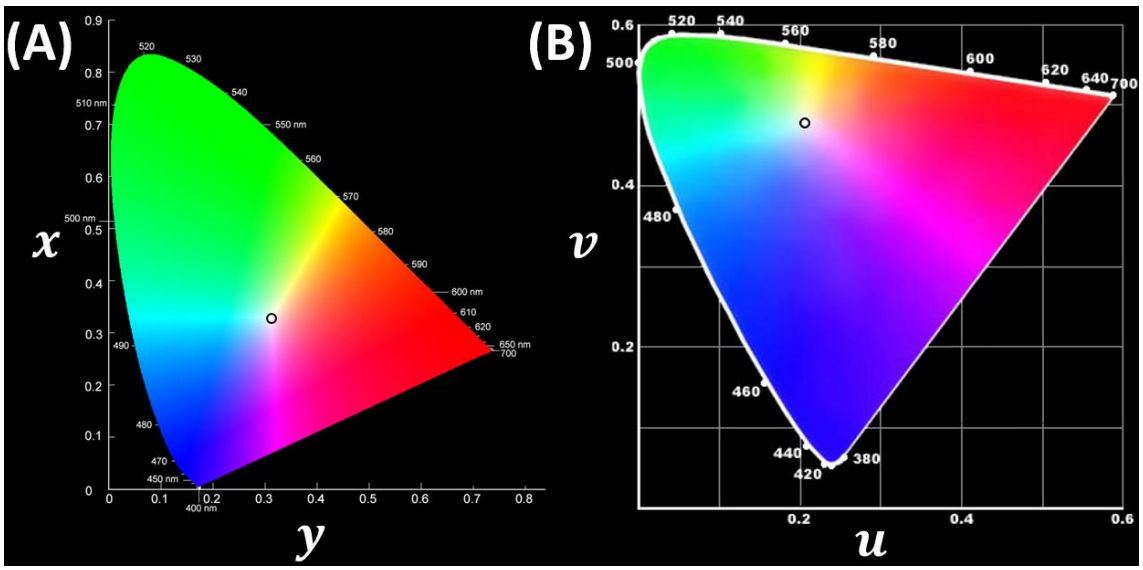

Figure 3.4. Two CIE chromaticity maps, the edges of each map represent a single pure wavelength, which is labelled. Colours become more mixed towards the white point (marked with a black ring) near the centre of each map. **(A)** CIE1931 chromaticity diagram. Adapted from [121]. **(B)** CIELUV chromaticity diagram. Adapted from [122]. Note that these images are an approximation if viewed on a display, as they are unable to reproduce all colours present on a CIE chromaticity map.

There are two stages to this conversion. Firstly the spectrum of interest (S) is converted into the CIE1931 tristimulus values X, Y and Z. X and Y determine chromaticity and Y luminosity. X, Y, and Z are calculated using equations 17 to20.

$$X = \frac{1}{N}\int_{380}^{780} S(\lambda)I(\lambda)\bar{x}(\lambda)d\lambda \qquad (17)$$

$$Y = \frac{1}{N}\int_{380}^{780} S(\lambda)I(\lambda)\bar{y}(\lambda)d\lambda \qquad (18)$$

$$Z = \frac{1}{N}\int_{380}^{780} S(\lambda)I(\lambda)\bar{z}(\lambda)d\lambda \qquad (19)$$

$$N = \int_{380}^{780} I(\lambda)\bar{y}(\lambda)\,d\lambda \qquad (20)$$

$\bar{x}$, $\bar{y}$, and $\bar{z}$ are the standard human observer functions, as shown in Figure 3.5. $S(\lambda)$ is the reflection or transmission spectra to convert into a colour, and $I(\lambda)$ is the wavelength dependant background or backlight irradiance. The units here are arbitrarily set using N so that Y equals one at maximum brightness, this is

because the function which creates Y (using $\bar{y}$) closely resembles the Luminosity function, which describes the spectral brightness sensitivity of a human eye.

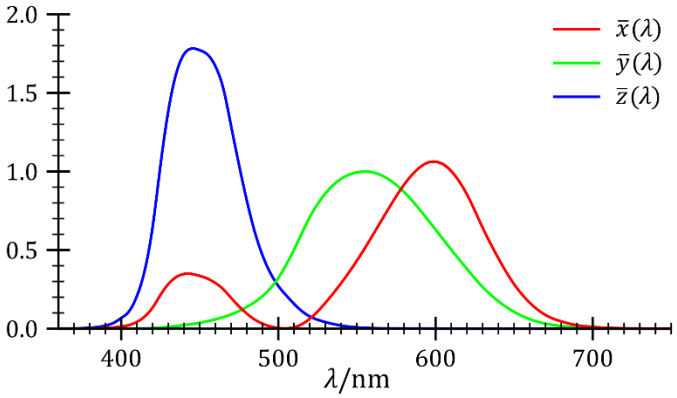

Figure 3.5. The three functions, $\bar{x}$, $\bar{y}$, and $\bar{z}$, used to convert reflection/transmission spectra into tristimulus colour values. Reprinted from [123].

The second stage is to convert X, Y and Z into x and y; these are the two coordinates used to identify a colour on the 2D CIE1931 chromaticity map (see Figure 3.4A). This conversion uses equations 21 and 22.

$$x = \frac{X}{X+Y+Z} \qquad (21) \qquad\qquad y = \frac{Y}{X+Y+Z} \qquad (22)$$

The percieved colour from the original reflection/transmission spectra can now be identified, with Y continuing to represent luminosity. In this work CIELUV diagrams (see Figure 3.4B) are often employed instead of CIE1931, the conversions are shown in equations 23 and 24.

$$u = \frac{4x}{-2x+12y+3} \qquad (23) \qquad\qquad v = \frac{9y}{-2x+12y+3} \qquad (24)$$

Parametric sweeps of devices produced by COMSOL were often used as the data source to map out the total colour space a particular device could produce if pixelated with different geometries.

3.2 Overview of Device Fabrication

While there are modelling results concerning a number of devices in this work, only the transmission filters were experimentally fabricated. Four different fabrication approaches were attempted and assessed for suitability. Details on each fabrication method are discussed later in the chapter.

The filter devices (see Figure 3.6) primarily consist of a metallic layer patterned with an array of holes. This is fabricated onto a transmitting (usually) low refractive index substrate. This produces band-pass filter with fixed centre wavelength. Finally, diffusion barriers and a phase-change material are deposited onto the structure to provide tunability.

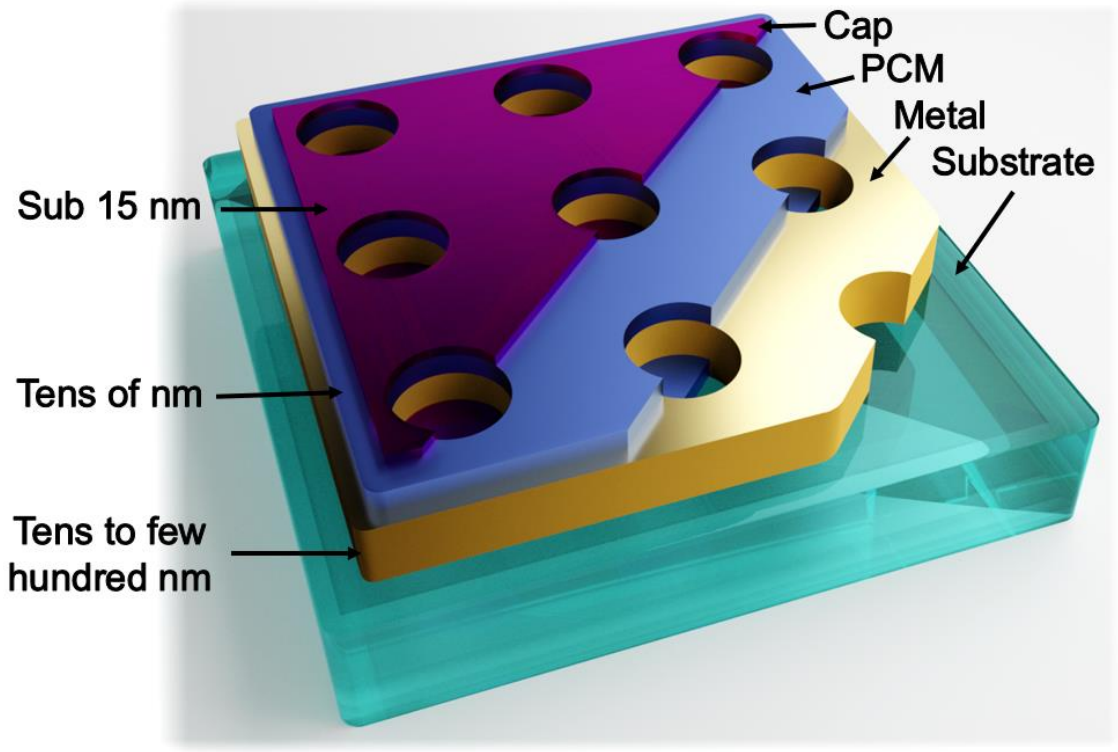

Figure 3.6. Rendered 3D image (Blender, Cycles Renderer) of filter device, with layers cut away (not to scale). Shown is a patterned metallic layer with circular apertures, all coated in a PCM, with a cap to protect from oxidation. No diffusion barrier is shown.

The substrate used for the majority of fabrication was CaF_2, as it has low losses for the entire spectral range of interest, and has a suitably low refractive index. CaF_2 is also readily available in many forms and relatively inexpensive. However, its hydrophobic properties can cause adhesion issues with lithography resists, and its low electrical conductivity causes charging due to electron beams, while its low thermal conductivity requires thermal processes be performed with care.

The four fabrication methods described below are each approaches to produce the patterned metallic layer, and are summarised in Figure 3.7. Thermal evaporation or DC magnetron sputtering were used to deposit the metallic layer, depending on the specific metal. RF magnetron sputtering was employed for the diffusion barriers and phase-change layers. These techniques are detailed later in the chapter.

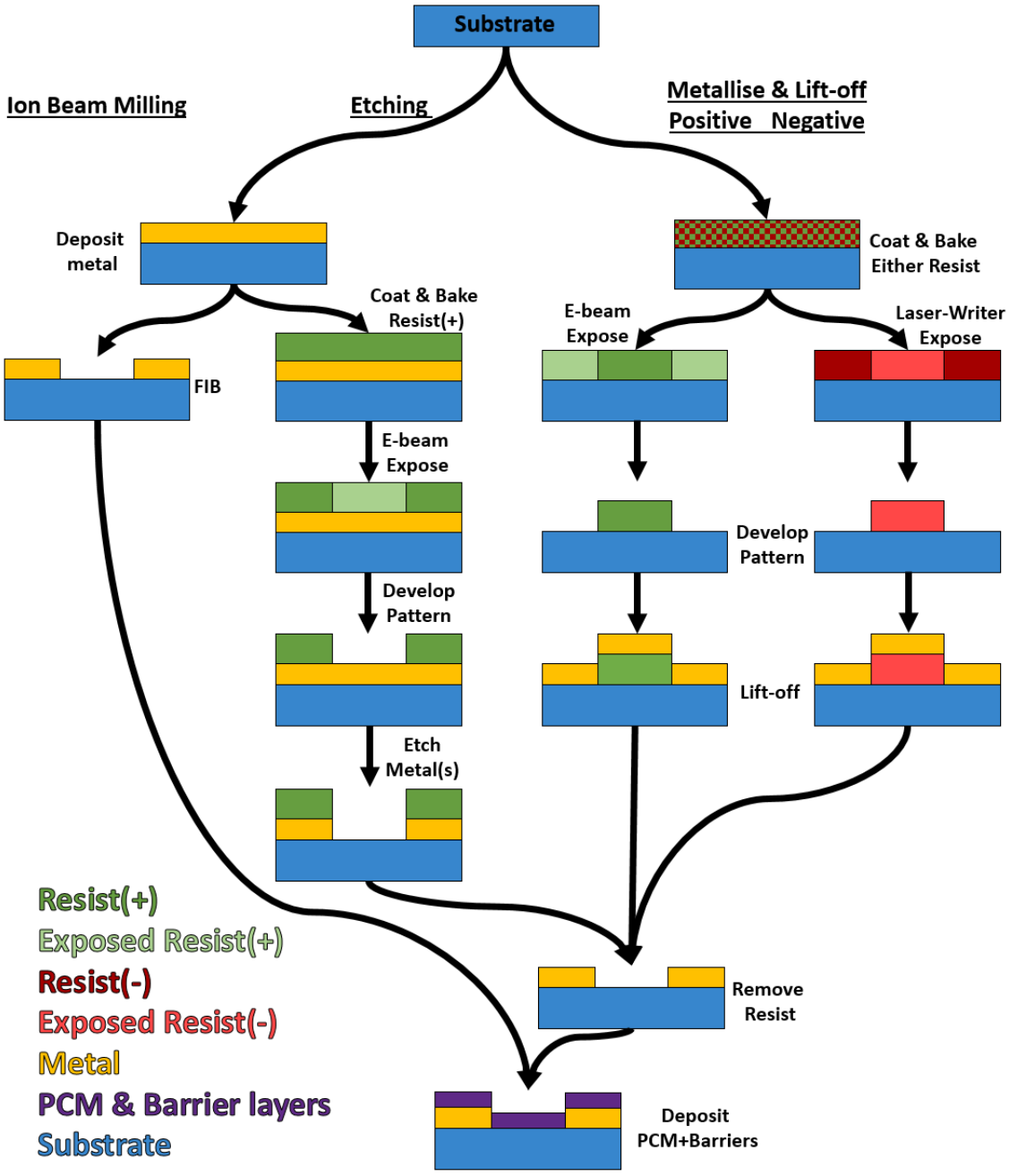

Figure 3.7. Process flow diagram for the four fabrication approaches evaluated for the filter devices.

Wet etching proved to be the most reliably successful approach, and was adopted for the vast majority of device fabrication in this work. Once a device's metallic patterned layer was completed (before phase-change layer deposition), the device's exact dimensions and extent of defects were assessed using atomic force microscopy (AFM). Fourier Transform Infrared Spectroscopy (FTIR) was then performed to evaluate the transmission spectrum of the device. Typically a

small 2 mm diameter aperture was employed during transmission measurements so that the size of devices and therefore lithography time could be minimised.

If the devices performed well at this stage, then a phase-change layer (and appropriate barriers) was deposited using magnetron sputtering. The previous two experiments (FTIR and AFM) were repeated; then the device was either placed onto a hot plate, or into a rapid thermal annealer (depending on specific PCM alloy) to switch the PCM phase. Transmission and surface topology experiments were repeated for a third time. The three transmission measurements were the primary result for each device. Figure 3.8 Shows a sample containing nine 3x3 mm filter devices on a 25 mm CaF_2 substrate which has been through the experimental process described above.

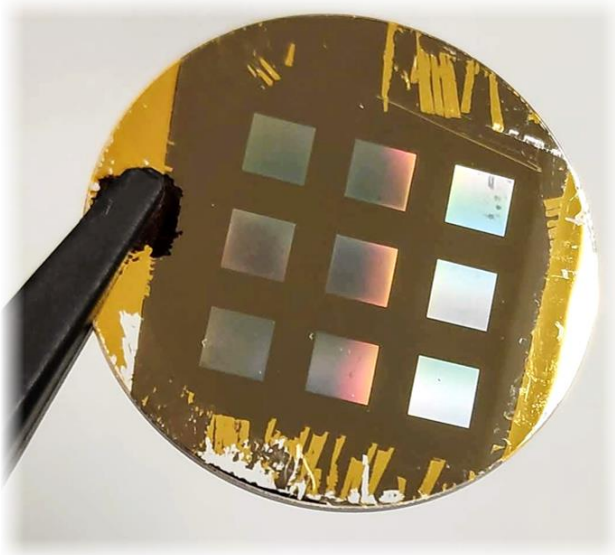

Figure 3.8. Image of nine 3x3 mm phase-change EOT filter devices on a 25 mm CaF_2 substrate. They were designed to operate in the long wave IR region, and underwent the full experimental process described previously.

3.3 MATERIAL DEPOSITION TECHNIQUES

The techniques described below were used for preparing materials for both characterisation and device fabrication. Whenever possible, deposition for device fabrication was done in an identical manner to the samples used for materials characterisation; excluding actual layer thicknesses.

3.3.1 Magnetron Sputtering (RF & DC)

Sputtering is a type of physical vapour deposition (PVD) and was the primary method for depositing thin films of material for our devices and other work. It is a widely used, and repeatable process which produces high quality films [124].

Sputtering works by applying a negative charge to a disc (named the target) of source material. So the target acts as the cathode, and the substrate/holder is the anode. This causes free electrons to flow from the target and collide with the high atomic weight noble gas (usually argon) within the chamber. These collisions remove outer electrons from the gas and cause it to become a positively charged plasma. The plasma ions are then attracted at high velocity towards the negatively charged target, and collide into it. These impacts cause atomic sized particles of the source material to break off and become ‘sputtered’. This material travels through the partial-vacuum within chamber, depositing onto the substrate.

Magnetron sputtering machines go a step further than the standard method previously described; magnetron sputtering incorporates permanent magnets or magnetrons behind the target, as shown in Figure 3.9A. This helps confine the electrons near the target, which increases the rate at which argon ions are created, which in turn increases sputtering rates. The power supply can be either DC or AC. Above describes the DC process, which is cheaper and provides greater sputtering rates, but cannot sputter dielectric materials. With AC sputtering, the first half of the AC cycle causes the gas and source material ions to remain near the target surface due to the polarisation of the target. The electric polarity then flips, ejecting the plasma ions and source material towards the

substrate. Typically very high AC voltages (200 – 1000 V) are used, which is the main contributor of the increased cost.

There are two main parameters to control during sputtering. The first is deposition power. Typically high powers are used to initiate the sputtering, called ‘striking’ the plasma, and changing the power has a linearly proportional effect (within limits) upon the deposition rate. The second parameter is gas pressure. Typically a higher pressure is used to strike the plasma; then a lower pressure will be used for deposition. The gas pressure can have a significant impact on the structural and mechanical properties of the deposited film, which can even lead to delamination see Figure 3.9B-E, and Figure 3.10 [125]. The mean free path is a measure of how far the average piece of sputtered source material can travel before colliding with a gas particle; a short path negatively impacts sputtering rates and directionality, and this is another parameter impacted by gas pressure. There is typically a relatively narrow range of pressure which provides both a stable plasma and high collision rate, whilst also maintaining an acceptable mean free path, and minimising internal stresses within the film.

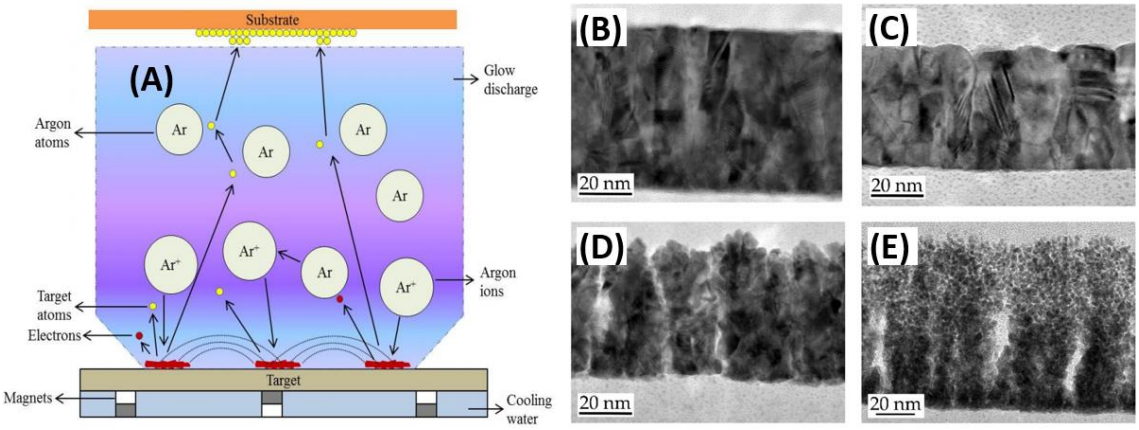

Figure 3.9. (A) Schematic representation of the operation of a magnetron sputtering system. Figure from [126]. TEM brightfield micrographs of iridium thin films sputtered at different pressures: **(B)** 1.87 mTorr, **(C)** 3.75 mTorr, **(D)** 22.5 mTorr, **(E)** 60 mTorr. Figure from [127].

The gas can also be a mixture of elements, this is typically done when performing reactive sputtering. In this case some of the gas will provide high energy collisions, while the remainder will readily react with the target material to produce a new material, such as an oxygen/argon mixture used with a silicon target to produce silicon dioxide films. Gas mixtures can also be used to compensate for

the fact that different elements sputter at different rates; for example, adding oxygen to ensure proper formation of SiO_2 films when sputtering from a SiO_2 target. Another method of compensating is called target conditioning, in which sputtering a target will eventually deplete the surface of higher yield-rate elements, somewhat compensating for differences in elemental sputtering rates. A better method of compensating when sputtering alloys is to produce a pre-conditioned target that has a composition adjusted for the different sputtering rates of constituent elements.

Re-calibration of gas pressures was occasionally required with new material/substrate combinations. Shown in Figure 3.10 are two films produced during the calibration of tungsten deposited onto calcium fluoride. Argon pressures of 1 and 2 mTorr produced significant stresses within the films, causing delamination and bunching. Further increasing the pressure to 3 mTorr resolved the issue.

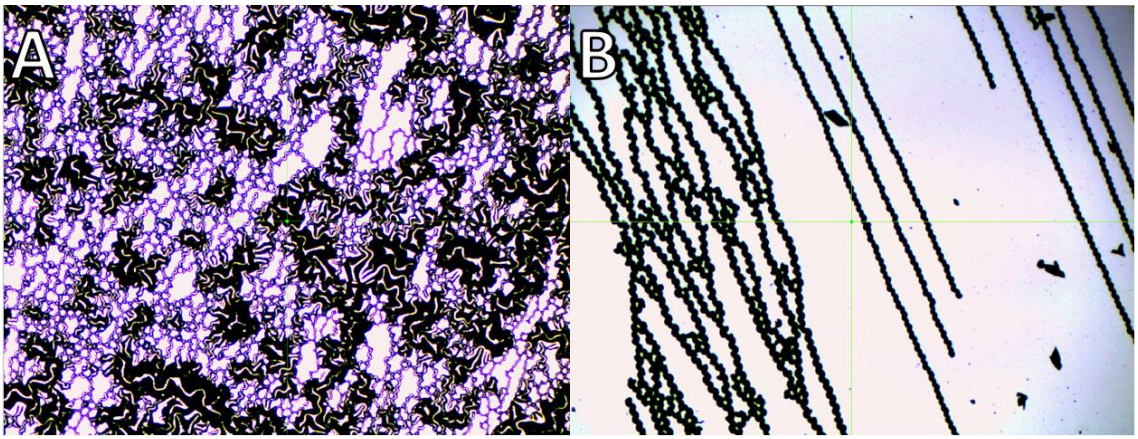

Figure 3.10. Microscope images at 5x magnification of two 150 nm thick tungsten films deposited at **(A)** 1 mTorr, and **(B)** 2 mTorr. A smooth film was produced using 3 mTorr.

Fabricating Sputtering Targets

For the GaLaS (GLS) phase-change material, sputtering targets are not commercially available, and therefore had to be custom made as part of this thesis' work. High-purity gallium sulphide (Ga_2S_3) and lanthanum sulphide (La_2S_3) powders were weighed and mixed together in an argon purged glove box (minimising oxide formation is critical). The mixed powder was then poured into

a two or six inch diameter cylindrical vitreous carbon crucible and melted at 1150 ^{o}C for 24 hours in an argon purged furnace to produce a homogenous bulk disc of GLS. After annealing, the GLS disc was then ground and polished to an eighth of an inch thickness and affixed to a copper backing plate using silver epoxy. Figure 3.11 summarises this process.

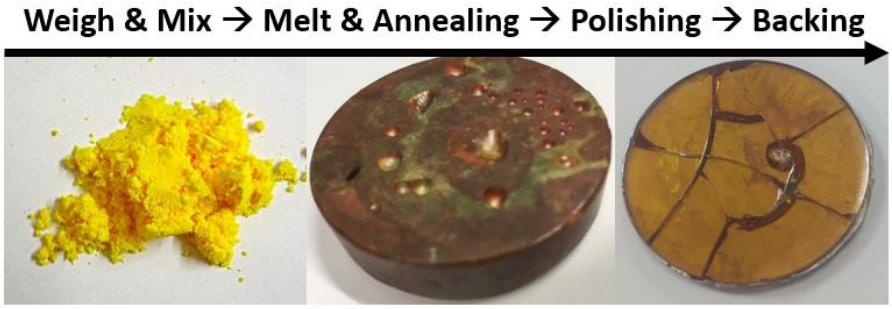

Figure 3.11. Summary of process flow for creating GLS sputtering targets.

This ratio resulted in a desired composition of $Ga_{26}La_{14}S_{60}$. However, while this was the intended composition of our films, the sputtering targets themselves required an over-stoichiometric composition with additional sulphur. This is because of the large discrepancy in atomic weights of the constituent elements, leading to differences between their sputtering rates.

3.3.2 Thermal Evaporation

Thermal evaporation is another physical vapour deposition (PVD) method. The systems themselves are more cost effective, and do not require expensive sputtering targets. They have excellent directionality, which is good for metallisation within a mask. However, impurity rates and film density are slightly worse than sputtering (for systems of comparable quality).

The process is very simple. A source material (usually a number of small pieces) is heated above its vaporisation temperature within a vacuum. This causes atoms to leave the liquid form and become a vapour, some of which deposits onto the substrate. Electric Joule heating is the most common heating method. More advanced systems use ion-beam assisted heating, which can increase maximum temperatures, film purity, deposition rates, and material utilisation efficiency.

3.4 STRUCTURAL PATTERNING

This section focuses upon experimental techniques for nano and micro scale patterning of thin films, and the primary technique (AFM) used in this thesis to evaluate the degree of patterning success.

3.4.1 Focused Ion Beam Milling

Focused Ion Beam (FIB) milling is a technique which allows extremely small shapes and patterns to be cut into the surface of a material [128]. It is analogous to reactive ion etching, except the pattern is dictated using a computer generated design, rather than a physical mask. The FIB used in this work was an xT Nova Nanolab 600, which uses liquid gallium as its ion source. The gallium is heated and flows up to the tip of a tungsten needle where the surface tension and tip's electric field form the gallium into an extremely sharp Taylor cone. At this tip, the electric field is so intense that the gallium is ionised and field emission occurs. These ions are then accelerated and focused in much the same way as electrons in a scanning electron microscope (SEM). If not correctly tuned, FIB systems can cause significant gallium contamination as the ions implant themselves into the sample, however, this can also be a useful process for surface doping.

FIB was employed in this work to cut cross-sections into stacks of thin films and devices; these cross-sections are then imaged using an inbuilt SEM. Initially the device fabrication was also attempted using FIB. These cross sections are useful for viewing layer thickness, elemental diffusion, and also shows how well a device has been fabricated. For the filters designed in this work, it was possible to see how much phase-change material was deposited into the metallic holes, rather than onto the holes side walls. Figure 3.12A shows early attempts at fabricating filter devices directly using FIB milling. The left image highlights the uneven milling issues encountered due to the tungsten layer having inhomogeneous strength. Figure 3.12B shows a cross section of a single hole, with the GST and tungsten layers clearly visible.

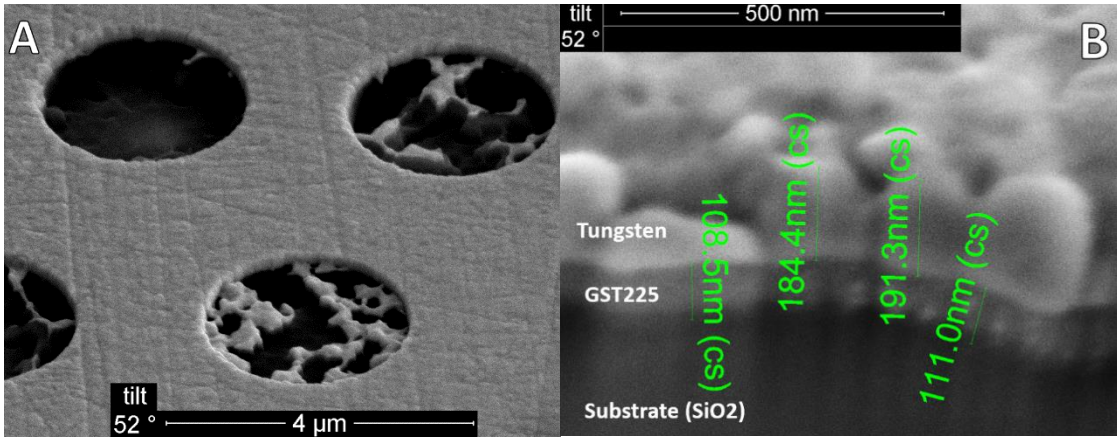

Figure 3.12. A) SEM images of holes milled into a GST/Tungsten stack at various beam currents. **B)** SEM image of stack cross section.

Four issues quickly led to FIB being abandoned for device fabrication in this work. The greatest issue was that of drift, in which the sample microscopically shifts over time, causing the pattern to distort. Second, the maximum fabrication area of the FIB used here (without requiring manual stitching) is just 100x100 µm, and transmission measurements required relatively large (few mm) devices be fabricated. There were also issues with gallium implantation into the substrate, and metallic debris cold welding to the sample surface.

3.4.2 Laser and Electron Beam Lithography

Lithography is a widely used fabrication method in the various nanotech industries for producing very small features (down to tens of nm). It is the primary method with which devices in this work were fabricated. The critical stage of lithography is in creating a mask. Masks are a polymer layer patterned with holes and/or trenches; into these holes/trenches new materials can be deposited, or etching chemicals/gases can be introduced [129].

Initially the filter devices were fabricated using metallise and lift-off; this was later exchanged in favour of etching. Both processes are summarised below, and in Figure 3.7.

Fabricating a mask using lithography has three main stages.

1. Resist preparation: The substrate is coated with polymer(s) which are sensitive to light or electrons, named the resist. In this work a spin coater was used, but for large-scale production spray coating is employed.
   The resist(s) are then baked to solidify and strengthen them. Multiple resists are sometimes stacked to improve adhesion, electron charge dissipation, or modify the light/electron sensitivity in the vertical direction to produce non-vertical side walls. The selection of resist(s), their thickness, and the baking temperature(s) are the most critical parameters.
2. Patterning: The samples are exposed to focused light or electrons, which draws out the desired shapes/patterns. This is normally achieved by scanning the sample on a motorised stage; but some forms of lithography, such as Talbot techniques, create a diffraction pattern of electrons to simultaneously expose large areas [129]. Depending on the resist used, light/electron exposure will either strengthen (negative resist) or weaken (positive resist) the exposed areas. This creates a large contrast in the resist's solubility. The energy delivered to a given area of resist is called the dose, and is a critical parameter to optimise the masks geometry.
3. Development: The samples are placed into a development chemical which dissolves the resist. The duration of development is another critical parameter, and ties in closely with the dose. A higher dose weakens a positive resist more, such that a short development is adequate. Conversely a high dose to a negative resist will further strengthen it, requiring a longer development. Balancing these two parameters is typically done by fixing a development time based on the manufacturer specifications, and then fabricating many small scale devices with different doses.

Lithography is a challenging process to optimise due to the large number of inter-dependant variables. The most critical of which are, firstly, the resist selection coupled with baking time & temperature, secondly, the dose strength of the electrons or light, thirdly, the development chemical, its dilution, and time.

Mask fabrication is either followed by a material deposition (henceforth referred to as metallisation) or an etching process; and finally the resist is cleaned away in a wet chemical process.

Metallisation adds further challenge to the entire fabrication process, as the newly deposited material may coat everything (including side-walls of the resist pattern). This can make it impossible for the resist mask to be removed (called lift-off), as there is no longer a path for the removal chemical to access the resist. Solutions to this problem involve creating an undercut in the resist so that there is some overhang which creates a ‘shadow’ during the deposition. Another commonly used solution to this issue is to sonicate the pattern, which causes cracks to form in the newly deposited material, and therefore a path to dissolve the resist. Another issue of metallisation is the build-up of material on the side walls of the mask. This was a major issue with the filter devices fabricated in this work, as metallisation left a lifted ring of metal around every hole. Simulations suggested this would not greatly impact performance; however, in practise these rings were highly non-uniform due to tearing during sonication, and performance (transmission and Q-factor) was only ≈20% of expected.

Wet etching requires that the metallisation step be completed before lithography, and there is an additional step in which an etching chemical is introduced to the sample. This etchant flows into gaps within the mask and dissolves parts of the material under the mask. The side-walls of the resulting pattern are not etched evenly, with areas towards the top of the pattern receiving longer exposure. For wide, shallow features (such as the filters in this work) this is not an issue. The additional step of etching is often worthwhile, as it simplifies a number of other steps. In this work it enabled the use of magnetron sputtering for the metal layer, because the diagonally oriented sputtering guns were only suitable for depositing continuous films. The choice of resists also became far less critical, as an undercut was no longer required, furthermore a conductive polymer layer wasn’t needed as the substrates were gold coated prior to exposure.

3.4.3 Atomic Force Microscopy

Abbreviated as AFM, this technique creates very high resolution maps of surface topology, with angstrom levels of precision. This is achieved by raster scanning an extremely sharp tip across a surface, which is connected to a cantilever; irregularities in the surface topology causes the cantilever to deflect. This deflection is measured by minute changes in the reflected angle of a laser focused onto the cantilever, as shown in Figure 3.13A. The sharpness of the tip of often the limiting factor in accurately measuring steep or very deep/tall features. It is worth noting that there are many modes of AFM operation, with continuous scanning and tapping being the standard employed for topology measurements. It is also possible to manipulate a surface using the tip (thermal, electrical, magnetic excitations). In this work AFM was used to evaluate the success of device fabrication, and to accurately measure steps in film thickness for use in materials characterisation. Figure 3.13B shows a typical AFM image of a filter device rendered in 3D.

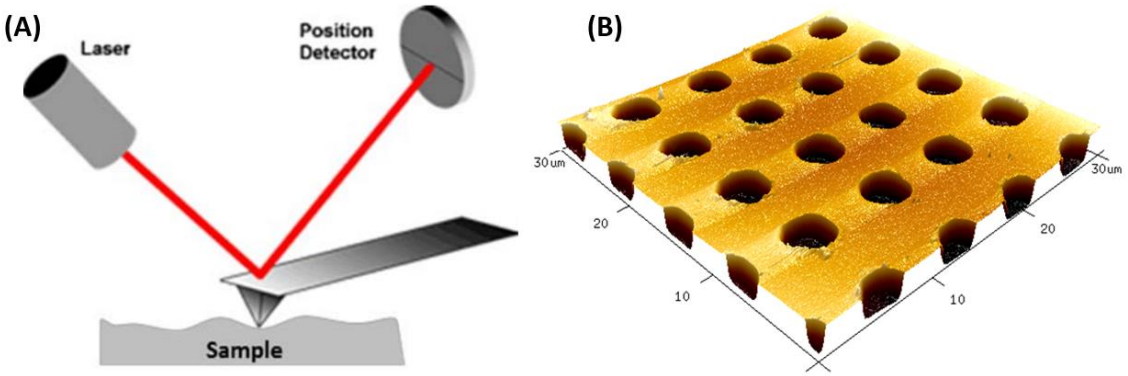

Figure 3.13. (A) Schematic representation of the operation of a typical AFM. A laser is reflected off a cantilever and onto a position detector, which measures the vertical deflection as the cantilever's tip scans across a surface. Reprinted from [130]. **(B)** Typical AFM image of a fabricated filter rendered in 3D, taken using a Bruker Innova.

3.5 CHARACTERISATION METHODS

3.5.1 Evaluating Elemental Composition and Structure

3.5.1.1 Electron Dispersive Spectroscopy (EDS)

When material samples are sputtered for the first time, it is important to check their composition to ensure that differences in elemental sputtering rates had not significantly deviated the samples from the desired elemental ratio. It was also important to evaluate the extent to which materials oxidise.

Electron Dispersive Spectroscopy (EDS) was the technique employed in this work for elemental composition analysis. EDS systems consist of an X-ray detector and software, which are typically mounted within a scanning electron microscope, which provides the high energy electron beam. These systems measure the (X-ray) photon energy emitted by elements due to high energy electron bombardment; the energy (keV) of these X-ray emissions is determined by the specific element being bombarded. EDS does have a number of limitations, primarily the fact that most elements exhibit multiple energy peaks, which often overlap with other elements, meaning some elements cannot easily be differentiated from each other. Another drawback is that light elements are difficult to detect due to their small size, and therefore low electron scattering rates [131]. Therefore detecting small (<5%) amounts of elements like oxygen is not typically possible. A typical results plot of the scattering electron count versus scattered electron energy is shown in Figure 3.14 below. Software is used to extract the most likely elemental composition of a sample from this data.

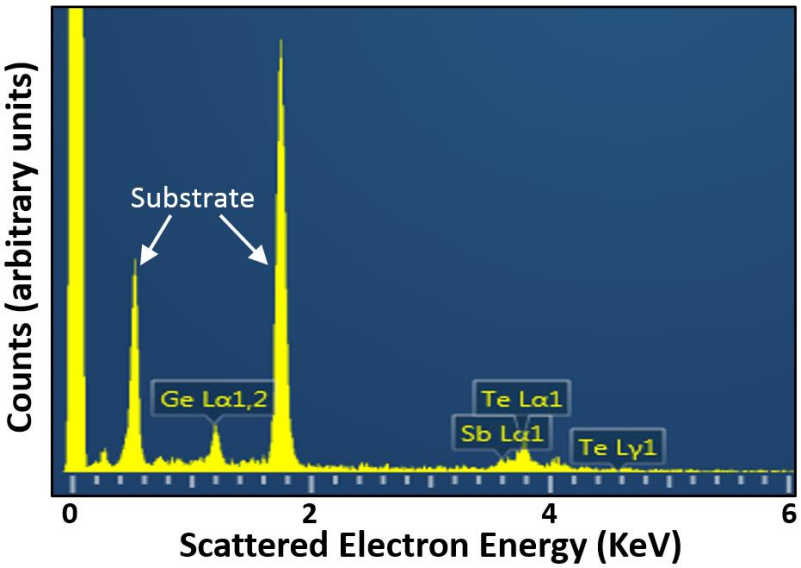

Figure 3.14. Example of EDS dataset. Scattering electron count (arbitrary units) versus scattered electron energy (keV) from an EDS measurement of a thin film $Ge_2Sb_2Te_5$ sample.

3.5.1.2 X-Ray Diffraction (XRD)

The wavelength of X-Rays is comparable to the spacing between atoms in a crystal. This means that when X-rays interact with matter they produce a diffraction pattern; this is caused by constructive and destructive interference determined by the crystalline structure of a material [132]. For an amorphous glassy material, the highly disordered nature of the atoms causes there to be no measurable diffraction pattern. For a crystalline solid, the ordered structure causes a distinct pattern, with intense reflection at specific incident angles caused by the cumulative effect of the multiple crystallographic planes. Braggs Law describes the condition at which constructive interference is greatest, as shown in equation 25, in which *n* is a positive integer (the order), *d* is the lattice spacing, and θ is the angle of incidence [133].

$$n\lambda = 2dsin(\theta) \tag{25}$$

The XRD machine used in this work was a Bruker D8; and is arranged with a source and detector positioned to reflect and capture X-Rays reflected off a sample at various angles. The raw data is the reflected intensity at each incident angle. The angular location, width, and height of the peaks can be used to

determine the composition of the analysed material, and the particular crystal structure. This is possible because the measured intensities are in reciprocal lattice space, and by applying Fourier theory it is possible to recover the Bravais lattice which fully describes the crystal structure.

In this work XRD measurements were primarily used to confirm crystallisation of phase-change materials, and secondly to investigate their crystalline structure. The Bruker D8 XRD is also equipped with a heating stage, meaning the dominant crystal structures at different temperatures could be easily identified. The third and final use for our XRD measurements was in performing X-Ray Reflectivity (XRR) measurements. This technique can measure the thicknesses of a multilayer stack of materials by arranging the X-ray source and detector to measure specular reflection. The intensity of the reflected X-rays will depend on the sharpness of the air/material interface, and any thin films present will alter the density at this interface, causing a deviation from Fresnel reflectivity. This deviation can be used to extract the density profile at the interface; and if the materials (and their densities) at the interface are known, then the layer thicknesses can be extracted.

3.5.1.3 Raman Spectroscopy

Raman scattering is a form of inelastic scattering which can occur when light is absorbed by a molecular bond. The inelastic nature of the process causes the light to be re-emitted with a different wavelength. The intensity and wavelength shift of the scattered light contains useful information, which is extracted from the location, height, and width of the peaks, as summarised in Figure 3.15. In this work Raman (specifically spontaneous Raman) measurements provided an additional approach to verify the molecular structure and extent of crystallinity of materials.

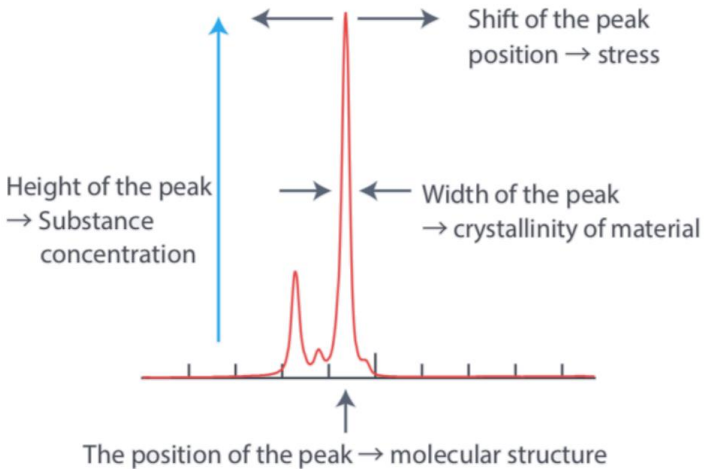

Figure 3.15. A simple guide for interpreting Raman spectra. Reprinted from [134].

3.5.2 Measuring Refractive Index

The determination of the real and imaginary parts (*n* and *k*) of the refractive index of the various materials used in this thesis was vital to properly design devices and interpret experimental results. Ellipsometry was the primary method used to determine n and k, although a number of other approaches were also employed. Once extracted, the *n* and *k* values would be used in the transfer matrix method to calculate the wavelength dependant reflectance spectrum for the sample of interest. The reflectance spectrum was then experimentally measured and compared to that calculated. A good match would confirm that the ellipsometry (or other method), had found a reliable solution.

3.5.2.1 Ellipsometry

Ellipsometry is an industry standard method for thin film characterisation [135]. It is also the primary method used in this work. It works by measuring how the polarisation of light changes as it reflects or transmits from a material structure, see Figure 3.16. Two quantities are directly extracted by the measurement; Phi (Ψ) is the change in polarisation (from linear to elliptical) represented as an amplitude ratio, and Delta (Δ) is the phase difference. The wavelength dependant Phi and Delta are determined by the sample's material(s) and thicknesses. Thus ellipsometry is primarily used to evaluate optical constants or film thickness; although evaluating both simultaneously can be challenging. In this work lithography was used to create a step in deposited films which were measured using AFM; this removed thickness as a variable. Ellipsometry can also determine roughness, crystallinity, layer gradation, doping concentrations, and other material properties which effect optical response.

Because ellipsometers do not directly measure optical properties, mathematical models are required to estimate and fit optical properties to theoretically produce the measured Ψ and Δ response. Care must be taken when fitting, as many combinations of *n* and *k* may produce an acceptable fit whilst also being incorrect or even unphysical. The majority of n and k values obtained via ellipsometry, and presented in this work, were fit using a Tauc-Lorentz oscillator, often combined with another oscillator and/or Drude contributions if appropriate. Particularly challenging data was initially fit using B-Spline models, and then parameterised into an oscillator model.

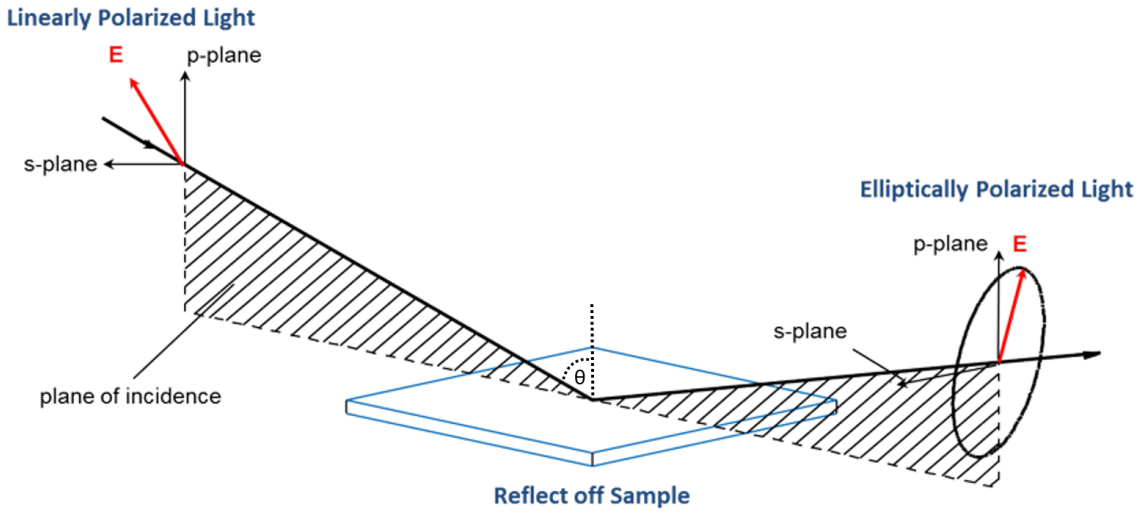

Figure 3.16. Schematic representation of the operation of an ellipsometer. Linearly polarised light is reflected off a sample at multiple angles of incidence (relative to normal incidence). The sample will alter the phase and polarisation of the light, which is measured by a detector. Adapted from [136].

3.5.2.2 Swanepoel Method

The Swanepoel method is an analytical approach for extracting the refractive index from a thin film on a substrate with a known refractive index. The transmittance spectra of a thin film possesses wavelength dependant peaks and valleys caused by interference effects. Assuming coherent interference, then the locations of these peaks and valleys corresponds to the real refractive index $n(\lambda)$, described by equation 26, in which t is the film thickness, m is the interference order, and λ is the wavelength.

$$2t \cdot n(\lambda) = \mathrm{m} \cdot \lambda \tag{26}$$

As this expression contains the product of both thickness and refractive index, it alone cannot be used to extract either. Equation 27 below is the Swanepoel formula, it uses T_M and T_m which are each an envelope curve which follows either the peaks or valleys of a transmission spectra, see Figure 3.17. Provided the substrate refractive index is known, then the index of the thin film can be extracted, as the gap between the envelopes is a direct consequence of the refractive indices.

$$n(\lambda) = \frac{2S(T_M(\lambda) - T_m(\lambda))}{T_M(\lambda) * T_m(\lambda)} + \frac{S^2+1}{2} + \sqrt{\left(\frac{2S(T_M(\lambda) - T_m(\lambda))}{T_M(\lambda) * T_m(\lambda)}\right)^2 - S^2} \tag{27}$$

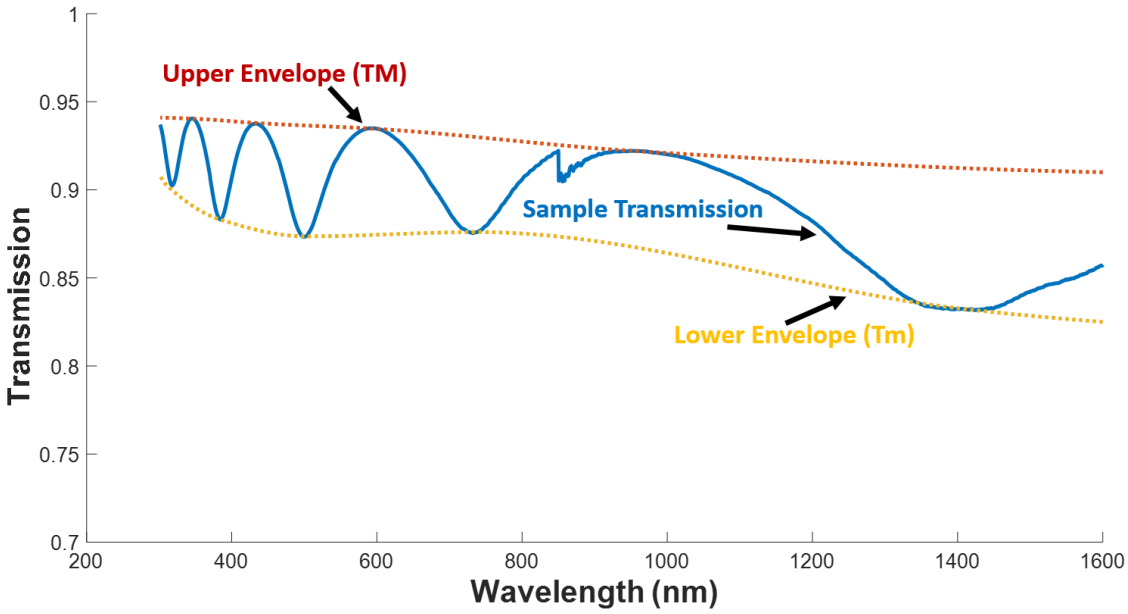

Figure 3.17. Transmission spectra of a thin film of $Ga_{13}La_7S_{30}$ on borosilicate glass. Also included are the upper (T_M) and lower (T_m) envelope curves used in a Swanepoel calculation.

The Swanepoel method was used in this thesis to determine refractive index for various films, particularly when no ellipsometry was available.

3.5.2.3 Matching of Reflection Spectra (Nanocavity fitting)

Reflection matching was initially used to tweak optical properties data from literature to better match the films deposited in our labs, and thus improve agreements between simulated and fabricated devices. This was necessary because n and k data in literature for many materials (particularly phase-change alloys) often disagrees substantially, despite the materials being notionally identical. Two sets of disagreeing n & k values from literature would be used to simulate the reflection spectra of a fabricated nanocavity, typically consisting of a PCM layer between an aluminium mirror and a SiO_2 top layer. The reflection of the sample would then be measured, and compared to the reflectivity simulated from literature, as shown in Figure 3.18.

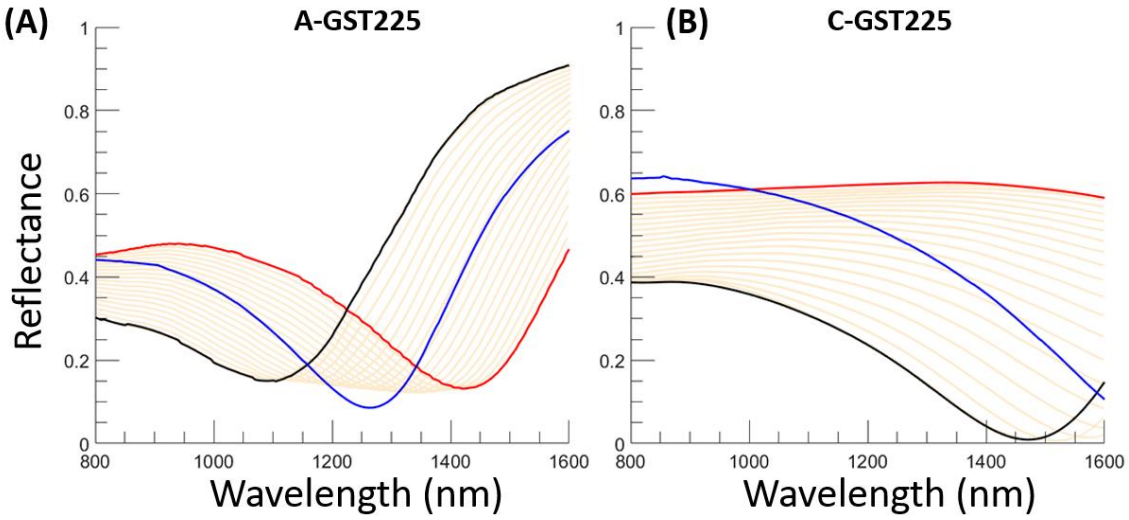

Figure 3.18. Blue curve: Measured reflectivity of a cavity consisting of 70nm of GST225 on top of an aluminium mirror and capped with 5 nm of SiO2. **Red** and **black** curves are reflectivity calculated using two n & k datasets from literature [57,137]. The **blue curve** is the measured reflectance of a fabricated sample, and the **Yellow curves** denote the 'trial space' encompassed by the literature datasets. **(A)** is for as-deposited amorphous GST225. **(B)** is for crystalline GST225.

Assuming proper selection of the literature data, then the measured reflectivity should fall somewhere between the two calculated spectra. Equation 28 is a weighted average function which was used to calculate refractive index based on literature data sets to produce one which exhibits excellent agreement between calculated and measured reflectivity.

$$\tilde{n}(\lambda) = \left(\frac{\tilde{n}_{Hi}(\lambda)+\tilde{n}_{Lo}(\lambda)}{2}\right) + W(\lambda) * \left(\frac{\tilde{n}_{Hi}(\lambda)-\tilde{n}_{Lo}(\lambda)}{2}\right) \quad (28)$$

Where $\tilde{n}(\lambda)$ or $\tilde{k}(\lambda)$ is the calculated optical property at a specific wavelength. $\tilde{n}_{Hi}(\lambda)$ and $\tilde{n}_{Lo}(\lambda)$ (or $\tilde{k}_{Hi}(\lambda)$ and $\tilde{k}_{Lo}(\lambda)$) are the optical properties from the two literature datasets. $W(\lambda)$ is the weighting coefficient which is calculated by a MATLAB script which calculates the reflection spectra for every value of $W(\lambda)$ between -1 and +1, and then for each wavelength selects the value which minimises mean square error. In some cases three or more literature data sets were used to improve agreement in reflection.

The second major use for reflection data was to help verify the accuracy of ellipsometry measurements. Measured reflectivity of a sample would be compared to spectra calculated from ellipsometry *n* and *k* results. Confidence in

the optical properties was then determined by the difference in shape and amplitude between the two spectra.

For both applications, samples which exhibited a Fabry-Pérot resonance in the measurable spectra range (200 to 1600 nm) were desirable; this resonance feature is sensitive to small deviations in refractive index, and the feature location provides an extra parameter to improve the uniqueness of any mathematical fitting. Equation 28 describes the phase delay (δ) of reflected light, and when this delay equals pi, then there will be a reflection minimum due to destructive interference. Under this condition equation (29 can be re-written as in equation 30. Plugging in the materials refractive index (or estimation of) and the desired resonance wavelength, the equation will then yield the film thickness to deposit. Figure 3.19 shows the range of thicknesses for a given refractive index which will produce a Fabry-Pérot resonance within the measurement range (250 to 1600 nm) of the UV/VIS spectrometer available in our laboratories.

$$\delta = \frac{2\pi}{\lambda} * 2n(\lambda)t \qquad (29)$$

$$t(\lambda) = \lambda/4n(\lambda) \qquad (30)$$

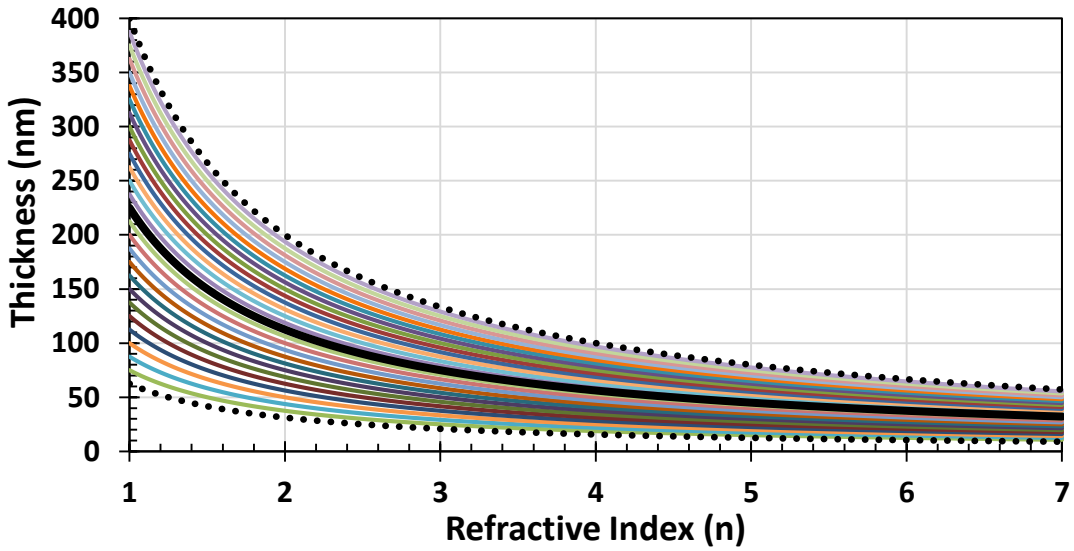

Figure 3.19. Curve calculated using Equation 30 showing the range of thicknesses which produce a Fabry-Pérot resonance within the measureable range of available spectrometers (250 to 1600 nm). The solid black line denotes a resonance at the central wavelength of 900 nm.

3.5.2.4 Evaluating Losses by Varying Sample Thickness

This approach was primarily used on bulk PCM samples, and uses the fact that the ratio of transmission through two samples of the same material is proportional to the thicknesses ratio of the samples. This is a simple approach in which the reflected intensity is the same for each sample (excluding wavelengths at which cavity effects due to the film thickness are present). Because reflection for both samples is equal, any change in transmission must be due to absorption, which is a function of thickness and the extinction coefficient, k. Equation 31 describes the transition through both samples as a ratio (assuming two air interfaces with bulk samples). Equation 32 is the re-arranged version to solve for the extinction coefficient *k*.

$$\frac{T_1}{T_2} = \frac{\overbrace{(1-R_{1st})}^{\text{1st Reflection}} \overbrace{\left(e^{-\frac{4\pi k t_1}{\lambda}}\right)}^{\text{Absorption from sample}} \overbrace{(1-R_{2nd})}^{\text{2nd Reflection}}}{(1-R_{1st})\left(e^{-\frac{4\pi k t_2}{\lambda}}\right)(1-R_{2nd})} = \frac{e^{-\frac{4\pi k t_1}{\lambda}}}{e^{-\frac{4\pi k t_2}{\lambda}}} \tag{31}$$

$$k(\lambda) = \frac{\lambda Log(T_1/T_2)}{4\pi(t_2 - t_1)} \tag{32}$$

3.5.3 Electro-Optical Crystallisation Measurements

The extent to which a phase-change material can be returned to its amorphous phase directly affects the useable optical contrast. For device applications both the specific PCM alloy and device structure contribute towards this useable contrast. In the work of this thesis a material property called *switchability* was defined; it is the percentage of practically accessible PCM properties contrast when compared to the contrast between the as-deposited amorphous phase and crystalline phase. It is determined by comparing the contrast in reflectivity from fully as-deposited amorphous to crystalline, compared to the reflectivity contrast when attempting to return from crystalline to amorphous, as illustrated in Figure 3.20. This metric was used to compare the relative useful optical contrast of a number of PCM alloys in a quantitative way.

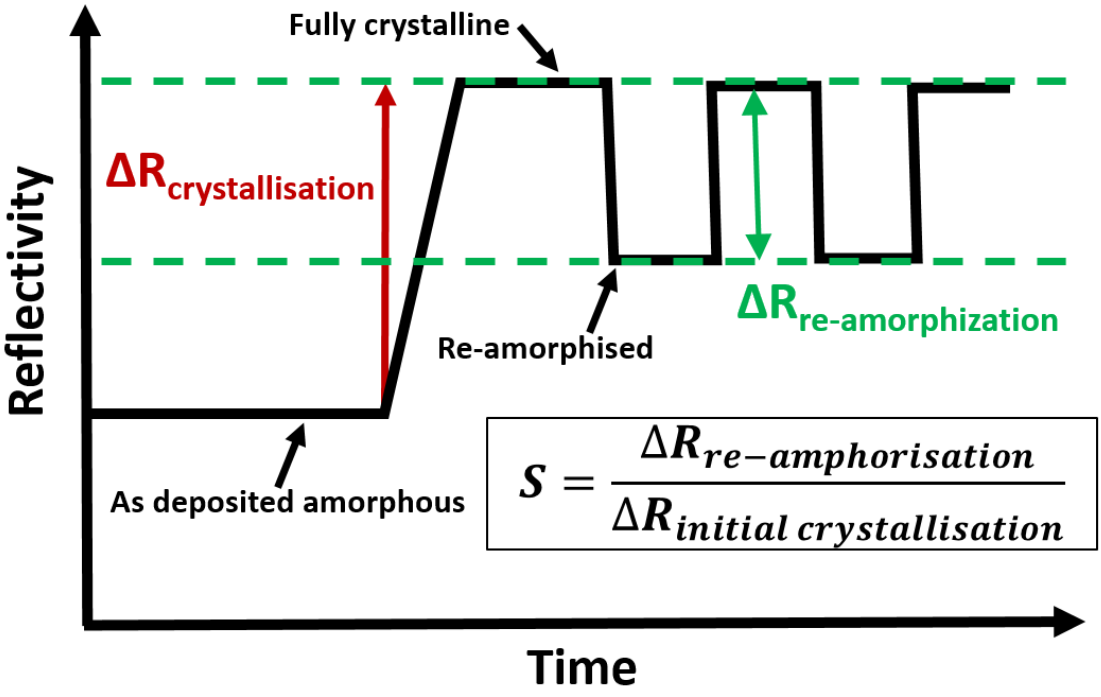

Figure 3.20. Expected reflectivity profile of an as-deposited PCM film as it is cycled.

To evaluate the switchability of phase-change alloys, a number of micro heater devices were fabricated using e-beam lithography and lift-off. These heaters are made from sputtered platinum, and consist of electrical contacts which taper into a micro-bridge heater. It is onto the micro-bridge, through a window of photoresist that the phase-change material and barriers are deposited, see Figure 3.21A.

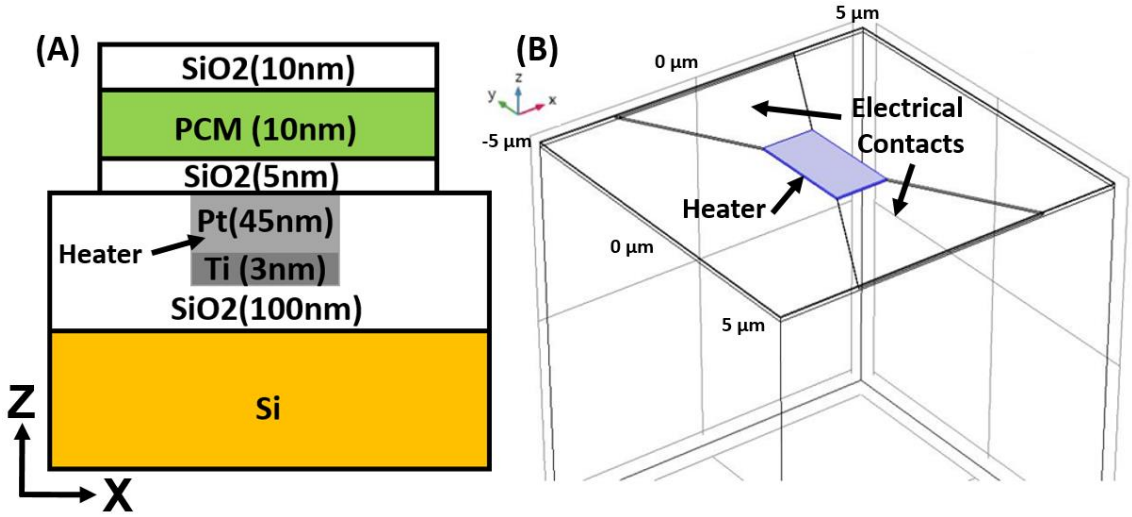

Figure 3.21. (A) Diagram (side view) of the heater devices used to evaluate crystallisation properties of PCM films. **(B)** Image of COMSOL model used to find the relationship between applied heater voltage and temperature.

These heater devices were electrothermally modelled in COMSOL (see Figure 3.21B) to provide an estimation of the heater temperature for a range of applied voltage pulses. The COMSOL models also used *n* and *k* values extracted via ellipsometry to estimate the reflectivity of the heater devices for both amorphous and crystalline phases of the PCM layer, which was used as a double-check for the crystallinity.

The reflectivity of these devices was then measured at three wavelengths (460, 540, and 610 nm) in real-time as electrical pulses were applied using the combined electro optical test station shown in Figure 3.22A. At some applied voltage the reflectivity of the device would change, indicating switching of the PCM layer. The device temperature could then be evaluated using the temperature-voltage relation calculated by COMSOL, as shown in Figure 3.22B. Once a device was fully crystallised the switchability could be evaluated by attempting to re-amorphise the device by using successively more powerful electrical pulses.

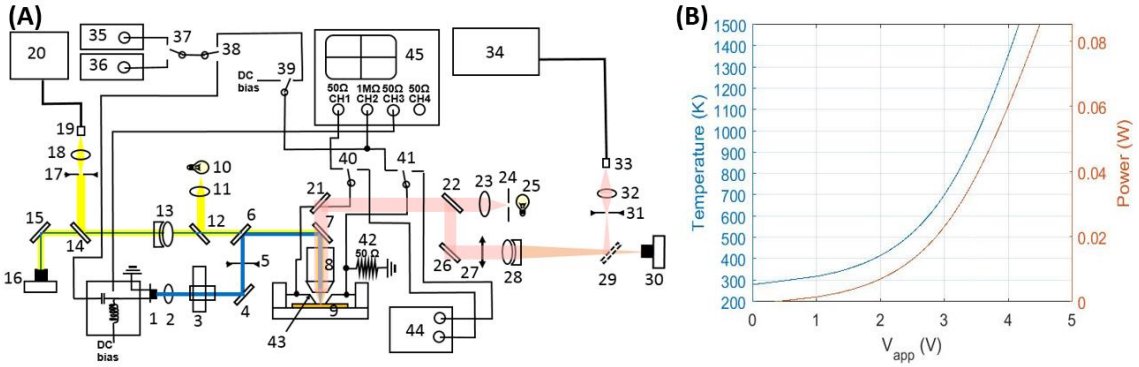

Figure 3.22. (A) Schematic diagram of the combined optical electrical test station used to measure reflectivity while simultaneously applying electrical pulses to micro heater devices. **1**: Laser diode. **2**, **11**, **18**, **23**, **32**: lens. **3**: Safety Shutter. **4**, **12**, **15**, **21**, **26**, **29**: mirror. **5**, **17**, **24**, **31**: aperture. **6**, **7**: Dichroic beam splitter. **8**: objective lens. **9**: sample. **10**, **25**: light source. **13**, **28**: achromatic doublets lens. **14**, **22**: beam splitter. **16**, **30**: CMOS camera. **19**, **33**: fibre optics coupler. **20**, **34**: spectrometer. **27**: polarizer. **35**, **36**: pulse generator. **37**, **38**, **39**, **40**, **41**: RF relay. **42**: shunt resistor. **43**: pico-probes, **44**: Keithley source meter, **45**: oscilloscope. Adapted from [138]. **(B)** Relationship (simulated) of heater power and temperature depending upon applied voltage.

3.5.4 Spectroscopic Methods

Spectral transmission and reflection measurements were vital for both characterisation of materials, and for evaluating the performance of fabricated devices. They were performed by three different spectrometers, depending on the specific sample.

3.5.4.1 UV to NIR Micro-spectrophotometry

For wavelengths between 200 and 1600 nm a Jasco MSV-5300 UV-Visible/NIR Micro-spectrophotometer was available. This can measure in both transmission and reflection. It also has three magnifying objectives and a camera, allowing for reflection spectra measurements and thus fabrication of smaller footprint devices in this wavelength range. There are also internal polarisers for use in measuring polarisation sensitive devices. Aside from the camera and lenses, the Jasco functions much like a standard spectrometer; the source is a broadband lamp, and a grating is used to separate out the wavelengths. There are two detectors, one for below 850 nm, and the other above; this requires that a dark baseline to be taken to correct the high noise levels at the changeover wavelength. The bright baseline in reflection was performed with a calibrated aluminium mirror.

Reflectivity measurements were used to help verify n and k values obtained via ellipsometry, as the spectral ranges of both machines overlap. Transmission measurements were used for characterisation via the Swanepoel method (refer to sub-section 3.5.2.2), and for determining absorption bands to feed into ellipsometry models.

3.5.4.2 Fourier Transform Infrared Spectroscopy (FTIR)

The operation of FTIRs is more complex than that of standard spectrometers. Instead of using a grating, an interferometer with a moving mirror is used to distinguish between wavelengths, see Figure 3.23. All wavelengths are simultaneously measured, and as the mirror moves particular wavelengths constructively and destructively interfere. This effectively alters the source signal as a function of time, with the sample acting as a filter. Computer software then

performs a fast Fourier transform on the resulting signal to convert it into frequency domain, so revealing a spectrum.

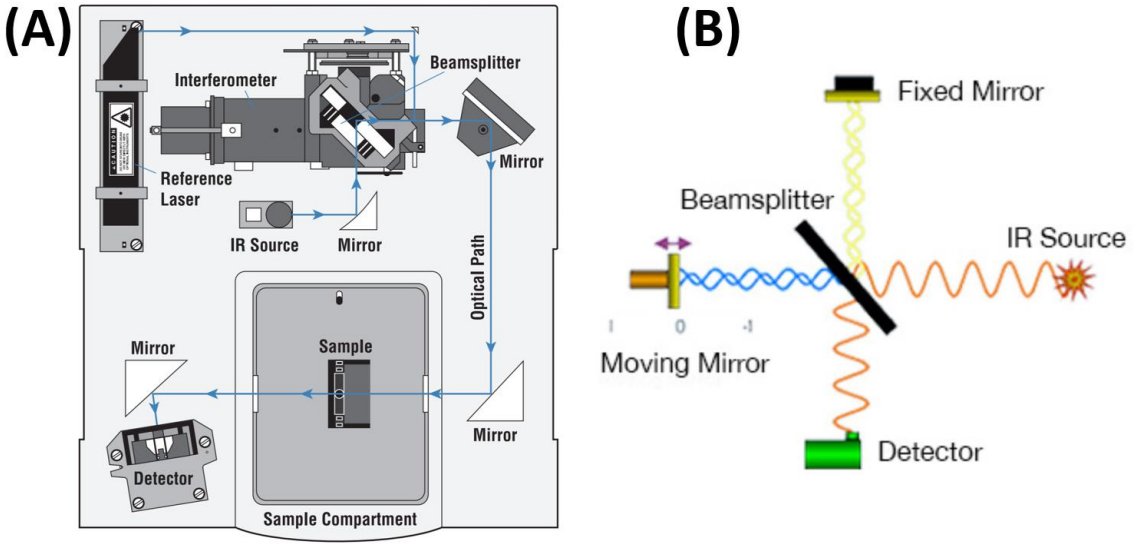

Figure 3.23. (A) Layout diagram of a typical FTIR. **(B)** Simple diagram of the interferometer setup used in FTIRs. The sample would be placed between the beam splitter and detector. Reprinted from [139].

To evaluate the filter devices fabricated in this thesis, transmission measurements in the mid and long wave infrared were required. For these measurements two FTIRs were available, and used depending on whether a vacuum was required. Most filters were designed to operate in an atmospheric transmission window, in which case a basic INTERSPEC FTIR was adequate. Otherwise a Bruker 80v FTIR was used, this FTIR has an excellent SNR, and the vacuum chamber removes absorption due to atmospheric water vapour.

Both FTIRs emit a relatively large collimated beam of light; to compensate, our devices were typically fabricated as 3 by 3 mm square arrays and paired with a 2 mm circular aperture. The spectral range of both FTIR machines is approximately 1.5 to 28 µm, with SNR rapidly deteriorating towards these extremes.

4 EXPLORATION OF NOVEL PHASE-CHANGE MATERIALS

As discussed in section 2.2, phase-change materials are those that can stably exist in either a glassy amorphous phase, or an ordered crystalline phase, and possess the ability to quickly and reversibly switch between phases. These phases also exhibit distinctly different properties, with high contrast in optical properties being of most interest for the devices in this thesis. These phase transitions are driven by controlling the material's temperature.

Desirable PCM properties can vary greatly depending upon application. While there are general trends in PCM properties, (such as greater losses in the crystalline phase), many properties are highly dependent on the specific alloy, and even deposition conditions. As such, a materials study was conducted to evaluate the properties of several promising phase-change materials, and determine their suitability for different applications. The PCMs for characterisation were selected based upon their presumed suitability for use in the filter device applications discussed in chapter 6. This selection typically prioritised low optical losses, and high switchability (ease of re-amorphisation).

Some of the alloys characterised in this work have been extensively studied previously (especially $Ge_2Sb_2Te_2$ [140–143]), however, some (such as GaLaS) had never been optically characterised before in both phases. The characterisation carried out in this thesis focuses upon a PCM's optical properties (n and k), and their ability to switch. However, some structural and elemental characterisation was necessary to ensure the alloys were of correct composition and had fully crystallised when desired.

4.1 PHASE-CHANGE ALLOYS EXPLORED

This section introduces the various alloys explored in this work, and the motivations for their inclusion in the study. The majority of alloys are chalcogenides containing germanium, antimony and tellurium. The specific alloys are listed below.

1. GeTe
2. $Ge_2Sb_2Te_5$
3. $Ge_3Sb_2Te_6$
4. $Ge_2Sb_2Se_1Te_4$
5. $Ge_2Sb_2Se_2Te_3$
6. $Ge_2Sb_2Se_3Te_2$
7. $Ge_2Sb_2e_4Te_1$
8. $Ag_{5.5}In_{6.5}Sb_{59}Te_{29}$
9. $Ga_{26}La_{14}S_{60}$

4.1.1 $Ge_xSb_2Te_y$ Series

$Ge_2Sb_2Te_5$ (GST225) was the natural starting point for this PCM characterisation study and for device simulations; this is chiefly because it is very well studied in literature, and has some desirable properties [140–143]. However, there are many applications in which GST225 is not ideally suited. GST225 is considered a nucleation dominated PCM, composed with optically switched memory in mind (DVD-RAM), in which low optical absorption and ease-of -amorphisation were not prioritised. Compared to many PCMs, GST225 is optically lossy, making it not particularly well suited for transmissive devices like those in this thesis. Furthermore, crystallisation occurs over a broad temperature range (130-620 °C) which impairs thermal stability and makes re-amorphisation challenging [57,144]. Because of these reasons, GST225 is a good proof-of-concept starting point for EOT devices, but leaves significant scope for performance gains by using a more suitable PCM alloy.

GeTe is another well studied PCM, especially for memory applications [145]. It has similar properties to GST225, but is somewhat more thermally stable (higher onset of crystallisation temperature). It was primarily included here to test the nano-cavity reflection fitting technique developed in this work and discussed in sub-section 3.5.2.3.

$Ge_3Sb_2Te_6$ (GST326) is a variant of GST225, with roughly a fifth of its antimony replaced with additional germanium, as shown in Figure 4.1. It is reported to possess similar properties to GST225, but with minor improvements to several important characteristics. Specifically, these properties are a larger contrast in refractive index, slower crystallisation rate, and a higher onset of crystallisation temperature [146,147]. Other GST compositions were not involved in this study, as previous high-throughput characterisation of the entire compositional range showed that GST326 possessed the greatest contrast in reflectivity, and therefore refractive index [148].

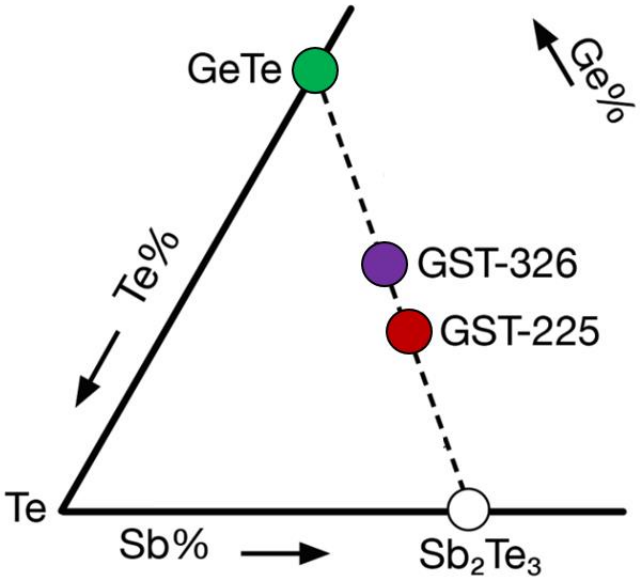

Figure 4.1. Ternary phase diagram of Ge, Sb, and Te, with the dashed GST line representing the compositional range of GST alloys. The PCMs experimentally investigated in this study are coloured. Adapted from [147].

The crystal structure of GST225 and GST326 is best described as distorted rocksalt, with the Ge and Sb atoms being located off centre with two different Ge(Sb)-Te bond lengths [149,150]. Face centre cubic and hexagonal crystal structures also form at lower and higher temperatures respectively [151].

4.1.2 $Ge_2Sb_2Se_xTe_y$ series

The need for low loss PCMs in both crystalline and amorphous phases prompted the investigation of the $Ge_2Sb_2Se_xTe_y$ (GSST) series, which were recently reported to have up to 600 times lower losses in the NIR compared to GST225 [152]. These alloys are effectively GST225 with some amount of tellurium substituted by selenium, such that x+y=5, as shown in Figure 4.2. The switching characteristics of GSST have also been reported as more favourable, with narrower crystallisation temperature range reported in [153]. Furthermore, the substitution of Se for Te increases the molten viscosity, which reduces crystal formation speed, as reported in the patents initially proposing GSST [154]. The GSST samples produced in this thesis were crystallised using a hot plate for 10 minutes at 280 ^{o}C.

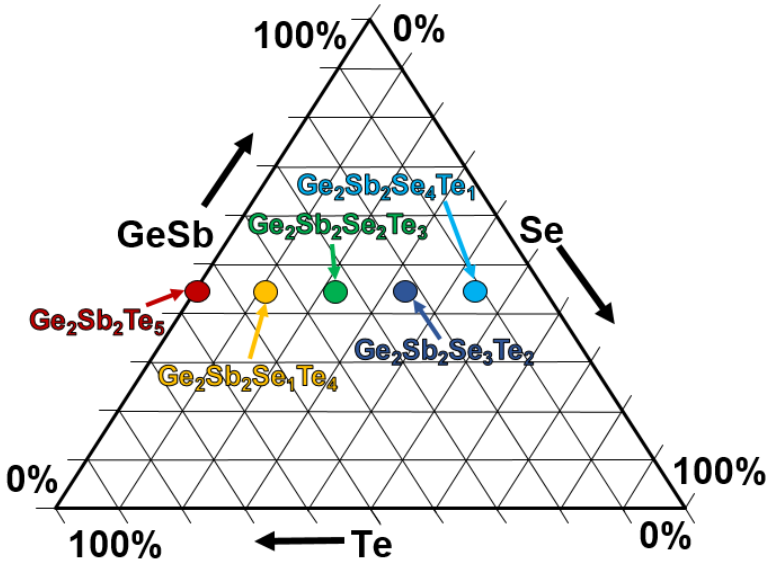

Figure 4.2. Ternary phase diagram of GeSb, Se, and Te. Coloured are GST225 and the GSST22xy series, which are experimentally investigated in this study.

4.1.3 GaLaS

Mixing Ga_2S_3 and La_2S_3 (typically in ratios near 65:35 respectively) produces GaLaS (GLS), a glass with a wide transparent region (0.5 μm to 14 μm) and a relatively low (compared to other IR transparent materials) refractive index of ≈2.4 [155]. This glass was first reported in 1976 [156], as a high index glass suitable for drawing into fibres and turning into lenses; making it a non-toxic

alternative to arsenic based glasses [155]. While GLS has received great interest for these uses, it has another interesting and relatively unexplored property; GLS is a phase-change material.

GLS does not share many of the drawbacks exhibited by other PCM alloys in the realisation of tuneable optical devices. Of greatest interest are low visible losses and the ease of re-amorphisation. There is a wide range of Ga_2S_3 and La_2S_3 ratios which can form a glass, with each possessing marginally different properties. In this work 13 compositions were created for characterisation (sub-section 3.3.1 details the creation of these sputtering targets), as shown in Figure 4.3. However, focus was quickly given to 65:35 (65% Ga_2S3, 35% La_2S_3) due to its excellent glass forming ability, and the availability of literature data on the properties of its amorphous phase [157,158] (though not, it should be noted, on the crystalline phase, nor for thin-films).

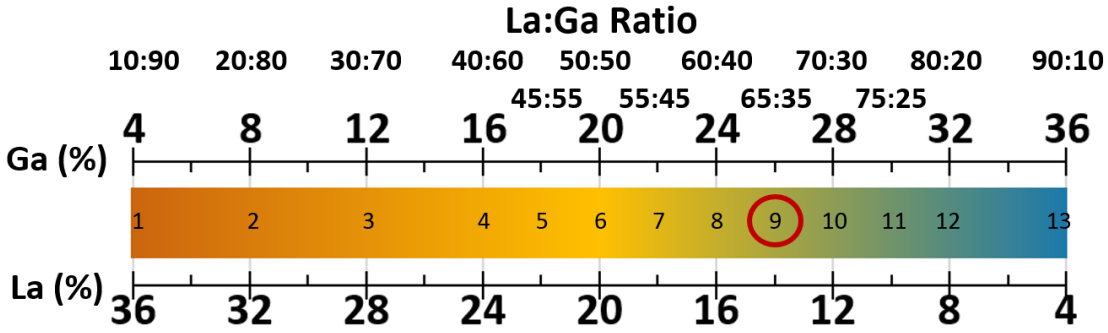

Figure 4.3. Diagram showing how the ratio of lanthanum and gallium vary throughout the entire GLS compositional range. The ratios above the bar relate to the ratio of gallium sulphide to lanthanum sulphide, with each being a composition created in this thesis. The numbers within the bar are labels for each composition, with number 9 (65:35) being the focus of characterisation.

Figure 4.4 shows an image of a small portion of the produced GLS samples. Of note are the amorphous bulk samples; these demonstrate the relative triviality of re-amorphising GLS compared to most other PCMs. Most of the compositions of fabricated sputtering targets also re-amorphised when removed from the furnace. In contrast, it is very challenging to re-amorphise most other PCMs, even for micron scale volumes.

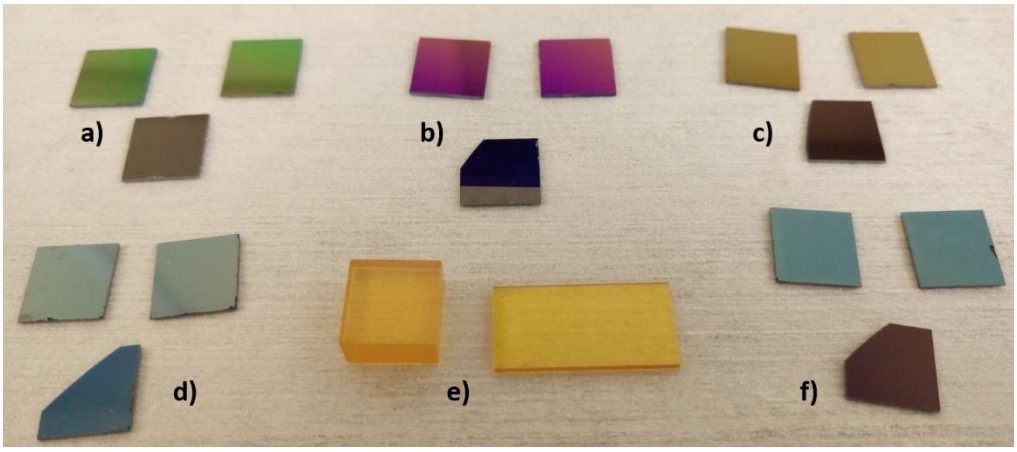

Figure 4.4. Image of a small selection of the GLS samples produced for the characterisation study. **a)** Two capped 33 nm 55:45 GLS samples and their corresponding ITO sample. **b)** Two capped 170 nm 65:35 GLS samples and their corresponding ITO sample. **c)** Two capped 58 nm 90:10 GLS samples and their corresponding ITO sample. **d)** Two capped 196 nm 55:45 GLS samples and their corresponding ITO sample. **e)** 1mm and 5mm thick 65:35 bulk GLS glass samples. **f)** Two capped 132 nm 90:10 GLS samples and their corresponding ITO sample.

Compared to the majority of PCMs, GLS is very thermally stable, with a glass transition temperature of 550 °C [159]; this is unusual for a sulphide glass, and is likely a result of the high coordination number of the sulphur atoms. GLS also possesses a very narrow crystallisation region and low crystallisation rate; these traits make re-amorphisation trivial, allowing for larger volumes to be practically used; see Figure 4.5 for a comparison of crystallisation properties to GST225.

The contrast in refractive index for GLS is comparable to many other alloys (as a percentage change), but (as shown later in Figure 4.13) exhibits very large contrast in optical losses and electrical resistance. Other properties such as the ability to readily accept dopants, and strong non-linearity make GLS an interesting candidate for further study [160,161]. The crystallisation recipe for all GLS samples used in this work was to slowly ramp to 740 ^{o}C and maintain for 10 minutes within an RTA in a low pressure argon atmosphere.

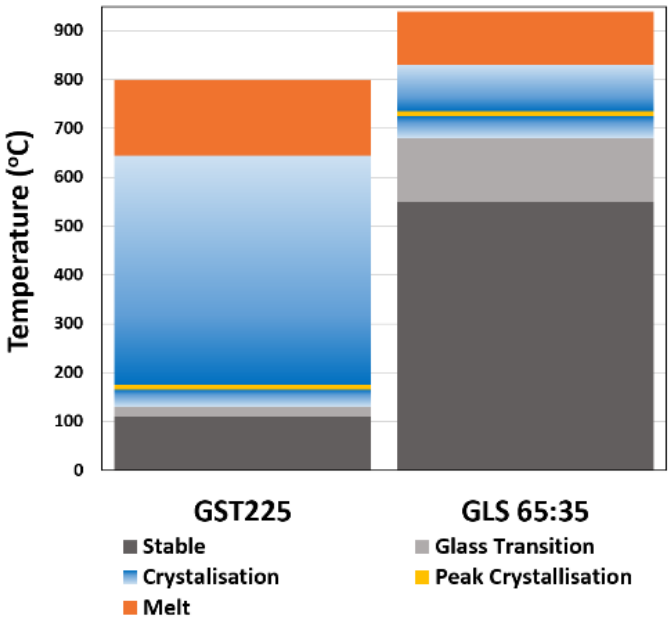

Figure 4.5. Comparison of thermal threshold temperatures related to PCM switching between GST225 and GLS65:35. The peakcrystallisation temperature refers to a single type of crystal structure only (different temperatures preferentially form different crystal structures). GST225 data from [159].

The remarkably broad transparent region exhibited by amorphous GLS, shown in Figure 4.6, opens up some interesting device applications, especially in the visible where GLS appears to be the only genuinely transparent PCM for the entire visible spectrum.

Antimony sulphide (Sb_2S_3) is another sulphur based PCM which was recently reported on [162]. Sb_2S_3 has similar visible optical properties to GLS, but with greater amorphous optical losses, and substantially lower crystalline losses. This makes antimony sulphide another useful PCM in the visible, but suitable for different applications in which relatively low losses in both phases are desired rather than a large contrast in losses. However, its study was beyond the scope of this thesis.

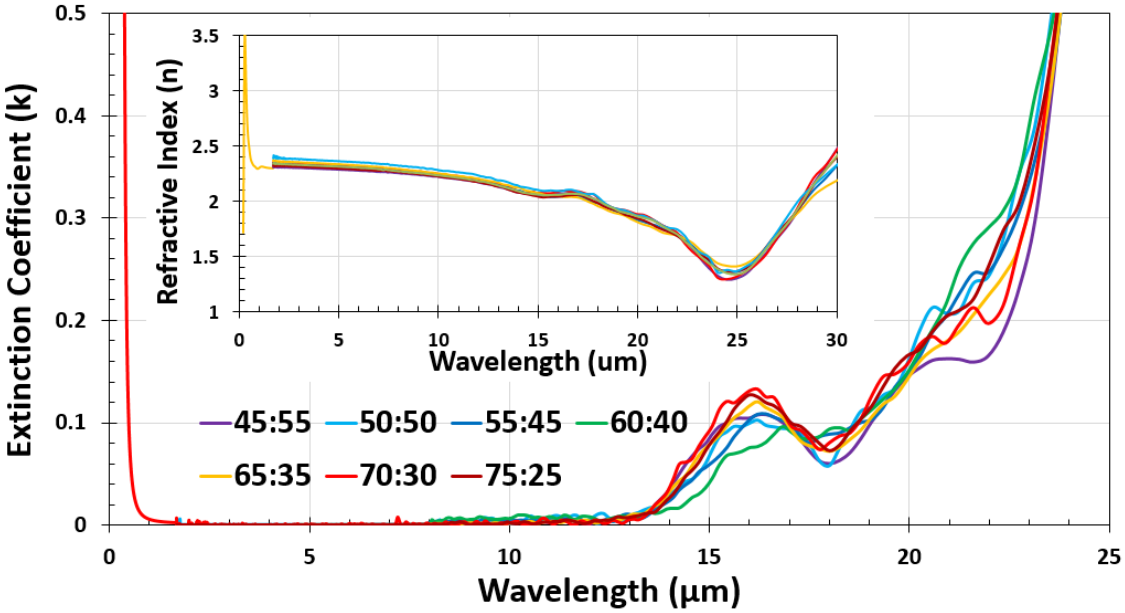

Figure 4.6. Optical properties (n & k) of five compositions of bulk GLS glass from visible to LWIR. Measurement performed via ellipsometry. Composition is denoted by two numbers, X:Y. X is the molecular percentage of gallium sulphide (Ga_2S_3) and Y is lanthanum sulphide (La_2S_3). **Inset:** shows the refractive index of a variety of GLS compositions obtained by performing ellipsometry on amorphous bulk samples.

4.1.4 AIST

AIST, (specifically $Ag_{5.5}In_{6.5}Sb_{59}Te_{29}$ is studied here) is a growth dominated PCM alloy used in commercial optical storage, most notably DVD-RW format [163]. The motivation to include AIST in this study was due to its slow crystal growth velocity when compared to GST225. As a growth dominated PCM, the crystal growth velocity is the main determinant of overall crystallisation speed. As shown in Figure 4.7, the maximum growth rates for AIST and GST225 are of similar order (good for fast crystallisation), however, for AIST this rate rapidly decreases with temperature (good for re-amorphisation). The resulting slow crystallisation speed during quenching was believed to make AIST relatively easy to re-amorphise, and therefore more suitable than GST for in-situ electrical switching.

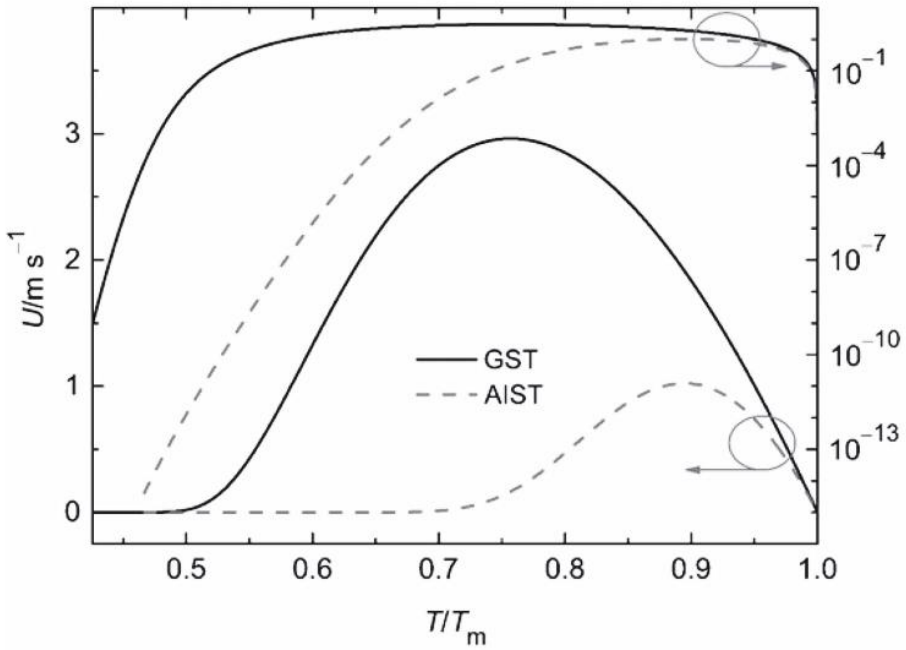

Figure 4.7. Comparison of crystal growth rates of AIST and GST from T_g to T_m. The logarithmic plots (right-hand abscissa) show that the maximum growth rates in the two systems are of similar order, relevant for fast PCM switching. Below 0.7 T_m, the kinetics in AIST become much slower than in GST, hindering homogeneous nucleation of crystals. This may contribute to AIST showing growth-dominated crystallisation. Reprinted from [164].

Current research into AIST mostly concerns electrical memory using ovonic threshold switching, as AIST appears to have some unique switching characteristics which make ovonic threshold switching particularly attractive [165]. Much like the GLS alloy described previously, AIST becomes very absorbing when crystalline, giving it substantial contrast in both real and imaginary parts of its refractive index (shown in Figure 4.13).

4.2 Elemental and Structural Characterisation

4.2.1 Elemental Characterisation

The elemental composition of a sputtered (alloy) film is not necessarily the composition of the sputtering target, and will invariably deviate by at least some amount. This deviation is caused by heavier elements being more able to travel through the plasma. Alloys composed of similarly sized elements are less susceptible to this effect (discussed in sub-section 3.3.1).

Once a new PCM alloy had been deposited in this work (for the first time), its elemental composition was checked using energy dispersive X-ray spectroscopy (EDS) to ensure the desired composition was obtained. Figure 4.8 shows one such EDS dataset explored here for each GST and GSST composition. Small deviations from the expected composition are acceptable due to the relatively large errors inherent in EDS (approx. ±4%), and as such all samples shown in Figure 4.8 were deemed acceptable. In fact, all samples of GST and GSST alloys possessed good elemental stoichiometry, likely owing to the similarity in weight of their constituent elements.

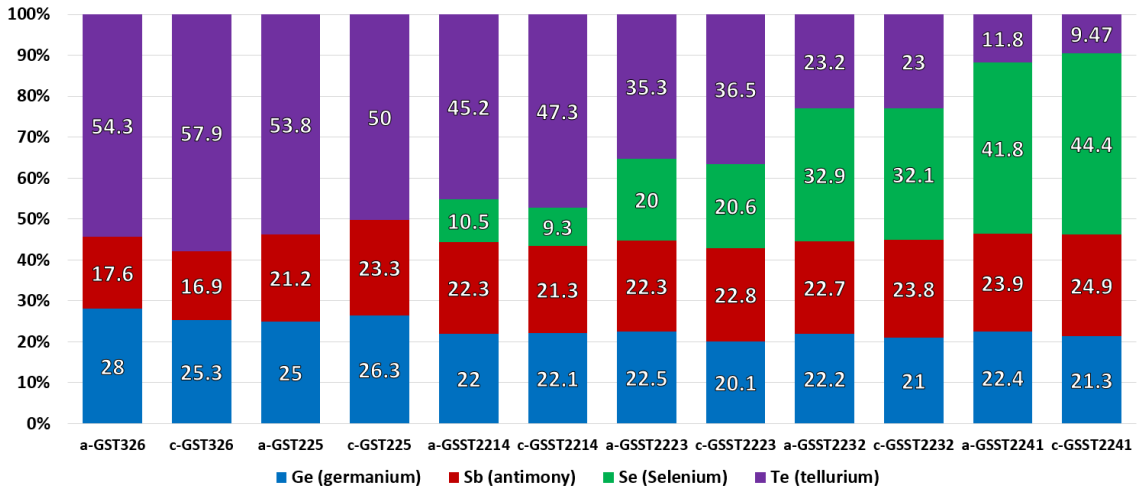

Figure 4.8. Example results from Energy dispersive X-ray spectroscopy (EDS) for all of the characterised compositions which include germanium, antimony and tellurium. Numbers within the colour bars denote their relative percentage. Electron acceleration voltage was 5 kV. Accuracy is roughly +/- 4%, depending on exact film thickness.

GLS required additional care to properly deposit and crystallise compared to the other PCM alloys in this thesis. Initially, uncapped GLS samples were fabricated, however, their properties changed in unexpected ways when annealed (a drop in refractive index). EDS was therefore conducted to check the sample's composition, and it was found that the amorphous phase was sulphur deficient, and that after annealing virtually all sulphur had sublimated, see in Figure 4.9A. This sublimation was occurring before the onset of crystallisation, thereby preventing a genuine phase-change from occurring. Sublimation was further confirmed as the issue by examining residue deposited onto the RTA's chamber walls. The extent of the sublimation was investigated by measuring the sulphur content of a bulk GLS sample (correct composition when amorphous), in which the sulphur levels dropped by half when annealed, see Figure 4.9B. This implied that the depth of sublimation was approximately half the penetration depth of the EDS, at around 300 nm. Subsequent GLS samples were capped with thick (at least 60 nm) layers of either SiO_2 or ZnS-SiO_2; the latter is an especially effective barrier material due to the small grain size and high thermal stability [166]. This capping resolved the sublimation issue, see Figure 4.9C.

The as-deposited GLS samples were still sulphur deficient; the reason was correctly suspected to be because the constituent elements of GLS vary hugely in atomic weight (lanthanum is 57 compared to sulphur at 16). This discrepancy manifests as less sulphur than expected reaching the substrate, requiring over-stoichiometric (sulphur rich) sputtering targets to compensate. Such targets were fabricated, and films deposited with them had near-ideal composition, as shown in Figure 4.9D.

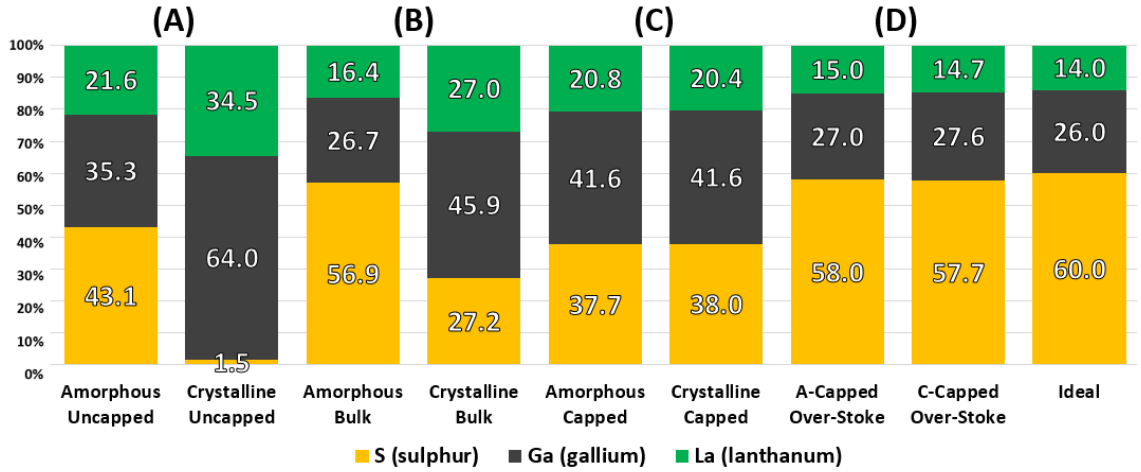

Figure 4.9. EDS measurements for a variety of GLS samples, compared to the ideal/target composition. **(A)** Few hundred nm of GLS on bare silicon without encapsulation. **(B)** 1 mm thick bulk samples of GLS **(C)** 240 nm of GLS capped with 67 nm of ZnS-SiO_2 **(D)** Few hundred nm of GLS on bare silicon, deposited using a sulphur rich over-stoichiometric sputtering target, capped with 100nm of ZnS-SiO2.

EDS was also used to evaluate oxidation of all PCM compositions examined here. Oxidation was significant for uncapped films of all the studied PCM alloys after annealing, but would otherwise take several days at room temperature (determined by comparing change of optical properties via ellipsometry). Of interest was the high levels of oxidation found in GLS, which was previously thought to be particularly resistant. However, just 10 nm of encapsulation (SiO_2, ITO or $ZnSiO_2$) was found to be sufficient defence against oxidation.

4.2.2 Raman Characterisation

Raman measurements were performed on the majority of the studied PCM alloys as a fast method to confirm crystallisation, and to ensure nothing unusual had occurred during annealing.

For the GSST alloys, only the 2241 composition has been previously reported in literature, with the characteristic crystalline peaks (in the raw data) occurring at 123 cm^{-1} and 153 cm^{-1} [167,168]. These peaks were also identified in the GSST2241 Raman measurements performed for this thesis. Also identified was the Boson peak (ubiquitously present in amorphous solids) at around 60 cm^{1} [169].

The Raman measurements performed on GSST samples in this work are presented here for additional GSST compositions (selenium concentration). This adds further confidence to the previously reported measurements, and also shows the general trends in the Raman signal as the selenium concentration is reduced. As selenium concentration is reduced back towards GST225 levels, then the characteristic peaks in the raw spectrum also shift towards those found in GST225. Specifically the peak at around 153 cm^{-1} moves towards a slightly greater shift as selenium decreases, this is in line with GST225 Raman data in literature, which reports a peak at around 158 cm^{-1}, which is typically attributed to Ge-Ge vibrational modes [169]. The peak at 123 cm^{-1} is already in line with GST225, but does become more prominent as the GSST composition approaches GST225 [170].

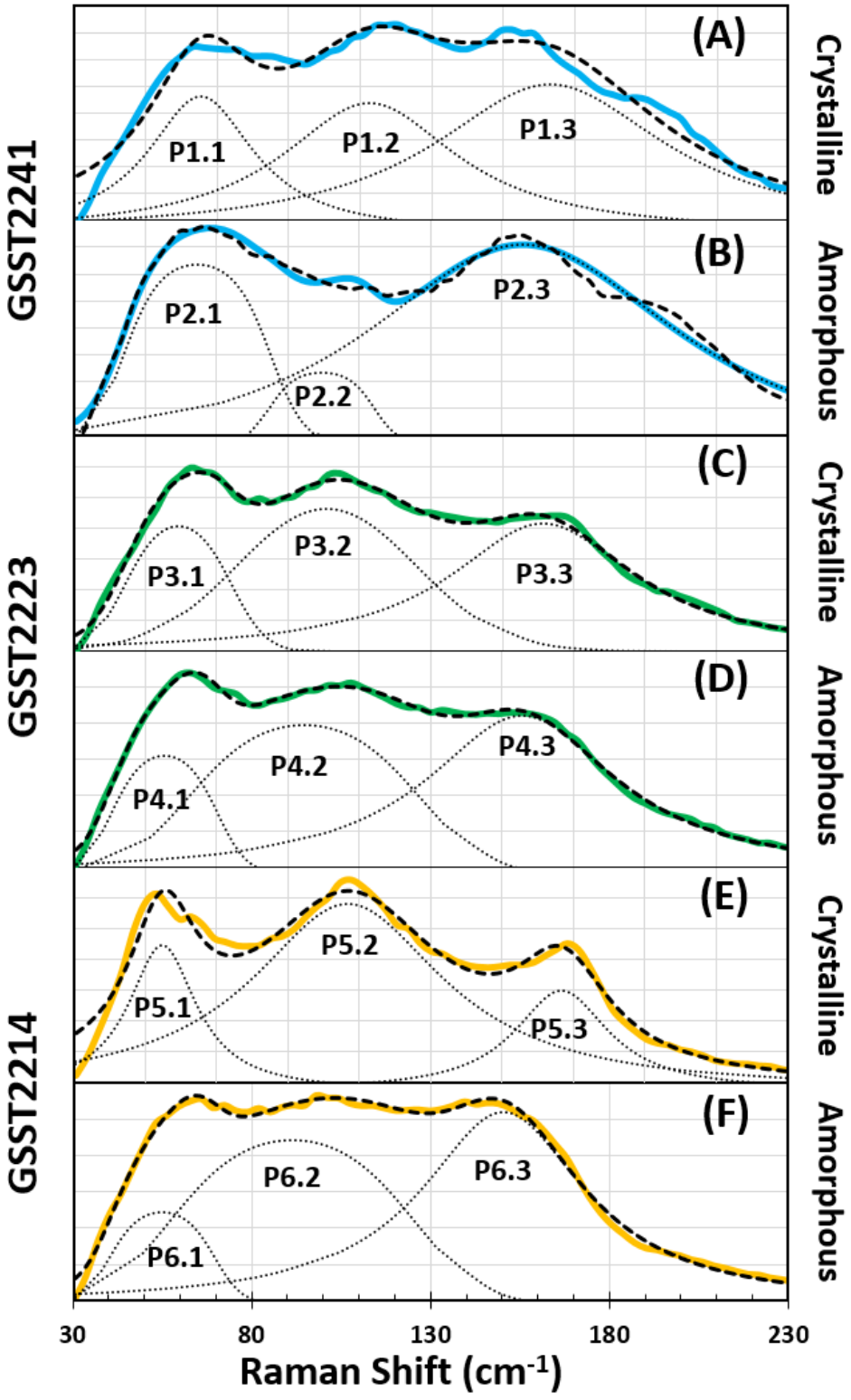

Figure 4.10. Raman spectra for three GSST compositions. Spectra for amorphous and crystalline samples of the same material are normalised to background intensity. Excitation laser wavelength was 530 nm. Each raw spectra has been fit using Lorentz or Guassian-Lorentz curves (fit curve details presented in Table 2). **Blue curves** are for **GSST2241** (most selenium), with **(A)** being crystalline, and **(B)** being amorphous. **Green curves** are for **GSST2223** (medium selenium), with **(C)** being crystalline, and **(D)** being amorphous. **Yellow curves** are for **GSST2214** (least selenium), with **(E)** being crystalline, and **(F)** being amorphous.

Table 2. List of characteristics for the curves which were fit the six Raman curves in Figure 4.10.

Peak Reference	Raman Shift (cm^{-1})	FWHM	Normalised Area
1.1	65.4	36	0.42
1.2	112.6	60	0.65
1.3	163.1	80	1
2.1	64.5	41.5	0.33
2.2	99.4	28.3	0.09
2.3	155.9	94.4	1
3.1	59.1	31.3	0.37
3.2	100.7	58.5	0.81
3.3	161.3	63.4	1
4.1	55.3	30.3	0.26
4.2	94.4	66	0.73
4.3	155.4	65.3	1
5.1	55	23.2	0.27
5.2	106.9	65.6	1
5.3	166.7	32.1	0.26
6.1	54.9	29.6	0.19
6.2	91.3	69	0.79
6.3	150.2	55.7	1

4.3 OPTICAL CHARACTERISATION EXPERIMENTS

Optical characterisation was done using the methods described in sub-section 3.5.2. The optical constants presented here were used in chapters 5 and 6 for the computational modelling. The samples for optical characterisation were magnetron sputtered onto silicon substrates, and were usually capped with 10 nm of SiO_2. Before deposition a droplet of photoresist was placed onto each substrate so that a clean step from substrate to film could be created for accurate AFM measurements to determine the precise film thickness. This thickness data was needed for both ellipsometry and reflectometry validation. Reflectometry validation involved calculating a reflectance spectrum from the measured refractive index (n & k) values, and then comparing it to a measured reflectance spectrum of the same sample. This was done for every characterised sample, with good agreement for the results presented here.

Figure 4.11 shows an example of the ellipsometry results for GST225 and GST326, with the inset showing good reflectance matching (for GST225). The optical constants for many PCM alloys, especially GST225 vary substantially in literature, and these results fall roughly in-between the two reported extremes [57,137]. The GST samples used here were annealed (crystallised) for 10 minutes on a hot plate set to 200 ^{o}C. Other devices (which are unrelated to this thesis) which were designed using the properties presented here showed good agreement between simulations and experimental measurements. Therefore the GST225 characterisation validated the characterisation methods employed in this work.

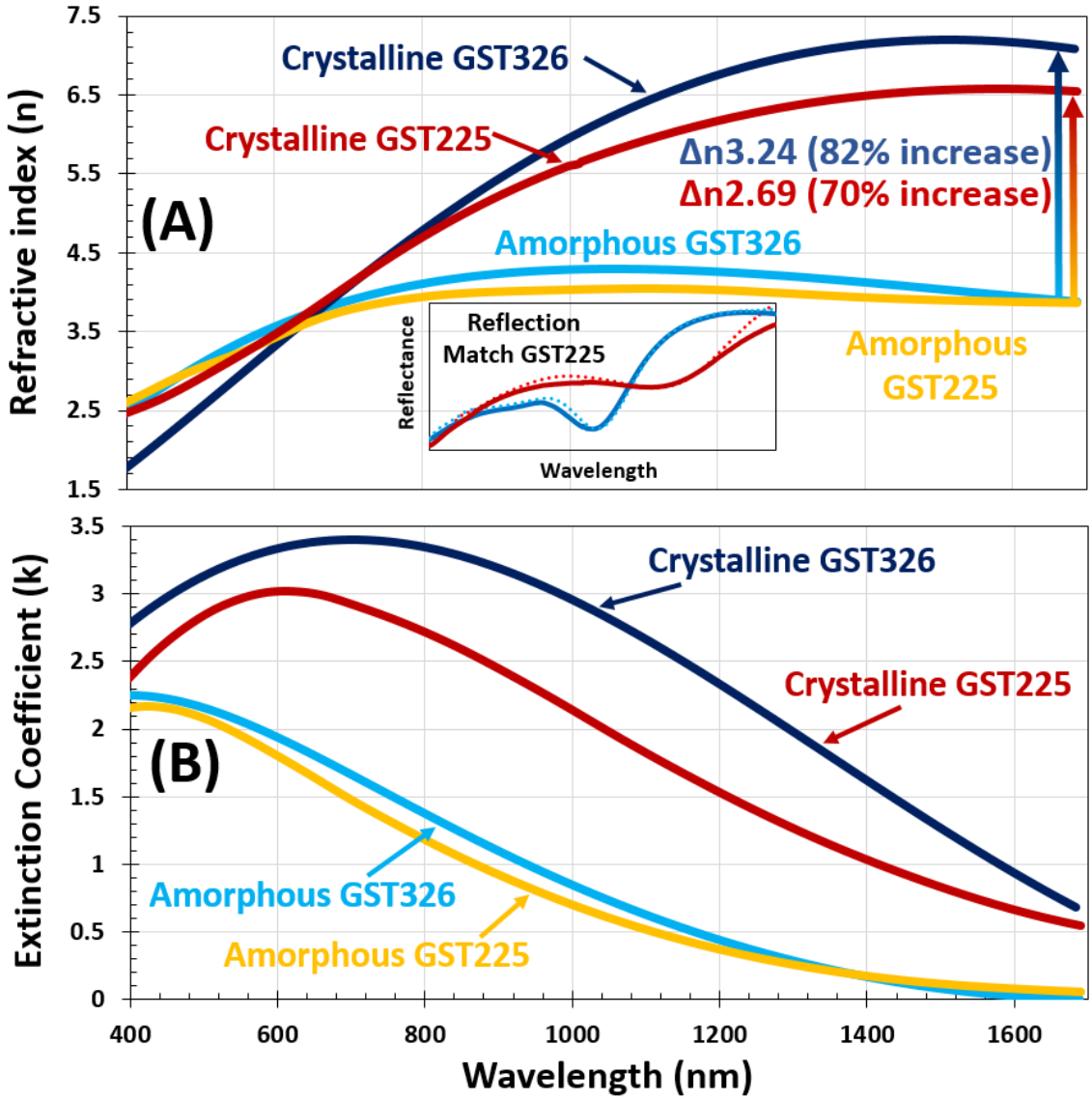

Figure 4.11. Optical constants (n & k) of GST225 and GST326, measured via ellipsometry**. (A)** shows the refractive index (n), and **(B)** shows the extinction coefficient (K) **Inset** compares measured reflectance of a GST225 sample against reflectance calculated using AFM and ellipsometry measurements. Both compositions were deposited onto silicon and capped with 10 nm of SiO_2. The thickness of the amorphous GST225 sample was 94.6 nm, which reduced to 85.1 nm after crystallisation (9.8% reduction). The thickness of the amorphous GST326 sample was 65.5 nm, reducing to 63.7 after crystallisation.

An alternative method for extracting n and k was also developed as part of this thesis, and tested on both GST225 and GeTe. This method compares measured and calculated reflection spectra of a Fabry Perot nano-cavity to determine n and k, and is described in detail in sub-section 3.5.2.3. The resulting n and k values for GeTe are shown in Figure 4.12, and also included are the same properties extracted via ellipsometry. The agreement between the two methods is generally excellent, although some discrepancy exists at the longer wavelengths. These

measurements further validate the use of ellipsometry as a reliable characterisation method; and demonstrate the usefulness of the nano-cavity approach for determining n and k in the absence of an ellipsometer.

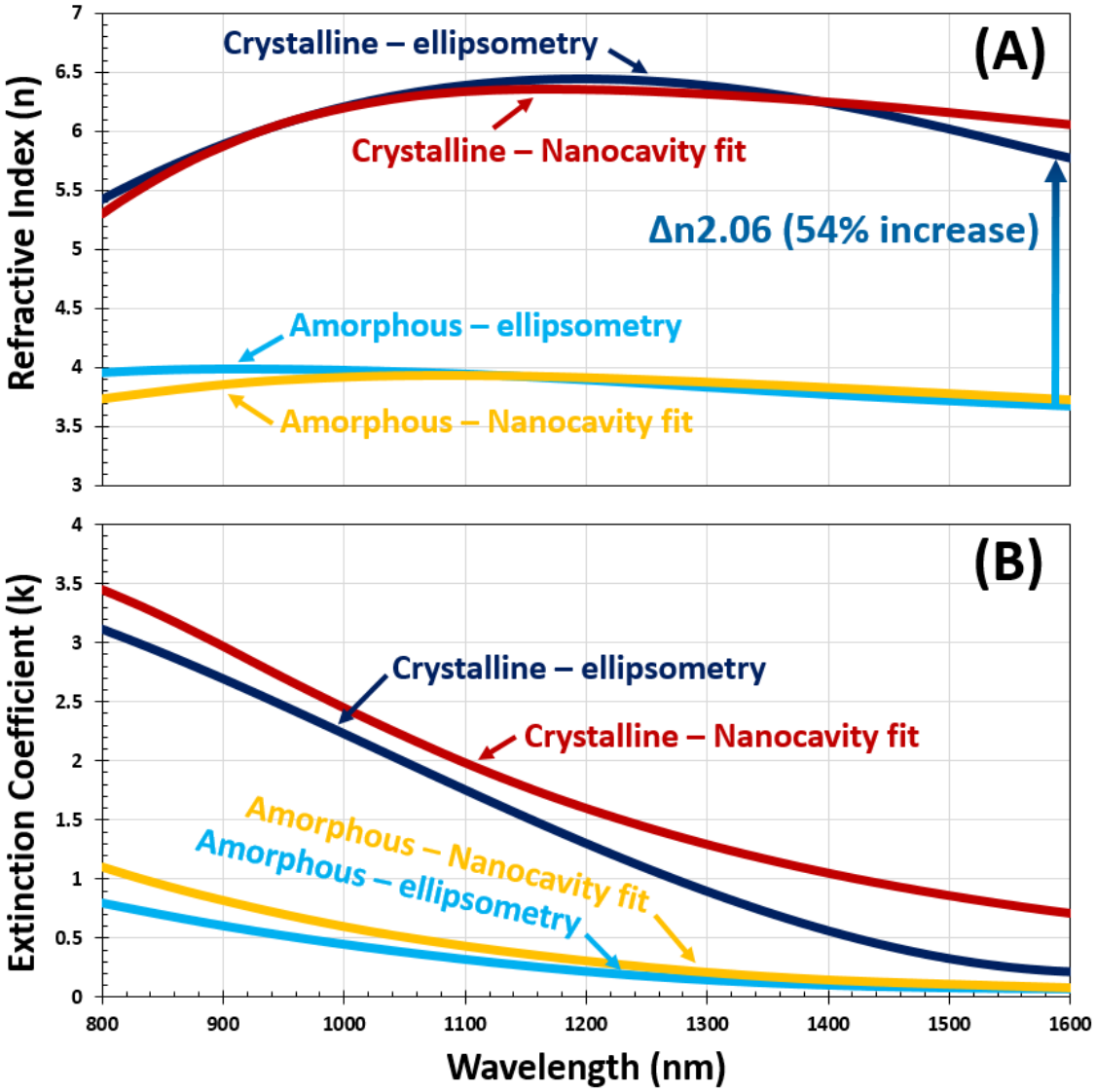

Figure 4.12. Optical constants (n and k) of GeTe, as measured by both ellipsometry and the nano cavity fitting method described in 3.5.2.3. The solid curves are ellipsometry measurements, and the dashed lines are from the nano-cavity fit. **Light blue** curves are amorphous GeTe, and **dark blue** is crystalline GeTe, both measured via ellipsometry. **Orange** curves are amorphous GeTe and **red** curves are crystalline GeTe, both measured via nano-cavity fitting. The GeTe sample measured here was 180 nm of GeTe deposited onto a 80 nm thick aluminium mirror, with a 10 nm SiO_2 cap.

The measured optical constants for AIST ($Ag_{5.5}In_{6.5}Sb_{59}Te_{29}$) and GLS65:35 are shown in Figure 4.13. These are both PCMs with excellent thermal properties in terms of switchability. They are distinct from the GST based PCM alloys because their contrast in losses (k) is exceptionally large. Crucially, the amorphous phases

are relatively transparent (especially for longer wavelengths) and their crystalline phases are opaque. This large contrast in losses is exploited in chapters 5 and 6 for ON/OFF switchable EOT filters (instead of tuneable). Of note are the optical properties of thin film GLS in both phases, as these are the first reported measurements in literature. If accurate these measurements make GLS the most transparent (when amorphous) PCM so far reported in the visible part of the spectrum.

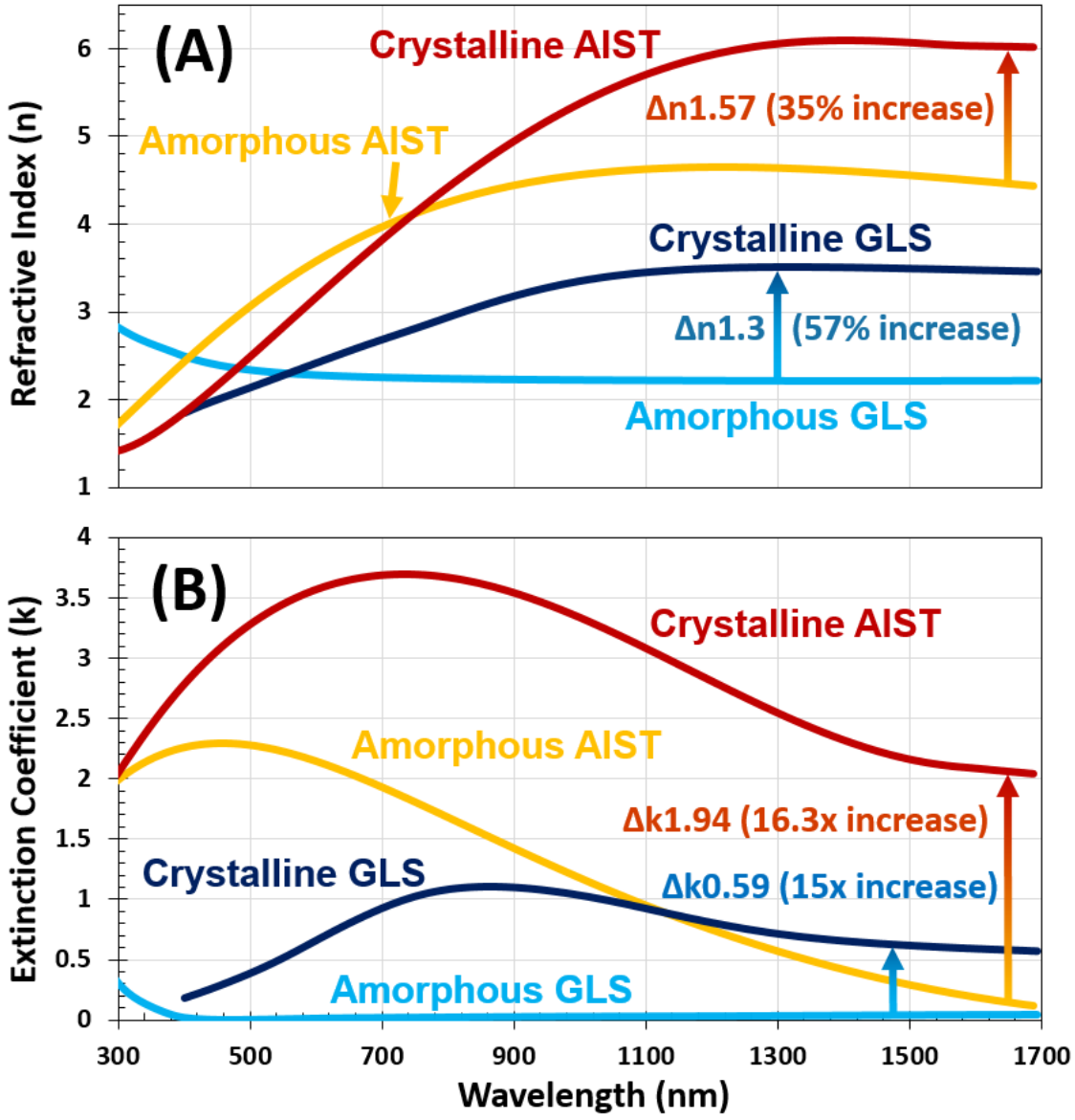

Figure 4.13. Optical constants (n & k) of GLS65:35 and AIST ($Ag_{5.5}In_{6.5}Se_{59}Te_{29}$). Also included is the proportional change in properties when switching from amorphous to crystalline. **Light blue** curves are amorphous GLS, and **dark blue** are crystalline GLS. **Orange** curves are amorphous AIST, and **red** curves are crystalline AIST. GLS samples were 100 nm thick, capped with 40 nm SiO_2, and deposited onto bare silicon. The AIST samples were 50 nm thick, capped with 10 nm SiO_2 and deposited onto silicon with 70 nm thermal oxide.

Shown next are the measured optical constants for the selenium doped GSST series, see Figure 4.14. All measured n and k spectra were validated using reflection matching, and an example of the match for GSST2241 is shown the inset of Figure 4.14. It can be seen that as the concentration of selenium increases both the real and imaginary parts of the refractive index decrease for both phases (confirming preliminary results in literature [152,153]). This trend is explicitly shown for the longest measured wavelength (1680 nm) in Figure 4.15. These low losses are especially advantageous for the filters in this work, as is discussed in sub-sections 5.4.1 and 5.4.

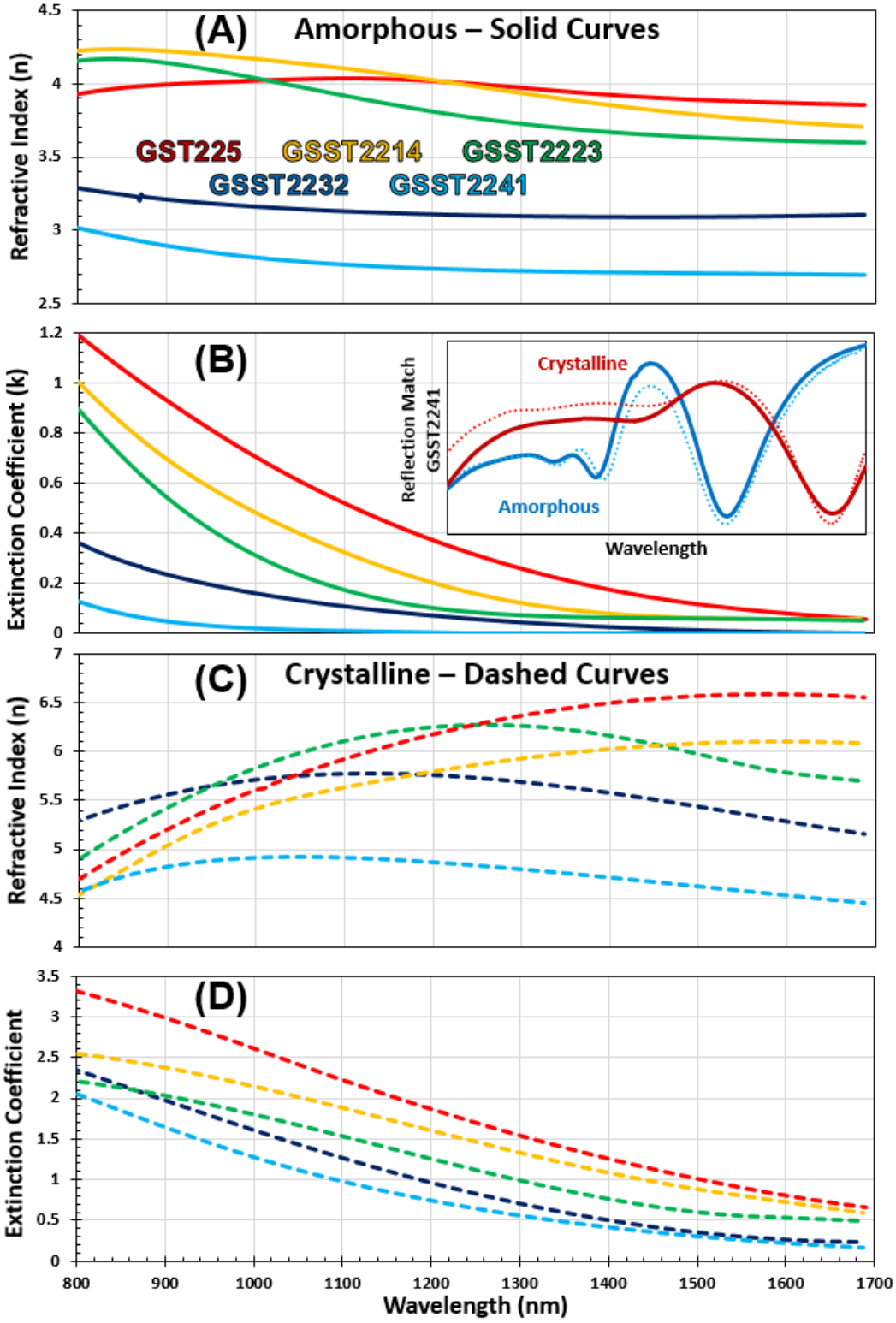

Figure 4.14. Optical constants (n & k) for GST225, and the entire GSST22xy series. compositionally, x+y=5, with x=**0**, **1**, **2**, **3**, **4**. **(A)** shows the real part of the refractive index (n) for the amorphous phases. **(B)** shows the extinction coefficient (k) for the amorphous phases. **(C)** shows the real part of the refractive index (n) for the crystalline phases. **(D)** shows the extinction coefficient (k) for the crystalline phases. **Inset in (B)** compares the measured reflectance of an amorphous GSST2241 sample against reflectance calculated using AFM and ellipsometry measurements.

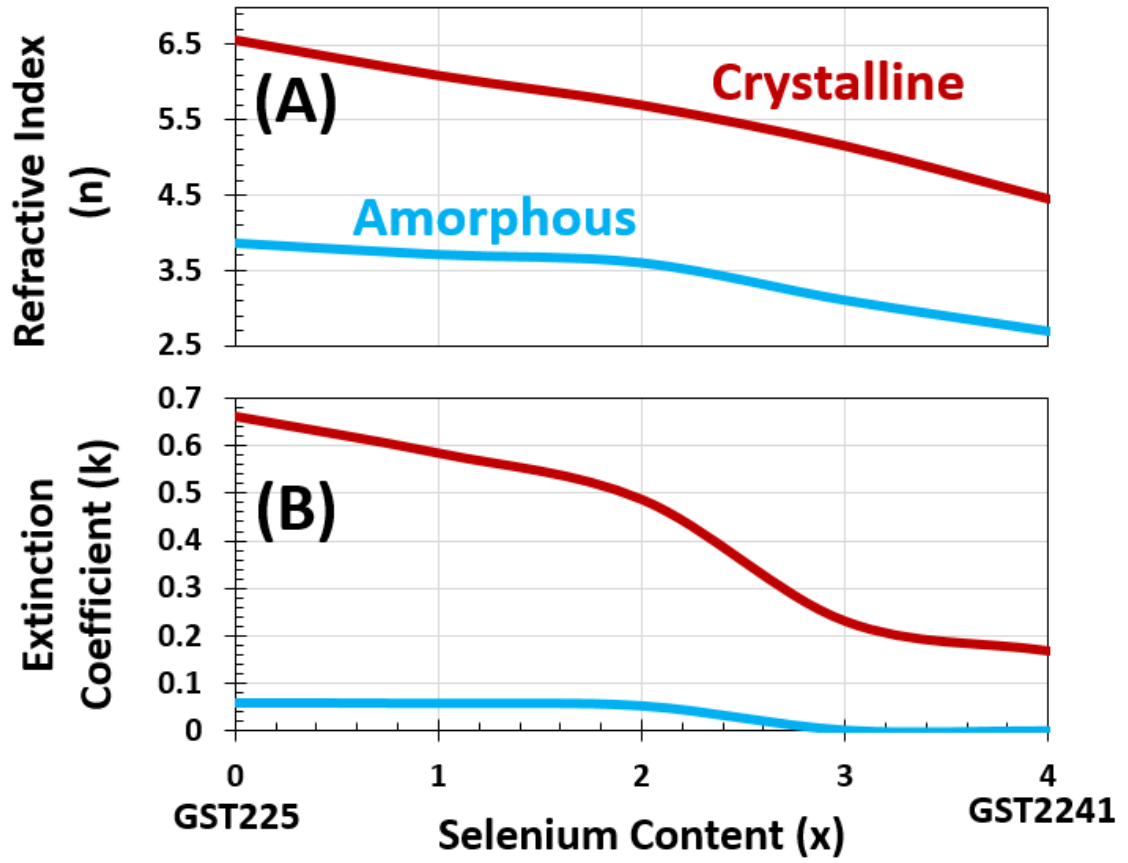

Figure 4.15. Comparison of optical properties at 1680 nm of GST225 and GSST22xy as a function of selenium content (x). **(A)** shows refractive index (n). **(B)** shows extinction coefficient (k).

The measurements shown in this chapter are for the visible and NIR, however, most of the devices in this thesis operate at longer wavelengths. In the absence of measured data at the longer wavelengths, n and k values were here extracted by extrapolation.

4.4 Crystallisation ‘Switchability’ Studies

High PCM contrast in optical properties is highly desirable for the devices in this work. However, this contrast is not useful if it cannot be practically accessed. In this work we defined ‘switchability’ as the ratio of practically accessible contrast to the maximum contrast of a PCM (i.e. as-deposited amorphous to fully crystalline contrast), as illustrated by Figure 4.16. Because accessible contrast is greatly affected by the device structure and PCM volumes employed, switchability can only be used as a figure of merit to compare different alloys, and not predict actual contrast in an arbitrary device. The methods employed for determining switchability are detailed in sub-section 3.5.3.

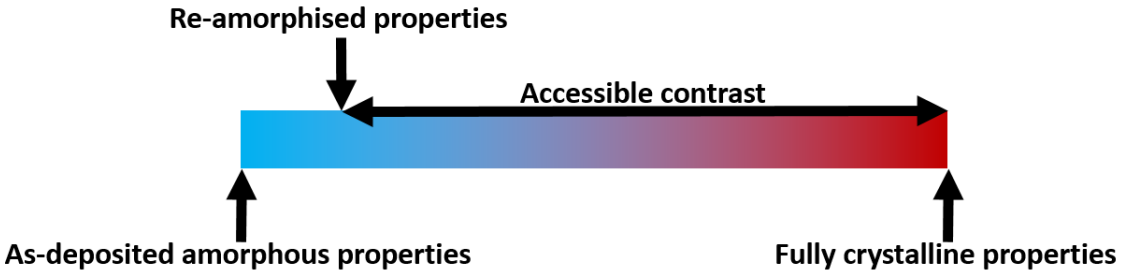

Figure 4.16. Diagram illustrating incomplete re-amorphisation. Not actual data.

The switchability of a PCM results from a combination of many material properties. These include, thermal conductivity and heat capacity, crystallisation and melting temperatures, molten viscosity, and crystallisation mechanism and speed. These properties determine the ability of a PCM to rapidly cool and thus minimise time spent at a crystallisation inducing temperature, and minimise the crystallisation that occurs per unit time.

Before switchability could be assessed it was first necessary to determine the device voltage (and therefore temperature) required to crystallise and to melt each PCM. As an example, Figure 4.17 shows the determination of the crystallisation temperature of GST2214. Figure 4.17A and B show the duration and amplitude of each electrical pulse respectively, and Figure 4.17C shows the reflectivity. The experiment is complete when additional pulses do not result in further reflectivity increases. All micro-heater devices shared the same structure, which included a 10 nm thick layer of PCM.

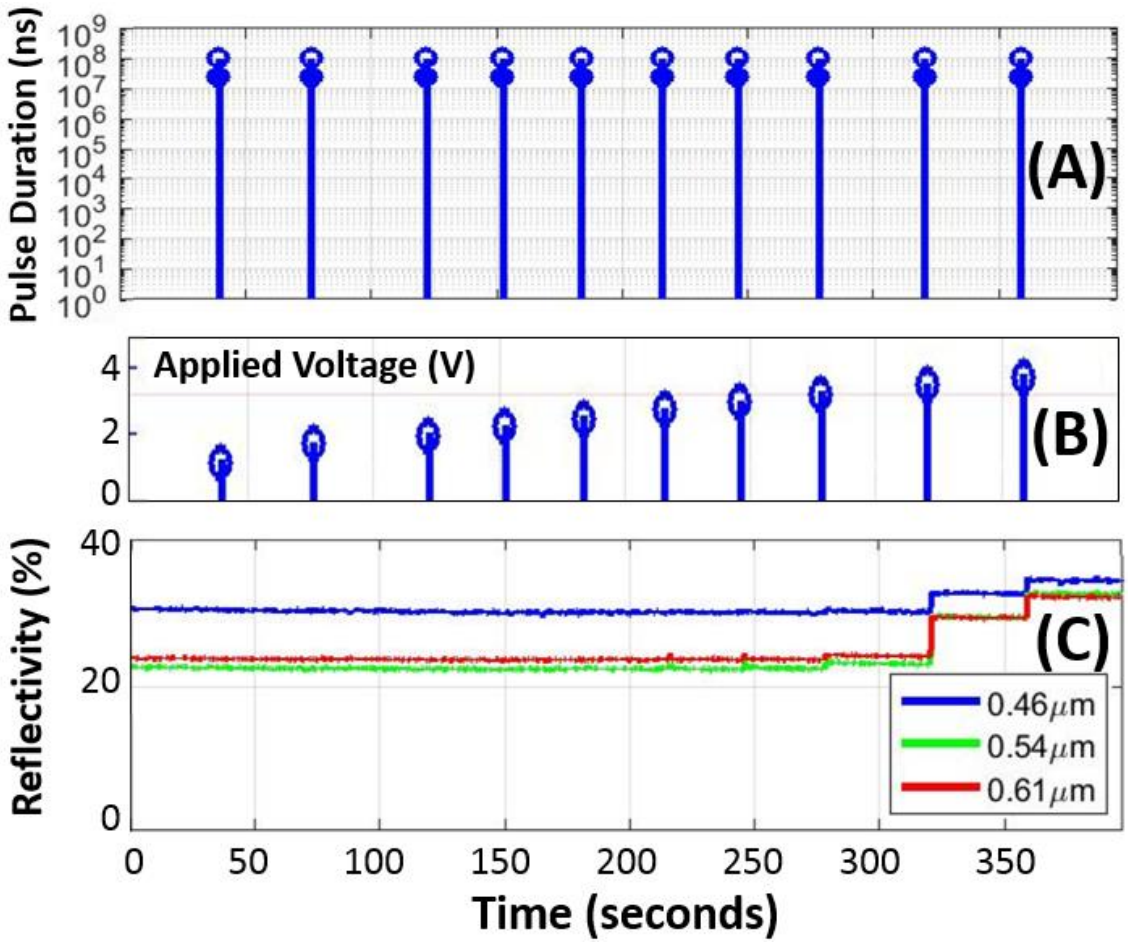

Figure 4.17. Experimental results used to determine the appropriate voltage (therefore temperature) required to crystallise GSST2214. This experiment was repeated for all studied alloys **(A)** shows the duration of each electrical pulse, in this case every pulse was 0.1 seconds. **(B)** Voltage applied for each pulse, with each successive pulse using a slightly higher voltage. **(C)** The reflectivity of the PCM layer on the micro-heater device as a function of time. Heater is 1x2 µm in size, with a resistance of 12.8 Ω, and total series system resistance of 112.8 Ω. This results in a crystallisation power of 14.5 mW, and energy of 1.45 mJ.

These experiments were repeated between two and four times (with different heater devices) depending on the quality and agreement of results. Shown in Figure 4.18 are the extracted crystallisation and melting temperatures for a selection of PCM alloys. For the crystallisation temperatures, agreement between repeat experiments was generally excellent (typically less than 1% deviation). For the melting temperature, agreement was still acceptable when multiple heater devices were measured and averaged. However, the maximum disagreement (shown with a checkered pattern in Figure 4.18) could be quite high. The crystallisation and melting temperatures extracted for GST225 agree well with literature [159]. This is the first reporting of such properties for the entire spread

of GSST alloys. Also included is AIST, as the primary motivation for its study was the suspected ease-of-amorphisation, which is further confirmed here.

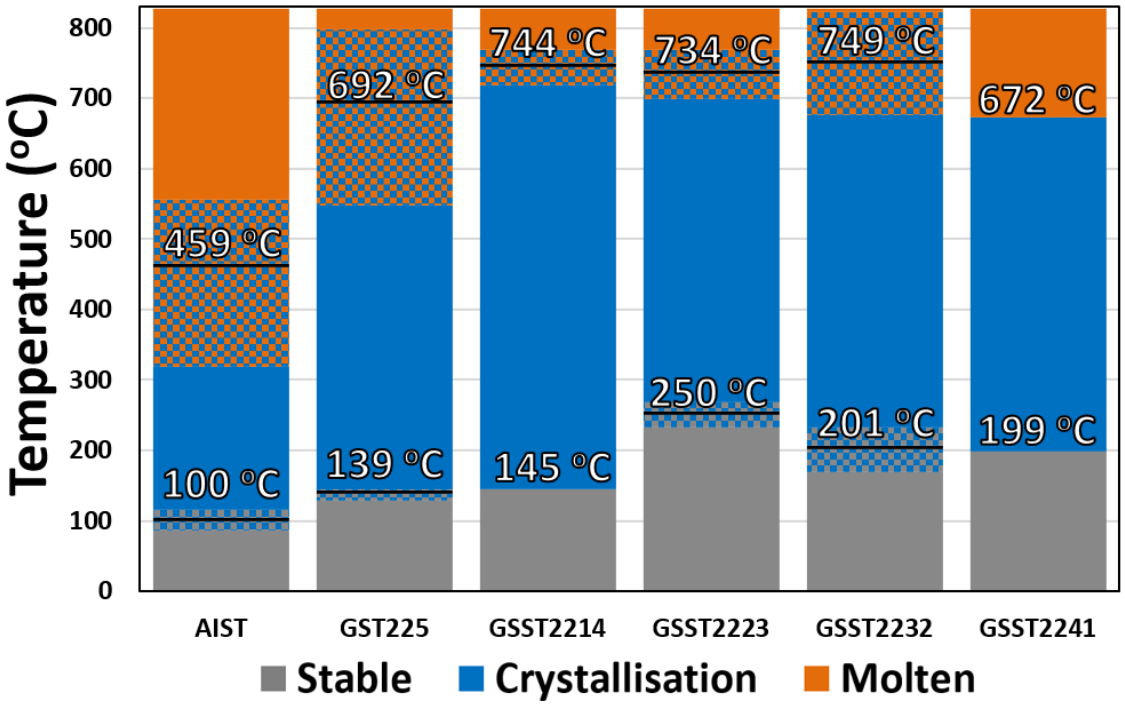

Figure 4.18. The extracted crystallisation and melting temperature for a selection of PCM alloys. The exactly temperatures (rounded to the nearest whole integer) are shown for each thermal transition point. The checkered regions show the maximum variation in thermal properties between different devices. The black lines within the checkered regions denote the average.

Table 3. Summary of temperatures required for crystallisation and re-amorphisation.

	AIST	GST225	GSST2214	GSST2223	GSST2232	GSST2241
Crystallisation (C°)	100	139	145	250	201	199
Melt	459	692	744	734	749	672

Once the required temperatures (and therefore voltage) required for switching had been determined the actual switchability assessment could begin. Figure 4.19 shows example results for GSST2214, in which slow (0.1 second) pulses of low voltage (3.8 V) were used to crystallise the sample, and fast (100 ns) higher power (5.9 V) were used to re-amorphise. The extent to which the reflectivity of the re-amorphised PCM returned to its as-deposited state was used to determine the extent to which the overall PCM properties had returned to their as-deposited amorphous state.

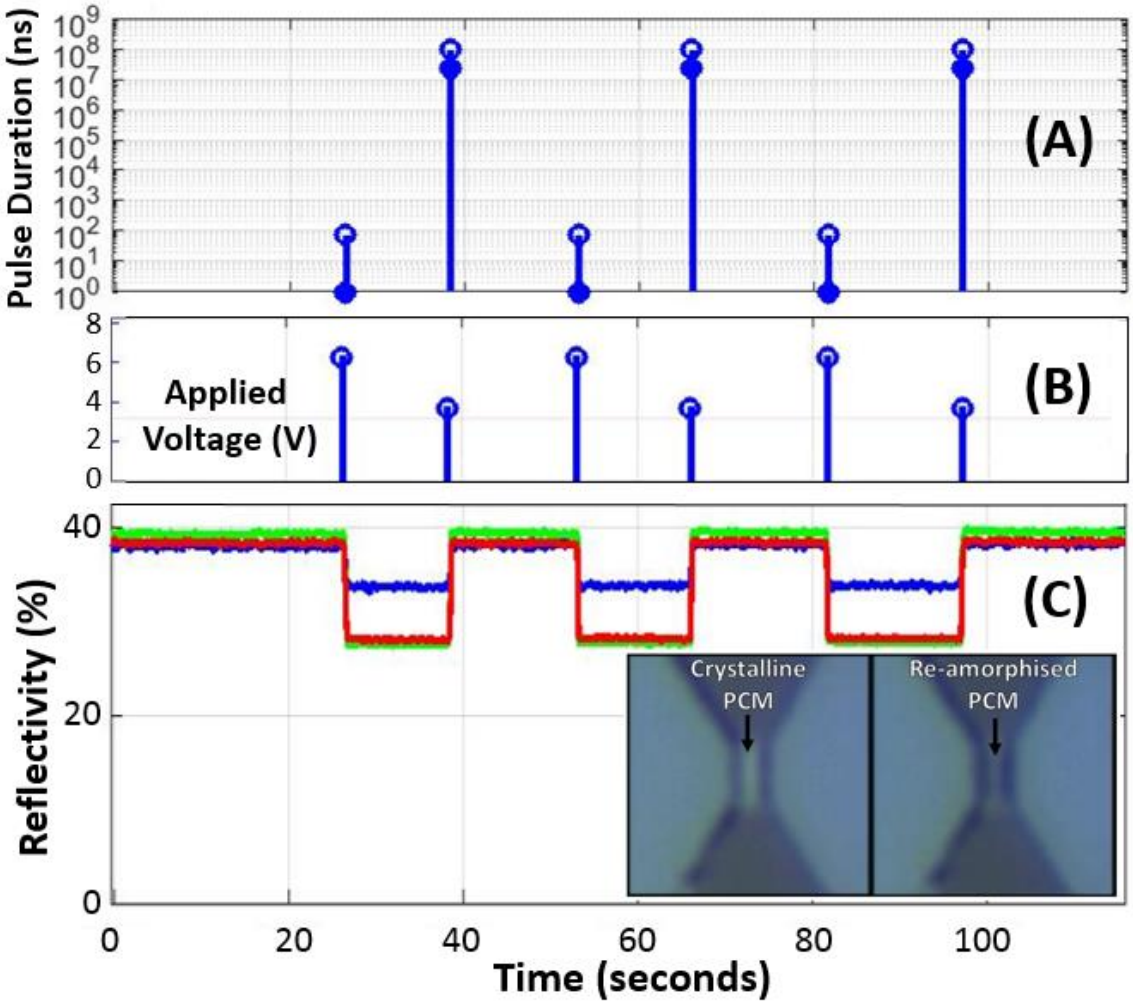

Figure 4.19. Repeated switching of GSST2214 layer in micro-heater device to determine switchability. **(A)** shows the duration of each electrical pulse. 0.1 seconds as used to crystallise, and 100 ns was used to re-amorphise. **(B)** The magnitude of each applied pulse. 3.9 V was used to crystallise, and 6 V was used to re-amorphise. **(C)** shows the reflectivity of the PCM layer as it is cycled between phases. **Inset** shows an image of the heater device when the PCM is crystalline (left) and amorphous (right). Heater is 1x2 µm in size, with a resistance of 12.8 Ω, and total series system resistance of 112.8 Ω. This results in a crystallisation power of 35 mW, and energy of 3.6 µJ.

The extracted relative switchability of the PCM alloys is shown in Figure 4.20. It should be noted that it is not practically possible to fully return a PCM to its as-deposited state. The as-deposited amorphous films generally possess a slightly different morphology when to compared to a re-amorphised film; this is compounded by any imperfections and voids during deposition which are likely to change or disappear during annealing.

GST225 is clearly a challenging material to re-amorphise, which experiences significant crystallite formation during each quenching cycle. AIST, as suspected,

(thanks to its relatively narrow temperature region of rapid crystallisation) performed well. Selenium doping was found to substantially improve the switchability of GST225, although this improvement appears to peak at a 2:3 selenium to tellurium ratio. Increased selenium concentration also had a corresponding change in crystallisation and melting temperatures, with the trend being that greater levels of selenium resulted in a narrower crystallisation temperature range. This is likely a contributor to its superior switchability, however, there are clearly other more significant mechanisms at play, otherwise GSST2241 (narrowest range) would possess the best switchability. These switchability scores are used in the following section to compare the materials using three figures of merit. Interestingly, the drop in GSST switchability once the selenium concentration exceeds that of tellurium also corresponds with a large reduction in optical losses (Figure 4.15).

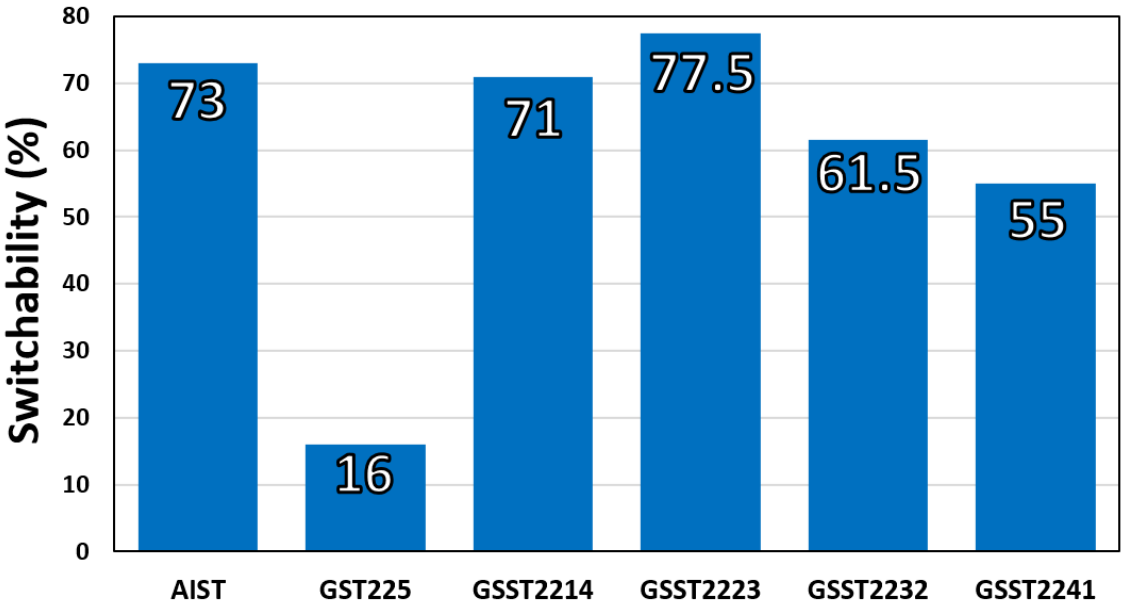

Figure 4.20. Relative switchability for a variety of phase-change alloys as extracted via micro-heater experiments.

4.5 PCM FIGURES OF MERIT

Desirable PCM properties can vary greatly, and are highly application specific; and so selecting a suitable PCM is critical when designing reconfigurable phase-change devices. This section discusses which of the PCM alloys characterised in this work are best suited to particular applications; and does this by defining a number of figure of merit for a quantitative comparison.

An often used figure of merit (FOM_1) for phase-change materials is described by equation 33 [153]. Here S is the switchability, Δn is the contrast between as-deposited amorphous and crystalline real refractive index, and k_{am} and k_{cr} are the extinction coefficients of the amorphous and crystalline phases respectively.

$$FOM_1 = S \cdot \frac{\Delta n}{(k_{am}+k_{cr})/2} \quad 33$$

For devices which exploit the contrast in a PCMs losses FOM_2 (equation 34) is a simple metric which can be used to compare PCM alloys. Low amorphous losses are typically desireable and improve the metric. High crystalline losses allow a smaller PCM volume to be employed, which is beneficial for both switchability and reduced absorbption in the PCM's amorphous phase. This metric does not divide by the amorphous losses as one might expect, as many PCMs have wavelength regions of genuine transparency, resulting in divide-by-zero errors. Instead, the metric is simply reduced by amorphous losses in a subtractive manner.

$$FOM_2 = S \cdot (\Delta k - k_{am}) \quad 34$$

For the EOT filter devices employed in this work which exploit a contrast in refractive index for spectral tuning, FOM_1 is not the most suitable figure of merit. This is because it does not place a great enough emphasis upon the absolute value and contrast in refractive index (refer to section 5.4 for why this is the case). As such, FOM_3 (equation 35) is more appropriate.

$$FOM_3 = S \cdot \frac{n_{cr}^2 - n_{am}^2}{(k_{am}+k_{cr})/2} \quad 35$$

Figure 4.21 shows each material's figure of merit at the wavelength of 1680 nm; this wavelength was chosen because it is the maximum operating wavelength of our ellipsometer, which was used to extrapolate n and k values at longer wavelengths when necessary. For each PCM alloy the figure of merit was calculated without taking switchability (S) into account, and then calculated again if switchability had been evaluated for that particular alloy. In the case of GLS it is valid to assume its switchability is near 100%, as discussed previously in sub-section 4.1.3. GLS appears to score relatively poorly by all metrics, however, it is worth recalling that GLS out performs all other alloys at visible wavelengths.

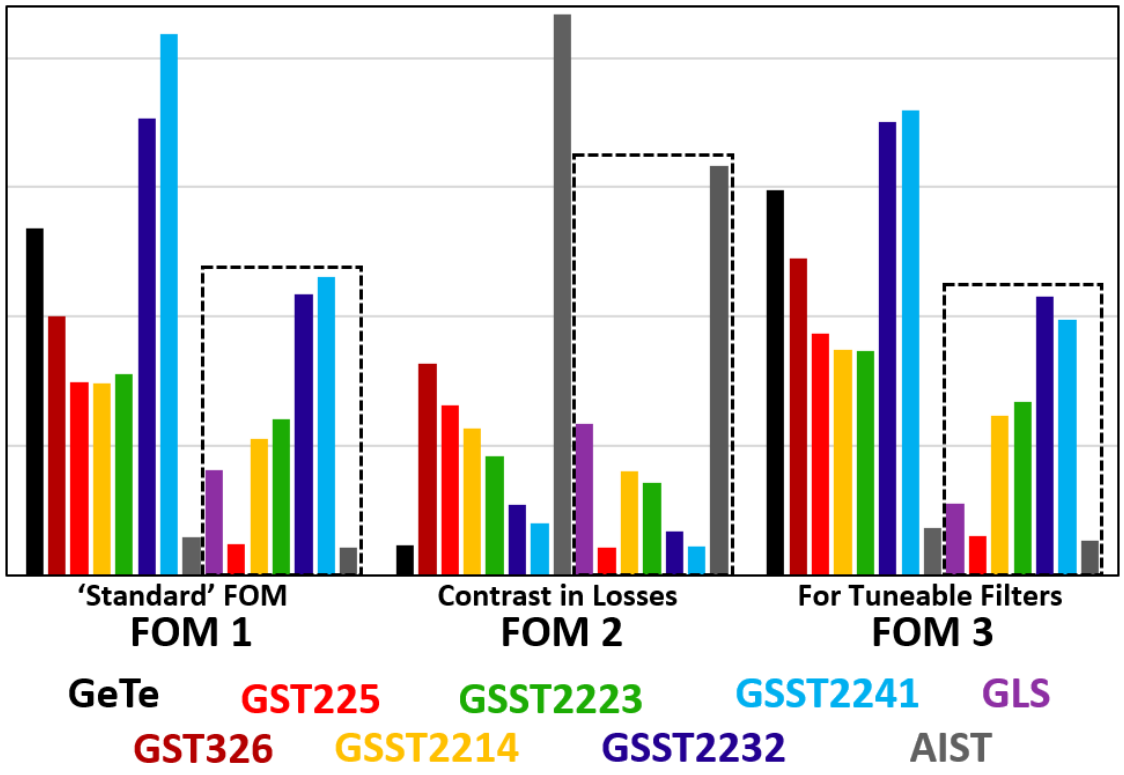

Figure 4.21. Comparison of optical properties at 1680 nm (using the three previously discussed figures of merit, described by equations 33, 34, and 35) of each studied PCM alloy. Each figure of merit has been scaled so as to make a better comparison between them. Results within the black dashed boxes have been scaled based upon their switchability, while all other results have omitted this variable. GLS is only shown once for each FOM, because it's switchability is effectively 100%, and therefore the FOM score would not change.

5 TUNEABLE FILTER DEVICE DESIGN AND SIMULATIONS

This chapter’s purpose is to act as a design guide for phase-change extraordinary optical transmission (EOT) filters, and details the computational modelling work undertaken to explore and design this type of tuneable filter. These filters work by combining phase-change materials (PCM) with an array of sub-wavelength apertures which support extraordinary optical transmission EOT. The EOT effect is detailed in sub-section 2.1.2. Phase-change materials in general are described in section 2.2, and several specific alloys are rigorously characterised in chapter 4. The modelling methods employed here are described in chapter 3.

The EOT effect works over a broad range of wavelengths, and the devices designed in this chapter reflect this broad range; with some devices operating in the visible, and other larger devices approaching the long wave infrared. Initially, fixed filters exploiting the EOT effect in general (no PCM) are investigated. This includes studies on ideal materials (substrate & metal), and how geometrical parameter affect performance (size, shape, spacing and depth of the apertures).

The chapter then moves onto studies which explore the inclusion of a PCM layer to add dynamic tunability to the filters. The ideal approach for including a PCM layer is investigated, and the various design trade-offs are explored, and suitable material properties are discussed. The viability of electrical (Joule heater) switching is then explored and confirmed with electro thermal modelling. Analysis of energy consumption and device scalability is also presented.

Unless explicitly stated otherwise, all results presented here are original computational results produced with COMSOL and/or MATLAB using the methods described in section 3.1.

5.1 General EOT Device Characteristics

The filters in this work exploit the EOT effect (as discussed in sub-section 2.1.2) specifically surface enhanced extraordinary optical transmission. This leads to devices which appear like a continuous metallic film to a wide range of wavelengths, but are nearly transparent for a narrow band. Unless otherwise stated, the EOT filters in this chapter have circular apertures which are arrayed in a square pattern with a diameter which is half that of their periodicity, like that shown in Figure 5.1.

Figure 5.1. Computer rendered image (Blender, Cycles renderer) of EOT structure with the ‘standard’ configuration in which apertures arranged with a square array, with their diameter being 50% of their spacing (period). Image is to scale.

The typical transmission response of an EOT filter structure floating in air is shown in Figure 5.2. Also included for interest is the reflectance spectrum. For wavelengths above the resonant wavelength (2.2 μm in this case) transmission is low and reflection is high, much like that of a continuous metal film. Below the resonant wavelength transmission is low, but less uniformly so. This is due to the numerous EM modes which are excited, most of which contribute towards increased absorption and cause a reduction in reflectance. The exception to this are the two surface plasmon modes relating to the aperture to nearest-aperture spacing, and the aperture to next-nearest-aperture spacing. These surface plasmons result in near-zero transmission, and instead re-radiate light back towards the source, causing a reflection maximum.

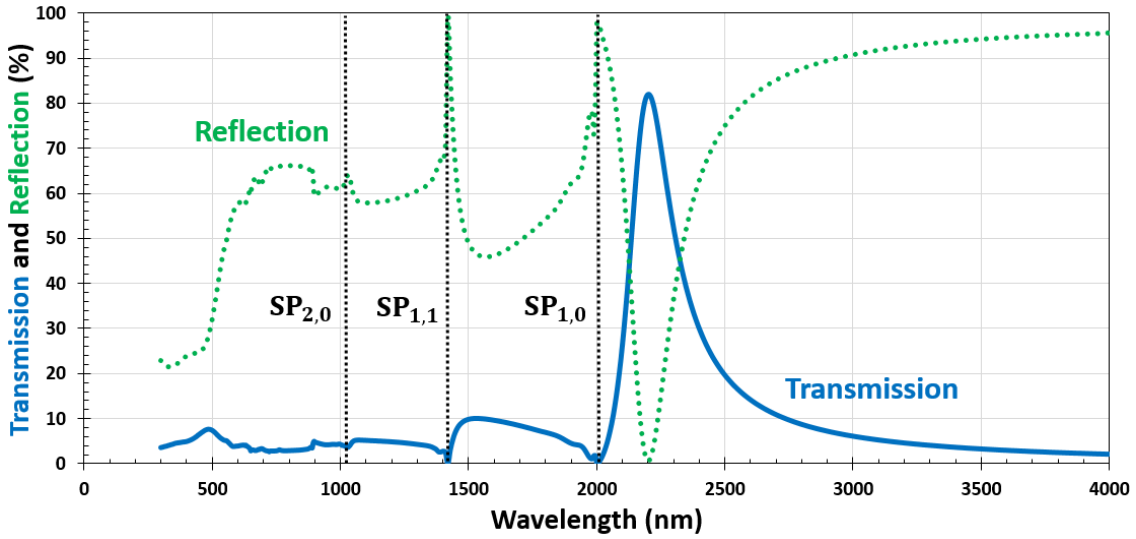

Figure 5.2. Simulated transmission (solid blue curve) and reflection (dotted green curve) for a 100 nm gold EOT structure with a periodicity of 2 μm and an aperture diameter of 1μm (50% ratio). Also shown by dotted black lines are the wavelengths of the surface plasmon modes. These refer to the aperture-to-aperture nearest neighbour ($SP_{1,0}$), next-nearest ($SP_{1,1}$), and next-next-nearest ($SP_{2,0}$) as shown in Figure 2.5.

Figure 5.3 shows the normalised (amplitude of all components) electric field distribution for an EOT structure for both on-resonance and off-resonance conditions. When the EOT structure is resonating the plasmons present at the sharp corners of the metal layer (within the apertures) are clearly visible.

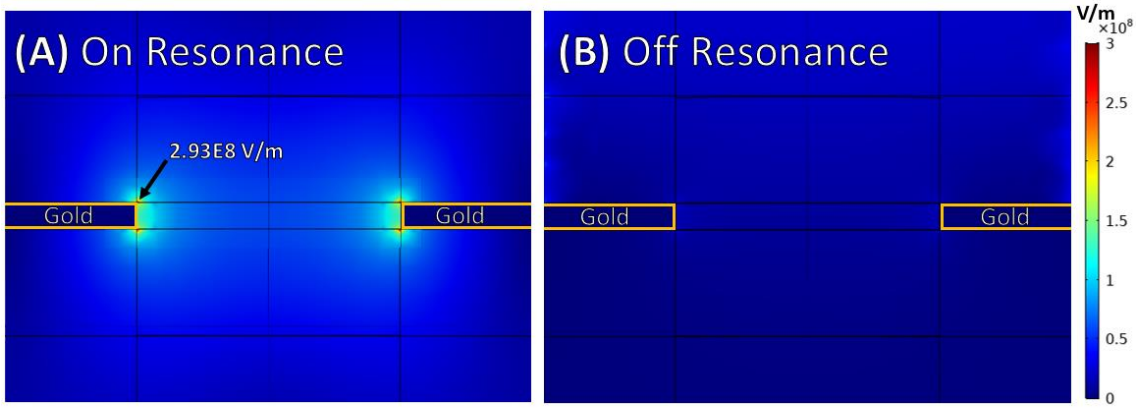

Figure 5.3. Simulated electric field (normalised) distribution for an EOT structure for both on resonance and off resonance conditions. EOT structure is 100 nm of gold on a CaF_2 substrate with a periodicity of 2 μm and an aperture diameter of 1μm. **(A)** At the resonance wavelength of 2.9 μm, with a maximum field strength of 2.93E8 V/m. **(B)** Off resonance with a wavelength of 4 μm.

The filter devices investigated in this work are very sensitive to the angle of incidence. Deviations from normal incidence significantly red-shift the transparent region, while also improving the Q-factor. This is illustrated in Figure 5.4, which

presents simulation results that show a nearly one-to-one ratio of incident angle (in degrees) to the resulting percentage of redshift. Also plotted is the quality factor, which swiftly improves for relatively small incident angles. However, at larger angles the EOT effect breaks down, and the quality factor suffers as a result.

In principle it would be possible to produce filters with an exceptionally large range of spectral tunability by combining both phase-change materials and filter rotation. However, this was not studied here as it is not applicable to the filter applications pursued in this work.

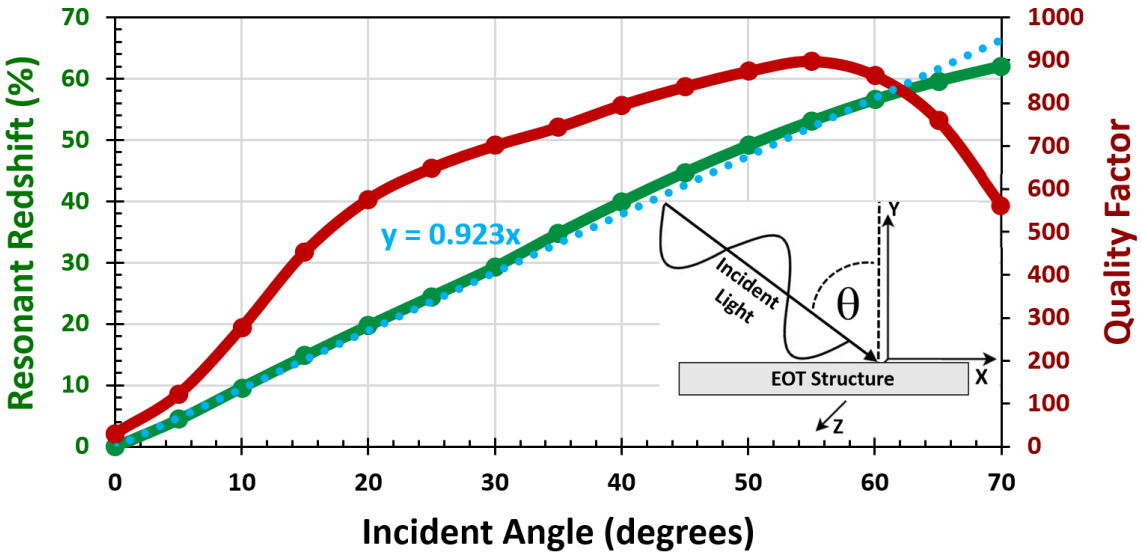

Figure 5.4. Effects of incident angle of light upon the filter performance. Diverging from normal incidence rapidly improves the Q factor, and redshifts the resonance peak with a nearly 1 to 1 relation between incident angle in degrees, and the percentage redshift from the normal incidence wavelength. Results from a filter designed for long wave infrared, but broadly applicable to any wavelength region. Q-factor calculated using $\lambda_{\mathrm{Res}}/\mathrm{FWHM}$, where λ_{Res} is the wavelength of maximum transparency. **Inset** defines the angle of incidence, showing that the angle is modified only relative to the vertical Y axis, and remains in plane with the X axis, and perpendicular to the Z. This is the same axis and orientation as shown in the 3D diagrams in Figure 3.2.

5.1.1 Materials Selection

5.1.1.1 Substrate Selection

The substrate plays a large role in the response of EOT filters. A high level of transparency and adhesion to the metal layer are always desirable, but the ideal refractive index is less obvious. As discussed in sub-section 2.1.2, the substrate’s index of refraction directly correlates with the resonance wavelength. However, the ideal substrate refractive index also depends upon the material above the EOT filter (superstrate). To maximise transmission, the permittivities above and below the EOT structure should match. For a bare metal filter (air superstrate) a low refractive index substrate is ideal. However, a high index dielectric within the apertures can boost transmission; this therefore requires the substrate’s refractive index to match that of the combination of the dielectric layer and the air. Another finding of this work is that a low refractive index substrate can increase the spectral shift caused by changes in the superstrate index (the addition of a (PCM) superstrate is discussed later in sub-section 5.2.1.1). As shown in the simulation results of Figure 5.5, for a filter with an air superstrate, a low index substrate performs best, with a linearly proportional drop in transmission intensity as the substrate’s index increases. As shown by Figure 5.5B, the resonance red-shifting broadly follows the position of the 1st order surface plasmon polaritons (SPP) mode. The drop in transmission intensity is also linearly proportional to the percentage mismatch of substrate and superstrate indices of refraction.

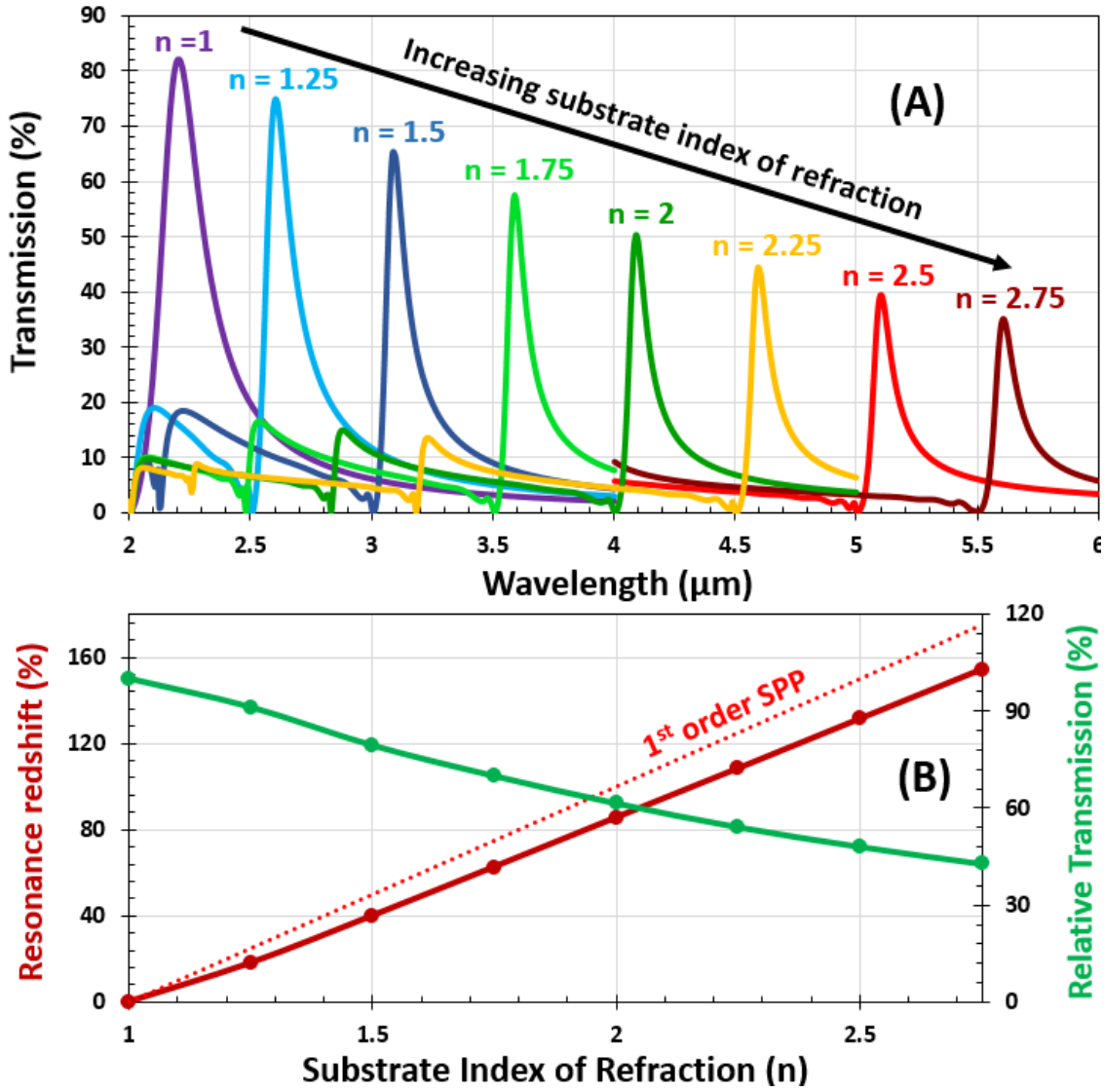

Figure 5.5. (A) Simulated transmission for an EOT structure on variety of substrates with varied index of refraction (zero losses in each case). **(B)** Percentage of spectral red-shifting as a result of changes to the substrates index of refraction. Also shown is the 1st SPP mode of the structure. EOT structure is 100 nm of gold with an aperture periodicity of 2 µm, and an aperture diameter of 1 µm (50% ratio).

For experimental purposes in which in-situ electrical switching of a PCM layer would not be attempted CaF_2 was selected as the substrate material. This is primarily because of its wide (0.2 to 9.5 µm) window of very high transparency (>95%), allowing the same substrates and therefore similar fabrication recipes to be used for devices designed for different wavelength regions. The low refractive index of refraction would maximise performance (especially in filters without a PCM), and the high chemical and thermal stability prevents diffusion into the gold and any PCM.

5.1.1.2 Metal Selection

A large variety of metals will support plasmons and the EOT effect, with their suitability being somewhat wavelength dependant. There are four considerations when selecting a metal for an EOT structure, these are summarised below.

1. As discussed in sub-section 2.1.2, excited surface plasmon polaritons are the primary mechanism behind EOT. These plasmons manifest as collective oscillations of free electrons, and collisions due to these oscillations causes energy to be converted as heat (ohmic losses). Without these losses, resonant transmission would be close to 100%, and therefore it is important to select metals which exhibit low losses due to surface plasmons oscillations. Figure 5.6 compares the at-resonance absorption (primarily due to plasmon oscillations) for variety of metals comprising EOT structures designed to operate at three different wavelengths.
2. During the re-amorphisation process the PCM layer must be molten, and using the metal layer as a heater requires that it doesn’t itself melt. While experiments have shown that a relatively thin barrier layer mitigates physical deformation, molten metals are substantially more resistive, greatly increasing voltage drive requirements. The melting point of the studied metals is shown in Figure 5.6 inset A.
3. Electrical resistance determines how much current will flow for a given voltage drop across an EOT device. The inset of Figure 5.6 inset B compares the DC resistance of the studied metals. Unsurprisingly there is also a strong correlation between low losses due to electron oscillations and low electrical resistance.
4. The extent to which a metal diffuses into PCM alloys is an important consideration. Such mixing substantially degrades the properties of the PCM, and effectively removes the dielectric-metal interface needed to support surface plasmons. This therefore requires barrier layers to mitigate. Other materials like silicon also readily mix with the metallic layer, further reducing design options for some metals.

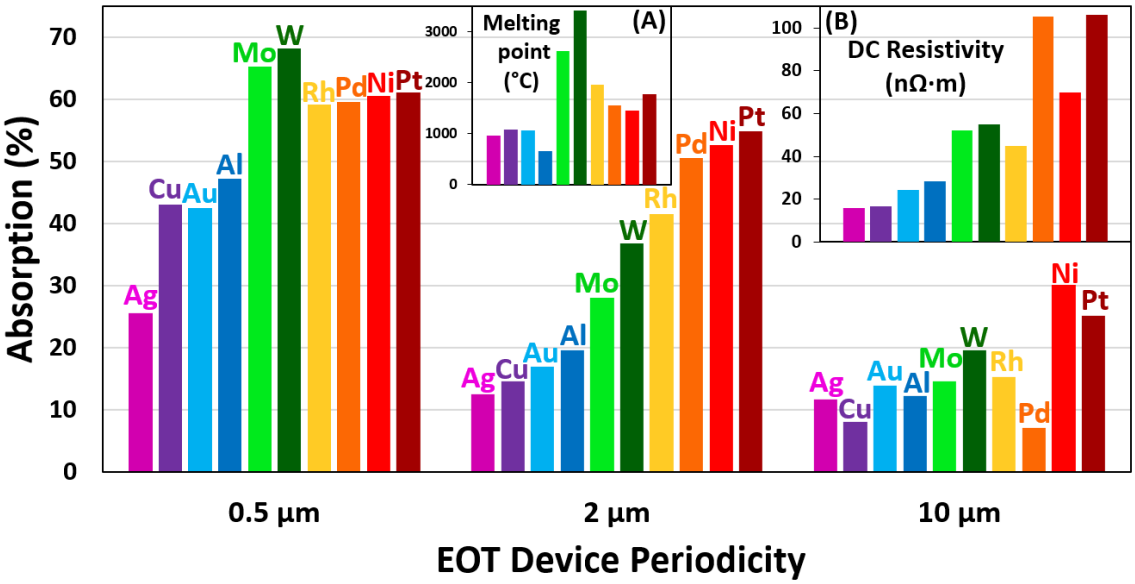

Figure 5.6. Optical absorption at resonance for three different EOT structures, each made from ten different metals. Resonant wavelengths occur at a slightly longer wavelength than the devices periodicity, and vary slightly depending on the metal. All EOT structures have an aperture diameter 50% of their periodicity. EOT structure with 0.5 µm period is 80 nm thick, 2 µm period is 100 nm thick, and 10 µm period is 200 nm thick. The metal optical properties were calculated using the Lorentz-Drude model. **Inset A** charts the melting point of each studied metal. **Inset B** charts the electrical DC resistivity of each studied metal.

For longer wavelengths (10 µm) all of the studied metals start to behave more like perfect conductors, and as such absorption is relatively low. Most metals make suitable EOT candidates at these wavelengths. For the shorter wavelength infrared region (2 µm) only a few metals remain relatively low-loss, these are silver, copper, gold, and aluminium; these metals also possess the lowest electrical resistance and are the obvious choices for devices. However, both silver and copper are particularly contaminating concerning deposition equipment due to their high reactivity with other materials. This leaves gold and aluminium as good candidates. However, pure aluminium can be challenging to sputter or evaporate without any oxide formation, and its low melting point makes it far less suitable as a heater compared to gold. As such, gold was used here for the majority of infrared device fabrication and simulations. In the visible, all of the metals except for silver become very lossy. Due to the issues with silver described above, aluminium or gold were nevertheless used for EOT devices operating in the visible.

5.1.2 Tailoring Transmission with Geometry

5.1.2.1 Hexagonal vs Square packing

It was suspected that hexagonal packing would offer superior performance to square packing, as it would be possible to fit more apertures into a given area. Hexagonal patterning would also increase the number of nearest neighbour apertures, enhancing the 1st order surface plasmon, whilst increasing the separation to next-nearest neighbours. However, as shown in Figure 5.7 simulations show that there is not a significant difference either way, with the square packing exhibiting a slightly superior quality factor. The majority of EOT studies in literature use square packing without justification. However, EOT structures fabricated using nano-sphere lithography (not used in this thesis) are restricted to hexagonal packing [53]. This does not appear to be a critical design decision, and as shown here the effects upon performance are minimal.

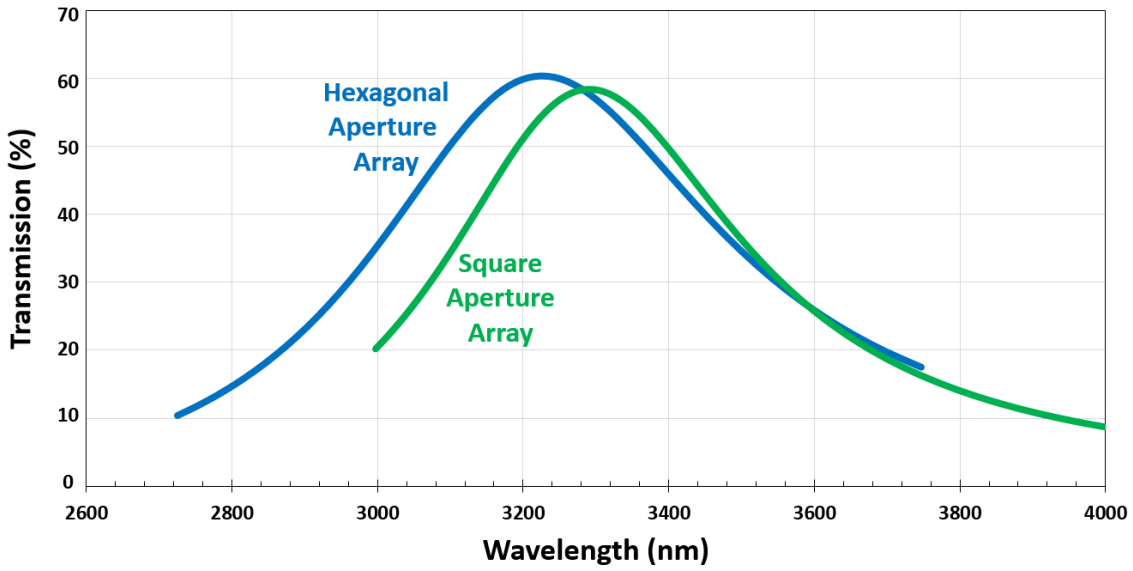

Figure 5.7. Simulated transmission of EOT structures with different aperture array structures. Blue curve is for hexagonally patterned apertures, and the green curve is for the ‘standard’ square array structure. EOT device made in 100 nm of gold, with an aperture periodicity of 1.6 μm, a diameter of 800 nm and 70 nm of GST225.

5.1.2.2 Controlling Resonant Wavelength

As discussed in sub-section 2.1.2, the peak transmission wavelength of an EOT structure is primarily determined by the periodicity (aperture spacing), and the permittivity of surrounding materials. Other geometrical parameters such as diameter to period ratio have an almost negligible impact on resonant wavelength. Figure 5.8 illustrates this by plotting simulation results of the resonant wavelength against periodicity; in this case the substrate is CaF_2, and the aperture diameter is always 50% of the period. If the period and surrounding material properties were the only determinant of resonant position, then one would expect the ratio of resonant wavelength to periodicity to closely follow the refractive index (as a function of wavelength) of the substrate. This ratio is also plotted in Figure 5.8, and does indeed closely resemble the refractive index of the CaF_2 substrate.

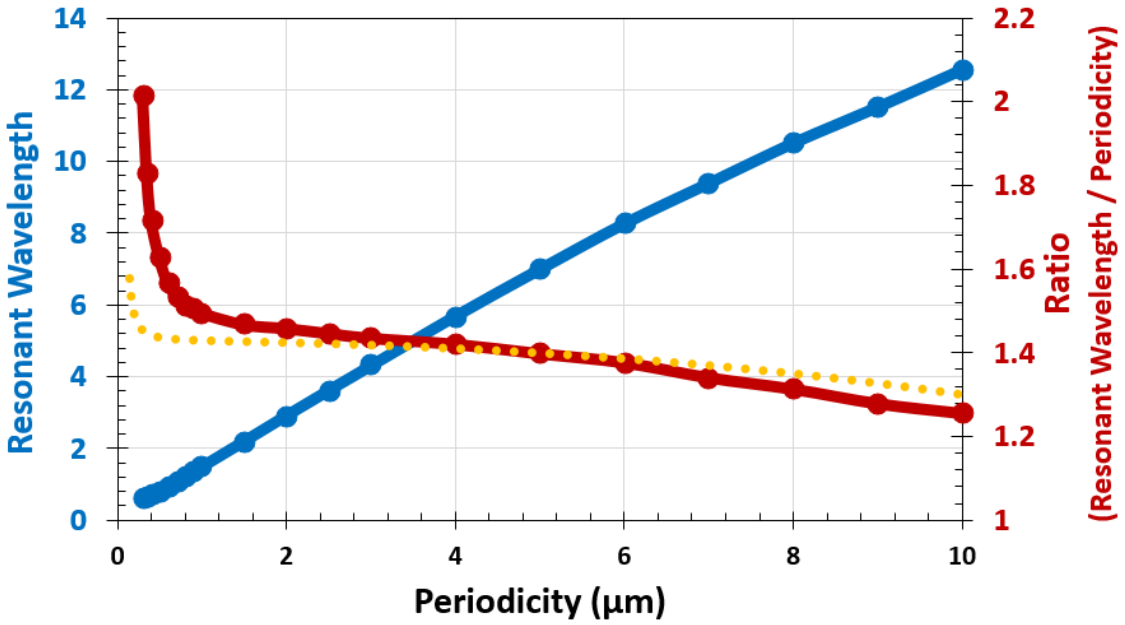

Figure 5.8. **Blue curve** is simulated **r**esonant wavelength of standard EOT structure as a function of periodicity. **Red curve** is the ratio between the resonant wavelength and the periodicity. The dotted **yellow curve** shows the refractive index of the substrate (CaF_2 in this case), which closely resembles the ratio in red, especially when the resonant wavelength and periodicity are similar.

5.1.2.3 EOT Aperture Size

The size of the apertures (as a function of periodicity) controls the pass-band transmission and width, which both increase together with the aperture size. As shown in the results Figure 5.9, the quality factor is very high for small apertures, but the percentage transmission is uselessly low; conversely, once the aperture size exceeds ≈60% of the period the increase in transmission suffers from diminishing returns, and the pass-band becomes very broad. There is a relatively narrow range of aperture sizes which have both acceptable quality factors and usefully high transmission, this range is roughly 40 to 60% of the period. If the aperture is filled with a high permittivity dielectric then the aperture diameter has a marginal impact on resonant wavelength. It is also worth considering that larger apertures have a more favourable aspect ratio which aids with fabrication.

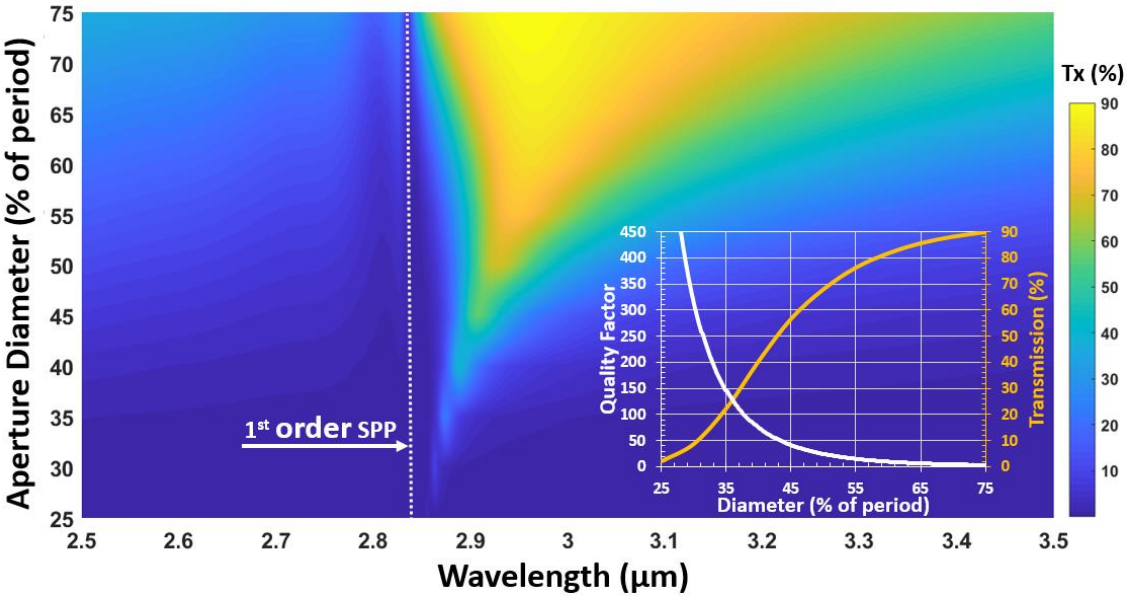

Figure 5.9. Colour plot showing the effects of the aperture diameter as a percentage of the EOT periodicity. **Inset** shows the quality factor (in white) and transmission intensity (in orange) as a function of aperture size. EOT structure made from 100 nm of gold, on a CaF_2 substrate with a periodicity of 2 µm.

5.1.2.4 EOT Metal Thickness

The thickness of the metal layer alters the nature of the EOT effect, as discussed in sub-section 2.1.2.1; relatively thin layers can support coupling between substrate and superstrate plasmons, while genuinely opaque films suppress this coupling. However, thicker layers increase Q-factor and reduce stop-band transmission, which may be critical depending on the application (such as displays). Longer wavelengths require thicker layers due to the increased penetration (skin) depth, and as such it can be useful consider the metal thickness as a percentage of target resonance wavelength.

Increasing thickness reduces pass-band transparency, whilst also increasing the sharpness of the transmission peak. As shown in the results of Figure 5.10, very thin metal layers have an extremely broad and red-shifted response; as the thickness increases the spectral position stabilises, and the main performance change is in peak intensity and sharpness. From the Figure 5.10 it’s clear that there is an ideal thickness region which produces a good compromise of transmission amplitude and resonance sharpness. Another observation is that once a certain thickness threshold has been exceeded, the change in both stop-band transmission and secondary peak shape and size is relatively unchanged. These observations are valid for a broad range of EOT devices, and not just the structure used in Figure 5.10. To apply this study more generally, the EOT thickness can be quantified as a proportion of the resonant wavelength (λ_{res}), in this case the thickness would vary from ≈0.3% to ≈10%.

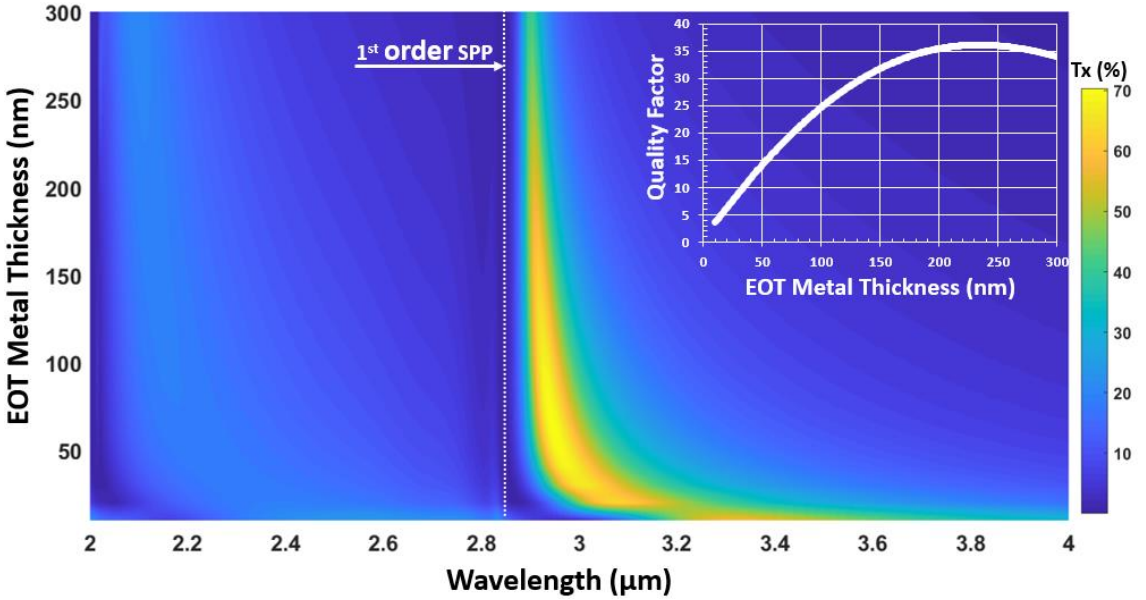

Figure 5.10. Colour plot showing the effects of varying metal layer thickness on EOT transmission. **Inset** shows the quality factor as a function of EOT metal thickness. EOT structure made from gold, on a CaF_2 substrate, with a periodicity of 2 µm, and an aperture diameter of 1 µm (50%).

It is worth noting that stacking several EOT filters in series produces a very different response when compared to a single EOT filter with a single layer of the same total metal layer thickness, as shown in the results of Figure 5.11.

Multiple EOT filters stacked in series combine their response in a multiplicative manner, with the response of the previous filter multiplied by that of the next. This multiplication produces a near-zero stop-band transmission, substantially attenuating all but the primary transmission peak. Conversely, increasing the thickness of a single layer filter has a minimal effect on the secondary peak, and shrinks the primary peak intensity in a near linear manner (for thicker films), while simultaneously increasing the Q-factor. Another interesting effect which can be produced by stacking EOT filters in series is that of producing a left-handed metamaterial, as described in [171].

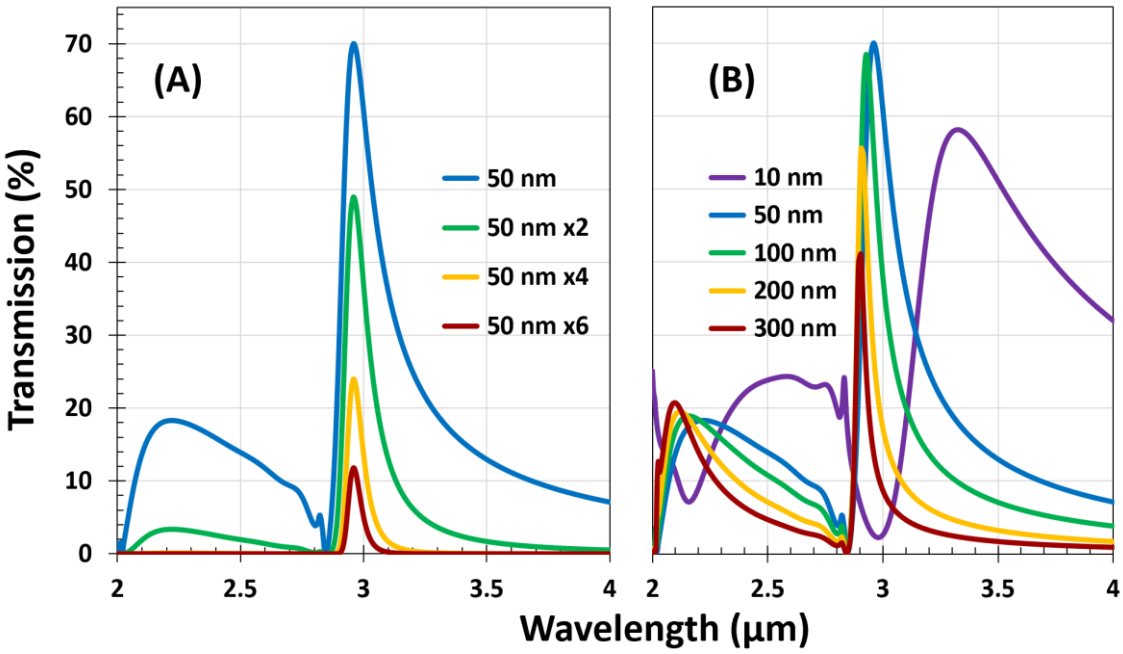

Figure 5.11. Comparison of transmission of multiple stacked thin EOT structures (A), versus a single thicker EOT structure (B). **(A)** Transmission for multiple 50 nm thick EOT structures placed in series. Note that each filter in a stack was simulated separately, and therefore does not account for internal reflections between filters. These reflections will be minimal due to the near-zero reflectivity and relatively high absorption of these filters around their transmission wavelength (see figure Figure 5.2). Thus, any internal reflections will be quickly attenuated. **(B)** Transmission for EOT structures of varying metal thickness. EOT structure is gold with an aperture periodicity of 2 µm, and an aperture diameter of 1 µm (50%), substrate is CaF_2.

The approach of stacking multiple filters in series is used for the display devices detailed in section 6.2. This choice was made due to the low stop-band transmission, which improves the spectral purity of the colours and the contrast ratio.

5.1.3 Adding Additional Functionality

5.1.3.1 Controlling Angular Sensitivity

Often angular sensitivity is undesirable. Receiving light from multiple angles would cause the EOT filters discussed so far to appear to have a substantially broader transmission peak (as compared to normal incidence only). This occurs when focusing light from a (non-collimating) lens, or if light is being collected from a scene.

Controlling this angular sensitivity is possible by modifying the aperture from a circular hole into a cross shape. While this approach slightly reduces transmission for all incident angles, the primary transmission peak remains almost unchanged until an angle of 20° is exceeded, see the results of Figure 5.12. The use of cross-shaped apertures also adds an additional degree of design freedom, in that the arm length to thickness ratio can be varied to further tailor the response.

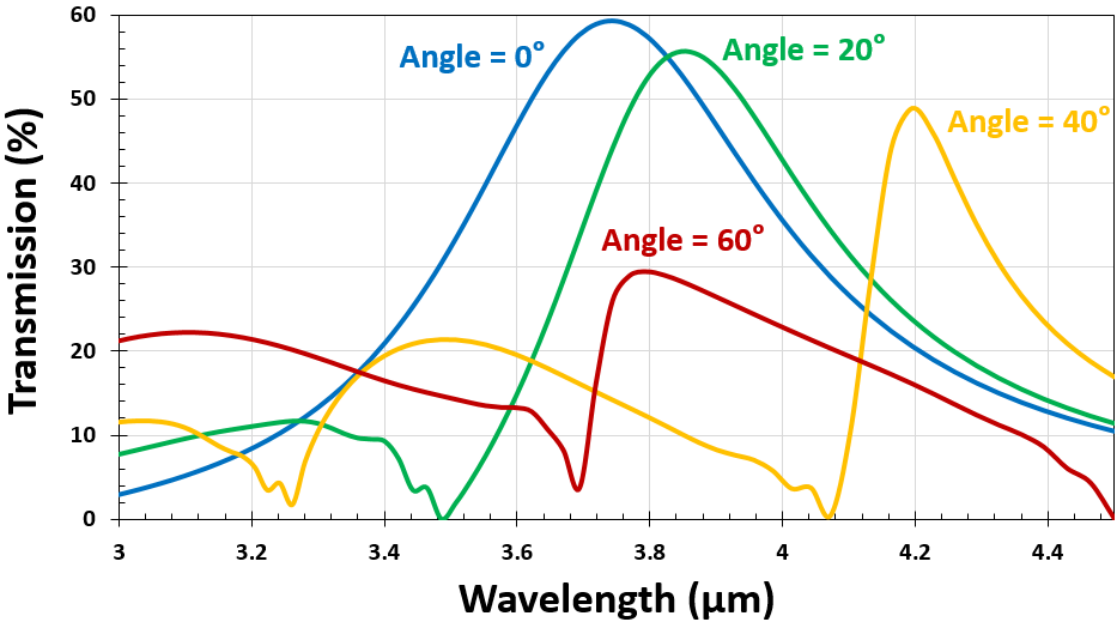

Figure 5.12. Transmission of EOT filter with cross shaped apertures for three incident angles of light. EOT structure made in 100 nm of gold, periodicity is 2 µm, the cross arm lengths are all 1.3 µm nm and their arm width is 165 nm.

5.1.3.2 Polarisation Control

The ability to control polarisation was investigated by replacing the circular EOT apertures with an aperture which lacks rotational symmetry. This was indeed found to produce polarisation sensitivity. U-shaped horseshoe like apertures (like that shown in Figure 5.13) were found to provide good performance whilst exhibiting polarisation selectivity. For light linearly polarised in the X direction the apertures function similarly to square apertures, and so have high transmission (although the increased number of higher order EM modes caused by this aperture shape also produces a particularly broad and intense secondary peak). For light polarised in the Y direction, the aperture appears like a thin slit, which produces a lower amplitude, sharper resonance, as shown in Figure 5.13.

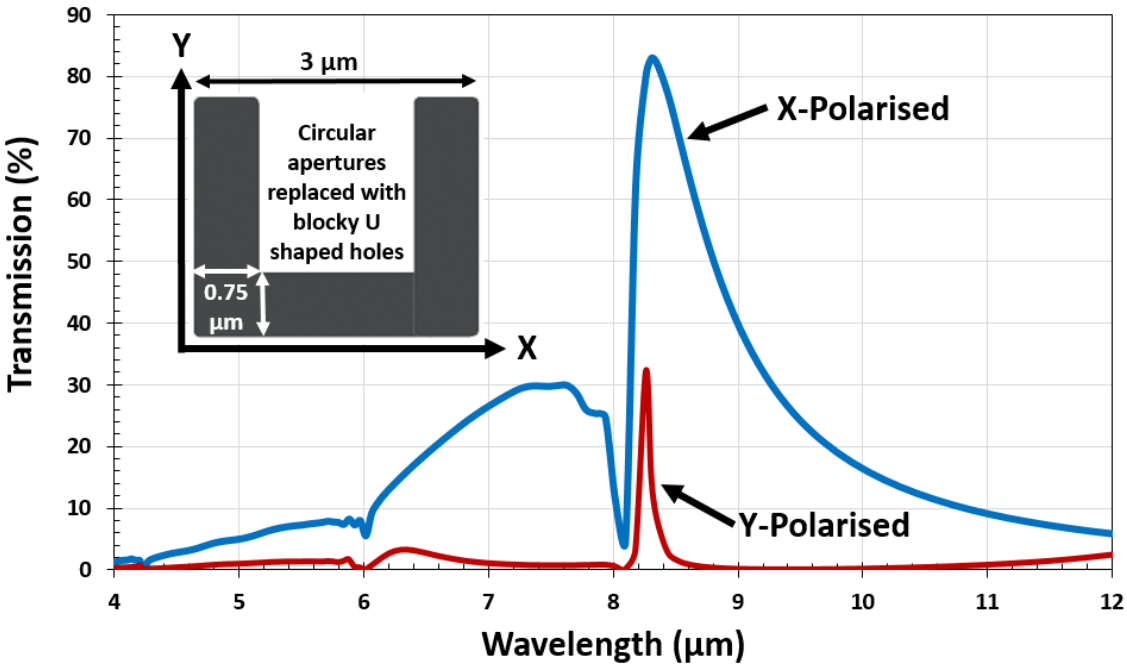

Figure 5.13. Transmission for an EOT structure with polarisation sensitive ‘horseshoe’ apertures. EOT structure made in 200 nm of gold with a periodicity of 6 µm, aperture wall length is 3 µm, and aperture trench width is 0.75 µm.

5.2 PHASE-CHANGE EOT TUNEABLE FILTERS

This section details the modelling studies conducted to produce a design framework for incorporating phase-change materials into EOT structures. These studies produced numerous critical parameter relationships (both material property and geometry) which must be balanced if one is to design well performing filters which can be practically realised and switched.

These studies include investigations on how to best incorporate a PCM, and how to best match a PCM and substrate. The purpose of adding a PCM is to provide spectral tuning range to a filter, and this range should be maximised while attempting to maintain good transmission and Q-factor. It is also vital to consider how changes to a design may affect the thermal switchability of the device, and the energy efficiency of this switching.

5.2.1 How Best to Incorporate the PCM

Initially it was unclear how to best incorporate a PCM into an EOT supporting structure as there are several approaches; those which can be fabricated in a single lithography stage are listed below, and illustrated in Figure 5.14.

1. Continuous PCM film below the EOT structure.
2. PCM on top of EOT structure and within apertures.
3. PCM only within apertures.
4. PCM on top, but with reduced thickness within the apertures.
5. A combination of the above approaches.

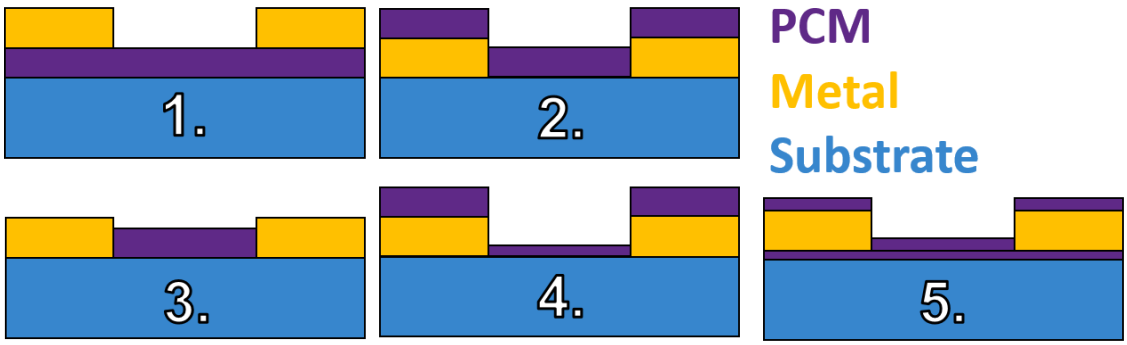

Figure 5.14. Cross sectional side view of a unit cell of an EOT structure incorporating a PCM. Six different approaches to incorporating the PCM are shown, and correspond to the list above. **Blue** is the substrate, **purple** is the PCM, and **yellow** is the metal.

The first question is raised by approaches 1 and 2: should the PCM be below the EOT structure, deposited on top, or a hybrid involving both? Simulations were conducted to answer this, as shown in Figure 5.15. In this study the total PCM thickness was always 70 nm, with this volume being divided between the top and bottom of the EOT structure. It was thought that a thin PCM layer below the EOT structure, with most deposited on top, would yield the greatest spectral shift, as the plasmons present at the substrate/metal interface would be fully confined within the PCM. However, spectral shift was virtually unchanged, and only slightly reduced for the case in which no PCM was in the aperture. However, the enhancement to LEOT (see sub-section 2.1.2) due to a higher permittivity environment in the apertures provided a boost to transmission, especially for the crystalline phase which suffers from sub-optimal superstrate and substrate matching. This rules out approaches which involve incorporating the PCM below the metal layer, leaving approaches 2, 3 and 4.

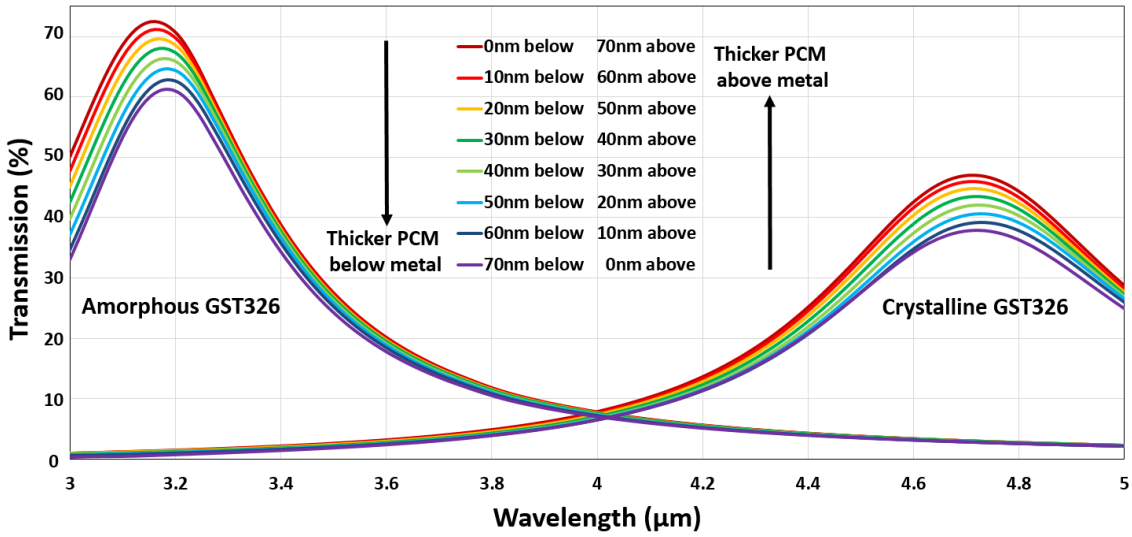

Figure 5.15. Simulated transmission of EOT structure patterned into 100 nm of gold with differing distributions of a PCM (GST326 in this case). The two distribution extremes are: 1) all of the PCM deposited onto the substrate, and therefore underneath the metal layer, and 2) all of the PCM deposited on top of (and within the apertures) of the EOT structure.

The second question concerned optical losses within the PCM, and whether they played a large role. Evaluating the impact of losses would also help determine guidelines for PCM thickness. However, the PCM within the apertures provides the filters with the majority of their spectral shift, and therefore losses would need to be very large to make approach 4 worth pursuing.

To assess the effects of optical losses, a gold EOT structure with a thin layer of 'lossy air' (n=1, k=0.1) was incorporated instead of PCM, in the manner described by option 2 (Figure 5.14). This layer has typical losses for a partially crystalline PCM, but is otherwise identical to air. The thickness of this layer was then varied, thereby increasing the lossy region while all else remained equal. As shown in Figure 5.16, light absorption within the PCM can play a large role, with transmission dropping from 68.4% (for an uncoated filter) to 51.9% for 100 nm (enough to fill the aperture) of 'lossy air'. However, the effects of additional lossy material decrease and flatten out once approximately 85% of the aperture's depth is filled. This is because the energy is concentrated within the centre of the aperture and within the plasmons (at both interfaces), which are mostly contained by the first 50-60 nm of material deposited onto the EOT structure. In practise, light absorption within the apertures is somewhat mitigated by the high permittivity of PCMs, which helps support additional EM modes through the apertures; this

effect is not present here due to the refractive index of 1. This results in option 4 being ruled out.

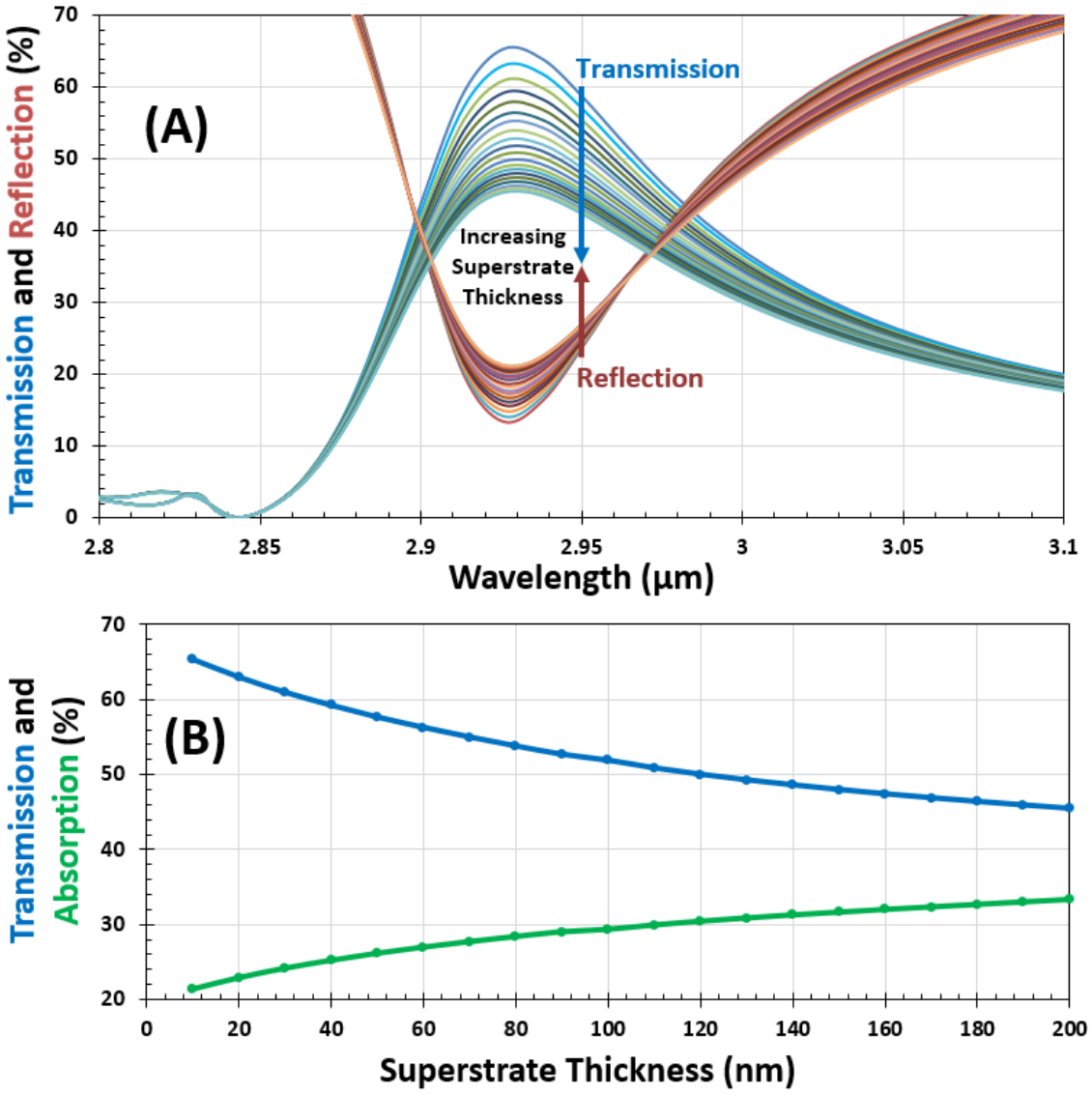

Figure 5.16. Effects of increasing thickness of a lossy n=1superstrate (PCM). **(A)** **Transmission (mostly blue)** and **reflection (mostly orange)** of an EOT structure for various (superstrate) thicknesses of lossy material deposited on top of and within the apertures. Aside from losses (k=0.1) this material is identical to air. **(B)** **Transmission** and **absorption** of this EOT structure as a function of superstrate thickness.

Options 2 and 3 remain viable, however, while there is minimal performance difference between them, option 3 is less suitable for fabrication via etching. Therefore option 2 was selected as the best approach, and unless otherwise stated, all phase-change EOT devices in the remainder of this work use this approach.

Figure 5.17 shows a typical example of normalised (amplitude of all components) electric field distribution for an EOT filter with a PCM deposited on top of the structure and within the apertures (i.e. approach 2 from Figure 5.14). Compared to the field distribution for a bare (metal only) EOT structure (see Figure 5.3) there are a number of observations. Firstly, the intensity of the plasmons for the on-resonance condition is substantially reduced with a PCM (compared to a bare EOT structure); the intensity of off-resonance plasmons is virtually unchanged. The second observation, which is true for both on and off resonance, is that electric fields are now more-so concentrated within the apertures; this is discussed in chapter 2 concerning the addition of a high-index dielectric concentrating fields and supporting additional EM modes within the apertures.

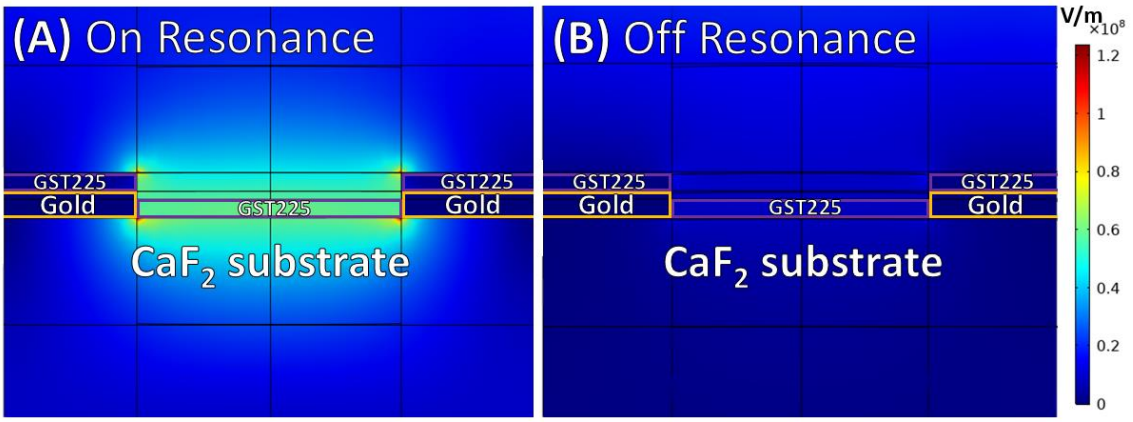

Figure 5.17. Simulated electric field (normalised) distribution for an EOT structure for both on resonance and off resonance conditions. EOT structure is 100 nm of gold on a CaF_2 substrate with a periodicity of 2 μm and an aperture diameter of 1μm, with 50nm of amorphous GST225 deposited on top and within the apertures. **(A)** At the resonance wavelength of 3.2 μm, with a maximum field strength of 1.23E8 V/m. **(B)** Off resonance, with a wavelength of 5 μm.

5.2.1.1 Matching the PCM and Substrate

Ideally the superstrate and substrate indices of refraction should match in order to maximise transmission (as discussed in sub-section 2.1.2). With a phase change material as the superstrate a compromise is required, and intuitively one would match the substrate to the properties of the PCM when half-crystallised. However, the PCM layer is much thinner than the incident wavelength, and therefore the actual effective superstrate properties will be some combination of the PCM, barrier layers, and the air. To act as a comparative baseline, the effects of increasing the refractive index of an infinitely thick superstrate were

investigated for two different substrate indices. Figure 5.18 shows the results of this study. As expected, the performance is best when the substrate and superstrate match.

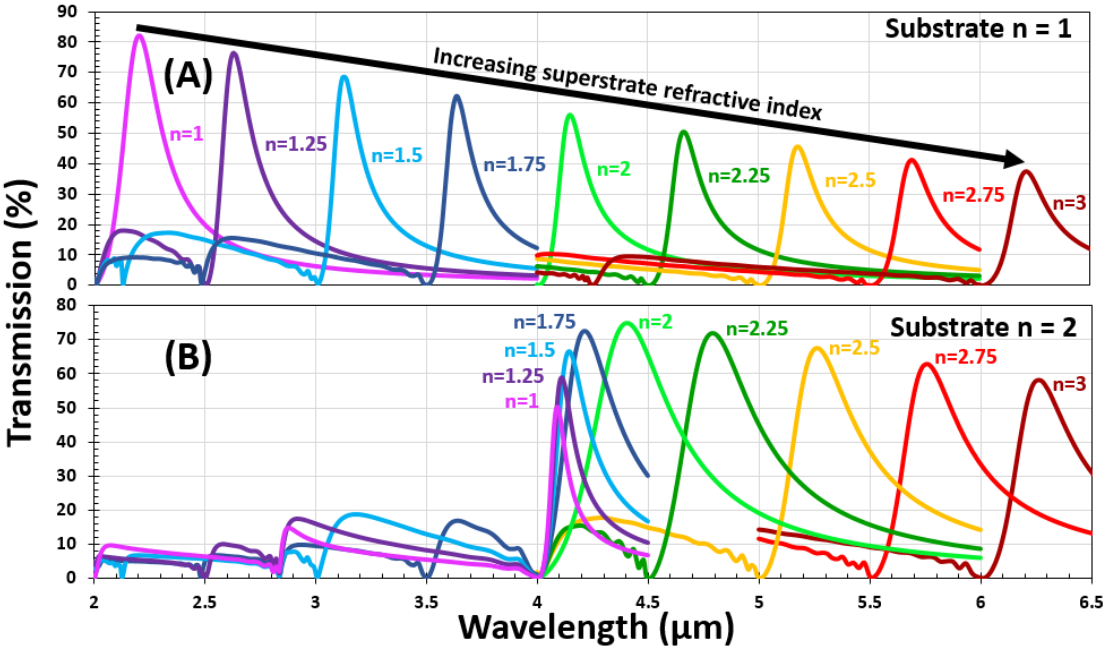

Figure 5.18. Effects of increasing superstrate index of refraction for two different lossless substrates. **(A)** substrate with refractive index of two. **(B)** substrate with refractive index of one.

Another observation, (explicitly shown by Figure 5.19) is that the spectral peak position converges once the superstrate index exceeds the substrate index. Therefore the resonant position is dominated by either substrate or superstrate, depending on which has the largest refractive index. Thus, if one wishes to maximise a filters spectral range (thereby making full use of a PCM's contrast), the PCM should be paired with a substrate with a refractive index that is close to, but slightly lower than the combination of the PCM's amorphous properties and the air above it. This almost always results in the lowest possible refractive index substrate (that is transparent) being the ideal choice. However, this will result in a significant refractive index mismatch once the PCM is crystalline; and so maximising transmission in both PCM phases will always come at the cost of spectral tuning range.

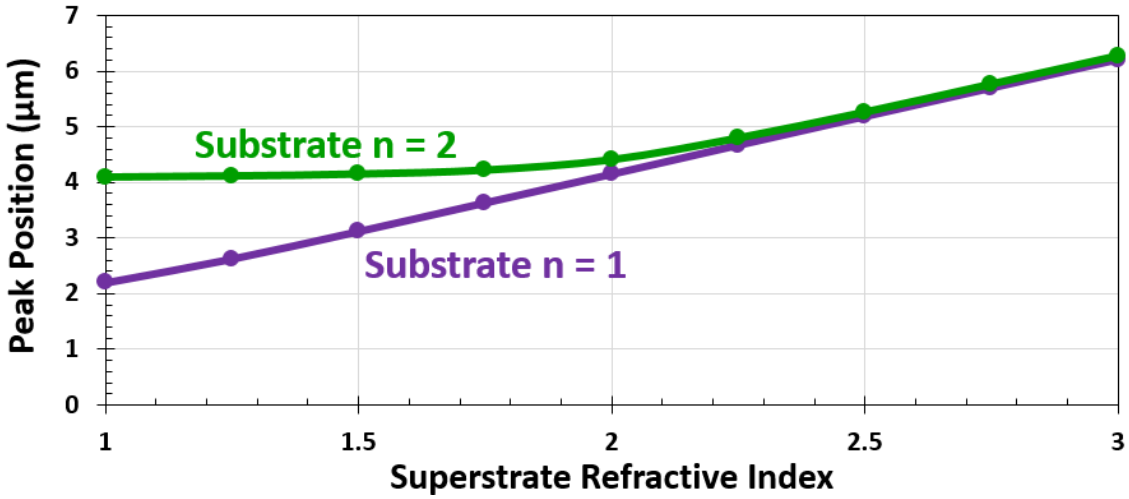

Figure 5.19. Primary transmission peak position as a function of superstrate index, for both substrates. EOT structure made in 100 nm of gold, period is 2µm, aperture diameter is 1µm (50%).

The spectral shifts shown in Figure 5.19 are very large due to the effectively infinite PCM (superstrate) thickness. In practise the thickness is limited by optical losses and the difficulty of adequately quenching thick PCM layers for re-amorphisation. These practically switchable but thin PCM layers will not provide the same effective superstrate refractive index as their infinite counterparts; and so to evaluate the effective total superstrate refractive index (resulting from a combination of PCM layer and air), the study presented in Figure 5.20 was conducted. This study is analogous to that in Figure 5.16, in that the PCM layer is identical to air, except for one property (refractive index in this case). Refractive indices of 3 and 6 were chosen, as they are typical amorphous and crystalline PCM values. The thickness of this superstrate was gradually increased from 0 until the EOT effect began to break down and multiple transmission peaks occurred. While the maximum PCM thickness shown is 400 nm, this is for curiosity only, as thickness as thin as 200 nm would not be practically switchable for the vast majority of PCM alloys.

The most important thing to note from this study is that doubling the refractive index (from 3 to 6) results in an approximately five-fold greater spectral shift. This leads to the observation that using smaller volumes of PCMs with a greater refractive index contrast is preferable to thicker layers with less contrast (300 nm of n=3 is equivalent to 60 nm of n=6). Another observation is that while the n=3 case appears to have greater transmission, both cases have a similar

transmission for the same spectral shift. For both cases the shift in resonant position has a linear region, which is between 50 and 250 nm for the n=3 case, and 10 to 50 nm for n=6. Once these thicknesses are exceeded the spectral shift per nm of PCM thickness starts experiencing diminishing returns. For the n = 3 study, the transmission intensity peaks at around 120 nm, this indicates that the total effective superstrate properties are equal to the substrate (CaF2) for this thickness. For the n = 6 case, even 10 nm of superstrate appears to mis-match the substrate and superstrate properties. The quality factor for the n=3 case is substantially greater than the n=6 case while the PCM thickness remains relatively low, but rapidly drops off once the transmission intensity is maximised. For thicker PCM layers both the n=3 and n=6 cases have similar quality factors.

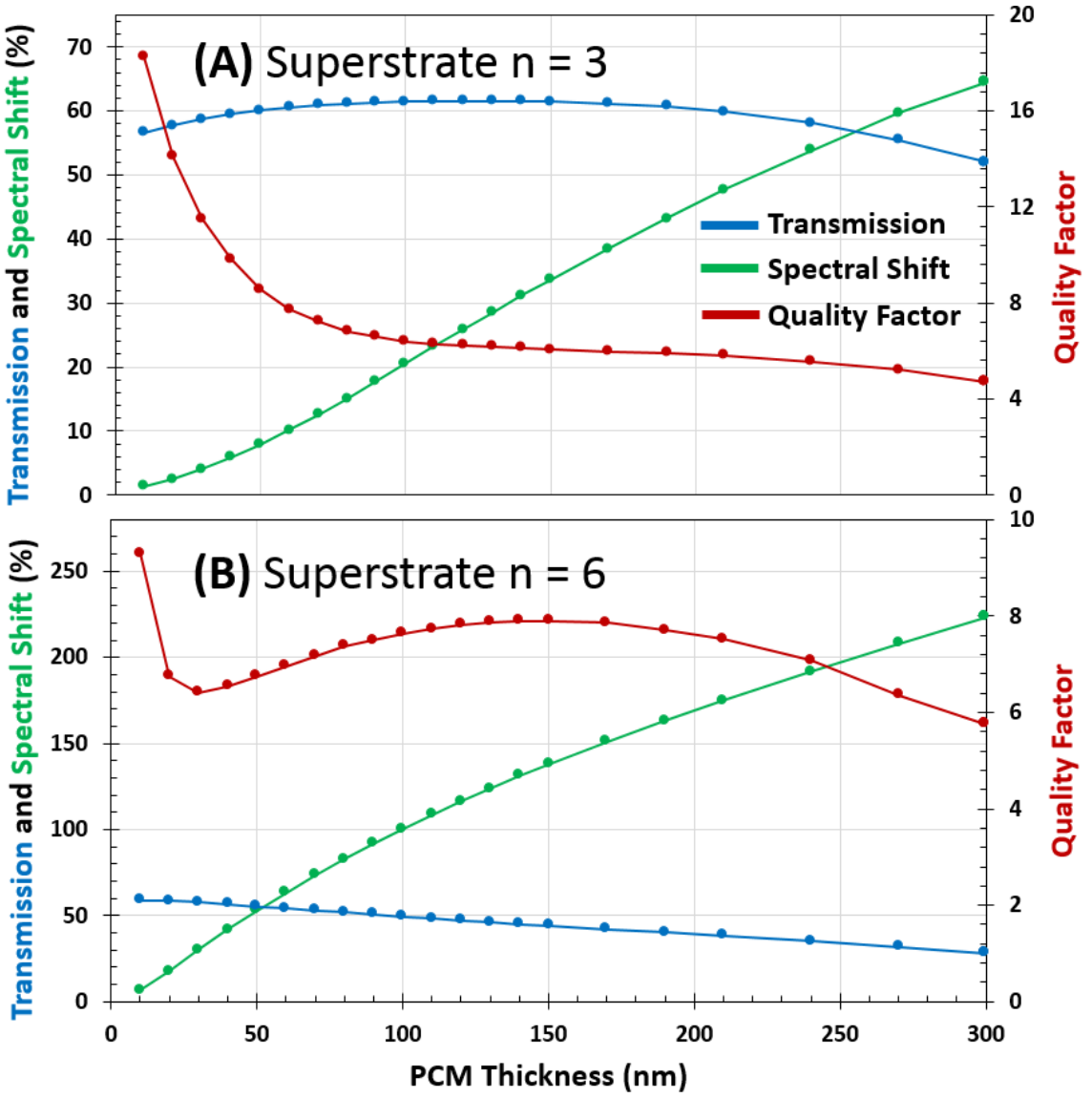

Figure 5.20. Performance of a phase-change filter device as the thickness of a lossless high refractive index superstrate increases. **Blue** curve is the percentage of transmitted light. **Green** is the percentage of resonant spectral shift compared to a metal-only EOT structure of the same dimensions. **Red** curve is the quality factor of the transmission peak. **(A)** is for a superstrate refractive index of 3. **(B)** is for a superstrate refractive index of 6. EOT structure made in 100 nm of gold, with an aperture period of 2 μm, an aperture diameter of 1 μm, on a CaF2 substrate.

While it is clear that a large contrast in refractive index is preferable to a larger volume of lower loss PCM, it remained unclear if a proportional or absolute increase in index contrast would yield the greatest spectral tuneability. A study in which two lossless 'PCMs' of different refractive indices (2.5 and 5 versus 4 and 8) and thickness (80 nm vs 40 nm) was undertaken. In this case they both experience a 100% increase of refractive index when 'crystallised', but with the higher index PCM having half the volume. This is shown in Figure 5.21.

It is clear that there is a significant advantage to selecting high refractive index PCMs. Not only do they provide a greater spectral shift, but they can do so while having a much smaller volume, further improving their ease of re-amorphisation and reducing optical losses.

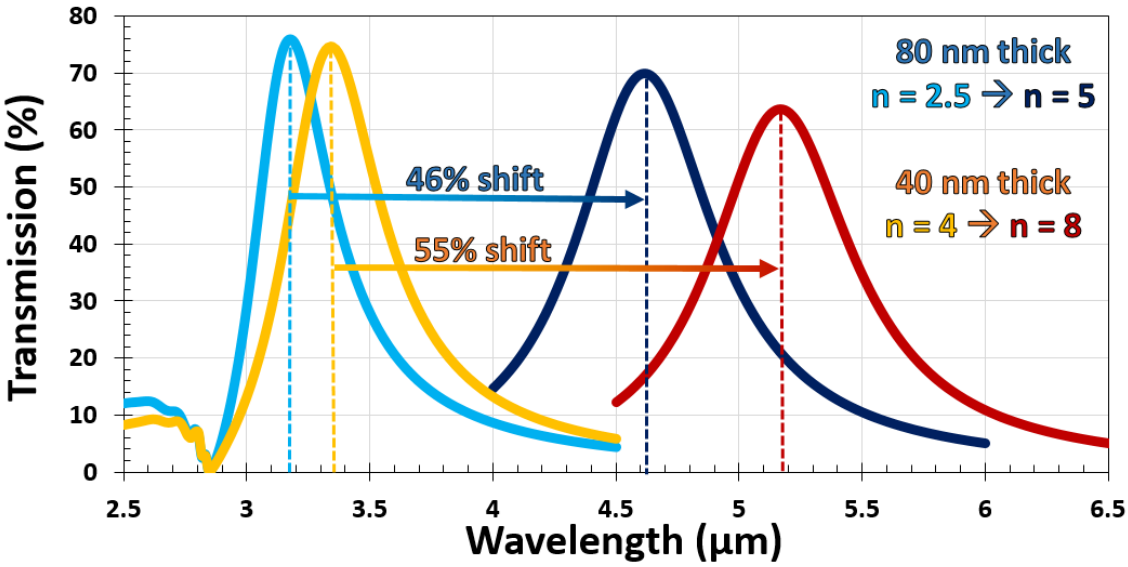

Figure 5.21. Simulated transmission of two phase-change EOT devices. Each filter has a different thickness of material deposited within the apertures, and for each filter this material has a different refractive index. Each material has the same proportional change in refractive index, but with a different absolute change.

5.2.1.2 ON/OFF Switching Functionality

When switching a PCM from amorphous to crystalline phase, the refractive index (both real and imaginary components) increase. Most PCMs, even when crystalline, have a relatively low loss region. However, some PCMs exhibit a massive increase in losses when crystalline; this blocks virtually all transmission through EOT devices. This means using these high loss contrast materials modifies our filters from spectrally tuneable into switchable ON/OFF. The three materials explored for this role are GLS, AIST, which were found to be particularly lossy when crystalline, and vanadium dioxide (VO_2). Furthermore, these materials were initially investigated due to their ease of re-amorphisation, and so thermal constraints applicable to other filters could be relaxed. This type of ON/OFF filter is explored for use as a display in sub-section 6.2.4 (using GLS).

Figure 5.22 shows example performance for three such filters, two using AIST, and another using VO_2. VO_2 is unique compared to the PCMs in this thesis, as its phase-transitions are volatile, and driven by relatively low temperatures (≈66°C). Because the high losses within the PCM disable the EOT resonance, the filter structure exhibits high, uniform, specular reflection when the PCM is crystalline.

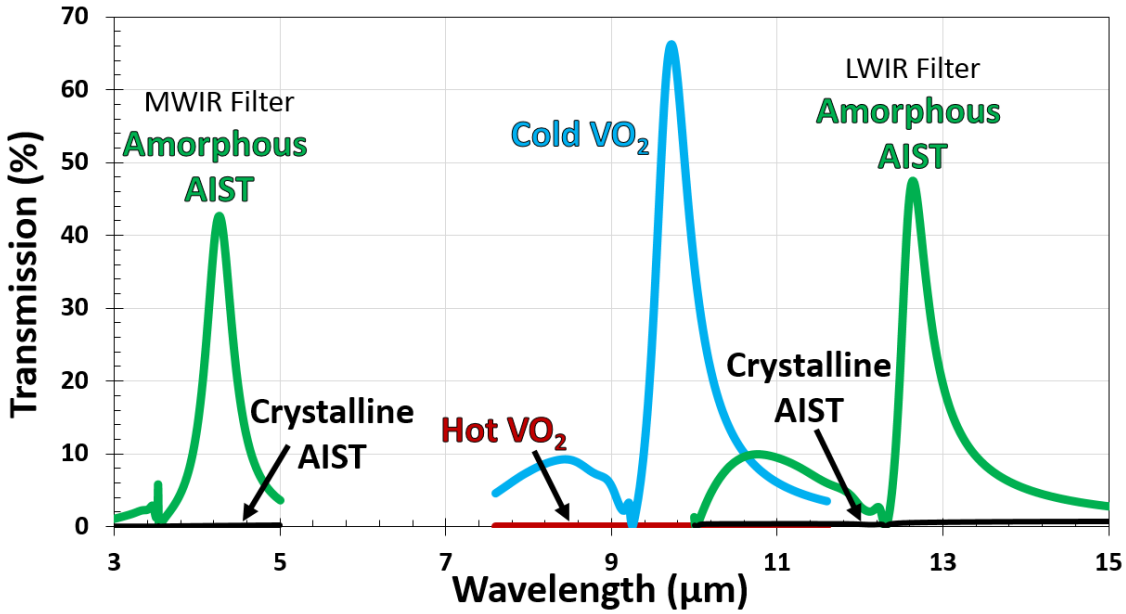

Figure 5.22. Simulated transmission for three different amplitude-tuneable filters for both fully amorphous and fully crystalline PCM phases. Two filters incorporate AIST, and another VO_2 as the PCM. Shorter wavelength (MWIR) EOT filter uses 70 nm of AIST, and is made from 150 nm of gold with 1 μm apertures with a periodicity of 2.5 μm. Longer wavelength (LWIR) EOT filter made from 300 nm of gold with 4 μm apertures with a periodicity of 10 μm, and also incorporates 70 nm of AIST. The VO_2 filter is made from 120 nm of gold, with a periodicity of 7 μm and aperture diameters of 2.8 μm.

5.3 THERMAL SIMULATIONS

Thermal simulations were conducted to evaluate the feasibility of using the metallic EOT structure as an electrical Joule heater. Previous work successfully and repeatably switched a thin (20 nm) layer of GST225 deposited onto a continuous gold layer (used as a heater), with a silicon substrate [172]. However, the feasibility and parameter relationships of switching a PCM within a metal aperture remain unclear.

The objective of this study was to evaluate the thermal design requirements for a variety of substrates and phase-change materials. Also of interest was evaluating the energy requirements and effects of device scale on switching characteristics. This is important, as PCM selection is limited by what can practically be switched, as many have challenging-to-achieve thermal profiles for successful re-amorphisation. An example of this challenge is illustrated in Figure 5.23, which shows the kind of thermal profile one might aim for to achieve near-complete switching of GST225. The re-amorphisation stage here takes just 25 ns, and cools at an average rate of 20 K/ns.

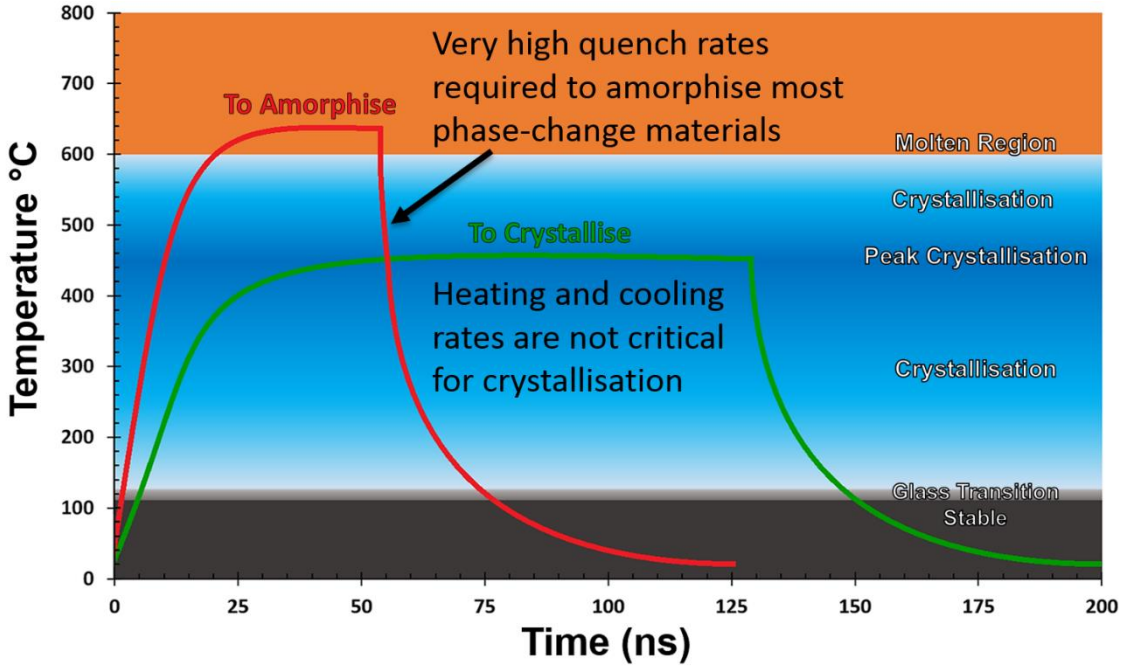

Figure 5.23. Plot showing ideal heating/cooling profiles to both crystallise and re-amorphise GST225. Also included (as background colour) are the different temperature regions of GST225. The cooling rate shown for re-amorphisation is 20 K/ns.

Figure 5.24 shows a 2D slice of the COMSOL results, this snapshot is taken shortly after a rectangular electrical pulse (sufficient to melt the PCM) has ended, and shows that the substrate (rather than the air) provides virtually all heatsinking during the cooling phase. Also of note is the relatively uniform heat distribution within the PCM layer, although this gradually stops being the case for larger scale devices (the aperture size here was just 680 nm). The metal used in the thermal studies here is gold, and the PCM is GST225 with appropriate barrier layers. GST225 was selected as comprehensive thermal property studies have been conducted, and data is readily available [159]. While the simulations conducted here did account for conductivity changes due to increases in temperature (for all materials), they did not account for property changes due to structural alterations within the PCM. Instead thermal properties for the amorphous phase were used, as this is the more insulating phase these results can be considered conservative and pessimistic. For a more detailed description of the thermal models, refer to sub-section 3.1.2.

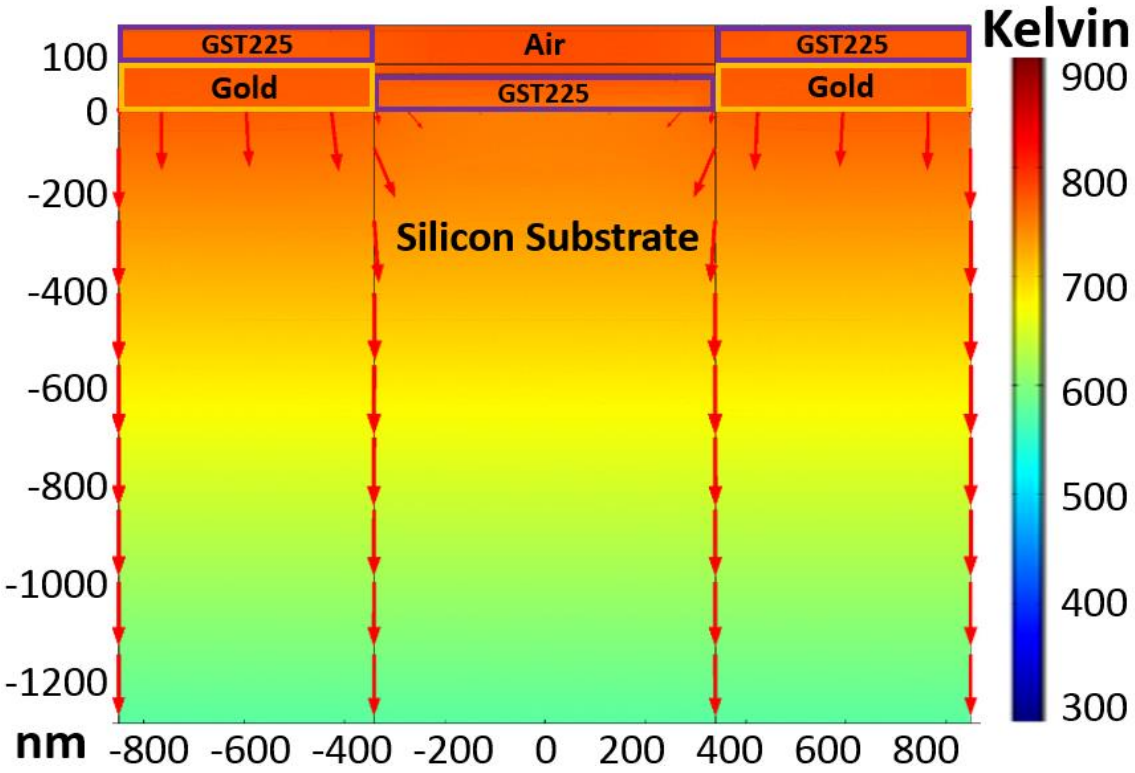

Figure 5.24. 2D slice of a thermal model coloured by temperature half way through the quenching stage of a re-amorphisation cycle. The arrows indicate the amplitude and direction of heat flow. This EOT filter has a period of 1700 nm, and an aperture size of 680 nm (40%).

5.3.1 Effects of Substrate - Energy and Quench Rates

The heatsinking abilities of different substrates vary significantly; this is primarily caused by differences in thermal conductivity and specific heat capacity. A greater ability to draw heat away from the EOT structure necessitates additional current flow through the metal to reach a given temperature, (but significantly aids rapid quenching). Five good substrate candidates, (SiO_2, CaF_2, SiN_4, Al_2O_3, Si) were evaluated for their energy requirements to melt the filter device's PCM, as shown in Figure 5.25. This was necessary to evaluate the current required to melt GST225, which was needed for the subsequent study. Because energy rises with the square of the current, the energy consumption to switch is heavily dominated by the substrate choice.

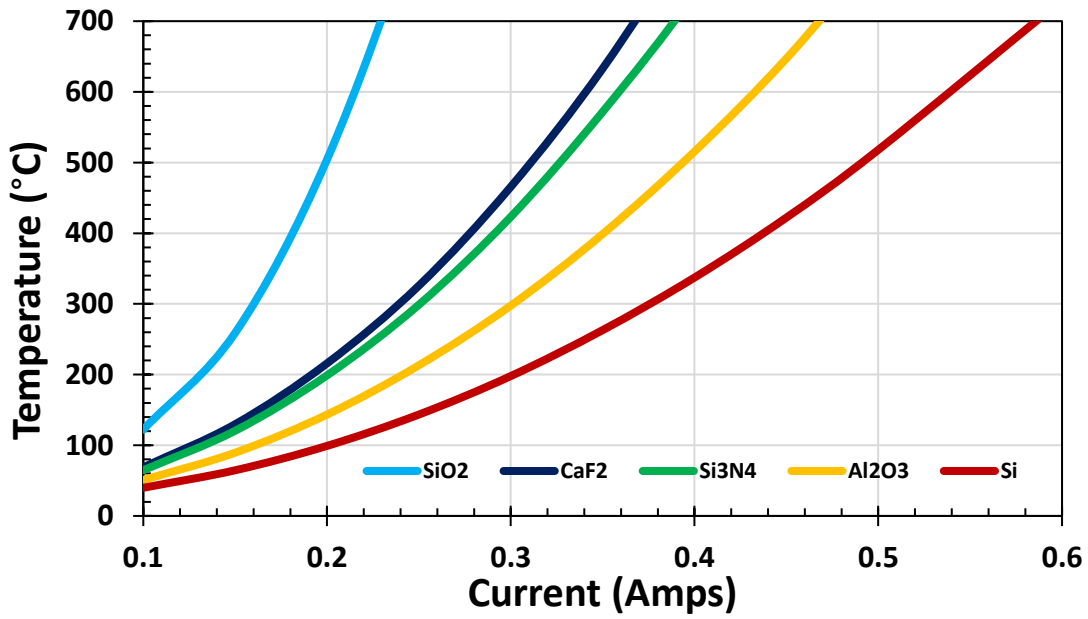

Figure 5.25. Maximum temperature at the centre of a 70 nm thick GST225 volume within an aperture as a function of current (pulse duration 200 ns) for a variety of substrate candidates. EOT structure made from 100 nm of gold with a period of 2 μm and an aperture diameter of 0.8 μm (40%), yielding a resistance of 0.177 Ω.

Once the energy requirements for each substrate were evaluated, it was possible to evaluate the quenching capabilities of each substrate. The quench rate determines how fully a PCM can re-amorphise; a high quench rate effectively enables access to the full contrast of a PCM's properties between phases. PCMs which require high quench rates will have to be paired with highly conductive substrates, which in turn greatly increase energy switching requirements.

Conversely, PCMs with forgiving switching characteristics can use more insulating and energy efficient substrates. Figure 5.26 shows the heating/cooling profile for the same device as described in Figure 5.25. For each substrate the current required to reach 650 °C (≈30 °C above melting point of GST225) was used. In this case silicon was the only substrate material able to adequately quench the GST225 volume, with an average quench rate of 3.5 K/ns; this is still relatively slow for GST225, and would result in incomplete re-amorphisation [173]. However, more forgiving (easier re-amorphisation) PCM's such as GLS, would be adequately quenched even by the SiO_2.

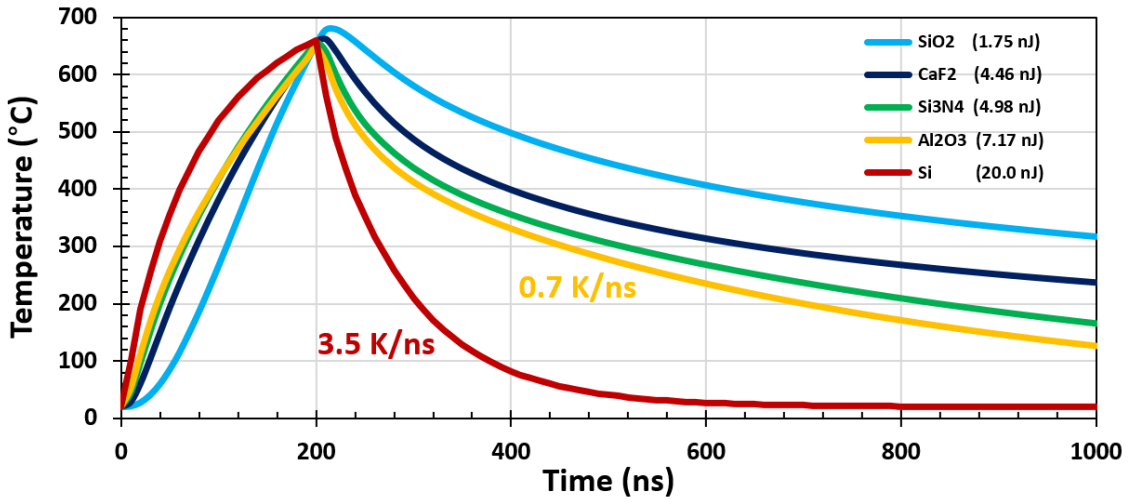

Figure 5.26. Heating and cooling profile of an example device for a variety of substrates. Specifically the temperature at the centre of the PCM volume. Included in the legend is the energy required for re-amorphisation (i.e. energy to bring centre of the PCM volume in each EOT structure to 650 °C. Also included are the average quench rates for the two substrates able to quench below the crystallisation temperature within the simulated time span. EOT structure made from 100 nm of gold with a period of 2 µm and an aperture diameter of 0.8 µm (40%), yielding a resistance of 0.177 Ω.

Table 4. Electrical parameters of the simulations used to produce Figure 5.26.

Material	Current (mA)	Voltage (mV)	Power (mW)	Energy (nJ)
SiO_2	223	39.38	8.76	1.75
CaF_2	355	62.84	22.3	4.46
Si_3N_4	375	66.38	24.9	4.98
Al_2O_3	450	79.65	35.8	7.17
Si	565	100	56.5	20.0

5.3.2 Device Scaling and PCM Considerations

As devices scale up for longer wavelengths the aperture size increases, this results in the centre of the PCM volume (within the apertures) being further from the metallic heating structure. This places a greater importance on the PCM's conductivity. The same is true (to a lesser extent) for increases in PCM thickness. EOT filters become relatively power-hungry at large scales, as the metallic heater must reach temperatures which far exceed the PCM's melting point in order to transfer enough thermal energy.

The scaling relationship (switching energy vs period) was investigated using tuneable filters designed for the 3 to 5 μm atmospheric transmission window, with CaF_2 as the substrate (see Figure 5.27). The energy to switch a single unit cell increases rapidly as the device scale increases, as described by the power equation within the figure. This rapid increase is due to a combination of the increased contact area (heat loss) to the substrate, and the increased distance to the PCM centre (higher metal temperatures required). This is further compounded by increased resistance in the metal, as it must become significantly hotter for the same PCM temperature. Once the EOT device area is accounted for, this scaling relationship becomes linear, with a doubling in period resulting in an approximately 25% increase in energy per area consumption.

This results in the observation that EOT devices designed for shorter wavelengths are inherently more efficient at switching their PCM volumes. This is especially true for PCMs with a low thermal conductance, such as the GST225 used here. As shown by the dark blue curve in Figure 5.27 (GST225 with tripled thermal conductivity), the switching energy does not rise as rapidly as period increases (slope of 2.53 vs 2.26). The above assumes that the metal layer (the heater) is thicker than the PCM, in which case the heater to PCM contact area PCM remains unchanged.

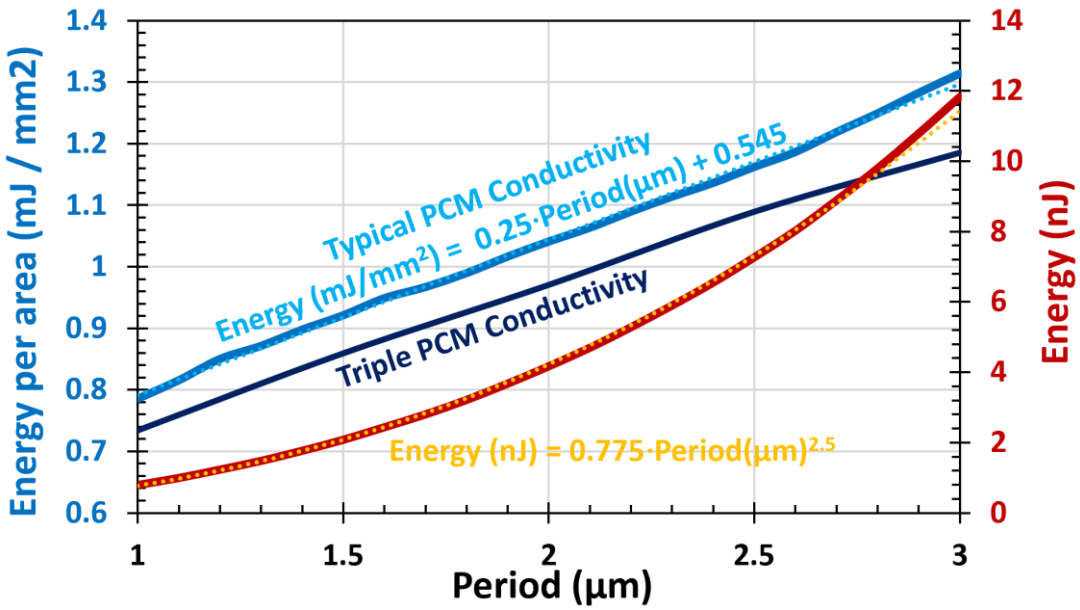

Figure 5.27. Energy (nJ) required to switch a single unit cell of a filter device depending upon its size (period). Full thermal simulation performed for each 100 nm increment in periodicity. **Red curve** is energy (nJ) per unit cell, described by the equation in orange. **Lighter blue line** is the switching energy (mJ) per device area (mm^2). **Darker blue line** is the switching energy for GST225 with its thermal conductivity tripled. Metallic layer was 100 nm thick (0.177 Ω), with a diameter equal to half the period in every case. The PCM was 70 nm of GST225, and the substrate CaF_2. The current and voltage used was the minimum which would rise the centre of the GST volume to 650 °C in 200 ns.

The resistance of a single EOT structure unit cell (and therefore the excitation voltage required) is only affected by the metal's thickness and conductivity. Imagining the EOT unit cells arrayed like resistors in a parallel and series block, it is simple to deduce that increasing the width of an EOT array (adding additional resistors in parallel) will not affect voltage requirements as the total current required will increase in step with the resistance decreasing. Increasing the length of an EOT array (resistors in series) will however increase the voltage requirements, as resistance (i.e. distance between electrical contacts) will increase.

The electrical driving requirements (especially current) for tuning these filters are extremely high, as shown in Table 3. Re-amorphising an entire filter comprised of a million EOT apertures with a 2 µm period (2x2 mm) like those described above, would require a 355 amp, 22.3 KW pulse. Switching efficiency is improved by increasing the metal thickness to lower resistance. While the current requirements slightly rise due to the increased metal volume, the primary heat loss through the substrate remains unchanged.

5.4 SUMMARY OF DESIGN GUIDELINES

This section briefly summarises the finding of the various modelling studies, such that filters for a specific application can be quickly designed.

5.4.1 Selecting an Appropriate EOT Filter Geometry

The most critical design parameter to select is that of the periodicity. Assuming that one has selected a PCM with appropriate thickness and optical properties such that it is the superstrate, and not substrate, that determines the resonant position, then this effective superstrate refractive index and desired operational wavelength can be used to calculate the required device periodicity. See sub-sections 2.1.2 and 5.1.2.2.

Aperture diameter should not be significantly varied from half of the periodicity, as a large variation degrades the filter's ability to support EOT, and should be kept between 40% and 60% of the period. Increases in aperture size reduce quality factor and increase transmission (both off and on resonance). A further side effect of larger apertures (albiet a small one) is an increased power requirement for PCM switching. See sub-sections 5.1.2.3 and 5.3.2.

Determining the thickness of the metal layer depends upon how much stop-band transmission is acceptable, and the required sharpness of the peak (Q-factor). Thicker metal layers improve both of these metrics at the expense of transmission intensity. However, once the metal thickness exceeds approximately 10% of the periodicity Q-factor and transmission rapidly degrade. If greater fabrication complexity is acceptable, then a multi-layer filter performs better for the same total metal thickness, as shown in sub-section 5.1.2.4.

Summarised in Table 3 are the effects of altering geometrical parameters of an EOT filter upon the filter's performance.

Table 5. Effect of critical geometrical parameters on filtering and switching performance.

Geometry	Transmission	Q-Factor	Spectral Range	Resonant Position	Switchability	Switching Efficiency
Thicker EOT metal	Reduced	Increased	N/A	Blue-shift (Slightly)	N/A	Increased
Thicker PCM	Reduced	Reduced	Increased	Red-Shift	Reduced (slightly)	Reduced (Slightly)
Aperture Diameter to Period ratio	Increased	Reduced	N/A	Red-Shift (Slightly)	Reduced	Reduced

5.4.2 Selecting Ideal Materials

Selecting an appropriate PCM is the most complex materials choice, listed below are a summary of guidelines for appropriate selection. The effects of various PCM properties upon EOT filter devices are also summarised in Table 4.

1. High absolute PCM refractive index (in both phases) increases spectral shift, and also enables a broader selection of appropriate substrates.
2. A large proportional (%) increase in refractive index is also desirable (to a lesser extent) for the same reasons stated above.
3. The above two enable the use of smaller volumes, which also improves switchability and means greater losses can be tolerated.
4. A low switchability is a direct reduction on PCM contrast (effectively increasing amorphous n), and must be taken into account.
5. Lower losses are always preferable, but usually not at the cost of lower refractive index. This depends on the precise magnitudes, however, an increase in losses is worthwhile if there is a proportional increase in refractive index.
6. A high thermal conductivity aids energy efficiency and switchability, but is only significant for large periodicity devices.

Table 6. Effect of increasing critical material properties on filtering and switching performance.

Material Property	Transmission	Q-Factor	Spectral Range	Resonant Position	Switchability	Switching Efficiency
Substrate Index	Depends	N/A	Depends	Red-Shift	N/A	N/A
Substrate Thermal Conductivity	N/A	N/A	N/A	N/A	Increased	Reduced
PCM Index Contrast	Reduced	Reduced	Increased	N/A	Increased	N/A
PCM Thermal Conductivity	N/A	N/A	N/A	N/A	Increased (for large apertures)	Increased

It is almost always preferable to select substrates with low refractive index that are still transparent in the filter's operational range. See sub-sections 5.1.1.1 and 5.2.1.1. However, thermal properties must also be considered, especially in conjunction with harder-to-switch PCM alloys. Typically a high conductivity is desirable, as discussed in sub-section 5.3.1.

Metal selection is extremely important at shorter wavelengths, with silver being the only strong performer in the visible. Aluminium performs reasonably well, and should not be omitted as it is more compatible with standard semi-conductor manufacturing, and its oxide layer is a good diffusion barrier. At NIR wavelengths the noble metals and other high-conductivity metals such as copper perform well. At longer wavelengths metals start to act more like perfect conductors, and plasmonic performance is generally good regardless of metal choice. See sub-section 5.1.1.2.

6 FILTER EXPERIMENTS AND APPLICATIONS

This chapter covers the experimental realisation of the previously discussed EOT filters, and the modelling work used to evaluate the feasibility and performance of a variety of practical applications.

This chapter starts with a brief discussion of filter fabrication, and then moves onto the experimental performance of fabricated filters. The issues faced during fabrication and the challenges yet to be overcome are discussed. Three potential applications of these filters are then introduced, followed by both electromagnetic and thermal simulations to predict their performance and practical feasibility.

6.1 EXPERIMENTALLY REALISED FILTERS

Following the EOT filter design guidelines presented in chapter 5, a phase-change EOT filter using GST225 was designed to cover the 3 to 5 μm atmospheric transmission window. This wavelength region was chosen because multispectral imaging applications (discussed in sub-section 6.2.1) were the initial focus of this thesis. GST225 was selected as the PCM alloy not because of its properties, but because it's a good proof-of-concept PCM thanks to greater study in literature and experimental process refinement. This device's structure is 100 nm of gold patterned with 850 nm diameter apertures with a periodic spacing of 1.7 μm, with 70 nm of GST225 and a 10 nm SiO_2 encapsulation layer. Electrical contacts were not proposed at this stage, and crystallisation was instead achieved using a hot plate.

Early fabrication attempts used focused ion beam milling. However, issues with debris, erroneously milling into the substrate, gallium contamination, and limits to maximum device size prompted this approach to be discarded in favour of lithography. Some success was had using laser lithography and a negative photoresist, but the devices were at the limit of the laser writer resolution resulting in inconsistencies in aperture shape, which produced an unacceptably broad filter response. To address this the switch to e-beam lithography was made. Figure

6.1 shows AFM measurements of one such filter device. From Figure 6.1A it's clear that the apertures are reasonably (but not perfectly) uniform in shape. Figure 6.1B confirms that the dimensions are almost exactly as designed, except for the verticality of the aperture side walls. Although it is not obvious from the AFM image due to the difference in axis scale, AFM suggests that the side walls are significantly slanted, with a deviation of 50.9º from vertical. The slanting may be caused by the undercut present in the lithography mask, but more likely it is an artefact of the AFM imaging, as extra-sharp tips were not used.

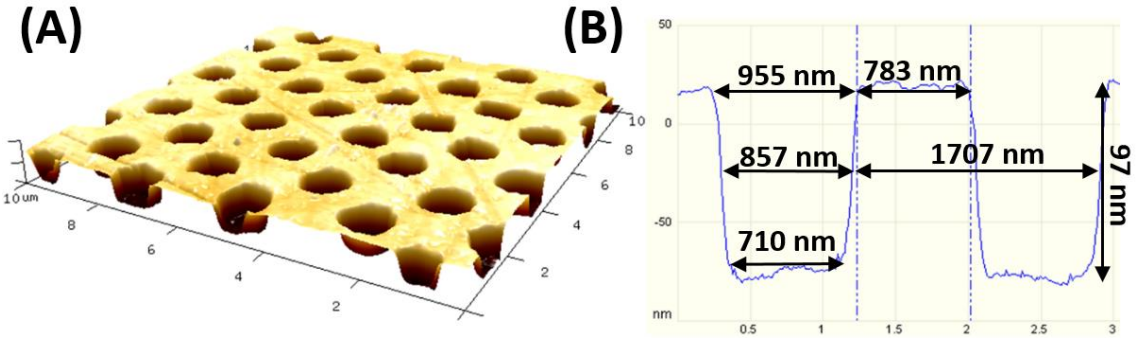

Figure 6.1. AFM Measurements of EOT filter before PCM deposition. **(A)** 10x10 **µ**m 3D AFM image. **(B)** AFM cross section showing two holes, confirming the aperture depth and size to be as designed. Intended EOT structure is 100 nm of gold with an aperture periodicity of 1.7 µm and a diameter of 850 nm.

This particular filter device then had 70 nm of GST225 magnetron sputtered onto it, followed by a 10 nm silicon oxidation barrier; however, no barrier was deposited between the PCM and gold. The sputtering machine uses 6 inch targets, and uniformly deposits material at normal incidence. Despite the normal incidence sputtering, a significant amount of PCM coated the aperture side walls, as can be seen by the reduction in aperture diameter shown in Figure 6.2. In fact, the diameter appears to have been reduced by an amount significantly thicker than the intended thickness of PCM. The aperture side wall slanting was not significantly changed, and was found to be 53.8º. Crystallisation was performed using a hot plate set to 260 Cº for 15 minutes; this did not alter the device structure.

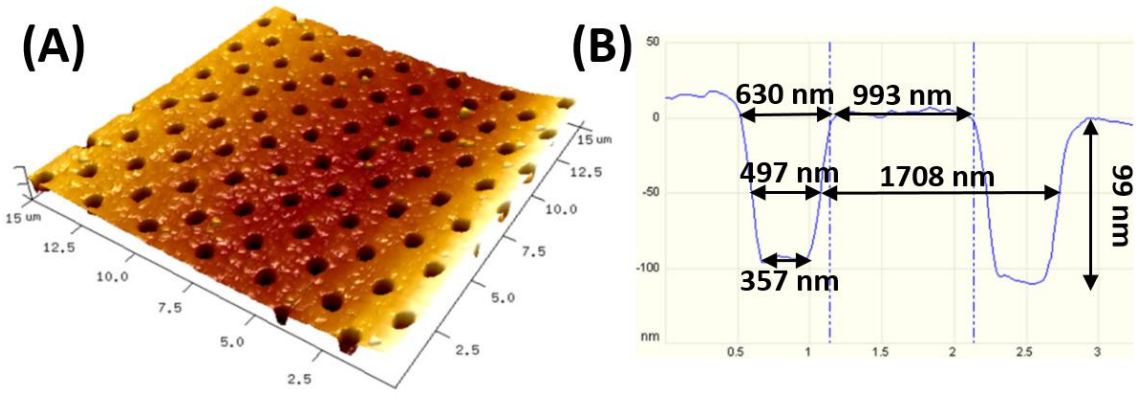

Figure 6.2. AFM Measurements of EOT filter after 70 nm of PCM deposition, and 10 nm oxidation barrier. **(A)** 10x10 µm 3D AFM image. **(B)** AFM cross section showing two apertures, confirming the aperture depth and size to be as designed. Intended EOT structure is 100 nm of gold with an aperture periodicity of 1.7 µm and a diameter of 850 nm.

Figure 6.3 shows the measured transmission of the previously discussed filter device, and compares this to simulations. Dimensions obtained via AFM were used in the simulations for a more appropriate comparison. For the bare metal EOT filter agreement between simulations and experiments was good for both spectral location (2.54 µm versus 2.60 µm), and transmission amplitude (62.1% versus 61.5%). For the amorphous GST225 case, agreement was less close, but still relatively good. Comparing simulations to experiments, spectral locations were 3.47 µm and 3.64 µm respectively, and transmission amplitudes 73.2% and 67.9%. However, there was significant discrepancy regarding quality factor. Simulations predicted a quality factor for the bare metal of 28.5, but only 8.8 was achieved experimentally. For the amorphous GST case the predicted quality factor was 6.3, with 3.3 experimentally achieved. Aside from general fabrication defects, these deviations between experiment and simulation are likely due the aperture slanting and PCM deposition onto the sidewalls not being included in simulations.

After crystallisation, a shift in transmission peak position did occur, as predicted, but the transmission amplitude dropped far below that predicted by simulations. The reasons for the greater (cf. simulations) drop in transmission for the crystalline phase are not entirely clear, but XRD measurements revealed that after crystallisation this device had considerable mixing of GST225 and gold (with in fact the formation of Te-Au compounds). This mixing disrupts the metal-

dielectric interface required to support plasmons, as well as changing the properties of the GST, and so most likely plays a major role in the reduced transmission peak.

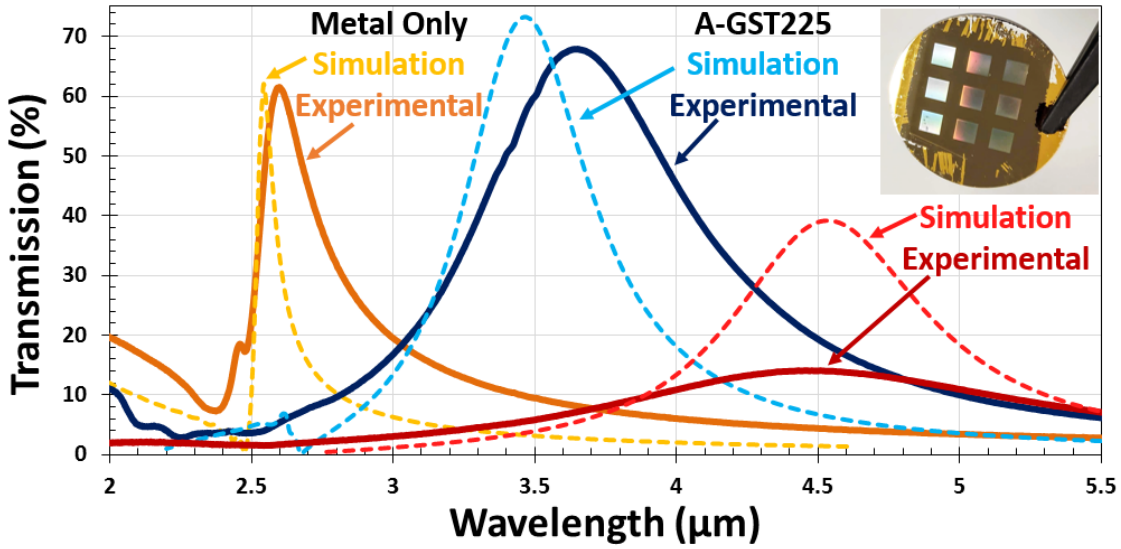

Figure 6.3. Transmission of EOT filter fabricated using e-beam lithography and lift-off, (solid darker curves) compared to simulations (dashed lighter curves). **Inset:** is a photograph of the fabricated device, with nine 3x3 mm devices on a single 1mm thick CaF2 substrate. EOT structure is 100 nm of gold with an aperture periodicity of 1.7 µm and a diameter of 850 nm. PCM is 70 nm of GST225. Crystallisation conducted at 260 C^{o} for 15 minutes.

After the discovery of GST225 and gold mixing, all subsequent devices had 10 nm of SiO_2 deposited as a barrier layer both above and below the GST. However, reliably coating the aperture side walls proved challenging and crystalline performance was not greatly improved. This is discussed in the future work section (7.2).

6.2 APPLICATIONS FOR BAND-PASS FILTERS

This section discusses applications for the filters designed in this work. Specifically multispectral imaging, chemical sensing, and displays (both visible and IR). Significant computational modelling results are presented to evaluate the performance and viability of each potential application.

6.2.1 Multispectral Imaging

A typical colour image contains information for three spectral bands, red, green, and blue. A multispectral image takes this a step further, increasing the number of spectral bands and usually covering a large spectral range.

The filters designed in this work could be well suited to this kind of imaging. Multispectral imaging systems typically focus on a single atmospheric transmission band per detector. These atmospheric transmission bands are shown in Figure 6.4, labelled SWIR (short-wave infrared), MWIR (mid-wave infrared), LWIR (long-wave infrared). A different filter device and corresponding design would be needed for each of these three infrared atmospheric transmission bands.

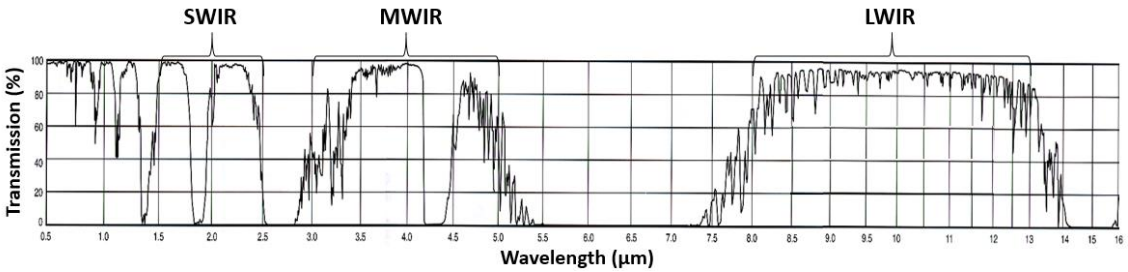

Figure 6.4. Atmospheric transmission from 0.5 to 16 µm through a 1 km horizontal air path at 15 °C, 101 kPa, and 46% relative humidity. Adapted from [174].

To produce Multispectral images, a filter would be placed in the optical path between a scene and a high-speed, broadband, monochrome camera, as shown in Figure 6.5A. This camera would be sensitive in the operating range of the filter. The general principle of operation would then be that images are taken by the camera, and each would correspond to a particular filter response, see Figure 6.5B and 6.5C.

There are two approaches to tuning (crystallising) the filter; either the filter is tuned in discrete steps, with an image taken for each step, or the filter is continuously tuned, and as many images as possible would be taken during this process. The discrete approach has some major advantages. Firstly, calibration of the filter would be much easier, as it can be placed into a spectrometer after each partial-crystallisation step to evaluate the new spectral response. Secondly, the filter can be allowed to cool before an image is taken, thereby mitigating any background IR noise generated by the filter itself. However, discrete crystallisation would result in substantially fewer total images (compared to continuous tuning) and therefore a reduced final spectral resolution.

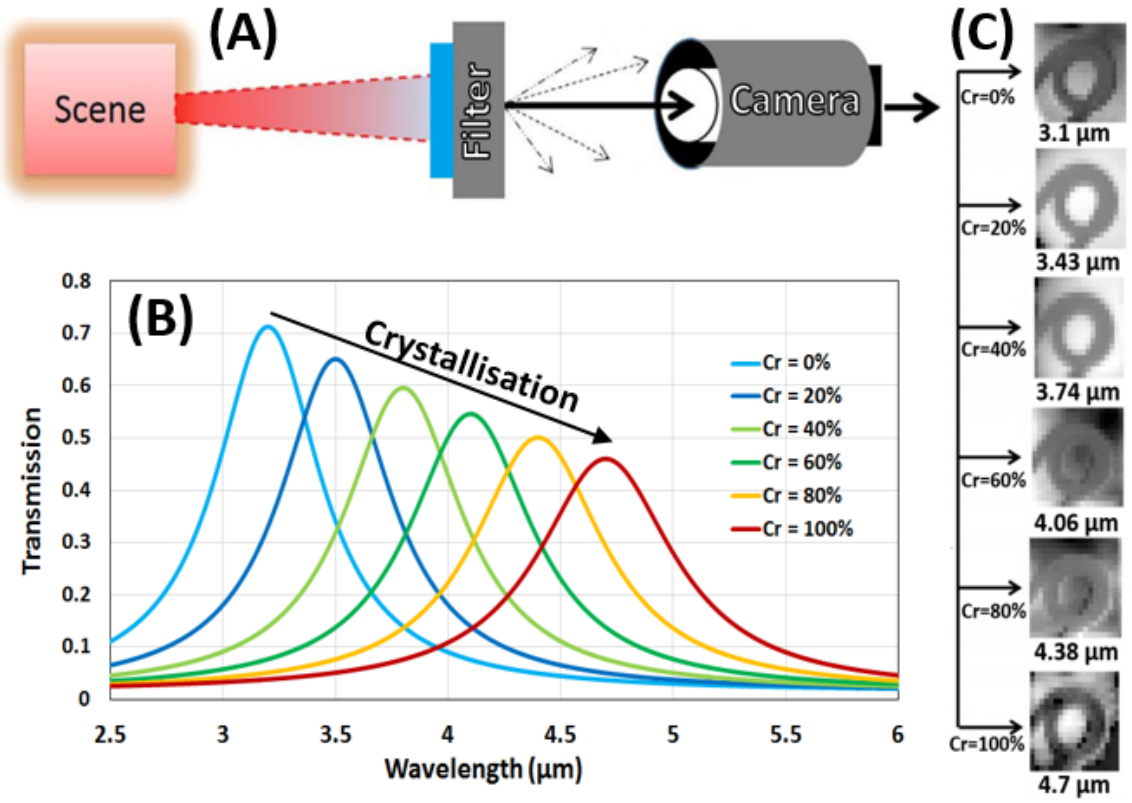

Figure 6.5. An overview of the imaging method given that the camera takes six images during the crystallisation process. **(A)** Diagram of the proposed imaging setup, with the filter in the optical path of a broadband camera. **(B)** PCM band-pass filter responses at evenly spaced crystalline percentages. **(C)** Images taken of a hot iron ring through a number fixed response (non-tuneable) EOT filters (adapted from [175] and used here for illustrative purposes only).

Continuing the example shown Figure 6.5, the raw data from this system would be six intensity values per pixel, and each of these intensity values would have a corresponding filter response curve. Assuming that the filter response is known for all six intensity values, then the overlapping nature of the filter's response can

be exploited to resolve much smaller wavelength intervals than might be expected given the Q-factor of each individual peak. This could be achieved, for example, by using a weighted linear combination of all of the overlapping responses [175]. This is analogous to the operation of a human eye, in which three colour cones with overlapping spectral sensitivities (see Figure 6.6) can resolve approximately a million distinct colours [176].

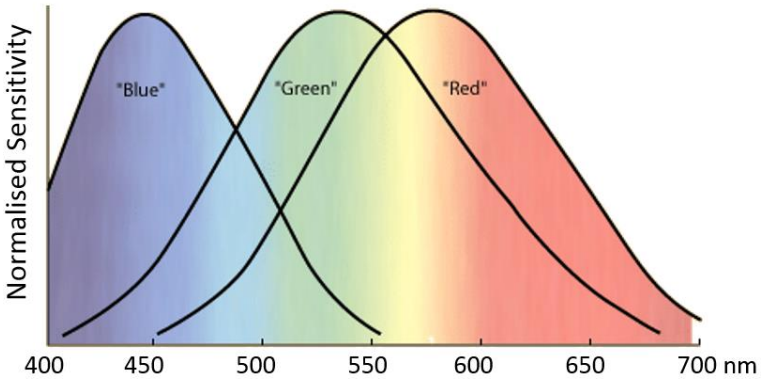

Figure 6.6. Response of the three colour cones within a normal human eye. Note the three overlapping nature of the colour cones. Adapted from [177].

For many applications (such as imaging a distant scene) infrared detectors are often starved of photons, and so the transmission percentage for the higher crystalline fractions may be lower than desired. The transmission can be increased, for the same spectral range, by enlarging the apertures or by thinning the metal, which broadens the peaks and increases unwanted stop-band signal respectively. However, these drawbacks can be somewhat compensated for by taking additional images. This is because the resolution of the reproduced spectra after post processing is dependent upon not only the Q-factor of the filter's transmission peaks, but also how many total data points there are available. If the high-speed infrared camera employed has a framerate of one thousand images per second at full resolution, then if 10 images were to be taken per crystallisation cycle that would necessitate a crystallisation cycle take 10 milliseconds. This crystallisation time is slow for most PCM alloys, and as such much lower than usual crystallisation temperatures would be needed.

For the case of continuous filter tuning, additional thought must be given to characterising the filters response (so as to match camera frames and crystallisation state), and to mitigate unwanted thermal noise. The goal of

characterising the filter as it tunes is to have a spectral response curve available as a function of time. This characterisation is particularly challenging because crystallisation does not occur uniformly over time. Instead the majority of crystallisation occurs over a small proportion of the total crystallisation time; this means that the response cannot simply be extrapolated from a partially crystalline filter. FTIRs also do not possess the speed to measure such a filter in real-time as it tunes. Solutions to this problem are discussed in the future works section 7.2.

Another challenge will be mitigating infrared emissions from the filter itself during the crystallisation process (as this requires heat). This means care must be taken when selecting an appropriate crystallisation temperature, so as not to produce high background infrared noise levels in the desired detection range. The crystallisation rate will be relatively slow (millisecond range) in order to match with a typical high-speed IR camera; this allows for relatively low crystallisation temperatures to be used. Figure 6.7 shows the peak black body emission wavelength for a range of temperatures; also included are the temperatures ranges which would be most suitable for switching each type of filter. Suitability of a temperature was determined by the amplitude of thermal emission (due to crystallisation at that temperature) within the operating wavelength of each filter type.

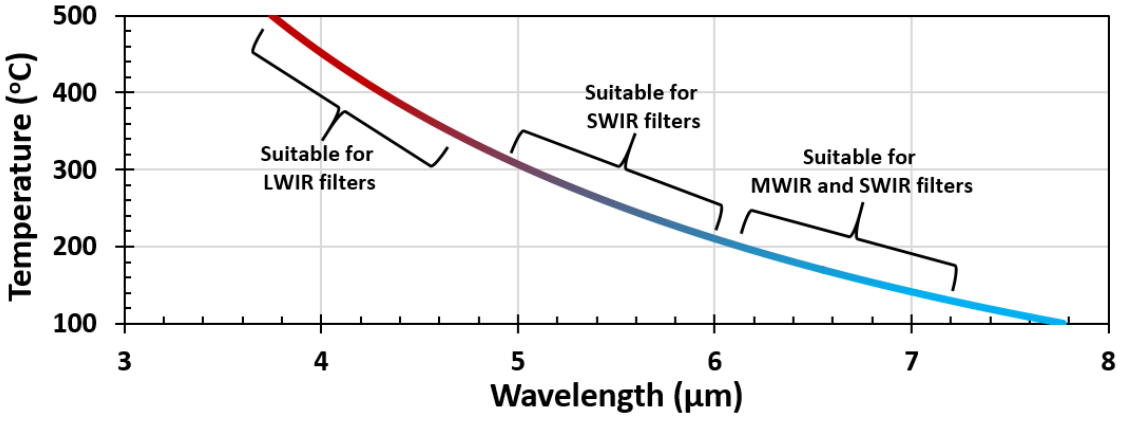

Figure 6.7. Peak black body emission wavelength vs. temperature. Calculated using Wien's Displacement Law. Also shown are the suitable temperature ranges for tuning filters designed for each atmospheric transmission window.

6.2.2 Chemical Sensing

There are several optical approaches to identifying the concentration of an analyte within a solution [104]. The approach proposed here identifies the analyte concentration by measuring absorption at specific wavelengths. A solution containing the analyte would be poured onto a phase-change EOT array (entering the apertures), and light would be shone through the coated array and into a broadband photodiode, as shown in Figure 6.8A. The designed filters have a high quality factor transmission peak located to spectrally coincide with the analyte's strongest absorption peak. The filter can then be tuned to a nearby wavelength which is unaffected by the analyte, but equally absorbed by the solvent see Figure 6.8B. A second transmission measurement can then be made, and the difference between them will be due to the presence of the analyte. This approach is therefore self-referencing, and able to compensate for any changes in detector or source performance due to any reason.

This kind of device is also particularly amenable to miniaturisation, and could be a suitable component in a lab-on-chip device. A phase-change EOT filter was designed to fulfil this role, with the performance benefiting significantly from the relatively small required spectral tuning range (and therefore small PCM volume) required. This filter was designed using 150 nm of gold, with an aperture periodicity of 6.2 μm, and an aperture diameter of 2.48 μm (40% of period), and 30 nm of GST326.

If the analyte of interest is present within the solution then the high field enhancement within the apertures (see Figure 6.8C) will further enhance absorption and therefore reduce transmission. This field enhancement only occurs at the filter's transmission wavelength. This combination of field enhancement and transmission should improve both the wavelength selectivity and absorption sensitivity of the sensor. This approach could provide a compact and low-cost method of detecting the concentration of a specific compound within solution. Sensor designs in this thesis have focused on detecting glucose in an aqueous solution by detecting absorption at around 9.6 μm. This absorption peak is due to the vibrational modes of carbon-oxygen, and carbon-carbon bonds.

Transmissive detection of glucose via absorption is particularly attractive as it offers a route to non-invasively detect blood sugar concentrations in humans.

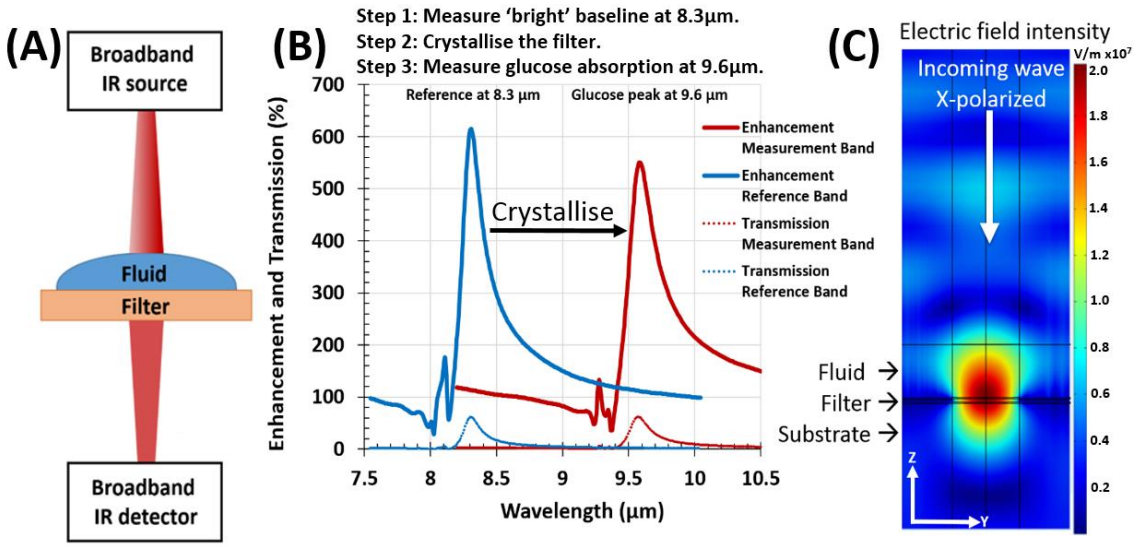

Figure 6.8. Overview of chemical sensing method. **Left:** Electric field enhancement within the holes compared to E-field strength far above them as function of wavelength, also included is the transmission spectra through the filter. **Centre:** Image of simulated electric field intensity at resonance, showing an approximately order of magnitude field enhancement within the holes. **Right:** Illustrative image of proposed sensing setup.

X10^7 Several devices were fabricated for this application, and experimental attempts to measure glucose concentrations were made by collaborators at the University of Cambridge (preliminary results indicated that the quality factor of the devices was insufficient to accurately determine even the presence of glucose).

6.2.3 Infrared Display

Infrared displays are much like visual displays, but typically aim to recreate a thermal emission spectrum at each pixel rather than a visible colour. They have a handful of niche applications, such as training/testing control/defence systems on simulated scenes. However, they are currently quite primitive and typically use arrays of micro-resistors, with each resistor acting as a pixel. An electrical current is passed through each resistor corresponding to the desired temperature, and therefore desired infrared emission. These micro-resistors are slow to switch, provide a poor spatial resolution, and because they emit via black-body radiation, the shape of the infrared spectra they can emit is limited.

The EOT-PCM filters designed in this thesis could be used to create infrared displays. The general principle involves a broadband backlight, and then the desired wavelength can be selected by tuning the filter. However, this approach cannot control transmission intensity, only wavelength. Both wavelength and intensity could however be selected by arranging two filters in series, as shown in Figure 6.9A, and as described in sub-section 5.1.2.4. These filters would have a spin-coated transparent spacer lay between them, and each filter would have a slightly different design. The top filter (closest to backlight) would have a relatively broad and high transmission peak, while the bottom filter would have lower transmission but higher quality factor. The spectral location of the bottom filter would determine the emitted wavelength of the display. The spectral mismatch between the top and bottom filters would determine the transmission intensity. This arrangement was chosen because it enables transmission to be more accurately selected due to the shallower slopes of the top filters transmission peaks. An example of the transmission produced by the two filters in this arrangement is shown in Figure 6.9B. This assumes that six repeatably accessible crystallisation states for each filter are possible.

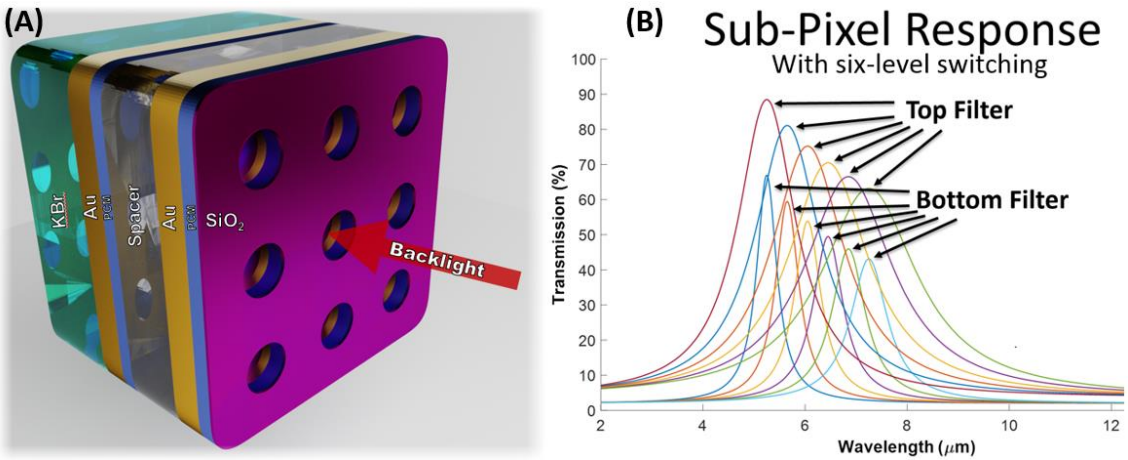

Figure 6.9. (A) Rendered image of dual-layer filter structure for display applications. **(B)** Response of both filters layers assuming six crystalline states can be reliably accessed. Curves are for illustrative purposes, and are not direct simulation results.

A very large spectral range could be covered by building each pixel from a number of sub-pixels. These sub-pixels would each have a different spectral range. This sub-pixilation would be possible through differences in only the

periodicity and aperture diameter of the EOT structure, without the need to alter material layer thicknesses.

Such an IR display was designed, with a pixel comprising nine sub-pixels, with the assumption that each sub-pixel can reliably access six distinct crystalline states. Figure 6.10 shows the transmission for the nine sub-pixels. Each sub-pixel has a partially overlapping spectral response with its neighbours, and despite each pixel being formed from nine sub-pixels, the spatial resolution could still far exceed that of micro-resistors, with 0.09 mm^2 (7167 PPI) being a reasonable super-pixel size.

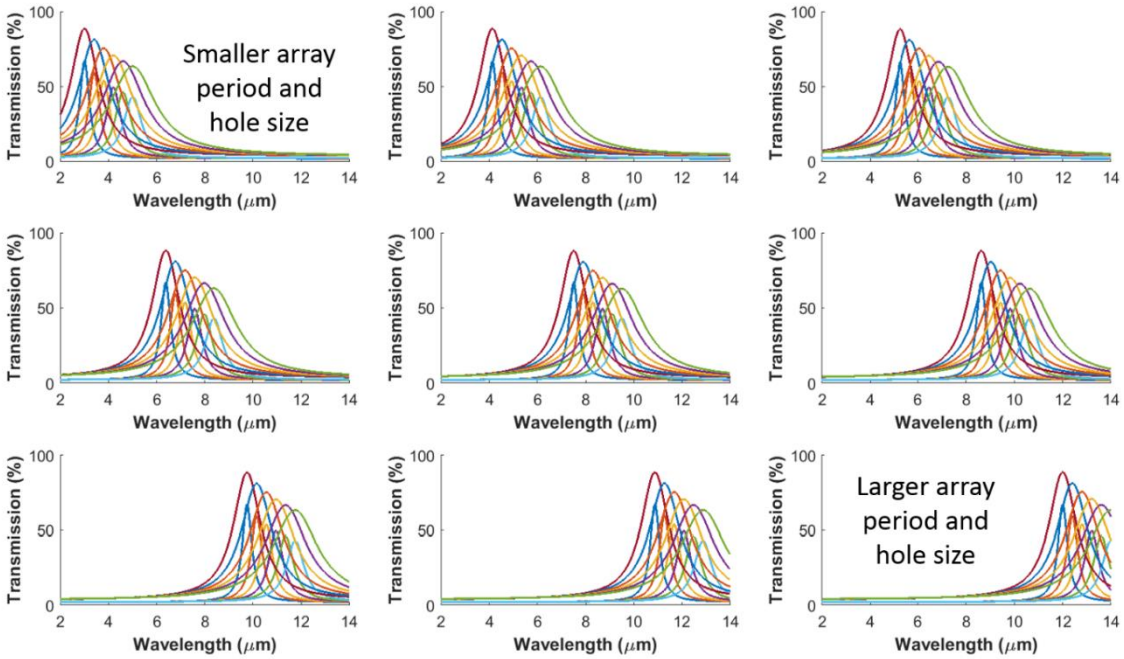

Figure 6.10. Response for nine different filter geometries covering most of the thermal emission range. Shown here are not direct simulation results. A Lorentz distribution was fit to several simulation results over the displays operational range. This fitting was used to produce the majority of curves shown here.

By selecting an appropriate crystalline state for each filter of each sub-pixel it is in principle possible to create almost any arbitrary thermal spectrum, with just over 10^{14} possible combinations from just six crystalline levels. As an example, Figure 6.11A shows an attempt to maximise transmission at both 4 and 12 μm, with a half transmission at 6 and 10 μm. Shown are the responses for each sub-pixel (series combination of both top and bottom filter), and Figure 6.11B shows the combined response of the entire ‘super-pixel’.

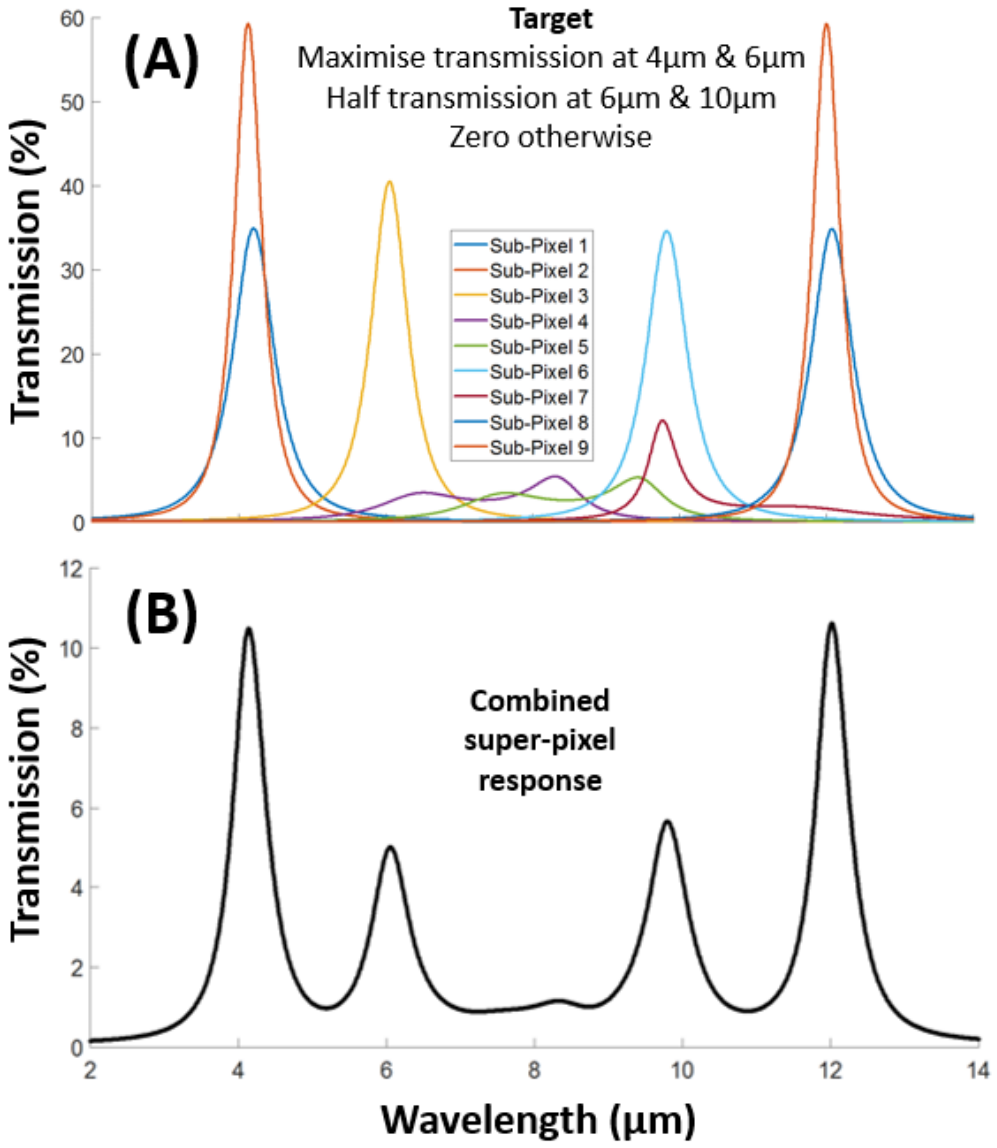

Figure 6.11. (A) Response of each sub-pixel (combination of both top and bottom filters). Crystallisation states have been selected to maximise transmission at both 4 and 12 microns, with half transmission at 6 and 10 microns. **(B)** Combined response of all nine sub-pixels. Peak transmission is 11%.

This approach to creating an IR display is not without its drawbacks. Firstly, the peak transmission when all sub-pixels are combined is quite low; this would require a powerful IR backlight. This backlight would be power hungry and also warm the filters making re-amorphisation slightly more challenging. Another issue is the relatively high reflectivity of EOT based filters (refer to section 5.1). This would require that the displays be at least somewhat isolated from thermal background noise. The final drawback concerns switching the PCM layer. The phase-change process is thermally driven, and so the act of tuning a pixel would

itself produce a brief unwanted burst of IR emission, which would interfere with the IR 'colour' quality. Like the filters for multispectral imaging, this issue could be somewhat mitigated by carefully selecting the temperatures used for switching.

6.2.4 Visible Display

Displays using phase-change materials have experienced increasing interest, primarily thanks to their non-volatile nature and low energy requirements. The originally proposed PCM displays employed a cavity containing GST225, as shown in Figure 6.12A [178]. This concept has been spun out into Bodle Technologies Ltd. A more complex display which makes use of metasurface perfect absorbers has recently been reported, which produces subtractive colour, shown in Figure 6.12B [179].

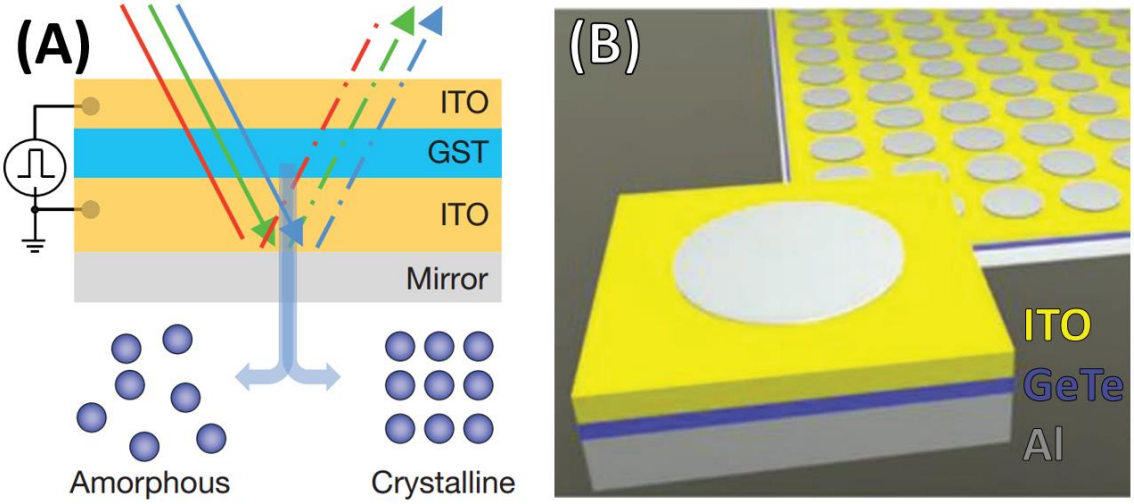

Figure 6.12. Display device diagrams for two displays which use a PCM as the active switching material. **(A)** shows the originally proposed PCM display, operating in reflection (this structure without the mirror also works in transmission, but poorly). The colour of each pixel is determined by the thickness of the bottom ITO layer. Adapted from [178]. **(B)** shows a metasurface perfect absorber display to produce subtractive colour in reflection. Adapted from [179].

Both of the previously described displays struggle to produce a good OFF state (i.e. pure white or black). Furthermore, they only work well in reflection, primarily due to the high visible absorption of the PCMs available during their development. Now, thanks to the characterisation of GLS (refer to section 4.3) this particular limitation is removed. As such a number of phase-change EOT based displays have been designed in this thesis which incorporate GLS.

The visible display designed here has a similar structure to that shown in Figure 6.9, with multiple EOT filters placed in series. The key difference here is that the spectral location (colour) is not determined by the crystallisation-state of the filter. Instead, the crystallisation fraction determines the transmission amplitude by exploiting the high contrast in losses between GLS phases; this absorption is further amplified by the field enhancement within the apertures. The colour is fixed, and determined by the EOT filter structure. Three pixels (red, green and blue) would therefore be required to cover the entire visible spectrum for a full colour pixel.

Shown in Figure 6.13 is the simulated performance of two pixels, both designed to produce red light, (transmission and reflection as a percentage of backlight and ambient intensity respectively). One pixel has a double filter layer configuration, and the other a triple layer configuration. The curves are coloured based upon chromaticity simulations to show how a human eye would perceive this device. The particular EOT structure used for this pixel was chosen with a multi-layer filter in mind, and could therefore favour high transmission over quality factor (aperture diameter is 65% of periodicity). The double layer design produces an RGB colour of RGB 255,79,66, and the triple layer can create flawless red, RGB 255,0,0. The OFF state (fully crystalline GLS) transmission is well below 1% resulting in contrast ratios of 119:1 (double layer) and 2009:1 (triple layer) respectively. In practice, ambient light reflection will factor into how dark the OFF state is perceived. This ambient reflection is both low (≈8%) and almost monochrome (RGB 169,254,255) and so shouldn’t significantly affect colour reproduction.

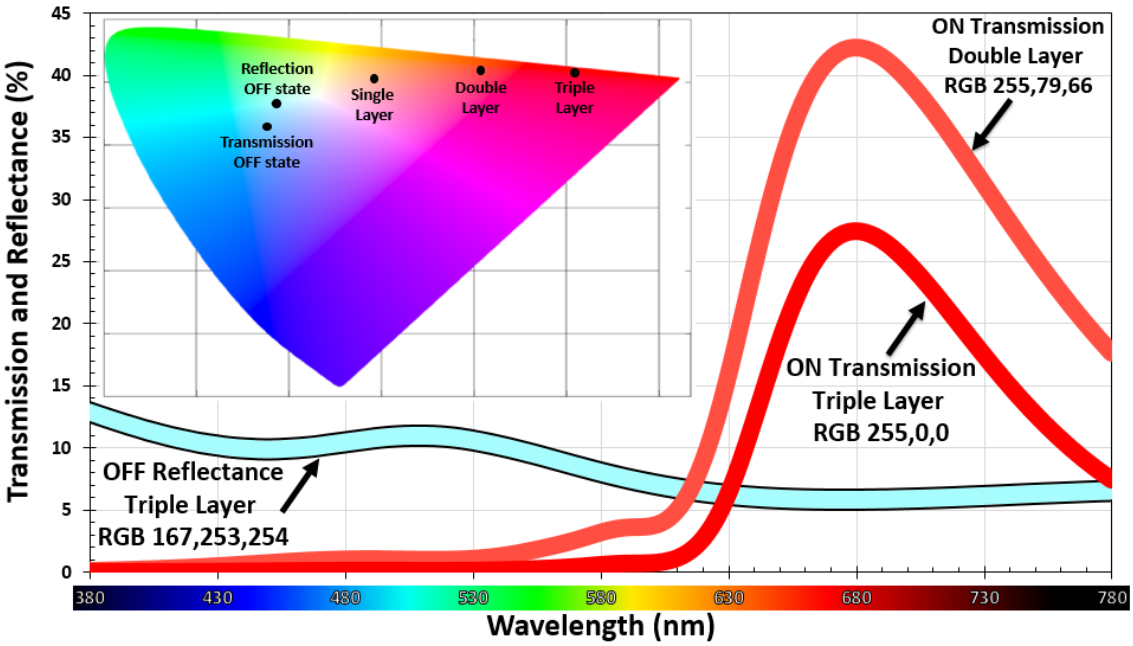

Figure 6.13. Transmission of two red pixels when they are ON, (GLS is amorphous). One pixel is two filters in series (double layer), the other is three in series (triple layer. Also shown is the reflectance from the first layer when the GLS is crystalline (OFF) state. The lines are coloured based upon the colour that a human eye would perceive calculated from the transmission & reflection of the pixel. OFF transmission is not shown as it is near 0. **Inset:** Colour of pixels as located on the CIELUV 1976 chromaticity diagram. EOT structure is made on SiO_2 substrate in 80 nm of aluminium with an aperture spacing of 150 nm and an aperture diameter of 98 nm (65% of period), with 60 nm of GLS capped with 10 nm of SiO_2.

Switching could be achieved by passing current through the metallic layer of the device. Electro-thermal simulations (shown in Figure 6.14) suggest each unit cell of each filter layer could be re-amorphized using a 100 ns 18 mA pulse at 7.4 mV, for 13 pJ. This would raise the centre of the GLS volume to 851 °C (melt is 829.3 °C), the GLS would then cool below the onset of crystallisation temperature (679.2 °C) in just 39.6 ns. These rapid cooling rates are easily sufficient to solidify the GLS into the amorphous phase with minimal crystallite formation.

For example, an augmented reality contact lens using this technology with a display area of 5x5 mm would require 1.11 billion EOT apertures. This would result in an energy consumption of 14.4 Joules to re-amorphise every pixel. This represents a significant energy consumption, despite the small display area; therefore this technology would best suit applications in which pixels are seldom updated, a few of which are discussed later.

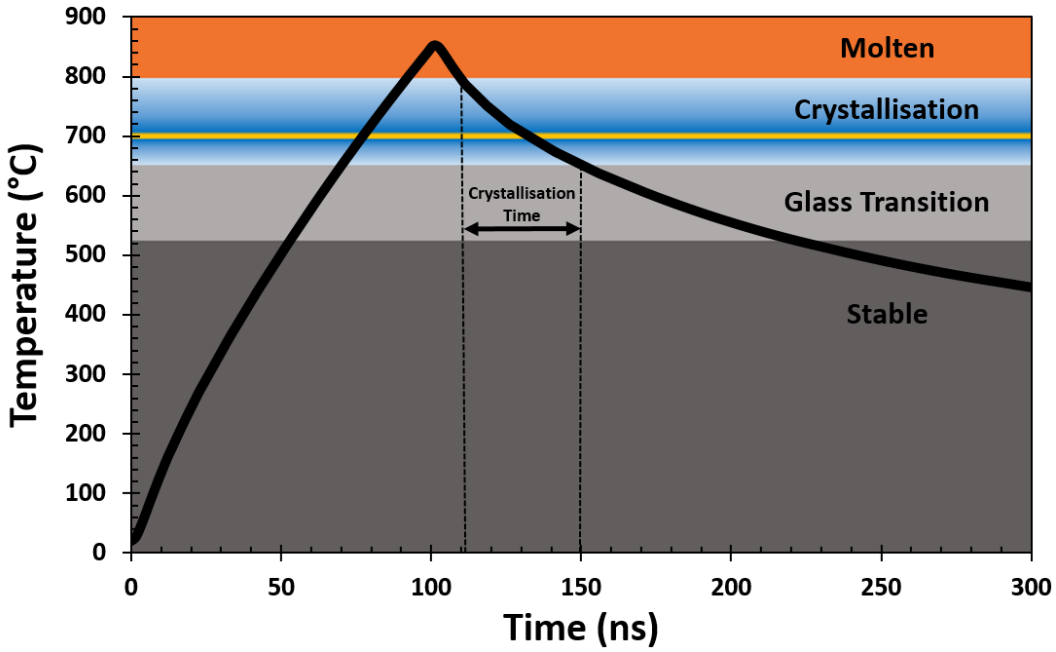

Figure 6.14. Simulated temperature at the centre of the GLS volume within an aperture of the display device (described in Figure 6.13) following a 100 ns electrical pulse. The plot background is coloured according to the thermal state of the GLS at each temperature.

Because each filter layer within the display is just 140 nm thick (excluding substrate), this display is therefore a kind of reconfigurable thin-film coating to dynamically control transmission. As such this device could be fabricated onto flexible substrates, lenses, windows, or other light sources. Each unit cell has a periodicity of just 150 nm, and so producing pixel sizes of a few microns would be possible if such a super-resolution is desired.

There is however one major drawback to this device, in that the ON state reflection is relatively high. Therefore, for comparable backlight and ambient illumination intensity this display would appear pale and washed out. Mitigating this problem would require that the display have a powerful backlight, or is the primary source of illumination in an otherwise darkened space. As such this kind of display could not compete as a general purpose display with matured technologies like LCD and AMOLED. However, there are some roles this display may fit well. Thanks to the non-volatility of GLS, one application could be as reconfigurable ‘stain glass’ windows using sunlight as a backlight, and therefore being the primary source of illumination for the space. Or alternatively as message or information boards in spaces where illumination is controllable, such as an underground train.

6.3 ALTERNATIVE NON-EOT DISPLAY DEVICES

The previous discussions used the tuneable filters developed previously in this thesis to create infrared and visible displays using a backlight. This section discusses two alternative display devices, both of which also include GLS to provide switchability. The first is a type of metal-insulator-metal 'perfect' absorber which operates in reflection, and produces subtractive colour. The other device is fully dielectric, and produces subtractive colour in transmission, and additive colour in reflection.

6.3.1 Perfect Absorber Subtractive Displays

Perfect absorbers have been applied to display devices previously [106,180], and because they operate in reflection, they do not necessarily require a low-loss PCM. They can be switched using micro-heaters (as discussed in sub-section 2.2.2.1), or this can be achieved optically [181]. The absorber display device designed in this work is similar in structure to that previously reported, but operates in a different way (uses GLS contrast in losses rather than GeTe's ability to switch between dielectric and metallic). GLS also has the advantage in that it is relatively trivial to switch compared to other PCMs. Figure 6.15 shows the structure of the designed GLS-based perfect absorber, in which circular metallic (aluminium) patches are formed in an array on top of a GLS layer, which sits upon a metallic (aluminium) mirror. This device supports a resonant condition when the GLS is amorphous. When crystallised the refractive index remains almost unchanged (in the visible), meaning the resonant condition is still present. However, the large increase in optical losses strongly attenuates this resonance, causing the reflection to be relatively flat.

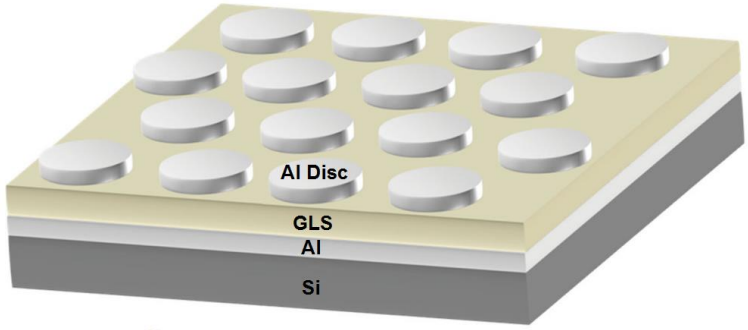

Figure 6.15. Diagram showing the device structure of the CYM absorber display. Barrier layers produced by aluminium oxidation are not included. Adapted from [18].

Figure 6.16 shows the reflectance of the GLS perfect absorber for both the fully amorphous (ON) and crystalline (OFF) states of the GLS. This particular display was optimised to produce cyan, in which (ideally) all red is subtracted from the light spectra. The amorphous 'ON' performance of the device designed here is excellent, producing near-perfect cyan. When switched 'OFF' the device is designed to produce white, and nearly achieves this, instead producing a very pale blue.

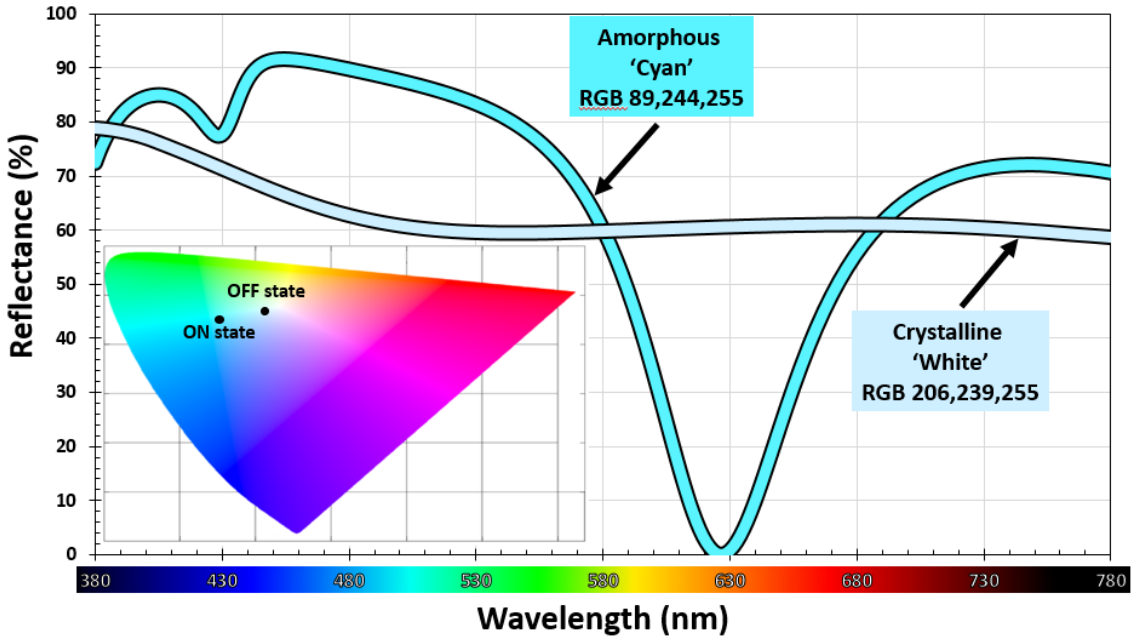

Figure 6.16. Reflectance of a perfect absorber pixel designed to generate cyan in reflection when the GLS is amorphous. When the GLS is crystalline reflectance is near-white. Transmission is <<1 for both ON and OFF states. **Inset:** Colour of pixel in ON and OFF states as located on the CIELUV 1976 chromaticity diagram. Device uses 60 nm of GLS with a patch diameter of 200 nm and a periodicity of 250 nm.

Similar devices to that reported above were fabricated during the work of this thesis, and the colour they produced is shown in Figure 6.17. These devices were selectively crystallised to form an image of a warning sign. (A) shows the simulated image, and (B) is a reproduced image using colours extracted by measuring the reflectivity of a fabricated display device. (C) shows a device which has been selectively crystallised using a Raman system set to high power with a motorised stage. Inconsistencies in crystallisation and imperfections in fabrication are evident, but this device demonstrates that the principle of perfect absorber based displays is sound.

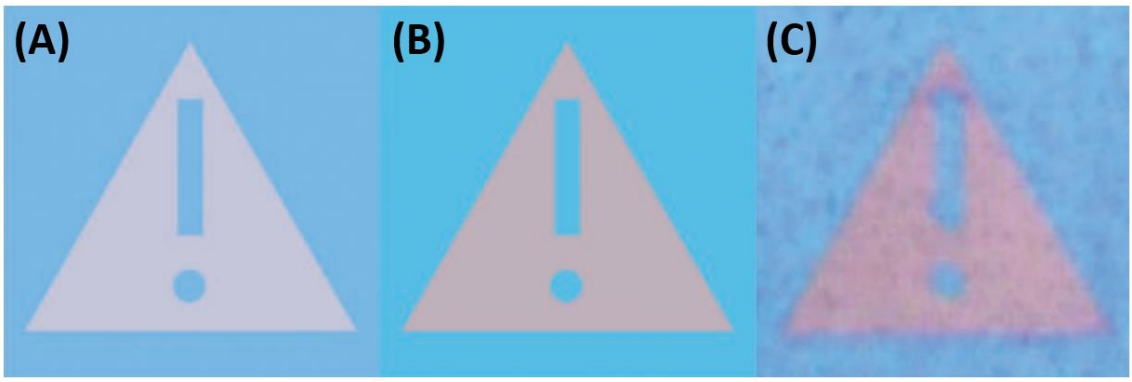

Figure 6.17. Shows a warning sign created using cyan pixels of a previously designed perfect absorber display using GeTe. The central triangle being is the OFF white state, and otherwise the sign is in the fully ON colour state. **(A)** uses simulated reflection spectra **(B)** uses colour extracted from measuring reflectivity spectra of a fabricated device. **(C)** is a microscope image of a fabricated device which has been selectively crystallised using a Raman system operating at high power. Reprinted from [179].

The spacing between the metallic ground mirror and the arrayed patches is a critical variable in determining the response. However, just by altering the size and spacing of the patches a wide colour gamut can be achieved. This means lithography alone can determine colour. Figure 6.18 shows the produced colours for a range of patch sizes and spacings.

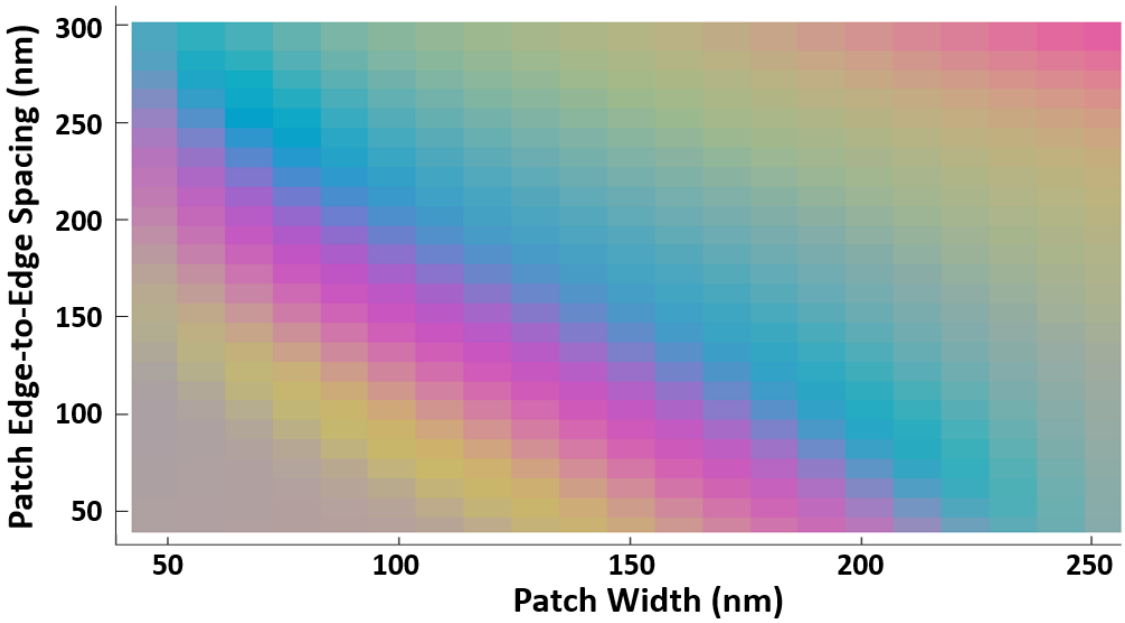

Figure 6.18. Colour map of perfect absorber pixels with 40 nm of amorphous GLS for a variety of patch diameters and spacing. The production of CYM colour (cyan, magenta and yellow) is clearly possible.

Besides e-readers, there are numerous other niche applications in which non-volatile reflective colour displays such as those described here may find great success. In fact, most scenarios in which displayed information is changed infrequently could benefit from significant energy savings by switching to non-volatile reflective technologies. These include information signs, advertisements, retail prices, and much more. Two examples are shown in Figure 6.19.

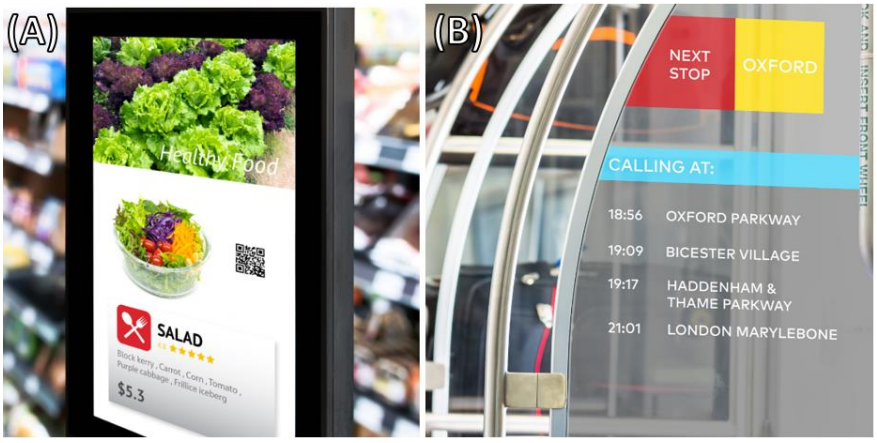

Figure 6.19. (A) Advertisement display in a shopping centre, updated every few minutes. **(B)** Schedule for a train, updated after each stop. Adapted from [182].

6.3.2 All-Dielectric PCM Displays

There is great interest in re-creating the functionality of plasmonic metasurfaces (those that include metals) with devices consisting entirely of dielectric materials [183]. The motivation for this is to avoid the often large Ohmic losses in plasmonic devices, and therefore increase device efficiency.

The display devices designed and reported on here were inspired by a previously reported device [107]. This previously reported device consists of an array of dielectric cylinders, with a small PCM volume included (within the cylinder) at the electric field anti-nodes of a Mie resonance mode, so that the PCM losses could be used to selectively suppress this mode. These devices provide a high degree of control over the transmission and reflection spectra of a surface, and due to the lack of plasmonic resonances have excellent efficiency. For the devices designed in this work GLS was used instead of GST225. This enabled our devices to operate in the visible spectrum, and thanks to the ease of re-amorphising GLS and its low amorphous losses, the entire cylinder could be composed of PCM, see Figure 6.20. With the entire cylinder composed of a PCM, the effects of switching the phase are maximised, along with the optical absorption within the cylinder required to suppress the resonant modes.

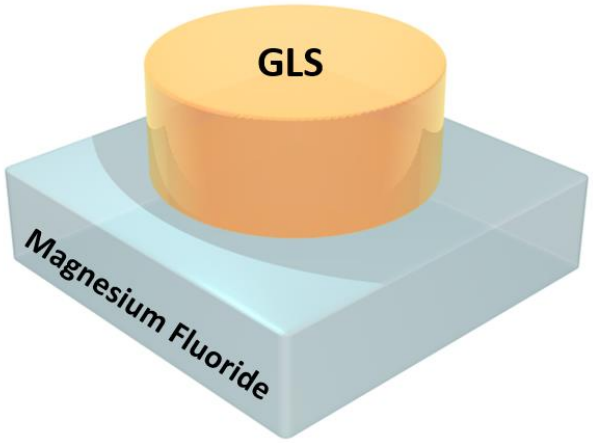

Figure 6.20. Rendered image (Blender) of a single unit cell of the dielectric cylinder structure. In which a cylinder of PCM sits upon a transparent substrate.

This type of device (see Figure 6.20) has two resonant modes when the GLS is amorphous. The mode at shorter wavelengths produces a sharp reflectance peak, and the mode at longer wavelengths produces a broad transmission region.

This is shown for an example designed display device in Figure 6.21, in which (for amorphous GLS) the reflected light is analogous to RGB colour, producing blue in this case. The transmitted spectral region is broad enough to transmit all light except for blue, thereby generating subtractive colour (greenish yellow in this case).

Because the PCM volume in this design is maximised, and the absorption of crystalline GLS is high, it is possible to substantially attenuate all resonance conditions via crystallisation. This results in all light that would have been resonantly reflected to instead be absorbed, producing black in reflection. The transmitted spectrum becomes relatively uniform across the visible spectrum, producing an off-white in transmission.

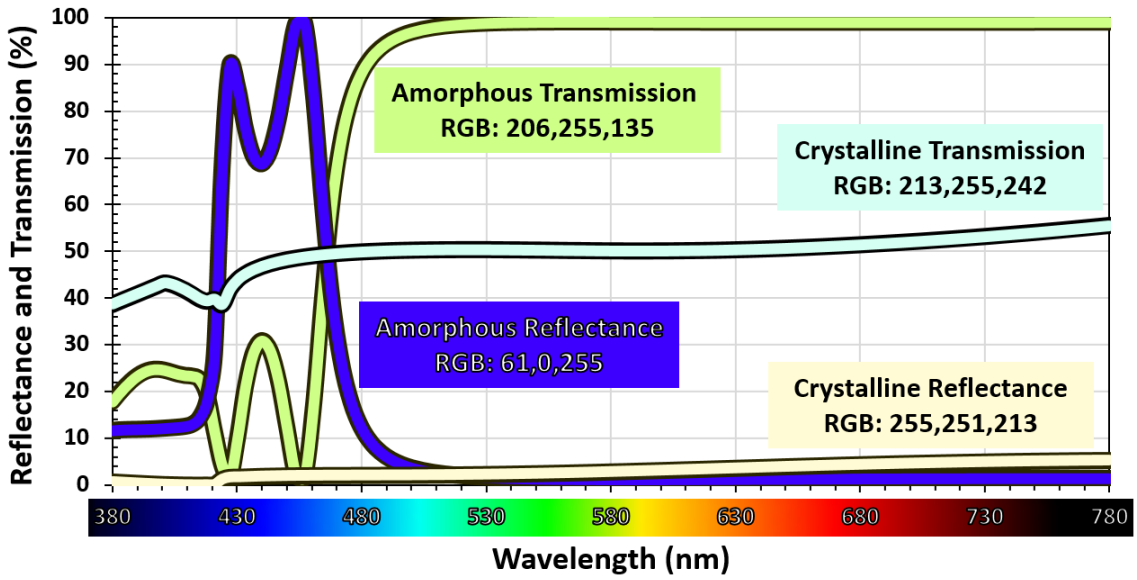

Figure 6.21. Transmission and reflectance spectra for a pixel created from cylinders of GLS65:35 in both amorphous and crystalline phases, and shown by the curves is their RBG value. Each curve is coloured depending on what a human eye would perceived based upon the spectra; intensity is not taken into account (e.g. crystalline reflectance would actually appear black). Device structure is GLS cylinders 200 nm in diameter and 140 nm tall, with an edge-to-edge spacing of 110 nm.

There are three critical geometrical parameters that determine the response of this type of device. These are the cylinder height, cylinder radius, and cylinder spacing. Figure 6.22 shows the colours produced when the cylinder radius is fixed, and the height and spacing are allowed to vary; colour is shown in both transmission and reflection for both amorphous and crystalline GLS phases. It's clear that when amorphous, vivid colours are produced for a wide variety of

geometrical parameters, especially in reflection, which has a superb gamut. When crystallised, the display's colour washes out, and the intensity drops, producing off-whites.

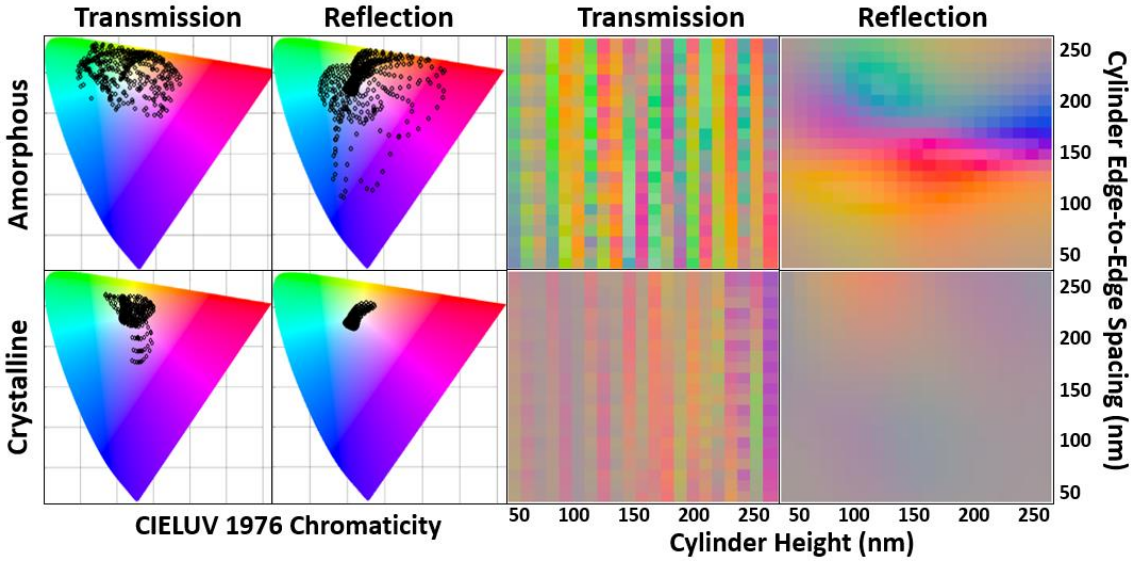

Figure 6.22. Colour gamut for a wide variety of GLS cylinder heights (x axis) and spacing (y axis). The left images show the gamut on the CIELUV chromaticity map. The right images show the colour based on device geometry. Both transmission and reflection are shown for every geometrical combination, and for both amorphous (top row) and amorphous (bottom row) phases. Cylinder diameter is fixed at 280 nm.

Practical switching of this device would require that the cylinders be encapsulated with a thin barrier layer to prevent deformation during re-amorphisation. Switching could then be achieved via laser excitation or, more ambitiously, by incorporating transparent micro-heaters below the structure [168]. This would result in a non-volatile display capable of producing dichroic colour, with the ability to control the colour and amplitude via PCM crystallisation.

7 FINAL REMARKS

7.1 CONCLUSIONS

The combination of phase-change materials with plasmonic metasurfaces continues to be an important area of research thanks to the ability of PCMs to add high levels of dynamic tunability to a large variety of metasurfaces and metamaterials. The work presented in this thesis contributes towards this field of research by demonstrating novel types of tuneable bandpass optical filters obtainable by combining phase-change materials with EOT supporting metasurfaces.

Included in this thesis was a comprehensive and systematic study of bare metal only EOT filters, including the effects of both geometrical and material parameters on filter characteristics. Typically aperture sizes close to half that of their periodicity provide the best balance of quality factor and transmission, and the metallic thickness should ideally not exceed a tenth of the operational wavelength. This was followed up by an investigation of how to best include phase-change materials, and an evaluation of filter performance for a variety of approaches, whilst also considering fabrication complexity. It was found that including the PCM directly into the EOT structure's apertures was the best route, and that inclusions of PCM anywhere else were not worthwhile due to losses and phase-switching issues, A comprehensive set of design guidelines was then produced by studying how different PCM properties change the behaviour of the EOT effect. The most critical parameters when selecting a PCM are to ensure the PCM is relatively transparent in the filters operational wavelength region, and to maximise the absolute (not percentage) contrast in refractive index.

Furthermore, nine different PCM alloys were rigorously characterised both structurally and optically, with the resulting data used to improve device design and simulation results. These alloys include the high loss-contrast material AIST, the more widely studied GeTe and GST225 alloys, and variants of GST225, namely GST326, and four of selenium doped versions comprising the GSS_xT_y

series, and finally, the novel, visibly transparent PCM GLS. The ability of these materials to effectively transition between phases was also evaluated (an often overlooked but critical property). This was done by developing our own thermal characterisation approach involving the fabrication of micro-heater devices. It was found that a moderate amount of selenium doping dramatically improved the switching characteristics of standard GST. This study ultimately involved the production of a number of sputtering targets, hundreds of samples of various compositions, and the fabrication of numerous micro-heater and EOT devices. Many of the PCMs studied here are still regarded as novel, with incomplete information in literature. The characterisation work undertaken here improves the wealth of PCM properties data available in literature.

Finally, the viability of a number of applications exploiting the EOT effect and/or novel phase-change materials was thoroughly explored, with multispectral imaging and (IR and visible) displays being of greatest interest. Filters were designed for each atmospheric transmission band (1.5 to 2.5 μm, 3 to 5 μm, 7 to 12 μm), and several attempts at fabrication using a variety of methods were performed. Concerning the visible displays, two alternative metasurface device structures including the novel PCM GLS were investigated. All of the designed devices have at least some unusual characteristics which distinguish them from current commercial approaches; in many cases this gives them distinct advantages in certain applications, such as non-volatility, ultra-high refresh rates, and sub-micron thickness.

Chapter 4 explored a selection of nine phase-change materials, and assessed their suitability for a variety of devices and applications. Some of which, like GST225 had been very well studied in literature and provided a good test of our characterisation methods. Other alloys, like GLS, had very little information in literature, and this thesis is the first to report it’s crystalline optical properties. The focus of this study was to accurately calibrate sputtering processes, ensure good elemental compositions of films, induce and confirm crystallisation of the various PCM alloys, and finally to extract their optical properties (n and k). This study added confidence to our materials processing methods, and provided many lab users with accurate materials properties for design work, and the deposition

processes needed to produce the desired properties. Furthermore, the relative switchability (ease of re-amorphisation) of several PCM alloys was studied. This property is vital to consider when designing devices intended for repeated in-situ switching, and is poorly reported on in literature for the majority of PCM alloys. In addition, a novel technique for extracting optical properties (n and k) was developed, capable of producing results comparable to ellipsometry.

Chapter 5 used the experimentally gathered materials properties to conduct a systematic computational study on the behaviour of EOT devices, including those incorporating phase-change materials. This is the first study on such a combination, resulting in tuneable filters. A good understanding of these phase-change EOT filters was gained, and resulting design guidelines were produced. The thermal characteristics of these filters was also studied. It was found that the substrates thermal conductivity (rather than device geometry) plays the greatest role in both switching energy efficiency and the quench rates, (quench rate being a critical parameter that determines to what extent a PCM can be fully re-amorphised). These guidelines allow devices operating in different wavelength regimes and for different applications to be rapidly designed and optimised.

Chapter 6 detailed the experimental attempts to fabricate phase-change EOT filters. The tuneable filter devices performed well, and as predicted by simulations in their pristine (amorphous) state after fabrication. However, attempts to tune the filter devices met with limited success, and this is the priority of future work. Also explored in chapter 6 numerous of applications these filters are well suited for. In some cases the predicted performance of the EOT devices was competitive or superior to current technology. Specifically tuneable filters for multispectral imaging, chemical sensing, and a selection of novel display devices were studied.

In summary, this thesis has shown the potentially strong performance and application viability of phase-change EOT filters, with simulated filter performance implying they could be of great technological use. Solid groundwork for continued study and fabrication of these filters has been laid. The technical challenges encountered in this project leave significant scope for further work, and the path to overcoming many of these difficulties is now clear.

7.2 Future Work

There remains significant scope for future work. The initial focus of this continued research would be in overcoming metal-PCM diffusion issues; this is primarily a fabrication challenge. Once tuneable filter devices can be reliably produced, then proof-of-concept prototypes can be demonstrated, initially with demonstrations of multispectral imaging. The next step would then concern experimentally achieving in-situ electrical switching. While simulations suggest this is possible, there are numerous non-trivial technical challenges to overcome. There are few examples of electrical in-situ switching of nanoscale phase-change devices, and they typically employ relatively small volumes of PCM when compared to the devices in this thesis.

Resolve issues regarding PCM crystallisation within filter devices.

The filter devices fabricated in this thesis work well until PCM crystallisation is attempted. The causes for this were identified to be metal-PCM mixing. Barrier layers do mitigate this issue, however, fabricating EOT structures with an even, unbroken, and thin barrier layer remains a challenge. Diagonal sputtering met with limited success in coating the EOT aperture side walls, and still requires refinement. Alternative metals unlikely to mix or which produce chemically stable oxides will also be tested. Aluminium will be the first metal, as we have found its native oxide layer is sufficient as a diffusion barrier. Although the plasmonic and thermal properties of aluminium are not ideal, we have at least found that the oxide layer prevents structural deformation when the metal is molten.

Experimentally achieve in-situ switching.

Simulations suggest that in-situ switching using the metal EOT structure as an electrical Joule heater is viable, provided appropriate PCM and substrate combinations are used. Once crystallisation is demonstrated with more basic heating methods (hot plate or rapid thermal annealer), then the next step would be to replicate these results in-situ. This will involve fabricating devices with electrical contacts, and sourcing an appropriate impedance matched power supply. The system used for the micro-heater experiments (described in sub-

section 3.5.3) could be modified for this purpose. Crystallisation via Joule heating would be the first step, and can be confirmed using an FTIR to check spectral shift of the filters, and/or XRD measurements. The next challenge will be in re-amorphising a filter device. This requires much greater power and care must be taken to design devices tolerant to the relatively high current densities. This will also require the use of PCMs with a high switchability score, and may even necessitate substrates with a high thermal conductivity like silicon.

Multispectral imaging using phase-change EOT filters

Once the filter devices are working as intended, then multispectral imaging will be the first application practically tested; this is because of its relative simplicity compared to fabricating the proposed display devices.

This will first require the building of an imaging test setup. This setup will broadly involve just three components. Firstly, something to image; the emission of this sample must be well characterised in order to properly calibrate and then evaluate the filters. This sample could simply be a loop of tungsten wire which is Joule heated. The second required component will be optics to collect and collimate light onto the filter, as the performance is heavily impacted by incident angle. The final component required in the setup will be a broadband high-speed IR photodiode.

Once the test setup is completed then the use of discrete crystallisation steps can first be attempted. After each partial crystallisation step the response of the filter can be evaluated in an FTIR, and this information then used in post-processing. Calibration for the continuous tuning would be far more challenging, and would involve placing fixed narrowband filters (with a wavelength somewhere between the amorphous and crystalline response of the filter) between the IR source and the filter. At some time after crystallisation is initiated the photodiode will register a spike in light intensity; this spike will correspond to the fixed filter and EOT filter’s pass-band wavelengths matching, from this crystallisation percentage can be extracted. Doing this for several filters would build a time/crystallisation relationship for a specific filter.

With the filter calibrated it will then be possible to attempt to reproduce the emission spectra of the test sample using the filter and photodiode. This will require the development of post-processing software which is fed the detected light intensity for a number of known filter states, and will then attempt to reproduce the emission spectra of the heated sample.

Infrared and visible displays using phase-change EOT filters

Initially it would be prudent to fabricate single layer filters for display applications as a practical proof-of-concept. If successful then fabrication of multi-layer filters with a polymer spacer can be attempted. This polymer must be carefully chosen so that it is thermally stable once spin-coated (fully crosslinked). The polymer must also be at least as conductive as the substrate, otherwise re-amorphisation will not be possible. However, the displays can initially be crystallised using a hot plate. Testing of the infrared displays would simply involve FTIR measurements, with the FTIR itself effectively providing the backlight. The real challenge will be independently accessing different intermediate crystalline states for each filter layer. This will require additional thermal modelling to understand how the multiple filter layers interact.

The visible display devices are roughly an order of magnitude smaller than those designed for the infrared, as such new fabrication recipes will need developing. Thanks to the use of GLS, the visible displays should be relatively trivial to switch. Initially this concept can be tested using a single layer filter and a light source with a good CRI rating. Later experiments can include double layer filters to verify the superior colour reproduction using a spectrometer.

8 REFERENCES

1. V. L. Kalyani and V. Sharma, "Different types of Optical Filters and their Realistic Application," J. Manag. Eng. Inf. Technol. 2394–8124 (2016).

2. A. Ranzoni and M. A. Cooper, *Micro and Nanotechnology in Vaccine Development - Chapter One - The Growing Influence of Nanotechnology in Our Lives* (2017).

3. VIAVI Solutions, "Optical Filters for LIDAR Systems," White Pap. (2017).

4. H. A. Macleod, *Thin-Film Optical Filters* (2010).

5. N. Yu and F. Capasso, "Flat optics with designer metasurfaces," Nat. Mater. **13**, 139–150 (2014).

6. W. J. Padilla, D. N. Basov, and D. R. Smith, "Negative refractive index metamaterials," Mater. Today **9**, 28–35 (2006).

7. N. I. Landy, S. Sajuyigbe, J. J. Mock, D. R. Smith, and W. J. Padilla, "Perfect metamaterial absorber," Phys. Rev. Lett. **100**, (2008).

8. A. Ourir, S. N. Burokur, and A. De Lustrac, "Electronic beam steering of an active metamaterial-based directive subwavelength cavity," IET Semin. Dig. **2007**, (2007).

9. H. T. Chen, A. J. Taylor, and N. Yu, "A review of metasurfaces: Physics and applications," Reports Prog. Phys. **79**, 76401 (2016).

10. J. Callaway, "Plasma Losses by Fast Electrons in Thin Films," Phys. Rev. **184**, (1956).

11. B. R. D. Maleeha Khan, "Review on Evolution of Frequency Selective," Int. J. Adv. Res. Electr. Electron. Instrum. Eng. **5**, 2816–2822 (2016).

12. Y. N. Zhang, Y. Zhao, and R. Q. Lv, "A review for optical sensors based on photonic crystal cavities," Sensors Actuators, A Phys. **233**, 374–389 (2015).

13. R. S. Anwar, L. Mao, and H. Ning, "Frequency selective surfaces: A review," Appl. Sci. **8**, 1–46 (2018).

14. S. B. Glybovski, S. A. Tretyakov, P. A. Belov, Y. S. Kivshar, and C. R. Simovski, "Metasurfaces : From Microwaves to Visible," 1–87 (2016).

15. I. M. Ehrenberg, S. E. Sarma, and B. Wu, "A three-dimensional self-supporting low loss microwave lens with a negative refractive index," J. Appl. Phys. **112**, 23–27 (2012).

16. C. Körner and Y. Liebold-ribeiro, "A systematic approach to identify cellular auxetic materials," Smart Mater. Struct. **24**, 25013 (n.d.).

17. F. Lemoult, M. Fink, and G. Lerosey, "Acoustic resonators for far-field control of sound on a subwavelength scale," Phys. Rev. Lett. **107**, 1–5 (2011).

18. K. Chen, T. D. Dao, S. Ishii, M. Aono, and T. Nagao, "Infrared Aluminum Metamaterial Perfect Absorbers for Plasmon-Enhanced Infrared Spectroscopy," Adv. Funct. Mater. n/a-n/a (2015).

19. N. B. Kundtz, D. R. Smith, and J. B. Pendry, "Electromagnetic design with transformation optics," Proc. IEEE **99**, 1622–1633 (2011).

20. A. J. Ward and J. B. Pendry, "Refraction and geometry in Maxwell's equations," J. Mod. Opt. **43**, 773–793 (1996).

21. F. Sun, B. Zheng, H. Chen, W. Jiang, S. Guo, Y. Liu, Y. Ma, and S. He, "Transformation Optics: From Classic Theory and Applications to its New Branches," Laser Photonics Rev. **11**, 1–27 (2017).

22. and A. R. S.M. Dhawan, B.M. Gupta, Manmohan Singh, "Metamaterials research: A Scientometric Assessment of Global Publications output during 2007-16 S.M.," DESIDOC J. Libr. Inf. Technol. **37**, 320–327 (2017).

23. J. B. Pendry, D. Schurig, and D. R. Smith, "Controlling Electromagnetic Fields," 0–3 (n.d.).

24. D. Schurig, J. B. Pendry, and D. R. Smith, "Calculation of material properties and ray tracing in transformation media," **14**, 9794–9804 (2006).

25. D. Schurig, J. J. Mock, B. J. Justice, S. A. Cummer, J. B. Pendry, A. F. Starr, and D. R. Smith, "Metamaterial Electromagnetic Cloak at Microwave Frequencies," **11186**, 2004–2007 (2006).

26. H. A. Bethe, "Theory of diffraction by small holes," Phys. Rev. **66**, 163–182 (1944).

27. T. W. Ebbesen, H. J. Lezec, H. F. Ghaemil, T. Thiol, and P. A. Wolff, "Extraordinary optical transmission through sub-wavelength hole arrays," Nature **391**, 667–669 (1998).

28. J. R. Sambles, G. W. Bradbery, and F. Yang, "Optical excitation of surface plasmons: An introduction," Contemp. Phys. **32**, 173–183 (1991).

29. W. L. Barnes, A. Dereux, and T. W. Ebbesen, "Surface plasmon subwavelength optics," Nature **424**, 824–30 (2003).

30. G. Gay, O. Alloschery, B. V. De Lesegno, C. O'Dwyer, J. Weiner, and H. J. Lezec, "The optical response of nanostructured surfaces and the composite diffracted evanescent wave model," Nat. Phys. **2**, 262–267 (2006).

31. Z. Fan, L. Zhan, X. Hu, and Y. Xia, "Critical process of extraordinary optical transmission through periodic subwavelength hole array: Hole-assisted evanescent-field coupling," Opt. Commun. **281**, 5467–5471 (2008).

32. H. Liu and P. Lalanne, "Microscopic theory of the extraordinary optical transmission," Nature **452**, 728–731 (2008).

33. F. Van Beijnum, C. Rétif, C. B. Smiet, H. Liu, P. Lalanne, and M. P. Van Exter, "Quasi-cylindrical wave contribution in experiments on extraordinary optical transmission," Nature **492**, 411–414 (2012).

34. and L. M.-M. By Sergio G. Rodrigo, Fernando de Leo´n-Pe´rez, "Extraordinary Optical Transmission: Fundamentals and Applications," Proc. IEEE **104**, (2016).

35. A. Krishnan, T. Thio, T. J. Kim, H. J. Lezec, T. W. Ebbesen, P. A. Wolff, J. Pendry, L. Martin-Moreno, and F. J. Garcia-Vidal, "Evanescently coupled resonance in surface plasmon enhanced transmission," Opt. Commun. **200**, 1–7 (2001).

36. W.-Y. Jang, Z. Ku, J. Jeon, J. O. Kim, S. J. Lee, J. Park, M. J. Noyola, and A. Urbas,

"Experimental Demonstration of Adaptive Infrared Multispectral Imaging using Plasmonic Filter Array," Sci. Rep. **6**, 34876 (2016).

37. J. A. Hutchison, D. M. O'Carroll, T. Schwartz, C. Genet, and T. W. Ebbesen, "Absorption-induced transparency," Angew. Chemie - Int. Ed. **50**, 2085–2089 (2011).

38. S. G. Rodrigo, F. J. García-Vidal, and L. Martín-Moreno, "Theory of absorption-induced transparency," Phys. Rev. B - Condens. Matter Mater. Phys. **88**, (2013).

39. J. Olkkonen, K. Kataja, and D. G. Howe, "Light transmission through a high index dielectric-filled sub-wavelength hole in a metal film," Opt. Express **13**, 6980 (2005).

40. S. G. Rodrigo, O. Mahboub, A. Degiron, C. Genet, F. J. García-Vidal, L. Martín-Moreno, and T. W. Ebbesen, "Holes with very acute angles: a new paradigm of extraordinary optical transmission through strongly localized modes," Opt. Express **18**, 23691 (2010).

41. K. J. K. Koerkamp, S. Enoch, F. B. Segerink, N. F. van Hulst, and L. Kuipers, "Strong Influence of Hole Shape on Extraordinary Transmission through Periodic Arrays of Subwavelength Holes," Phys. Rev. Lett. **92**, 18–21 (2004).

42. Y. Liang, W. Peng, R. Hu, and H. Zou, "Extraordinary optical transmission based on subwavelength metallic grating with ellipse walls," Opt. Express **21**, 6139 (2013).

43. T. Ishi, J. Fujikata, and K. Ohashi, "Large optical transmission through a single subwavelength hole associated with a sharp-apex grating," Japanese J. Appl. Physics, Part 2 Lett. **44**, (2005).

44. M. J. Lockyear, A. P. Hibbins, J. R. Sambles, and C. R. Lawrence, "Surface-topography-induced enhanced transmission and directivity of microwave radiation through a subwavelength circular metal aperture," Appl. Phys. Lett. **84**, 2040–2042 (2004).

45. Y. Poujet, J. Salvi, and F. I. Baida, "90% Extraordinary optical transmission in the visible range through annular aperture metallic arrays," Opt. Lett. **32**, 2942 (2007).

46. L. Lin and A. Roberts, "Angle-robust resonances in cross-shaped aperture arrays Angle-robust resonances in cross-shaped aperture arrays," Appl. Phys. Lett **061109**, 1–4 (2017).

47. A. Peer and R. Biswas, "Extraordinary optical transmission in nanopatterned ultrathin metal films without holes," Nanoscale **8**, 4657–4666 (2016).

48. A. T. Waterman, "On the positive ionization from certain hot salts, together with some observations of the electrical properties of molybdenite at high temperatures," Yale University (1916).

49. S. R. Ovshinsky, "Reversible Electrical switching phenomena in disordered structures"," Phys. Rev. Lett. **21**, 1450 (1968).

50. H. Satoh, I., Fukushima, Y., Takagi, Y. Azumatani, Y., Hamasaka, "Multi-layered Optical Disk With Track and Layer Identification (U.S. Patent 5,428,597)," (1995).

51. M. Wuttig and N. Yamada, "Phase-change materials for rewriteable data storage," Nat. Mater. **6**, 824–832 (2007).

52. I. S. Kim, S. L. Cho, D. H. Im, E. H. Cho, D. H. Kim, G. H. Oh, D. H. Ahn, S. O. Park, S. W. Nam, J. T. Moon, and C. H. Chung, "High performance PRAM cell scalable to sub-20nm technology with below 4F2 cell size, extendable to DRAM applications," Dig. Tech. Pap. - Symp. VLSI Technol. 203–204 (2010).

53. S. R. E. D. Loke, T. H. Lee, W. J. Wang, L. P. Shi, R. Zhao, Y. C. Yeo, T. C. Chong, "Breaking the Speed Limits of Phase-Change Memory," Science (80-.). **336**, 1566–1569 (2012).

54. J. A. V and J. A. V, "A Cellular Automata Approach for the Simulation and Development of Advanced," (2012).

55. J. L. F. Da Silva, A. Walsh, S. H. Wei, and H. Lee, "Atomistic origins of the phase transition mechanism in Ge 2Sb2Te5," J. Appl. Phys. **106**, (2009).

56. J. E. Boschker and R. Calarco, "Growth of crystalline phase change materials by physical deposition methods," Adv. Phys. X **2**, 675–694 (2017).

57. K. Shportko, S. Kremers, M. Woda, D. Lencer, J. Robertson, and M. Wuttig, "Resonant bonding in crystalline phase-change materials," Nat. Mater. **7**, 653–658 (2008).

58. D. K. Rishabh Gupta, Rohit Raj, "Chalcogenide Glasses : A Review," Int. J. Sci. Technol. **3**, 114–119 (2016).

59. L. Lu, W. Dong, J. K. Behera, L. Chew, and R. E. Simpson, "Inter-diffusion of plasmonic metals and phase change materials," J. Mater. Sci. **54**, 2814–2823 (2019).

60. P. Noé, *Phase Change Memory* (Springer US, 2018).

61. H. Hayat, "A Study of the Scaling and Advanced Functionality Potential of Phase Change Memory Devices," University of Exeter (2016).

62. V. G. Karpov, Y. A. Kryukov, I. V. Karpov, and M. Mitra, "Field-induced nucleation in phase change memory," Phys. Rev. B - Condens. Matter Mater. Phys. **78**, (2008).

63. A. Sebastian, M. Le Gallo, and D. Krebs, "Crystal growth within a phase change memory cell," Nat. Commun. **5**, (2014).

64. H. B. M.J. Kuin, G.F. Zhou, H. Borg, "Crystallization behaviour o f Ge-Sb-Te phase change optical recording materials," Philips Electron. (1998).

65. A. Athmanathan, M. Stanisavljevic, N. Papandreou, H. Pozidis, and E. Eleftheriou, "Multilevel-Cell Phase-Change Memory : A Viable Technology," IEEE J. Emerg. Sel. Top. CIRCUITS Syst. **6**, 87–100 (2016).

66. D. Stroud, "The effective medium approximations : Some recent developments," Superlattices Microstruct. **23**, (1998).

67. C. Ríos, Y. Zhang, S. Deckoff-Jones, H. Li, J. B. Chou, H. Wang, M. Shalaginov, C. Roberts, C. Gonçalves, V. Liberman, T. Gu, J. Kong, K. Richardson, and J. Hu, "Reversible Switching of Optical Phase Change Materials Using Graphene Microheaters," Proc. CLEO, OSA paper SF2H.4 (2019).

68. D. Adler, M. S. Shur, M. Silver, and S. R. Ovshinsky, "Threshold switching in chalcogenide - glass thin films," J. Appl. Phys. **51**, (1980).

69. H. K. Henisch and R. W. Pryor, "On the mechanism of ovonic threshold switching," Solid State Electron. **14**, 765–774, IN1–IN2 (1971).

70. M. C. Cyrille, A. Verdy, G. Navarro, G. Bourgeois, J. Garrione, M. Bernard, C. Sabbione, P. Noe, and E. Nowak, "OTS selector devices: Material engineering for switching performance," ICICDT 2018 - Int. Conf. IC Des. Technol. Proc. 113–116 (2018).

71. A. Manivannan, S. K. Myana, K. Miriyala, S. Sahu, R. Ramadurai, A. Manivannan, K. Myana, K. Miriyala, and S. Sahu, "Low power ovonic threshold switching characteristics of thin GeTe6 films using conductive atomic force microscopy," Appl. Phys. Lett. **105**, 11–16 (2014).

72. M. Nardone, M. Simon, I. V Karpov, V. G. Karpov, M. Nardone, M. Simon, I. V Karpov, and V. G. Karpov, "Electrical conduction in chalcogenide glasses of phase change memory," J. Appl. Phys. **112**, (2012).

73. K. E. Petersen, D. Adler, J. A. Phys, K. E. Petersen, and D. Adler, "Erratum : A model for the on state of amorphous chalcogenide threshold switches," J. Appl. Phys. **50**, (1979).

74. N. Ciocchini, M. Laudato, M. Boniardi, E. Varesi, P. Fantini, A. L. Lacaita, and D. Ielmini, "Bipolar switching in chalcogenide phase change memory," Nat. Publ. Gr. 1–9 (2016).

75. J. O. H. Endrickson, H. A. L. Iang, and R. I. S. Oref, "Electrically actuated phase-change pixels for transmissive and reflective spatial light modulators in the near and mid infrared," Appl. Opt. **54**, 10698–10704 (2015).

76. H. Hayat, "A Study of the Scaling and Advanced Functionality Potential of Phase Change Memory Devices," (2016).

77. J. Von Keitz, J. Feldmann, N. Gruhler, C. Ríos, C. D. Wright, H. Bhaskaran, and W. H. P. Pernice, "Reconfigurable Nanophotonic Cavities with Nonvolatile Response," ACS Photonics **5**, 4644–4649 (2018).

78. N. Farmakidis, N. Youngblood, X. Li, J. Tan, J. L. Swett, Z. Cheng, D. C. Wright, W. H. Pernice, and H. Bhaskaran, "Plasmonic nanogap enhanced phase change devices with dual electrical-optical functionality," (2018).

79. X. Li, N. Youngblood, C. Ríos, Z. Cheng, C. D. Wright, W. H. Pernice, and H. Bhaskaran, "Fast and reliable storage using a 5 bit, nonvolatile photonic memory cell," Optica **6**, 1 (2019).

80. Z. Cheng, C. Ríos, N. Youngblood, C. D. Wright, W. H. P. Pernice, and H. Bhaskaran, "Device-Level Photonic Memories and Logic Applications Using Phase-Change Materials," Adv. Mater. **30**, (2018).

81. J. Feldmann, M. Stegmaier, N. Gruhler, C. Riós, H. Bhaskaran, C. D. Wright, and W. H. P. Pernice, "Calculating with light using a chip-scale all-optical abacus," Nat. Commun. **8**, 1–8 (2017).

82. C. Rios, N. Youngblood, Z. Cheng, M. Le Gallo, W. H. P. Pernice, C. D. Wright, A. Sebastian, and H. Bhaskaran, "Memcomputing on a photonic platform," Submitted **5**, 1–10 (2017).

83. N. Youngblood, C. Ríos, E. Gemo, J. Feldmann, Z. Cheng, A. Baldycheva, W. H. P. Pernice, C. D. Wright, and H. Bhaskaran, "Tunable Volatility of Ge 2 Sb 2 Te 5 in Integrated Photonics," Adv. Funct. Mater. **29**, (2019).

84. H. Bhaskaran, W. H. P. Pernice, Z. Cheng, C. Ríos, and C. D. Wright, "On-chip photonic synapse," Sci. Adv. **3**, e1700160 (2017).

85. J. Feldmann, N. Youngblood, C. D. Wright, H. Bhaskaran, and W. H. P. Pernice, "All-optical spiking neurosynaptic networks with self-learning capabilities," Nature **569**, 208–214 (2019).

86. C. H. Sie, "Memory Devices Using Bistable Resistivity in Amorphous As-Te-Ge Films," Iowa State University (1969).

87. H. Hayat, K. Kohary, and C. D. Wright, "Emerging Nanoscale Phase-Change Memories: A Summary of Device Scaling Studies," Ref. Modul. Mater. Sci. Mater. Eng. 1–26 (2016).

88. S. Raoux, F. Xiong, M. Wuttig, and E. Pop, "Phase change materials and phase change memory," MRS Bull. **39**, 703–710 (2014).

89. D. L. N. and G. M. R. G. Neale, "Non-volatile, re-programmable, read-mostly memory is here," 56–60 (1970).

90. N. et al Yamada, "High-speed overwritable phase-change optical disk material.," Jpn. J. Appl. Phys. **1**, 61–66 (1987).

91. J. Hrusk, "Intel, Micron reveal Xpoint, a new memory architecture that could outclass DDR4 and NAND," https://www.extremetech.com/extreme/211087-intel-micron-reveal-xpoint-a-new-memory-architecture-that-claims-to-outclass-both-ddr4-and-nand.

92. Intel Corporation, "The Challenge of Keeping Up With Data," 3–8 (2019).

93. Y. Hui, J. S. Gomez-Diaz, Z. Qian, A. Alù, and M. Rinaldi, "Plasmonic piezoelectric nanomechanical resonator for spectrally selective infrared sensing.," Nat. Commun. **7**, 11249 (2016).

94. A. Q. Liu, W. M. Zhu, D. P. Tsai, and N. I. Zheludev, "Micromachined tunable metamaterials: A review," J. Opt. (United Kingdom) **14**, (2012).

95. S. Walia, C. M. Shah, P. Gutruf, H. Nili, D. R. Chowdhury, W. Withayachumnankul, M. Bhaskaran, and S. Sriram, "Flexible metasurfaces and metamaterials: A review of materials and fabrication processes at micro- and nano-scales," Appl. Phys. Rev. **2**, (2015).

96. J. Kerr, " LIV. A new relation between electricity and light: Dielectrified media birefringent (Second paper) ," London, Edinburgh, Dublin Philos. Mag. J. Sci. **50**, 446–458 (2018).

97. M. Hajizadegan, D. Fathi, and M. S. Sakhdari, "All-optical metamaterial switch based on Kerr effect with MWCNT composite," Phys. E Low-Dimensional Syst. Nanostructures **48**, 1–6 (2013).

98. F. Yi, E. Shim, A. Y. Zhu, H. Zhu, J. C. Reed, and E. Cubukcu, "Voltage tuning of plasmonic absorbers by indium tin oxide," Appl. Phys. Lett. **102**, (2013).

99. E. Feigenbaum, K. Diest, and H. A. Atwater, "Unity-order index change in transparent conducting oxides at visible frequencies," Nano Lett. **10**, 2111–2116 (2010).

100. Y. W. Huang, H. W. H. Lee, R. Sokhoyan, R. A. Pala, K. Thyagarajan, S. Han, D. P. Tsai, and H. A. Atwater, "Gate-Tunable Conducting Oxide Metasurfaces," Nano Lett. **16**, 5319–5325 (2016).

101. J. Baek, J.-B. You, and K. Yu, "Free-carrier electro-refraction modulation based on a silicon slot waveguide with ITO," Opt. Express **23**, 15863 (2015).

102. J. Park, J. H. Kang, X. Liu, and M. L. Brongersma, "Electrically Tunable Epsilon-Near-Zero (ENZ) Metafilm Absorbers," Sci. Rep. **5**, 1–9 (2015).

103. W. De Cort, J. Beeckman, R. James, F. A. Fernández, R. Baets, and K. Neyts, "Tuning of

silicon-on-insulator ring resonators with liquid crystal cladding using the longitudinal field component," Opt. Lett. **34**, 2054 (2009).

104. A. Salim and S. Lim, "Review of recent metamaterial microfluidic sensors," Sensors (Switzerland) **18**, (2018).

105. C. R. de Galarreta, A. M. Alexeev, Y. Y. Au, M. Lopez-Garcia, M. Klemm, M. Cryan, J. Bertolotti, and C. D. Wright, "Nonvolatile Reconfigurable Phase-Change Metadevices for Beam Steering in the Near Infrared," Adv. Funct. Mater. **28**, 1–9 (2018).

106. S. G.-C. Carrillo, G. R. Nash, H. Hayat, M. J. Cryan, M. Klemm, H. Bhaskaran, and C. D. Wright, "Design of practicable phase-change metadevices for near-infrared absorber and modulator applications," Opt. Express **24**, 13563 (2016).

107. C. R. de Galarreta, I. Sinev, A. M. Alexeev, P. Trofimov, K. Ladutenko, S. G.-C. Carrillo, E. Gemo, A. Baldycheva, V. K. Nagareddy, J. Bertolotti, and C. D. Wright, "All-Dielectric Silicon/Phase-Change Optical Metasurfaces with Independent and Reconfigurable Control of Resonant Modes," 1–34 (2019).

108. A. Afridi, J. Canet-Ferrer, L. Philippet, J. Osmond, P. Berto, and R. Quidant, "Electrically Driven Varifocal Silicon Metalens," ACS Photonics **5**, 4497–4503 (2018).

109. D. T. G.Chasteen, "Tunable Monochromators," https://www.shsu.edu/~chm_tgc/primers/mono.html.

110. J. W. Jeong, I. W. Jung, H. J. Jung, D. M. Baney, and O. Solgaard, "Multifunctional tunable optical filter using MEMS spatial light modulator," J. Microelectromechanical Syst. **19**, 610–618 (2010).

111. R. A. Lipson, "A Tunable Micro-Electro-Mechanical Optical Filter in Silicon," Imperial College London (2006).

112. N. Gat, "Imaging spectroscopy using tunable filters: a review," Proc. SPIE **4056**, 50–64 (2000).

113. J. F. Algorri, D. C. Zografopoulos, V. Urruchi, and J. M. Sánchez-Pena, "Recent Advances in Adaptive Liquid Crystal Lenses," Crystals **9**, 272 (2019).

114. L. Bei, G. I. Dennis, H. M. Miller, T. W. Spaine, and J. W. Carnahan, "Acousto-optic tunable filters: Fundamentals and applications as applied to chemical analysis techniques," Prog. Quantum Electron. **28**, 67–87 (2004).

115. M. J. Khan, H. S. Khan, A. Yousaf, K. Khurshid, and A. Abbas, "Modern Trends in Hyperspectral Image Analysis: A Review," IEEE Access **6**, 14118–14129 (2018).

116. S. Gupta, K. Ramesh, S. Ahmed, and V. Kakkar, "Lab-on-chip technology: A review on design trends and future scope in biomedical applications," Int. J. Bio-Science Bio-Technology **8**, 311–322 (2016).

117. T. G. Mayerhöfer, R. Knipper, U. Hübner, D. Cialla-May, K. Weber, H. G. Meyer, and J. Popp, "Ultra Sensing by Combining Extraordinary Optical Transmission with Perfect Absorption," ACS Photonics **2**, 1567–1575 (2015).

118. T. G. Mayerhöfer and J. Popp, "Periodic array-based substrates for surface-enhanced infrared spectroscopy," Nanophotonics **7**, 39–79 (2018).

119. X. Ren, K. Ren, and C. Ming, "Self-reference refractive index sensor based on

independently controlled double resonances in side-coupled u-shaped resonators," Sensors (Switzerland) **18**, 1–10 (2018).

120. CIE, "ISO/CIE 11664-1:2019(E) Colorimetry," Int. Stand. Organ. (2019).

121. R. N. Clark, "CIE Chromaticity and Perception," https://clarkvision.com/articles/color-cie-chromaticity-and-perception/.

122. Hewlett Packard, "Modern color models," https://www.handprint.com/HP/WCL/color7.html.

123. A. C. Harris and I. L. Weatherall, "Objective evaluation of color variation in the sand-burrowing beetle Chaerodes trachyscelides White (Coleoptera: Tenebrionidae) by instrumental determination of CIE LAB values," R. Soc. New Zeal. **20**, 254 (1990).

124. Gianni Monaco, "Coating Technology : Evaporation Vs Sputtering," AR Coat. Technol. 1–8 (2016).

125. T. Karabacak, J. J. Senkevich, G.-C. Wang, and T.-M. Lu, "Stress reduction in sputter deposited films using nanostructured compliant layers by high working-gas pressures," J. Vac. Sci. Technol. A Vacuum, Surfaces, Film. **23**, 986–990 (2005).

126. D. Maurya, A. Sardarinejad, and K. Alameh, "Recent Developments in R.F. Magnetron Sputtered Thin Films for pH Sensing Applications—An Overview," Coatings **4**, 756–771 (2014).

127. A. Büttner, A. C. Probst, F. Emmerich, C. Damm, B. Rellinghaus, T. Döhring, and M. Stollenwerk, "Influence of sputtering pressure on microstructure and layer properties of iridium thin films," Thin Solid Films **662**, 41–46 (2018).

128. N. Atiqah, I. H. Jaafar, M. Y. Ali, and B. Asfana, "Application of focused ion beam micromachining: A review," Adv. Mater. Res. **576**, 507–510 (2012).

129. E. D. Le Boulbar, P. J. P. Chausse, S. Lis, and P. A. Shields, "Displacement Talbot lithography: an alternative technique to fabricate nanostructured metamaterials," Nanotechnol. VIII **10248**, 102480Q (2017).

130. M. Marrese, V. Guarino, and L. Ambrosio, "Atomic Force Microscopy: A Powerful Tool to Address Scaffold Design in Tissue Engineering," J. Funct. Biomater. **8**, 7 (2017).

131. J. Goodge, "Energy-Dispersive X-Ray Spectroscopy (EDS)," https://serc.carleton.edu/research_education/geochemsheets/eds.html.

132. A. A. Bunaciu, E. gabriela Udriştioiu, and H. Y. Aboul-Enein, "X-Ray Diffraction: Instrumentation and Applications," Crit. Rev. Anal. Chem. **45**, 289–299 (2015).

133. P. W. H. Bragg and W. L. Bragg, "The reflection of X-rays by crystals," Proc. R. Soc. **17**, 428–438 (1913).

134. Nanophoton Corporation, "Basics of Raman scattering | Nanophoton corp," https://www.nanophoton.net/raman-spectroscopy/lessons/lesson-1.

135. E. Garcia-Caurel, A. De Martino, J. P. Gaston, and L. Yan, "Application of spectroscopic ellipsometry and mueller ellipsometry to optical characterization," Appl. Spectrosc. **67**, 1–21 (2013).

136. J.A Woollam Corporation, "What is Ellipsometry? - J.A. Woollam,"

https://www.jawoollam.com/resources/ellipsometry-tutorial/what-is-ellipsometry.

137. B. Gholipour, J. Zhang, K. F. MacDonald, D. W. Hewak, and N. I. Zheludev, "An All-Optical, Non-volatile, Bidirectional, Phase-Change Meta-Switch," Adv. Mater. **25**, 3050–3054 (2013).

138. Y. Y. Au, H. Bhaskaran, and C. D. Wright, "Phase-change devices for simultaneous optical-electrical applications," Sci. Rep. **7**, 1–7 (2017).

139. B. Smith, "Introduction to FTIR," Fundam. Fourier Transform Infrared Spectrosc. 1–13 (1996).

140. A. V Kolobov, P. Fons, A. I. Frenkel, A. L. Ankudinov, J. Tominaga, and T. Uruga, "Understanding the phase-change mechanism of rewritable optical media.," Nat. Mater. **3**, 703–708 (2004).

141. D. Lencer, M. Salinga, and M. Wuttig, "Design rules for phase-change materials in data storage applications," Adv. Mater. **23**, 2030–2058 (2011).

142. J. Reifenberg, E. Pop, and A. Gibby, "Multiphysics modeling and impact of thermal boundary resistance in phase change memory devices," Therm. … 106–113 (2006).

143. W. Wełnic, A. Pamungkas, R. Detemple, C. Steimer, S. Blügel, and M. Wuttig, "Unravelling the interplay of local structure and physical properties in phase-change materials," Nat. Mater. **5**, 56–62 (2005).

144. J. J. G. Arciniega, E. Prokhorov, F. J. E. Beltran, and G. Trapaga, "Crystallization of Ge : Sb : Te Thin Films for Phase Change Memory Application," Cdn.Intechopen.Com (2005).

145. A. Fantini, L. Perniola, M. Armand, J. F. Nodin, V. Sousa, A. Persico, J. Cluzel, C. Jahan, S. Maitrejean, S. Lhostis, A. Roule, C. Dressler, G. Reimbold, B. DeSalvo, P. Mazoyer, D. Bensahel, and F. Boulanger, "Comparative assessment of GST and GeTe materials for application to embedded phase-change memory devices," 2009 IEEE Int. Mem. Work. IMW '09 (2009).

146. A. K. U. Michel, P. Zalden, D. N. Chigrin, M. Wuttig, A. M. Lindenberg, and T. Taubner, "Reversible Optical Switching of Infrared Antenna Resonances with Ultrathin Phase-Change Layers Using Femtosecond Laser Pulses," ACS Photonics **1**, 833–839 (2014).

147. A. K. U. Michel, M. Wuttig, and T. Taubner, "Design Parameters for Phase-Change Materials for Nanostructure Resonance Tuning," Adv. Opt. Mater. **5**, 1–8 (2017).

148. S. Guerin, B. Hayden, D. W. Hewak, and C. Vian, "Synthesis and Screening of Phase Change Chalcogenide Thin Film Materials for Data Storage," ACS Comb. Sci. **19**, 478–491 (2017).

149. A. Lotnyk, U. Ross, S. Bernütz, E. Thelander, and B. Rauschenbach, "Local atomic arrangements and lattice distortions in layered Ge-Sb-Te crystal structures," Sci. Rep. **6**, 1–9 (2016).

150. F. Rao, K. Ding, Y. Zhou, Y. Zheng, M. Xia, S. Lv, Z. Song, S. Feng, I. Ronneberger, R. Mazzarello, W. Zhang, and E. Ma, "Reducing the stochasticity of crystal nucleation to enable subnanosecond memory writing," Science (80-.). **358**, 1423–1427 (2017).

151. E. Morales-Sánchez, E. F. Prokhorov, A. Mendoza-Galván, and J. González-Hernández, "Determination of the glass transition and nucleation temperatures in Ge2Sb2Te5 sputtered films," J. Appl. Phys. **91**, 697–702 (2002).

152. Q. Zhang, Y. Zhang, J. Li, R. Soref, T. Gu, and J. Hu, "Broadband nonvolatile photonic switching based on optical phase change materials: beyond the classical figure-of-merit," Opt. Lett. **43**, 94 (2018).

153. Y. Zhang, J. B. Chou, J. Li, H. Li, Q. Du, A. Yadav, S. Zhou, M. Y. Shalaginov, Z. Fang, H. Zhong, C. Roberts, P. Robinson, B. Bohlin, C. Ríos, H. Lin, M. Kang, T. Gu, J. Warner, V. Liberman, K. Richardson, and J. Hu, "Extreme Broadband Transparent Optical Phase Change Materials for High-Performance Nonvolatile Photonics," MIT **7014**, 1–16 (2018).

154. S. S. Yamda Noboru, Kimura Kunio, Takao Masatoshi, "Reversible optical information-recording medium," U.S. patent 5,278,011 (1994).

155. A. K. Mairaj, M. N. Petrovich, Y. W. West, A. Fu, D. W. J. Harwood, L. N. Ng, T. M. Monro, and D. W. Hewak, "Advances in Gallium Lanthanum Sulphide Glass for Optical Fibre and Devices," **4204**, 278–285 (2000).

156. A. Loireau-lozac and M. Guittard, "Glasses formed by rare earth sulphides La2S3 with gallium sulphide Ga2S3," Mater. Res. Bull. **11**, 1489–1496 (1976).

157. A. Ravagli, C. Craig, G. A. Alzaidy, P. Bastock, and D. W. Hewak, "Optical, Thermal, and Mechanical Characterization of Ga2Se3-Added GLS Glass," Adv. Mater. **29**, 1–5 (2017).

158. H. E.-H. Guangming Tao, J. V. B. Alexander M. Stolyarov, Sylvain Danto, and and A. F. A. Yoel Fink, John Ballato, "Infrared Fibres," Adv. Opt. Photonics **7**, 379–458 (2015).

159. P. Bastock, C. Craig, K. Khan, E. Weatherby, J. Yao, and D. W. Hewak, "Properties of Gallium Lanthanum Sulphide Glass," OSA 3–5 (2015).

160. T. Schweizer, D. Brady, and D. W. Hewak, "Fabrication and spectroscopy of erbium doped gallium lanthanum sulphide glass fibres for mid-infrared laser applications," Opt. Express **1**, 102 (1997).

161. B. Gholipour, "Novel Chalcogenide Optoelectronic and Nanophotonic Information Storage and Processing Devices," University of Southampton (2012).

162. W. Dong, H. Liu, J. K. Behera, L. Lu, R. J. H. Ng, K. V. Sreekanth, X. Zhou, J. K. W. Yang, and R. E. Simpson, "Wide Bandgap Phase Change Material Tuned Visible Photonics," Adv. Funct. Mater. **29**, 1–9 (2019).

163. T. Academy, R. Academy, and S. S. Trakt, "Re-writable DVDs: what makes phase-change materials work the way they do," Appl. Phys. A **73**, 1–21 (n.d.).

164. J. Orava, D. W. Hewak, and A. L. Greer, "Fragile-to-Strong Crossover in Supercooled Liquid Ag-In-Sb-Te Studied by Ultrafast Calorimetry," Adv. Funct. Mater. **25**, 4851–4858 (2015).

165. K. D. Shukla, N. Saxena, S. Durai, and A. Manivannan, "Redefining the Speed Limit of Phase Change Memory Revealed by Time-resolved Steep Threshold-Switching Dynamics of AgInSbTe Devices," Sci. Rep. **6**, 1–7 (2016).

166. T. Ohta, N. Yamada, H. Yamamoto, T. Mitsuyu, T. Kozaki, J. Qiu, and K. Hirao, "Progress of the Phase-change Optical Disk Memory," MRS Proc. **674**, (2001).

167. J. B. C. Yifei Zhang, Junhao Liang, Mikhail Shalaginov, Skylar Deckoff-Jones, Carlos Ríos, C. Christopher Roberts, Sensong An, Clayton Fowler, Sawyer D. Campbell, Bilal Azhar, and J. H. Gonçalves, Kathleen Richardson, Hualiang Zhang, Douglas H. Werner, Tian Gu, "Electrically Reconfigurable Nonvolatile Metasurface Using Optical Phase Change

Materials," Conf. Lasers Electro-Optics, OSA Tech. Dig. **paper JTh5**, (2019).

168. C. Ríos, Y. Zhang, S. Deckoff-Jones, H. Li, J. B. Chou, H. Wang, M. Shalaginov, C. Roberts, C. Gonçalves, V. Liberman, T. Gu, J. Kong, K. Richardson, and J. Hu, "Reversible Switching of Optical Phase Change Materials Using Graphene Microheaters," Proc. CLEO, OSA, OSA **paper SF2H**, (2019).

169. K. S. Andrikopoulos, S. N. Yannopoulos, A. V. Kolobov, P. Fons, and J. Tominaga, "Raman scattering study of GeTe and Ge2Sb2Te5 phase-change materials," J. Phys. Chem. Solids **68**, 1074–1078 (2007).

170. T. Li, L. Wu, X. Ji, Y. Zheng, G. Liu, Z. Song, J. Shi, M. Zhu, S. Song, and S. Feng, "Carbon doping induced Ge local structure change in as-deposited Ge 2 Sb 2 Te 5 film by EXAFS and Raman spectrum," AIP Adv. **8**, 1–8 (2018).

171. M. Beruete, M. Sorolla, and I. Campillo, "Left-handed extraordinary optical transmission through a photonic crystal of subwavelength hole arrays," Opt. Express **14**, 5445 (2006).

172. F. J. G. De Abajo, H. Altug, and V. Pruneri, "Ultrafast and broadband tuning of resonant optical nanostructures using phase-change materials," Adv. Opt. Mater. **4**, 1–21 (2016).

173. M. Armand, D. Wright, and M. M. Aziz, "Electro-thermal process for probe storage on phase-change media," TuE15 (2014).

174. Santa Barbara Research Intitute, "Atmospheric Transmission," http://www.coseti.org/atmosphe.htm.

175. W.-Y. Jang, Z. Ku, J. Jeon, J. O. Kim, S. J. Lee, J. Park, M. J. Noyola, and A. Urbas, "Experimental Demonstration of Adaptive Infrared Multispectral Imaging using Plasmonic Filter Array," Sci. Rep. **6**, 34876 (2016).

176. K. Lin, "No TitleHow Many Colors Can Most of Us Actually See?," https://hyperallergic.com/187012/how-many-colors-can-most-of-us-actually-see/.

177. Purde University, "Biology II: Development, Structure, and Function of Organisms," https://wiki.bio.purdue.edu/biol13100/index.php/2011_Problem_Set_7_Number_11_Answer.

178. P. Hosseini, C. D. Wright, and H. Bhaskaran, "An optoelectronic framework enabled by low-dimensional phase-change films," Nature **511**, 206–211 (2014).

179. S. G. C. Carrillo, L. Trimby, Y. Y. Au, V. K. Nagareddy, G. Rodriguez-Hernandez, P. Hosseini, C. Ríos, H. Bhaskaran, and C. D. Wright, "A Nonvolatile Phase-Change Metamaterial Color Display," Adv. Opt. Mater. **1801782**, (2019).

180. S. G.-C. Carrillo, A. M. Alexeev, Y.-Y. Au, and C. D. Wright, "Reconfigurable phase-change meta-absorbers with on-demand quality factor control," Opt. Express **26**, 25567 (2018).

181. T. Cao, C. Wei, R. E. Simpson, L. Zhang, and M. J. Cryan, "Rapid phase transition of a phase-change metamaterial perfect absorber," Opt. Mater. Express **3**, 1101 (2013).

182. Bodle Technologies, "Applications of reflective displays," https://www.bodletechnologies.com/applications.

183. A. Krasnok, S. Makarov, M. Petrov, R. Savelev, P. Belov, and Y. Kivshar, "Towards all-dielectric metamaterials and nanophotonics," Metamaterials X **9502**, 950203 (2015).

9 APPENDIX

9.1 SCRIPT FOR CALCULATION OF COLOURS FROM SPECTRA

This MATLAB script takes a reflection or transmission spectra in the visible, and converts it into colour, displaying the information in a variety of manners, including RGB numbers and on CIE chromaticity maps.

```
lam = (380:1:780);
%% Reading and plotting reflectance spectra
% names of txt files with Freq/data. 1,1 = top layer, 2,1 is 2nd, etc.
if find_n_and_k > 0
    excelRX = xlsread('pixel transmission','sheet1');
    EX_RX = interp1(excelRX(:,1),excelRX(:,2),freq);
    ref_n = interp1(excelRX(:,1),excelRX(:,3),freq)
    ref_k = interp1(excelRX(:,1),excelRX(:,4),freq)
end

   Rcyan = interp1(Rcyan(:,1),Rcyan(:,2:12),lam*10^-9,'spline'); %
interpolating per nm
   Rmag = interp1(Rmag(:,1),Rmag(:,2:12),lam*10^-9,'spline');
   Ryel = interp1(Ryel(:,1),Ryel(:,2:12),lam*10^-9,'spline');

 figure(1) % plotting reflection spectra
  hold on
  subplot(3,1,1)
  plot(lam,Rcyan,'linewidth',1)
  title(filenames{1});
  xlim([380, 780]);

  subplot(3,1,2)
  plot(lam,Rmag,'linewidth',1)
  title(filenames{2});
  ylabel('Reflectance','fontsize',14);
  legend('0%','10%','20%','30%','40%','50%','60%','70%','80%','90%','100%');
  xlim([380, 780]);

  subplot(3,1,3)
  plot(lam,Ryel,'linewidth',1)
  title(filenames{3});
  xlabel('Wavelength (nm)','fontsize',14);
  xlim([380, 780]);
  fh = figure(1); % These 2 lines make the plot background white.
  set(fh, 'color', 'white');

%% Calling Pspectro for visual colour map
for i = 1:1:11;
    Rx_in(:,1,i) = lam;
    Rx_in(:,2,i) = Rcyan(:,i);
    [XYZ2degCyan(i,:),isp,lux,xyz2degCyan(i,:),cct,duv,Ra,R] =
pspectro(Rx_in(:,:,i));

    Rx_in(:,2,i) = Rmag(:,i);
    [XYZ2degMag(i,:),ispd,lux,xyz2degMag(i,:),cct,duv,Ra,R] =
pspectro(Rx_in(:,:,i));
```

```
    Rx_in(:,2,i) = Ryel(:,i);
    [XYZ2degYel(i,:),ispd,lux,xyz2degYel(i,:),cct,duv,Ra,R] =
pspectro(Rx_in(:,:,i));
end

%% converting to RBG, combining pixels, and converting back to XYZ
% normalised XYZ (xyz) -> to rgb -> combine pixels in rgb -> to XYZ -> LA
gamma = 2.2;
rgbtoXYZ = [0.4124564  0.3575761  0.1804375; % for SRGB D65 whitepoint
            0.2126729  0.7151522  0.0721750;
            0.0193339  0.1191920  0.9503041];
XYZtorgb = inv(rgbtoXYZ);

% convert from XYZ to rgb (linear rgb)
for i = 1:1:length(XYZ2degCyan)
    rgbCyan(i,:) = XYZtorgb * XYZ2degCyan(i,:)';
    rgbMag(i,:) = XYZtorgb * XYZ2degMag(i,:)';
    rgbYel(i,:) = XYZtorgb * XYZ2degYel(i,:)';
end

% finding all combinations of rgb
cnt = 1;
for i=1:1:length(rgbCyan)
    for j=1:1:length(rgbMag)
        for k=1:1:length(rgbYel)
            rgbmix(cnt,1) = (rgbCyan(i,1)+rgbMag(j,1)+rgbYel(k,1))/3;
            rgbmix(cnt,2) = (rgbCyan(i,2)+rgbMag(j,2)+rgbYel(k,2))/3;
            rgbmix(cnt,3) = (rgbCyan(i,3)+rgbMag(j,3)+rgbYel(k,3))/3;
            cnt = cnt + 1;
        end
    end
end

for i = 1:1:length(rgbmix)
    % Converting rgb (linear RGB) back into XYZ
    XYZmix(i,:) = rgbtoXYZ * rgbmix(i,:)'; % rgb back into XYZ

    % converting from XYZ into LAB
    LAB(i,:) = xyz2lab([XYZmix(i,1) XYZmix(i,2) XYZmix(i,3) ]); %converting
from CIE XYZ into LAB1976

    % converting from XYZ into normalised xyz for ploting onto CIE map
    xyzmix(i,1) = XYZmix(i,1) / sum(XYZmix(i,1)+XYZmix(i,2)+XYZmix(i,3));
    xyzmix(i,2) = XYZmix(i,2) / sum(XYZmix(i,1)+XYZmix(i,2)+XYZmix(i,3));
    xyzmix(i,3) = XYZmix(i,3) / sum(XYZmix(i,1)+XYZmix(i,2)+XYZmix(i,3));
end

%% plotting onto CIE 1931
figure(6)  % Plotting colours onto CIE 1930
    cieplot()
    hold on

     scatter(xyz2degCyan(:,1), xyz2degCyan(:,2), 'c','filled'); %Cyan
     scatter(xyz2degCyan(:,1), xyz2degCyan(:,2), 'k','LineWidth',1.5); %Cyan

     scatter(xyz2degMag(:,1), xyz2degMag(:,2), 'm','filled'); %Mag
     scatter(xyz2degMag(:,1), xyz2degMag(:,2), 'k','LineWidth',1.5); %Mag

     scatter(xyz2degYel(:,1), xyz2degYel(:,2), 'y','filled'); %Yel
     scatter(xyz2degYel(:,1), xyz2degYel(:,2), 'k','LineWidth',1.5); %Yel

    % adding labels to scatter points
    for i = 1:1:(numel(stack_thickness)/LayerNum)
```

```
        text(CIEx(i)+0.005, CIEy(i),
num2str(stack_thickness(i,:)*10^9),'FontSize',8);
    end
    fh = figure(6); % These 2 lines make the plot background white.
    set(fh, 'color', 'white');
    title('CIE 1931');
    hold off

%% Plotting colours onto CIE_LUV map
% Calculating CIELUV
for i = 1:1:numel(xyzmix(:,1))
         CIELUV_mix(i,1) = 4*xyzmix(i,1)/(-2*xyzmix(i,1)+12*xyzmix(i,2)+3);
         CIELUV_mix(i,2) = 9*xyzmix(i,2)/(-2*xyzmix(i,1)+12*xyzmix(i,2)+3);
end
for i = 1:1:length(xyz2degCyan)
    CIELUV_cyan(i,1) = 4*xyz2degCyan(i,1)/(-
2*xyz2degCyan(i,1)+12*xyz2degCyan(i,2)+3);
    CIELUV_cyan(i,2) = 9*xyz2degCyan(i,2)/(-
2*xyz2degCyan(i,1)+12*xyz2degCyan(i,2)+3);

    CIELUV_mag(i,1) = 4*xyz2degMag(i,1)/(-
2*xyz2degMag(i,1)+12*xyz2degMag(i,2)+3);
    CIELUV_mag(i,2) = 9*xyz2degMag(i,2)/(-
2*xyz2degMag(i,1)+12*xyz2degMag(i,2)+3);

    CIELUV_yel(i,1) = 4*xyz2degYel(i,1)/(-
2*xyz2degYel(i,1)+12*xyz2degYel(i,2)+3);
    CIELUV_yel(i,2) = 9*xyz2degYel(i,2)/(-
2*xyz2degYel(i,1)+12*xyz2degYel(i,2)+3);
end

 figure(2)  % Plotting colours onto CIELUV 1976
     CIELUV_pic = imread('CIELUV.png');
     imagesc([0 0.7], [0 0.6], flipud(CIELUV_pic))
     hold on
     %scatter(CIELUV_mix(:,1), CIELUV_mix(:,2)); % all combined pixels

     scatter(CIELUV_cyan(:,1), CIELUV_cyan(:,2), 'c','LineWidth',2); %Cyan
     scatter(CIELUV_cyan(:,1), CIELUV_cyan(:,2), 'k','LineWidth',0.5); %Cyan

     scatter(CIELUV_mag(:,1), CIELUV_mag(:,2), 'm','LineWidth',2); %Mag
     scatter(CIELUV_mag(:,1), CIELUV_mag(:,2), 'k','LineWidth',0.5); %Mag

     scatter(CIELUV_yel(:,1), CIELUV_yel(:,2), 'y','LineWidth',2); %Yel
     scatter(CIELUV_yel(:,1), CIELUV_yel(:,2), 'k','LineWidth',0.5); %Yel

     set(gca,'ydir','normal')
     fh = figure(2); % These 2 lines make the plot background white.
     set(fh, 'color', 'white');
     title('CIELUV 1976');
     hold off

%% Plotting CIELAB 3D
 plot_Lab(4,LAB',1,'k',24,0);
plot_Lab(2,LAB',1,'k',12,0);

    rgbCyanNorm = rgbCyan(11,:)./sum(rgbCyan(11,:));
    rgbMagNorm = rgbMag(11,:)./sum(rgbMag(11,:));
    rgbYelNorm = rgbYel(11,:)./sum(rgbYel(11,:));

RGBCyan = 255*rgbCyanNorm.^(1/gamma);
RGBMag = 255*rgbMagNorm.^(1/gamma);
RGBYel = 255*rgbYelNorm.^(1/gamma);
```

9.2 SCRIPT FOR DETERMINING EXTINCTION COEFFICIENT

This MATLAB script takes in the transmission spectra through two bulk samples and their respective thickness, and calculates the wavelength dependant extinction coefficient (k).

```
% thickness of two layers, in m
t1 = 35 *10^-9;    % thinner layer
t2 = 200 *10^-9;   % thicker layer
%Excel file to extract data from
filename = 'GLS Transmission.xlsx';
sheetname = 'GLS';

%Extracting transmission data from Excel
data = xlsread(filename,sheetname)

wavelength = (10^-9)*data(1:end, 1);  %Excel doc should contain it in nm
T1    = data(1:end, 2); % Transmittance
T2    = data(1:end, 3); % Transmittance

k = ( wavelength.*log(T1./T2) )/( (t2-t1)*(4*pi) );
k = ( wavelength.*log(T1./T2) )/( (t2-t1)*(4*pi) );

plot((10^9)*wavelength,k)
xlabel('Wavelength, nm');
ylabel('Extinction Coefficient');

%Writing to Excel file
warning('off','MATLAB:xlswrite:AddSheet')
col_header = {'Wavelength', 'k'};
xlswrite(filename,col_header,'K','A1');

xlswrite(filename,(10^9)*wavelength,'k','A2');
xlswrite(filename,k,'k','B2');
```